Title

Tracing Alfvén Waves, Turbulence, and Gaussian Structures in the Upper Corona and Inner Heliosphere with in-situ Measurements, Statistical Analyses, and Modeling

Author

Huang, Zesen

Publication Date

2024

Peer reviewed|Thesis/dissertation

UNIVERSITY OF CALIFORNIA
Los Angeles

Tracing Alfvén Waves, Turbulence, and Gaussian Structures in the Upper Corona and Inner Heliosphere with in-situ Measurements, Statistical Analyses, and Modeling

A dissertation submitted in partial satisfaction
of the requirements for the degree
Doctor of Philosophy in Geophysics and Space Physics

by

Zesen Huang

2024

ABSTRACT OF THE DISSERTATION

Tracing Alfvén Waves, Turbulence, and Gaussian Structures in the Upper Corona and Inner Heliosphere with in-situ Measurements, Statistical Analyses, and Modeling

by

Zesen Huang
Doctor of Philosophy in Geophysics and Space Physics
University of California, Los Angeles, 2024
Professor Marco C.M. Velli, Chair

Parker Solar Probe (PSP) was launched in late 2018, and since then it has been providing *in situ* measurements of the inner heliosphere and upper solar corona. The journey of PSP to the Sun is continuously pushing the frontiers of heliophysics. In this dissertation, by combining *in situ* observations and computer simulations, we aimed to bring new insights from PSP to our current understanding of Alfvén waves, turbulence, and solar wind structures. The primary results of this dissertation are the following: (1) Through 1D MHD simulation, we show that the total wave action is conserved in the linear mode conversion of magnetosonic waves at the equipartition layer (where the sound speed equals the Alfvén speed); (2) Close to the Sun, contrary to standard solar wind turbulence models, the energy-containing $1/f$ range disappears in solar wind turbulence. Instead, the low-frequency turbulence spectrum is characterized by a shallow-inertial double power law, where the low-frequency part scales like $f^{-0.5}$; (3) The *in situ* observed magnetic field magnitude B shows a surprisingly sensitive response to Gaussianity tests, which leads to a scale- and location-dependent Gaussianity scalogram, unveiling coherent structures spanning seven orders of magnitude in time. Notably, combined with Potential Field Source Surface (PFSS) modeling, we confirmed that the radially normalized B follows a near-perfect Gaussian distribution when PSP is immersed in magnetic field lines that are connected back to coronal holes. Additionally, computer simulations show that Gaussian distribution is the natural relaxation state for Alfvénic turbulence. (4) The shallow-inertial

double power law indicates a concentration of fluctuation energy around the 'bend' in spectral slopes. Based on statistics from the first 17 PSP encounters, we found a systematic trend that the primary fluctuation frequency decreases with solar wind advection time and eventually saturates at around 3 minutes for the most pristine solar wind. This is consistent with remote sensing observations of the chromosphere, and indicates that the Alfvén waves in the solar wind could ultimately be driven by p-mode oscillations in the photosphere. Our results have two primary implications: (1) Gaussianity of B serves as a good parameter for identifying structures in the solar wind, especially the time intervals that are magnetically connected to coronal holes; (2) Alfvén waves in the solar wind are likely originating from the solar convection zone resonance chamber. Therefore, this dissertation can serve as a preliminary study to provide constraints on the formation of $1/f$ energy containing range and coronal heating mechanisms.

The dissertation of Zesen Huang is approved.

Eduardo Paulo Da Costa Alves

Hao Cao

Vassilis Angelopoulos

Marco C.M. Velli, Committee Chair

University of California, Los Angeles

2024

Magnolia Collection

玉兰集

To my mother...

a single mom who bestowed life upon me

To my maternal grandparents...

who continually bless me with love and joy

To my paternal grandparents...

who instilled in me honesty and integrity

To my wife...

with whom I will share the rest of my life

TABLE OF CONTENTS

LIST OF FIGURES

LIST OF TABLES

PREFACE

I've wanted to write this preface numerous times over the past year, but now that my defense is over and I'm sitting in front of the computer, my mind is surprisingly blank. I had rehearsed the defense scene countless times in my head, but I never anticipated that everything would be so sudden and natural. When my advisor said, "Congratulations!" I was surprisingly calm; it was as if everything had fallen into place perfectly.

My Ph.D. journey began on September 3, 2019. That evening, I landed at Los Angeles International Airport at 7:45 PM and had my first meal at a small sushi restaurant in Little Osaka that was still open late at night. I particularly like to use the concept of "life density" to describe time. In those early days, my life density was extraordinarily high; every sunrise and sunset, every hour, and even every minute left an incredibly deep impression. My first impression of Los Angeles was very positive—the dry air, the lavender sunsets, the relatively clean streets (near my home)—all of which were immensely attractive to a 21-year-old. Although I didn't buy a car, I had my own bicycle, which allowed me to slowly explore the world around me. On weekend evenings, I could listen to bands play in Little Osaka and join dozens of strangers in loud sing-alongs. Such joyful times could easily captivate any student who had endured the arduous years of undergraduate life at the University of Science and Technology of China (USTC).

However, everything came to an abrupt halt during the Chinese New Year in 2020.

That day, I was in a hotel room at the Venetian in Las Vegas playing "Plague Inc." The events popping up in the game were eerily similar to the real-world news alerts. An uneasy feeling arose within me. That night, I bought out all the N95 masks (which turned out to be industrial dust masks and quite useless) from the pharmacies in Las Vegas and sent them back with my mom when she returned to China. In the following two months, although the weather remained the same, an unsettling feeling lingered in the air. Fewer and fewer students attended classes, cases increased across the United States, and large-scale infections began to emerge in Los Angeles. By March 19, 2020, sensing that things were getting out of hand, I hastily bought a ticket from China Southern Airlines

and fled back to China for refuge.

Unexpectedly, that departure lasted nearly two years.

To be precise, from March 21, 2020, to November 27, 2021, a total of 20 months. To make a long story short, during my time in China, due to my advisor's busyness and the difficulty of maintaining contact, I gave up on my studies and instead attempted to start a business with a group of people. Initially, things went quite smoothly; we successfully led a tour group to witness the launch of Tianwen-1 and later organized a second tour group to witness the launch of Tiangong-1. During this period, I didn't entirely abandon my work, but the unpredictable international situation, the ever-changing virus variants, and my advisor's intermittent presence made it almost impossible to advance my studies and research.

Looking back now, my experience wasn't all that bitter and painful. Compared to others, I might even say I was quite lucky during the pandemic. Although I lost a significant amount of money (for me) in the stock market, I perfectly avoided the Delta variant outbreak in the US and the large-scale lockdowns and mass testing caused by the Omicron variant in China (I didn't undergo any government-organized nucleic acid tests during my time in China!). Moreover, despite my advisor often being out of touch during the pandemic, I continued to receive my salary, so aside from psychological distress, my life was actually quite secure.

Before returning to the US (on November 12, 2021), I even got married. Honestly, getting married at 24 wasn't my original plan. Coupled with other unfortunate events over the past few years, I wasn't keen on facing this reality. However, looking back, those troubles, once resolved, gradually became endearing. The hysteria now seems somewhat ridiculous.

Getting back to the point, on November 21, 2021, I finally returned to Los Angeles after nearly two years away.

I remember the moment I pushed open the door to my office and found everything exactly as I had left it, as if time had frozen 20 months ago. The February and March

2020 calendars were still on the wall, showing that I had worked out ten times in February and needed to keep it up in March. I stood there, stunned, as memories from the past 20 months flooded my mind. I remembered that my roommate and senior, Xu Sixue, who had returned to China with me, had completely disappeared, fading from everyone's memory like my undergraduate classmate who had committed suicide.

I am a particularly conflicted person, cherishing friendships to an almost pathological degree, but I am also extremely sensitive to others' reactions, which sometimes makes me socially awkward. It took me a long time to come to terms with my roommate's (and senior's) disappearance. If the pandemic had any significant impact on me, this event was probably the most hurtful. However, life goes on. After returning to Los Angeles, I was lucky to be taken in by classmates and moved into UCLA's graduate dormitory, Magnolia Court, room 215, where I stayed for two and a half years.

I am someone who craves social interaction, and in this regard, I am quite fortunate. Due to pandemic lockdowns throughout 2022, both the news and communications from family depicted a dire situation in China, and I couldn't go back, making my marriage precarious. However, in the small 50-square-meter space of Magnolia Court room 215, we were incredibly happy. Every night, I would cook for a few people (mainly Li Yichen, Shi Xiaofei, and Kang Ning), and after dinner, we would go to the study room downstairs to play cards, living a life not unlike that of Hu Shi. It was immensely enjoyable!

After returning to the US, my research gradually got back on track. With the help of my senior Shichen and colleague Nikos Sioulas, I published my first and second papers (on 1D MHD simulations and observations of solar wind turbulence, respectively). Although there were occasional conflicts, the collaborations were generally smooth.

Since childhood, I have loved reading encyclopedias, with the most fascinating chapters being paleontology and stellar evolution (later I learned this process is called the Hertzsprung-Russell diagram). From a young age, my sole dream was to become an astrophysicist. Whether by talent or destiny, my educational journey has been quite smooth, leading me to join the School of the Gifted Young at USTC and choose space

physics as my major, where I unexpectedly performed well (I was actually top of my class). While applying for graduate school, I was doing a summer research program at Berkeley. I heard that NASA was about to launch a spacecraft to probe the solar corona called Parker Solar Probe, which was incredibly cool to a 20-year-old. So, I applied to UCLA, hoping to be part of this mission. Despite some bumps along the way, I ultimately achieved my goal.

Entering UCLA as a graduate student, I experienced an existential crisis for a long time. My lifelong dream had been realized so perfectly and precisely—I had truly become an "astrophysicist" (though not yet a full-fledged scientist, but that's just a matter of time). I suddenly felt my life might be meaningless. With my dream achieved, what else could I do? This sense of nihilism peaked after completing my first two projects: if I was merely following in the footsteps of others, doing work that would eventually be completed by someone, what was the point of "me"? I realized I needed to do something only "I" could do; if that wasn't possible, at least do something that would ensure everyone would remember "me."

In this regard, I am extremely fortunate. My third and fourth projects essentially resolved my existential crisis. My third project was based on some unexpected discoveries. These observations were not novel, but I was certain that this discovery required "my" perspective to be revealed. Shamelessly, it was "my" unique insight. My fourth project was a low-hanging fruit unprecedented in the field. Harvesting this fruit didn't require deep understanding or exceptional skill, just being in the right place at the right time, discussing it with the right people, and noticing it, and I happened to be that person—three lives' worth of luck, indeed.

First and foremost, I would like to thank my advisor, Professor Marco Velli. Without him, none of my research experiences would have been possible. Over the years, I have been fortunate to receive his guidance, and the insights into physical phenomena I gained from him will benefit me for a lifetime. As an advisor, he generously funded my academic activities and guided my studies without reservation during my five-year PhD journey. As a collaborator, he is one of the most brilliant physicists I have ever met, and discussing

with him has been my most enjoyable time. As a mentor, the life experiences he shared with me are invaluable. Next, I would like to thank my senior, Dr. Shichen. Without his selfless help, my PhD journey would not have been so smooth and successful. I also want to thank my colleague, Dr. Nikos Sioulas. Despite occasional conflicts over the years, the problems we discussed day and night formed the foundation of my work. Additionally, I want to express my gratitude to Professor Benjamin Chandran and Dr. Lorenzo Matteini; collaborating with them has been incredibly enriching. I also want to thank the members of my defense committee, Professor Vassilis Angelopoulos, Professor Hao Cao, and Professor Paulo Alves.

Outside of research, the support of friends has also been indispensable over these years. I want to thank Huang Sheng, Su Xue, Chen Hanzhang, Li Yichen, Shi Xiaofei, Kang Ning, Jia Yingdong, Liu Jiarui, Ma Donglai, and Xu Sixue. Their presence made my five years as a Ph.D. student far from boring and filled with joy. Finally, I want to thank three great cities: Guangzhou, Hefei, and Los Angeles, for nurturing, educating, and shaping me.

Looking back on my life, I can't help but marvel at how lucky I am. Although my childhood family life was somewhat tumultuous with my parents divorcing early, my mother, as a strong single parent, along with my grandparents, gave me nearly infinite love and care, allowing me to grow up healthy and happy. My paternal grandparents were also always present, encouraging me by example during the first twenty years of my life to become an upright, kind, and grateful person. Lastly, there is my wife and the eight cats she raised, whose presence has made my life endlessly interesting and brought me unprecedented happiness. My 21-year academic journey has been a consistent process of fulfilling a long-held wish: who could have imagined that the seed of hope to become a physicist planted in my childhood would grow into a robust tree 21 years later? This must be destiny, right?

Due to the COVID lockdown, realistically speaking, my 'real' PhD career only started in late 2021. For the last three years of my PhD career, I spent most of my time in Apt

215 of Magnolia Court, Weyburn Terrace. This tiny 2B2B apartment has witnessed many fun, warm, sad, depressed, and frustrated moments. Over time, I gradually developed some twisted feelings about this place. In 2022, even though the western world had mostly recovered from COVID and resumed international travel, the majority of Asian countries, especially China, remained closed to the rest of the world. Partially due to this reason, I was regularly cooking for 4-5 people daily to give myself a compensatory feeling of being home. During those days, we played poker every day after dinner (potentially occupying a significant portion of the time that should have been dedicated to research). One day, it suddenly came to my mind that I should give a proper Chinese name to the place where I had been living. However weird it may seem in western culture, it has been a millennia-old tradition for Chinese gentlemen to give their residences elegant, sophisticated nicknames as a representation of their noble, reputable virtues. At that moment, I realized that a literal translation of the name 'magnolia court' into Chinese '玉兰阁', where '玉兰' is magnolia and 'court' is '阁', is actually a very elegant choice. The symbolism of '玉兰' in Chinese is noble character and lofty aspirations, which aligns quite well with my own ideals inspired by my grandfather. Subsequently, I started to call my little apartment building '玉兰阁', and unintentionally this name gained some recognition among friends and acquaintances. As I progressed in my PhD career and gradually gathered some publications, I started to develop an idea that I should also name my dissertation '*magnolia collection*'. And this is the preface for it (a certified translation from the Chinese version by ChatGPT).

玉兰集序

去年到现在数次想动笔写这篇序，如今答辩通过后坐在电脑前，反而脑袋却空空如也了。脑子里曾经无数次预演答辩的场景，却未曾预料到一切竟会是如此的仓促而自然，当我老板从嘴里说出：“Congratulations！”的那一刻，我平静得出奇，正所谓水到而渠成。

我的博士生涯从2019年9月3日开始，那天晚上7点45分落地洛杉矶国际机场，晚上吃的第一顿饭是小大阪一家凌晨还在营业的小寿司店的彩虹加州卷。我特别喜欢用“人生浓度”这个概念来形容时间，初来乍到的那几天，人生浓度是高得出奇的，每个日出到日落，每个小时，甚至到每一分钟，都留下来极其深刻的回忆。我对洛杉矶的第一印象很好——干燥的空气、淡紫色的落日、还算整洁的街道（我家附近），这一切对于一个21岁的年轻人来说是有巨大吸引力的。虽然没有买车，但是拥有一辆自己的自行车，可以慢慢探索周围的世界，可以在周末的晚上听小大阪乐队的演奏，和数十个路人一起大声合唱，这样的快乐时光足以让任何一个在科大校园里熬过了苦大仇深的四年青春的学生沦陷。

当然，这一切在2020年的春节戛然而止。

那天，我在拉斯维加斯威尼斯人的酒店房间里玩《瘟疫公司》，游戏弹窗上显示的事件和真实世界新闻的推送惊人的相似，不安的感觉油然而生。当天晚上，我买空了拉斯维加斯所有药店的N95口罩（事后发现其实一点用都没有，因为是工业用的防尘口罩），后来让我妈回国的时候带上了。接下来的两个月，虽然天气依旧，但是空气里总是飘浮着不安的感觉——来上课的学生越来越少，全美各地的病例越来越多，直到洛杉矶逐渐开始大规模爆发感染。到了2020年的3月19日，我觉得事情不对，就临急临忙买了一张南航的机票，溜回国内避难了。

没想到这一走，就是接近两年。

确切地说，是从2020年3月21号到2021年11月27号，总共20个月。长话短说，这段在国内的时光，因为导师的忙碌，难以维持的联系，我干脆就直接放弃治疗转而试图和一群人一起创业去了。一开始其实还挺顺利的，我们成功带了一个旅游团去观摩天问一号的发射，后来也组织了第二次观摩团，去见证了天宫一号的发射。这期间我也不是不想工作，但是风云诡谲的国际形势，难以捉摸的病毒变异，时有时无的导师存

在都让我几乎无法推进我的学业和科研。

现在回过头去看，我自己的经历也并非那么苦大仇深，甚至比起旁人，我在疫情期间的经历可以算是相当幸运的了。我虽然在股市里亏掉了（对于我来说）很大一笔钱，但是我完美地躲过了美国的Delta变种疫情和国内的Omicron变种导致的大规模封控和核酸检测（我在国内的那段时间，我没有做过任何一次政府组织的核酸检测！）。而且虽然疫情期间我导师经常失联，但是我的工资是一直在发的，所以其实我除了心理上的折磨，生活上甚至可以说是十分安心的。

在回美国前夕（2021年11月12日）我甚至结了一个婚。诚实地说在24岁这个时间点结婚并非我的本愿，结合起前后几年发生的其他并不是很顺心的事故，我其实一直以来都不是很想直面这个现实。当然回顾过去，那些烦恼在都被解决之后竟慢慢变得可爱了起来，那些歇斯底里如今都显得多少有点可笑了。

言归正传，在2021年11月21日，我终于回到了阔别快两年的洛杉矶。

我还记得我第一次回到办公室推开门的那一瞬间，发现桌上的一切竟还是我离开的时候的样子，宛如时光冻结了一般，停留在了20个月前。墙上甚至还贴着2020年2月份和3月份的月历，显示我二月健身了10次，三月份仍需努力。那一刻我愣住了，脑子里开始涌出过去20个月的诸多回忆，我想起来和我一起回国的室友兼师兄许思学已经彻底消失不见，就像我本科跳楼自杀的同班同学一样，慢慢地在所有人的回忆中淡去。

我是一个特别纠结的人，我特别珍视（甚至有点病态）友情，但是我对他人的反应又特别的敏感，导致我有时候是一个社交上十分尴尬的人。其实对于室友（兼师兄）人间蒸发这件事，我花了很长时间才彻底接受。如果说疫情真的对我造成了什么伤害的话，这件事本身可以说是伤害最大的一例了。然而生活总是要继续的，回到洛杉矶之后我幸运地得到了同学的收留，住进了UCLA研究生宿舍Magnolia Court（玉兰阁）的215房，而这一住，就是两年半。

我还是一个极端渴求社交的人，在这一点上，我也是相当幸运的。由于疫情的封锁，2022全年，无论是从新闻还是通过家人通讯获取的国内消息都可以说是相当水深火热，而我也没有办法回去，因此我的婚姻也事实上岌岌可危。然而在玉兰阁215室，这五十平米见方的小空间内，我们却是无比快乐的——我每天晚上都会给几个人（主要是李一辰、石晓霏和康宁）做饭，饭后我们就会到楼下的学习室（棋牌室）打牌，

简直和胡适的生活别无二致，好不快活！

回到美国之后科研也逐渐走上正轨，在师兄时辰和同事Nikos Sioulas的帮助下，我也逐渐发表了我的第一和第二个工作（分别是一维的MHD模拟和太阳风湍流的观测工作）。在这个过程中，虽然偶有摩擦，但是合作上还是十分顺畅的。

我从小酷爱阅读百科全书，那个时候书上最吸引我的无非就是两个章节，分别是古生物学和恒星演化（后来知道这个过程叫做赫罗图）。于是自童年开始，我几乎就只有一个梦想，那就是成为一个研究天体的物理学家。说是天赋也好，宿命也好，我这些年求学的过程可以说是相当顺利的，最终我去到了中国科大少年班学院并选择了空间物理作为我的专业，并意外地成绩还不错（嘿嘿其实是专业第一）。当初申请研究生的时候，我正在伯克利做暑研，那时我听说NASA马上就要发射一个飞船去局地探测太阳大气，叫做Parker Solar Probe——这对于一个二十岁的小男生来说该有多酷啊！！于是我就义无反顾地申请了UCLA，希望能成为这个事业的一份子。显而易见，虽然稍有坎坷，但是最终我得偿所愿。

其实在进入UCLA成为研究生后，我有很长一段时间陷入了存在主义危机，因为我从小到大的梦想就这么完美、精确地实现了——我真的成为了一个“研究天体的物理学家”（虽然还没到“家”的地步，但是这是迟早的事）。那时我突然意识到，我的人生可能没有意义了，如果我的梦想已经被实现了，我还能干点啥呢？这种虚无感在我完成前两个工作后达到了顶峰：如果我只是遵循着前人的思路去做一些早晚都会被完成的工作，“我”的存在到底有何意义？在那之后我意识到我一定要做一些只有“我”才能做出来的工作；如果不行，那就退一步，做一些让大家一定会永远记住“我”的工作。

在这个层面上，我是极端幸运的，我的第三和第四个工作基本上解决了我的存在主义危机。我的第三个工作，是基于一些相当意外的发现，这些观测并不新颖，但是我确信这个发现必须要有“我”的观察才能被展现，恬不知耻地说，这是“我”独有的洞见。而我的第四个工作则是领域内前所未有的“low hanging fruit”。为了摘取这颗果实，并不需要某个人有多么深的理解，多么高超的技术，只需要他/她在正确的时间出现在正确的地方和恰当的人进行讨论并恰好注意到了这件事，而我，恰好成为了这个人，可谓是三生有幸。

在这里我想首先感谢我的导师Marco Velli教授，如果没有他，我的这些研究经历就压根无从谈起了。这些年有幸受他指导，在这个过程中领略到的他对物理现象的洞见，将让我终身受益。作为一个导师，在这五年博士期间，他十分慷慨地资助我的学术活动，并毫无保留地指导我的学业；作为一个合作者，他是我见过的最聪慧的物理学家之一，与他进行讨论，是我最愉快的时光；作为一位长者，他给予我的人生经验更是弥足珍贵。然后我想感谢师兄时辰博士，如果没有他无私的帮助，我的博士生涯必无可能如此顺利而圆满。我还想感谢同事Nikos Sioulas博士，这些年尽管我们偶有摩擦，但是与他昼夜探讨的问题大都成为了我的工作的基础。此外我想感谢在Benjamin Chandran教授和Lorenzo Matteini博士，与他们的合作，让我受益匪浅。我还要感谢我的博士答辩委员会的成员Vassilis Angelopoulos教授、曹浩教授和Paulo Alves教授。

在科研工作之外，这些年朋友的帮助也是不可或缺的。我想在这里感谢黄胜、苏雪、陈含章、李一辰、石晓霏、康宁、贾英东、刘佳睿、马东来、许思学，是他们的存在让我的博士五年远离乏味并充满了欢乐。最后我还想感谢三座伟大的城市：广州、合肥和洛杉矶，她们分别养育、教育和成就了我。

回首过往人生，我真是不得不感叹我是多么幸运的一个人。虽然童年时期的家庭略有坎坷，父母早早地就离婚了，但是我的母亲，作为一个坚强的单亲母亲，和我的阿婆阿公一起给了我近乎无限的爱与关怀让我健康快乐地成长；而我的爷爷奶奶也从未缺失，在我人生的前二十年以身作则地勉励我去成为一个正直、善良、懂得感恩的人；最后还有我的妻子以及她养育长大的8只猫猫，是她的存在让我的生活从不乏味，也让我体会到了前所未有的幸福。而我长达二十一年的漫漫求学路也是一个始终如一的夙愿得偿的过程：谁能想到小时候种下的那颗希望成为物理学家的种子，真的能在21年后成长为一棵茁壮的树木呢？这大概就是宿命吧？

事实上玉兰阁（Magnolia Court）这个雅名正是我在玉兰阁居住的这段时间起的，并意外地影响了不少周围的人，类似的翻译还有蓝楹轩（Jacaranda Court）、棕榈园（Palms Court）、橄榄庭（Olive Court）等等。玉兰乃是上海市花，象征高尚的品格和崇高的理想，与家祖对我的期待颇为契合。因此，一是得益于这段快乐时光，二是想借此机会附庸风雅，我决定遵循古制把我的博士论文集命名为《玉兰集》，并作此序。

CURRICULUM VITAE

2015–2019 B.S. in Geophysics and Space Physics, School of Earth and Space Sciences & School of the Gifted Young, University of Science and Technology of China

2019–2021 M.S. in Space Physics, Department of Earth, Planetary, and Space Sciences, University of California, Los Angeles

2019–2024 Graduate Student Researcher, University of California, Los Angeles

PUBLICATIONS

Huang, Z., Velli, M., Shi, C., Zhu, Y., Chandran, B. D. G., Réville, V., et al. (2024, May 24). 3-Minute Oscillations in the Upper Corona: Evidence from Parker Solar Probe. arXiv. Retrieved from http://arxiv.org/abs/2405.15967

Huang, Z., Shi, C., Velli, M., Sioulas, N., Panasenco, O., Bowen, T., et al. (2023). In situ Remnants of Solar Surface Structures from Jensen-Shannon Scalogram (Version 1). https://doi.org/10.48550/ARXIV.2312.08669

Huang, Z., Sioulas, N., Shi, C., Velli, M., Bowen, T., Davis, N., et al. (2023). New Observations of Solar Wind 1/f Turbulence Spectrum from Parker Solar Probe. The Astrophysical Journal Letters, 950(1), L8. https://doi.org/10.3847/2041-8213/acd7f2

Huang, Z., Shi, C., Sioulas, N., & Velli, M. (2022). Conservation of Total Wave Action in the Expanding Solar Wind. The Astrophysical Journal, 935(1), 60. https://doi.org/10.3847/1538-4357/ac74c5

Sioulas, N., Velli, M., **Huang, Z.**, Shi, C., Bowen, T. A., Chandran, B. D. G., et al. (2023). On the evolution of the Anisotropic Scaling of Magnetohydrodynamic Turbulence in the Inner Heliosphere. The Astrophysical Journal, 951(2), 141.

Davis, N., Chandran, B. D. G., Bowen, T. A., Badman, S. T., Wit, T. D. de, Chen, C. H. K., et al. (2023). The Evolution of the 1/f Range within a Single Fast-solar-wind Stream between 17.4 and 45.7 Solar Radii. The Astrophysical Journal, 950(2), 154. https://doi.org/10.3847/1538-4357/acd177

Sioulas, N., **Huang, Z.**, Shi, C., Velli, M., Tenerani, A., Bowen, T. A., et al. (2023). Magnetic Field Spectral Evolution in the Inner Heliosphere. The Astrophysical Journal Letters, 943(1), L8. https://doi.org/10.3847/2041-8213/acaeff

Shi, C., Velli, M., Lionello, R., Sioulas, N., **Huang, Z.**, Halekas, J. S., et al. (2023). Proton and electron temperatures in the solar wind and their correlations with the solar wind speed. arXiv Preprint arXiv:2301.00852.

Shi, C., Panasenco, O., Velli, M., Tenerani, A., Verniero, J. L., Sioulas, N., et al. (2022). Patches of Magnetic Switchbacks and Their Origins. The Astrophysical Journal, 934(2), 152. https://doi.org/10.3847/1538-4357/ac7c11

Sioulas, N., **Huang, Z.**, Velli, M., Chhiber, R., Cuesta, M. E., Shi, C., et al. (2022). Magnetic Field Intermittency in the Solar Wind: Parker Solar Probe and SolO Observations Ranging from the Alfvén Region up to 1 AU. The Astrophysical Journal, 934(2), 143. https://doi.org/10.3847/1538-4357/ac7aa2

Sioulas, N., Shi, C., **Huang, Z.**, & Velli, M. (2022). Preferential heating of protons over electrons from coherent structures during the first perihelion of the parker solar probe. The Astrophysical Journal Letters, 935(2), L29.

Hara, T., **Huang, Z.**, Mitchell, D. L., DiBraccio, G. A., Brain, D. A., Harada, Y., & Luhmann, J. G. (2022). A Comparative Study of Magnetic Flux Ropes in the Nightside Induced Magnetosphere of Mars and Venus. Journal of Geophysical Research: Space Physics, 127(1), e2021JA029867. https://doi.org/10.1029/2021JA029867

CHAPTER 1

Introduction

1.1 Solar Interior, Solar Atmosphere, and the Heliosphere

From an astronomical perspective, our sun is a G-type main-sequence star with a black-body temperature around 5800K and several absorption lines in its optical spectrum. Occasionally, black dots can be seen on the visible disk, and we often detect bursty signals in the radio band. However, from an astrophysical perspective, our sun is far more structured and interesting. In this section, we will introduce the structure of the sun using a 1D model: from the core to the photosphere, from the photosphere to the corona, and from the corona to the heliopause.

The sun has a core where proton-proton fusion occurs, extending from the center to about 0.20 solar radii. Beyond the core is the radiative zone, which is 0.51 solar radii thick. In this zone, energy is primarily transported outward by radiative diffusion and thermal conduction. Due to the steep density gradient, an upward-moving adiabatically expanded element has a lower density than its surroundings, resulting in downward buoyancy and preventing convection. The radiative zone rotates as a rigid body, while the convection zone above it features convective motion, differential rotation, and large-scale meridional circulation. The layer separating these two zones is known as the tachocline, which is believed to play a significant role in the solar dynamo. Nevertheless, it has been recently argued that the solar dynamo takes place close to the solar surface (Vasil et al., 2024).

The convection zone extends from 0.71 solar radii to the solar surface. Convection develops in this layer due to the high opacity, which makes radiative heat transfer less efficient, and thus mode of heat transfer switches from radiation to convection. The precise

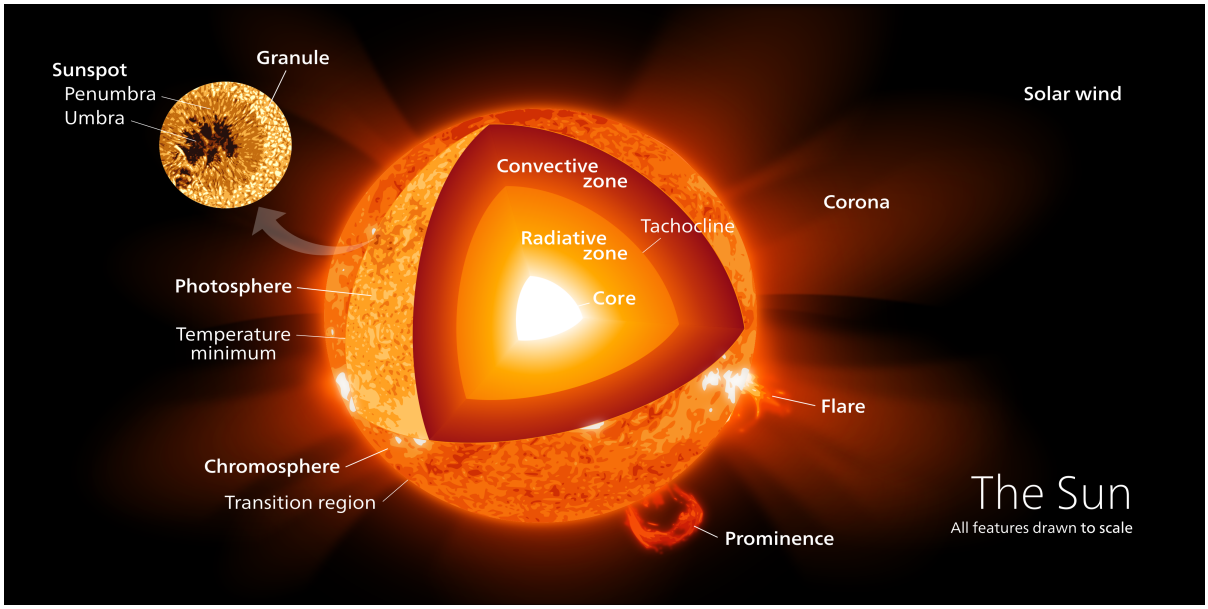

Figure 1.1: Illustration of the Sun's structure, taken from https://en.wikipedia.org/wiki/Sun

location of the tachocline was unknown until the surprising discovery of 5-minute oscillations on the solar surface (Leighton et al., 1962; Noyes and Leighton, 1963; Simon and Leighton, 1964), which was later elegantly explained by Ulrich (1970). These oscillations were found to be a legion of resonant modes excited by photospheric granulation and trapped within the resonance chamber bounded by the tachocline and the photosphere, i.e., the convection zone. This discovery led to the birth of helioseismology, which later revealed much more detailed structures of the solar interior.

The photosphere defines the outer boundary of the sun and is a thin layer of partially ionized plasma with a blackbody temperature of around 5800K. The thickness of the photosphere is defined optically; it extends into the solar surface until the plasma becomes opaque, corresponding to an optical depth of approximately 2/3. Below the photosphere, the solar plasma is in hydrostatic equilibrium. The upper boundary of the photosphere is traditionally defined as the altitude of the minimum temperature (see Figure 1.2). Below this minimum temperature, the plasma is dense enough that non-radiative heat sources are not strong enough to significantly modify the balance between radiative and convective energy input and radiative cooling (Linsky, 1980, 2017).

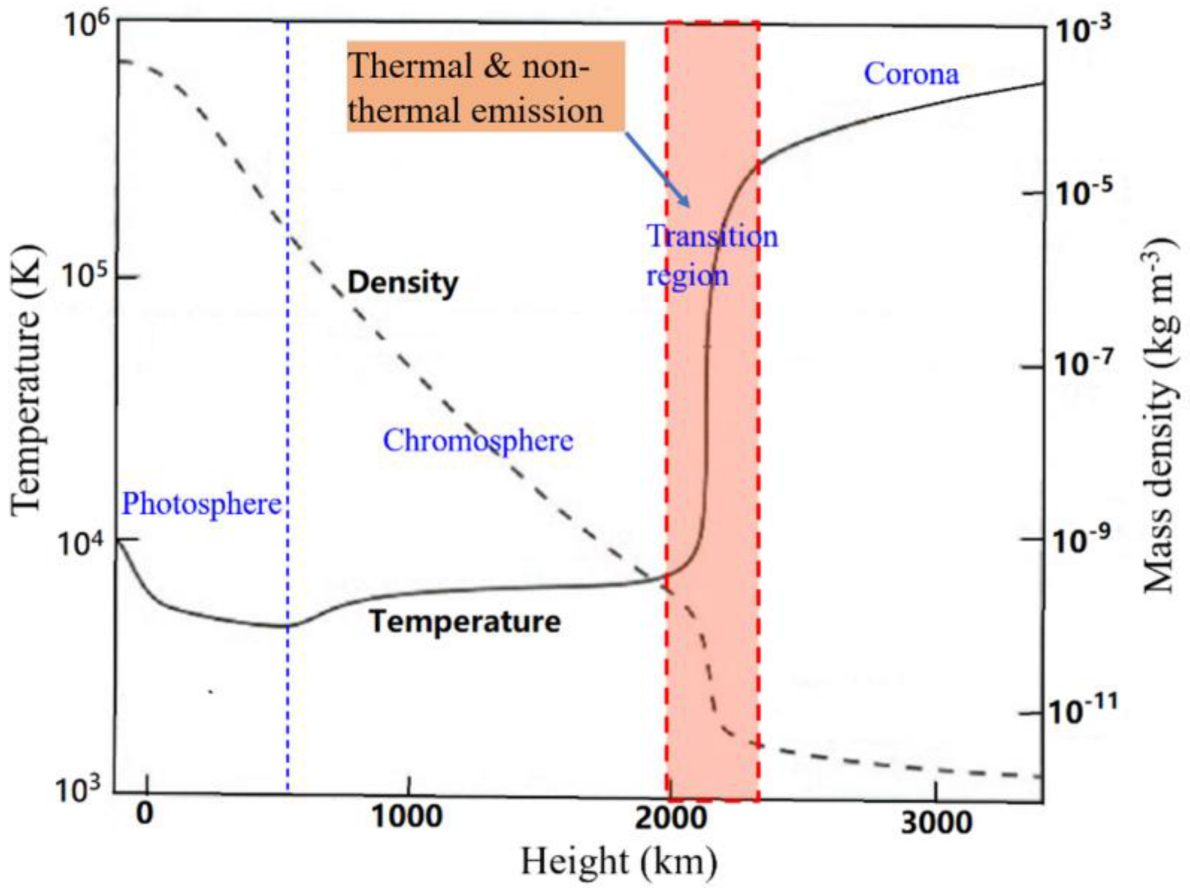

Figure 1.2: Temperature and Density profile of solar atmosphere in 1D model, taken from (Tan et al., 2024)

From the upper photosphere, the density drops exponentially, more slowly at first, through the chromosphere, and then dramatically, in the transition region. Consequently, the radiative cooling capability of the plasma rapidly decreases and gradually the non-radiative heat source begins to heat the plasma, and hence temperature rises to enhance radiative cooling. In this layer, the primary emission line in visible band is the $H\alpha$ line, which dyes this layer into the iconic rosy-red color. However, as the density continues to decrease, the increment in radiative cooling from raised temperature would not be able to balance the non-radiative heat source, and thus a strong temperature gradient is created, i.e. the transition region and the million-degree corona lying above. A simple argument can be found in chapter 7 of (Vial and Engvold, 2015):

If flow and thermal conduction are both negligible, the energy conservation equation

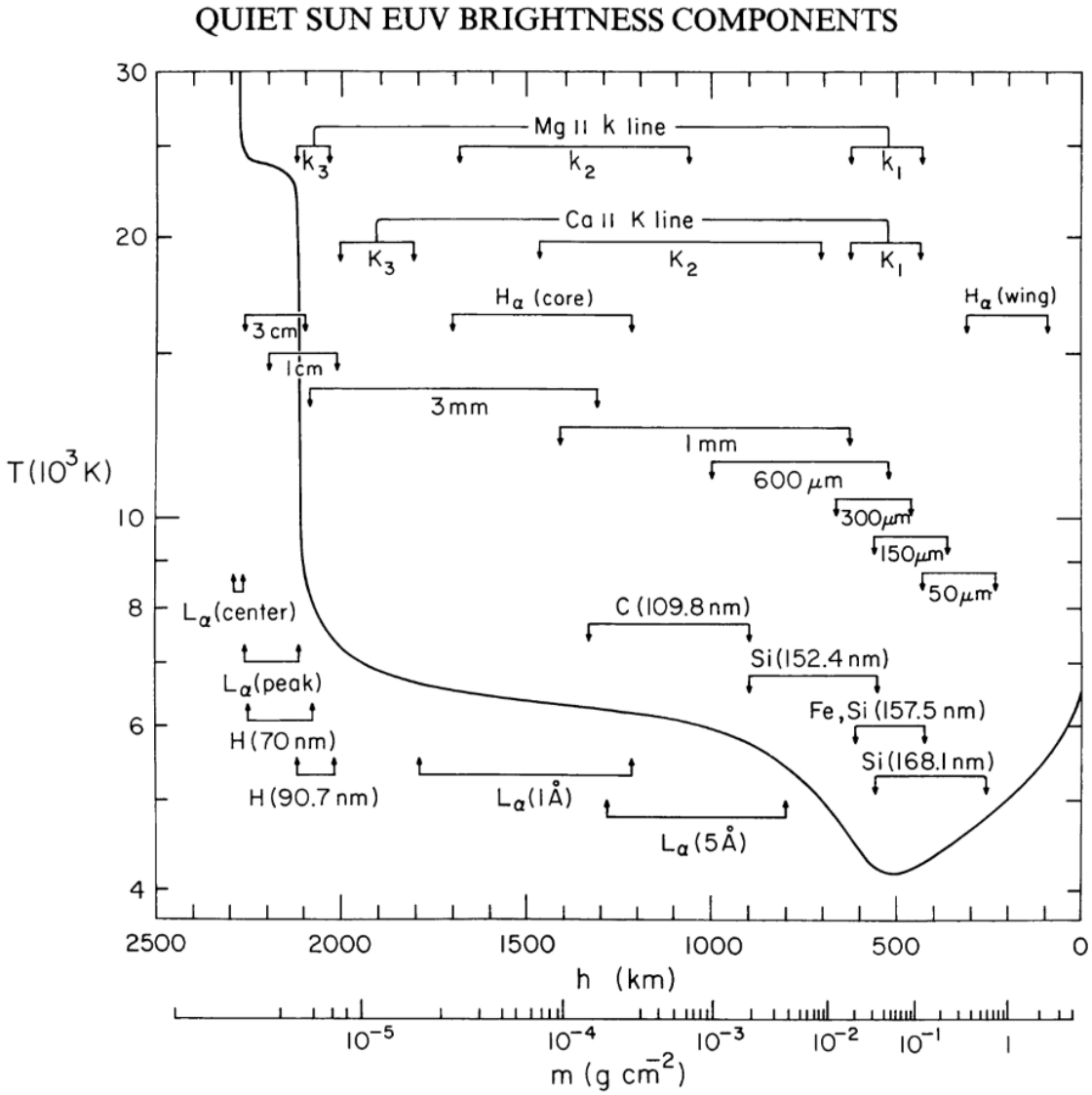

Figure 1.3: The average quiet-Sun temperature distribution derived from the EUV continuum, the $L\alpha$ line, and other observations. The approximate depths where the various continua and lines originate are indicated. Taken from (Vernazza et al., 1981)

is:

$$3nk\frac{\partial T}{\partial t} = Q - L \tag{1.1}$$

where Q is the mechanical heating rate, and L is the radiative cooling rate. The plasma is thermally stable when the radiative cooling rate increases with temperature: If the mechanical heating rate exceeds the radiative cooling rate ($Q > L$), then the local temperature increases with time; whereas if $Q < L$, the local temperature decreases with time. This way, the plasma is thermally stable. Using a dimensional analysis, the radiative cooling L can be expressed as:

$$L = n^2 R(T) \tag{1.2}$$

where n is the hydrogen number density and $R(T)$ is an complex function of the temperature. Therefore in the equilibrium state, the radiative cooling balances the mechanical heating $Q = L$, i.e.

$$R(T) = Q/n^2 \tag{1.3}$$

Thermal instability arises when the scale height of Q is larger than that of L, i.e. the scale height of n^2. In this case, the temperature will increase with increasing height, and eventually the temperature will reach the $Ly-\alpha$ cooling peak temperature ($\sim 2\times10^4 K$). Beyond this point, we enter the unstable region of the constant-pressure radiative cooling curve ($Q > L$), and temperature will increase without bound. As a result, we need to consider the thermal conduction:

$$3nk\frac{\partial T}{\partial t} + \nabla \cdot \vec{q} = Q - L \tag{1.4}$$

In a stable case, we have:

$$\nabla \cdot \vec{q} = Q - L \tag{1.5}$$

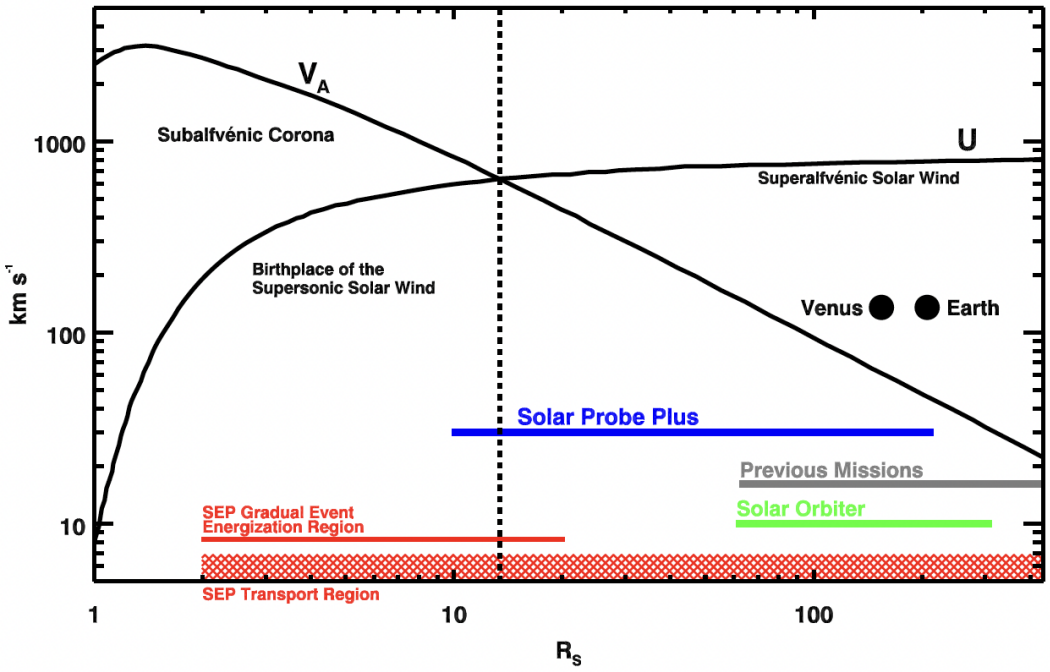

Figure 1.4: 1D model of Alfvén speed and solar wind speed in the solar corona and solar wind. The blue bar shows the orbit coverage of Parker Solar Probe (Solar Probe Plus). Figure taken from (Fox et al., 2016)

And the heat flux density can be written as:

$$\vec{q} = -\kappa T^{5/2} \nabla T \tag{1.6}$$

At a temperature below $5 \times 10^4 K$, the plasma is a very good thermal insulator. Therefore the only way thermal conduction can mitigate the thermal instability at these low temperatures is with an extremely strong temperature gradient. It is for this reason that the temperature rises so steeply in the lower transition region and levels off in the corona (see Figure 1.2), where the plasma has become a better thermal conductor than copper, so that only a mild temperature gradient is needed to transport a significant heat flux via thermal conduction.

Passing the transition region, we reach the solar corona. The solar corona is the place where solar wind gradually accelerates into the supersonic (super-alfvénic) state. In 1D model, the Alfvén speed drops as a function of R^{-1} and the solar wind accelerates

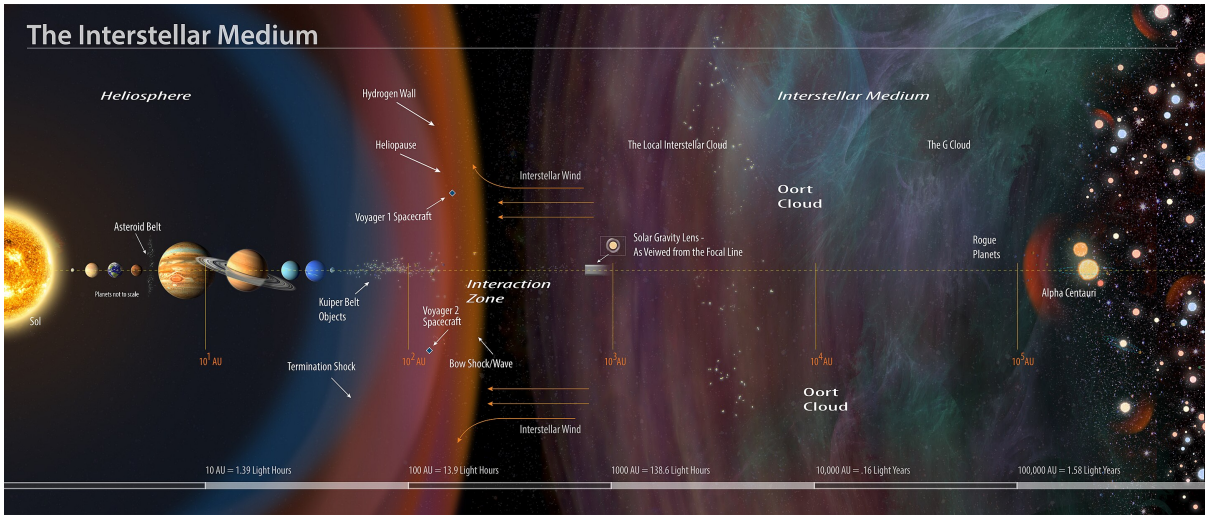

Figure 1.5: An annotated illustration of the heliosphere and the interstellar medium. Figure taken from https://en.wikipedia.org/wiki/Heliosphere

.

exponentially. The location where $U = V_A$ at around 15 $R_\odot$ is known as the Alfvén surface, which marks the upper boundary of the solar corona. Unlike the boundaries in the lower solar atmosphere (photosphere-chromosphere boundary or the transition region), the Alfvén surface is less well-defined as a physical boundary. Beyond the Alfvén surface, the information carrier (Alfvén waves) can not propagate backwards to the solar surface, and hence the Alfvén surface marks the causal disconnection of individual packets of plasma and magnetic flux from the sun itself (DeForest et al., 2014).

Above the Alfvén surface we enters a region known as the heliosphere (permeated with super-alfvénic solar wind). Using an Earth analogy, the heliosphere is the magnetosphere of the sun and all of the solar system planets are located within the heliosphere. Due to the interaction with interstellar medium, the solar wind will gradually slow down, and at around 90 AU, the solar wind becomes subsonic again and this boundary is known as the termination shock. As of 2007, both Voyager 1 and Voyager 2 has traveled across the this boundary. Outside of the termination shock is the heliosheath, where the subsonic solar wind plasma are compressed by the interstellar medium. And finally at around 121 AU, Voyager 1 detected a rapid increase in galatic cosmic rays in May 2012, followed by Voyager 2 in Nov 2018, indicating that both spacecraft has passed the heliopause and

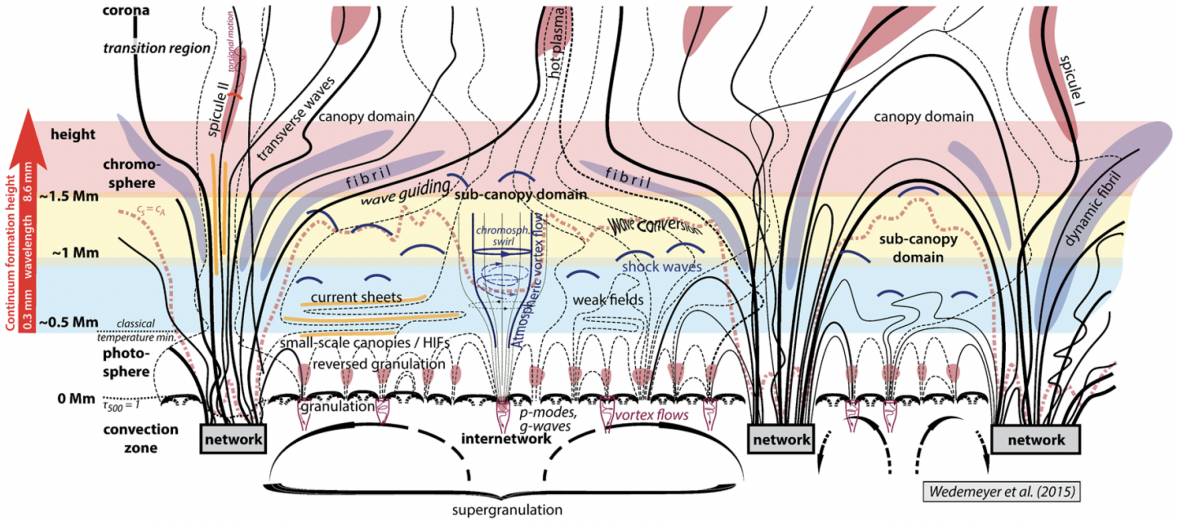

Figure 1.6: Detailed illustrations of the processes and structures in the Sun's atmosphere from photosphere to lower corona, taken from (Wedemeyer et al., 2016)

entered the interstellar medium (Borovikov and Pogorelov, 2014; Gurnett and Kurth, 2019).

In this dissertation, we focus on the physical processes in the inner heliosphere, and more specifically in the upper corona and inner heliosphere measured by Parker Solar Probe (PSP) (Fox et al., 2016). Combining *in situ* observations, statistical analyses, and modeling, we aim to trace the origin of Alfvén waves, turbulence, and Gaussian structures in the primitive solar wind at its source.

1.2 Structures and Processes in the Chromosphere, Transition Region, Corona and Solar Wind

The solar atmosphere beyond the photosphere is highly dynamic, anisotropic, and complex. The anisotropy at zeroth-order is introduced by the global magnetic field of the sun. Figure 1.6 shows a modern physical picture from the photosphere to lower corona. Obviously the solar atmosphere is far from equilibrium state and is highly complex both spatially and temporally in nature. The primary focus of this dissertation is to provide a collection of novel observations from PSP that contribute to the state-of-the-art under-

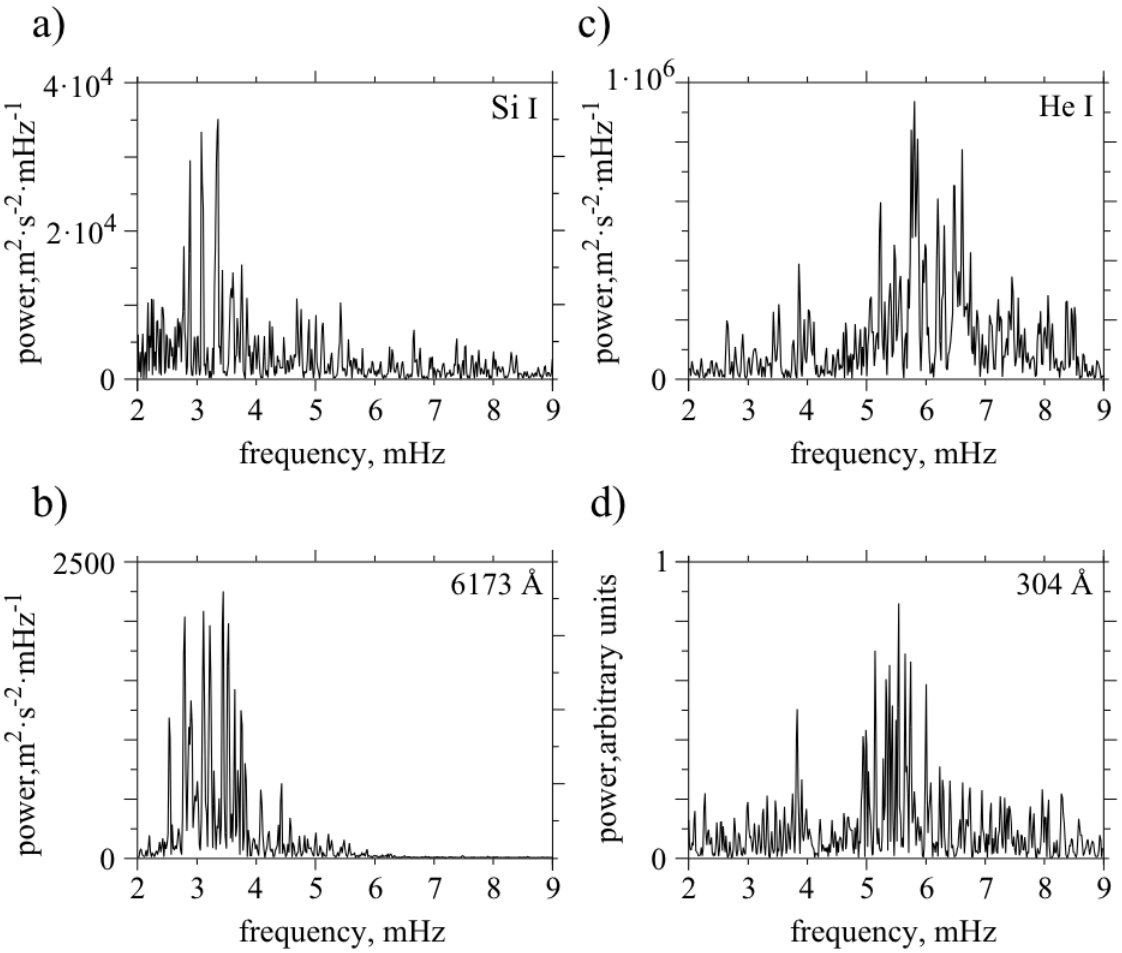

Figure 1.7: Umbral oscillation power spectra from the photosphere to the transition zone for the a) Si Si_I 10827 LOS velocity; b) Fe_I 6173 LOS velocity; c) He_I 10830 LOS velocity; d) Si_{II} 304 intensity signal. LOS is line of sight. Figure taken from (Kobanov et al., 2013)

standing of the physics of the sun. Therefore, in this section, we are going to introduce some important solar atmospheric structures and processes that are specifically relevant to this dissertation.

1.2.1 Fluctuations in the Solar Atmosphere

One of the most important and relevant phenomenon in the solar atmosphere is of course the oscillations in different layers. Acoustic waves (p-modes) excited by the photosphere granulation can be trapped within the convection zone acting as a resonance chamber (Leighton et al., 1962; Noyes and Leighton, 1963; Simon and Leighton, 1964; Ulrich,

1970; Leibacher and Stein, 1971). The energy can leak into the chromosphere, and the fluctuation energy is observed to be concentrated around 3-minute (Orrall, 1966; Elliott, 1969; Deubner, 1974; Cram, 1978). The shift of the fluctuation frequency is shown in Figure 1.7. Each of the panels shows the fluctuation power spectrum measured by different emission lines (see Figure 1.3 for the depth of each emission lines) which indicates different layers in the solar atmosphere. It can be seen that the primary period drifts from 5-minute in the photosphere to 3-minute as the altitude becomes higher and enters into the chromosphere. One of the leading explanation to the 3-minute oscillation is the resonant excitation of the acoustic cut-off frequency mode in a stratified atmosphere (Fleck and Schmitz, 1991). Going further up, the primary fluctuation frequency become slightly higher but there is less consensus. Generally speaking, the fluctuations in the upper chromosphere, transition region, and lower corona distributes about 100-500s (De Pontieu et al., 2007; Morton et al., 2012, 2019). Additionally, standing-wave like decayless oscillations have been found in the coronal loops with much higher frequencies (Mandal et al., 2022; Zhong et al., 2023; Shrivastav et al., 2023). PSP is the first spacecraft that has ever entered the solar corona. And thus it is of great interests to explore in the measurements that whether there are remnants or signatures of these oscillations excited in the lower solar atmosphere. Consequently, in Chapter 5, we provide the first evidence from PSP that the primary fluctuation frequency in the lower corona concentrates at around 3-minute, consistent with the chromosphere 3-minute oscillations.

1.2.2 Magnetic Canopy and Double Mode Conversion

One of the most important parameters in plasma is the plasma $\beta = 2\mu_0 P/B^2$, i.e. the ratio between plasma pressure and magnetic pressure. Going from the fluid-like photosphere on quiet part of the sun to tenuous and highly magnetic corona, there is a important paradigm drift happening in between. In the photosphere, plasma β is generally larger than unity outside of the sunspots, and thus the magnetic field are controlled by the plasma motion itself. However in the lower corona, the plasma β is much smaller than unity, and hence the plasma is controlled by the magnetic field.

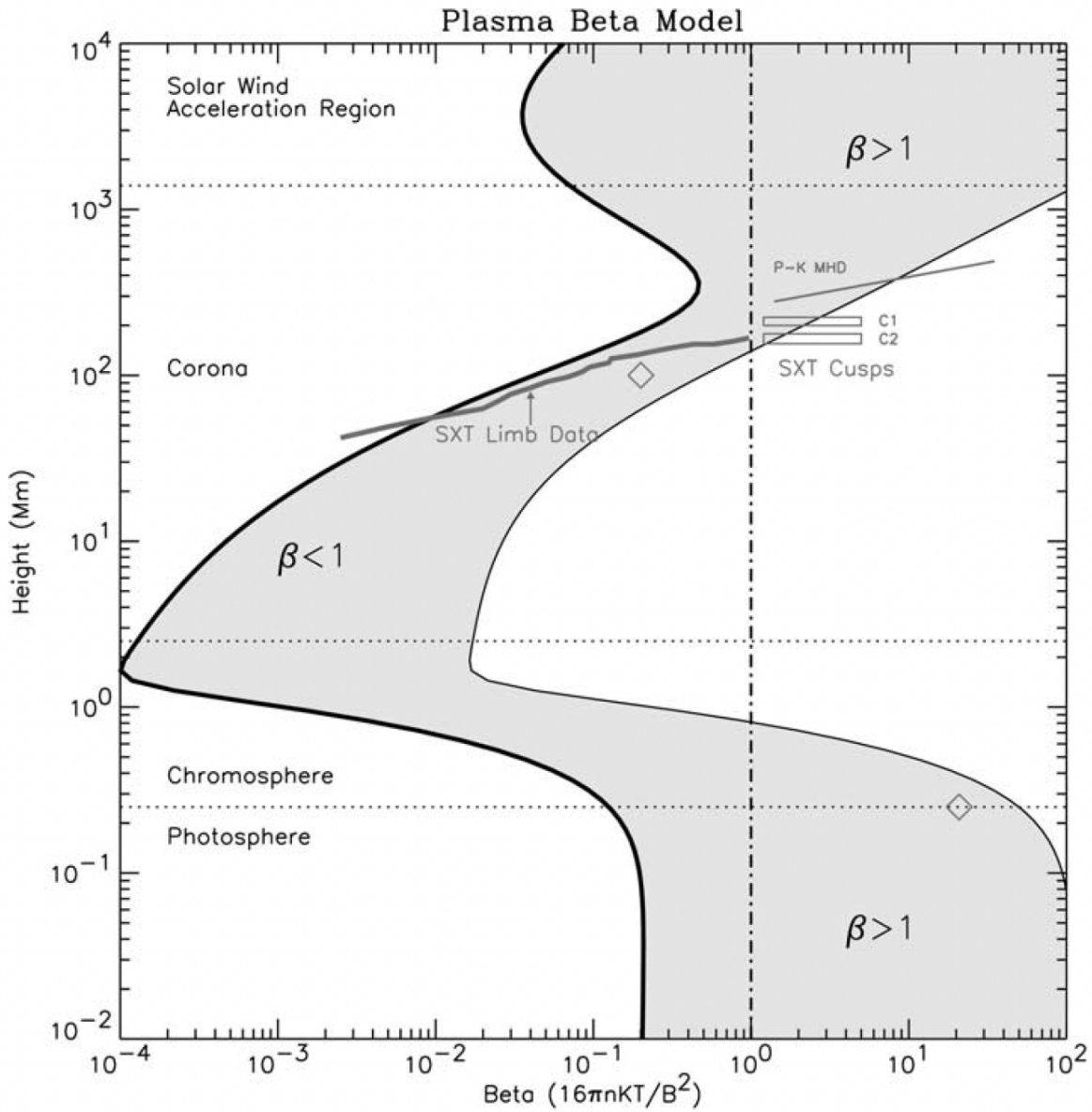

Figure 1.8: Plasma β model over an active region as a function of height. Figure taken from (Gary, 2001)

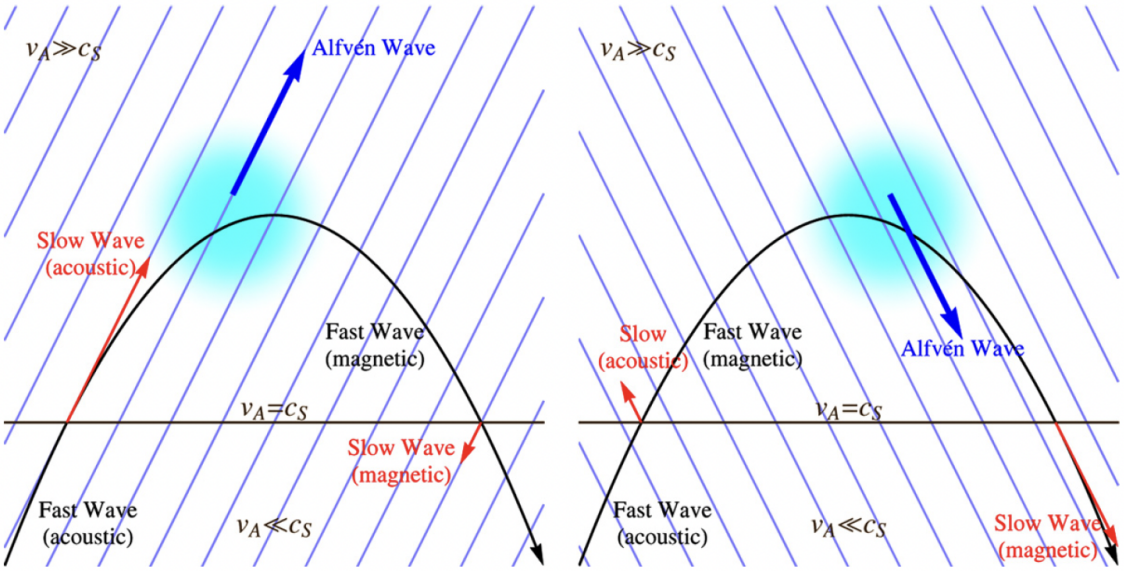

Figure 1.9: Double mode conversion from p-mode to Alfvén mode. Figure taken from (Khomenko and Cally, 2012).

Consequently, somewhere in the middle of chromosphere lies a layer where plasma β passes unity, and this layer is known as the magnetic canopy (more precisely the layer where sound speed c_s equals Alfvén speed v_A, and $\beta = \frac{2}{\gamma}\frac{c_s^2}{v_A^2}$) (Rosenthal et al., 2002; Bogdan et al., 2003).

This layer is particularly interesting because the two MHD magnetosonic modes can linearly convert to each other right at the $c_s = v_A$ boundary. Below the canopy, $c_s > v_A$, the fast mode is sonic and isotropic, whereas the slow mode is magnetic and anisotropic; above the canopy, the fast mode is magnetic and isotropic, whereas the slow mode is sonic and anisotropic. Consequently, the fast mode driven by p-mode from the photosphere beneath can propagate into mid-chromosphere and linearly convert to the magnetic fast mode at the canopy. Subsequently, the fast mode will further propagate upwards and be refracted down due to the steep Alfvén speed profile (see Figure 1.10). Right at the height of the refraction, the fast mode will linearly couple with Alfvén mode and convert a substantial amount of wave energy. This process is illustrated in Figure 1.9 and is known as the double mode conversion (Spruit and Bogdan, 1992; Cally and Bogdan, 1997; Cally, 2000; Crouch and Cally, 2003; Bogdan et al., 2003; Morton et al., 2023). In this dissertation, we will discuss in details of the linear mode conversion between fast

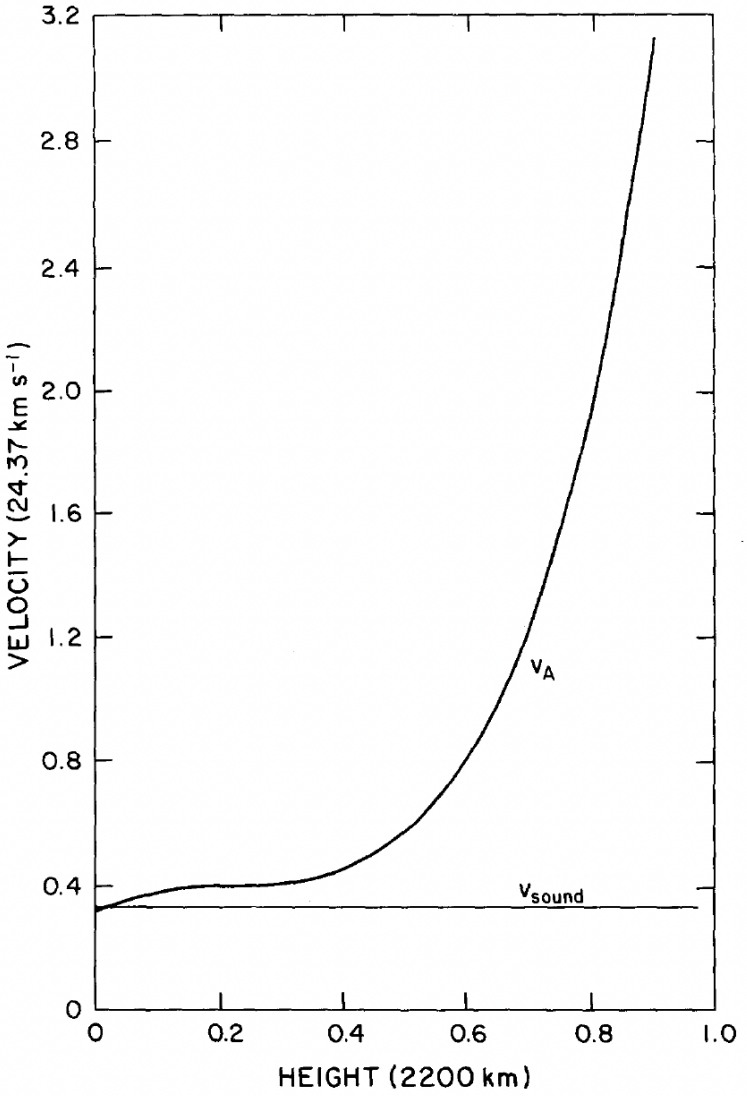

Figure 1.10: Alfvén speed profile above the magnetic canopy. Figure taken from (Hollweg et al., 1982).

and slow mode at the $c_s = v_A$ layer, and show that the linear mode conversion conserves total wave action in Chapter 2. In addition, a detailed discussion of the double mode conversion and its relevance to *in situ* observations from PSP at around the Alfvén surface is provided in Chapter 5.

1.2.3 Spatial Structures in Corona and Solar Wind

One can already see from Figure 1.6 that above the hydrostatic equilibrium, the solar atmosphere is full of dynamics and is extremely anisotropic. The corona is of course part of it and the static structures in the solar corona is extremely rich. During solar minimum, the ecliptic plane is characterized by the large helmet streamer (or simply streamer, elongated cusp-like structure which is consisted of closed photospheric magnetic field lines, and the magnetic fields are oppositely pointing outside of the structure) which typically extends up to 1.5 solar radii above the solar surface, and the two polar regions are characterized by polar coronal hole with numerous plumes that can extend much farther. On the other hand, during solar maximum, the magnetic topology becomes much more complex, and we can find streamers, pseudo-streamers (similar to a streamer, but the magnetic fields share the same polarity outside of the structure), and mid-latitude coronal holes with the corresponding plumes anywhere on the disk. Notably, the coronal plumes can be observed using white light images up to 15 $R_\odot$ during solar maximum, which is well-above of the perihelion of PSP. Therefore, PSP can provide *in situ* measurement of the plumes in the coronal holes during solar active phase from 2022 to 2026.

The solar wind is the heated and accelerated coronal plasma and thus shares a number of features. During solar minimum, the solar outflows measured at high latitudes, as been confirmed by the Ulysses mission (McComas et al., 2000, 2003; Neugebauer et al., 1995; Bame et al., 1992), are high speed solar wind with speed stably around 750km/s. The fluctuations in the polar solar wind are primarily spherically polarized Alfvén waves with constant magnetic magnitude, and it has been confirmed to originated from the polar coronal holes. The solar wind at low latitudes around the ecliptic plane is slow and

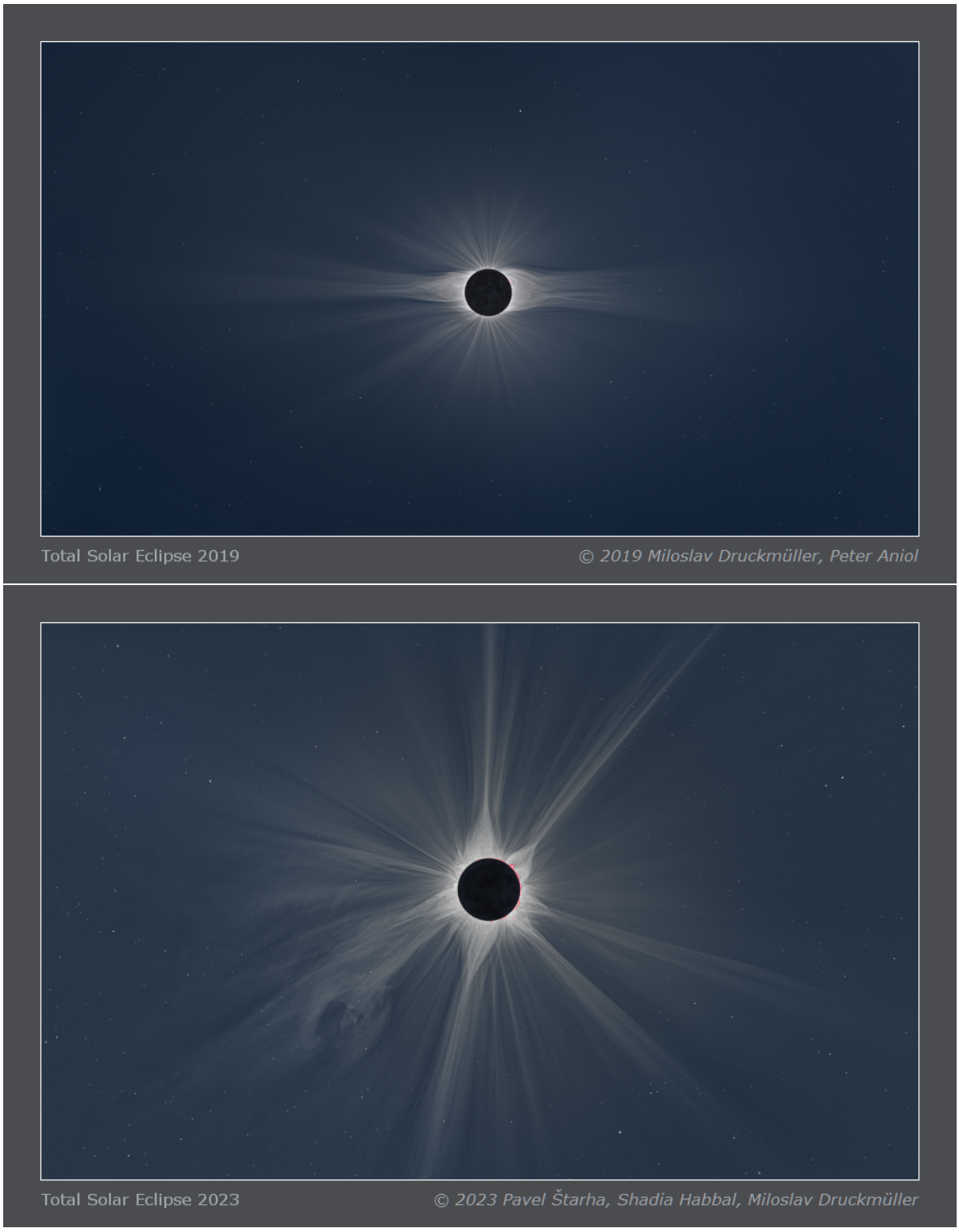

Figure 1.11: Solar Corona during total eclipses. Upper panel: solar minimum in 2019; Lower panel: close to solar maximum in 2023. Copyrights are shown in the figures.

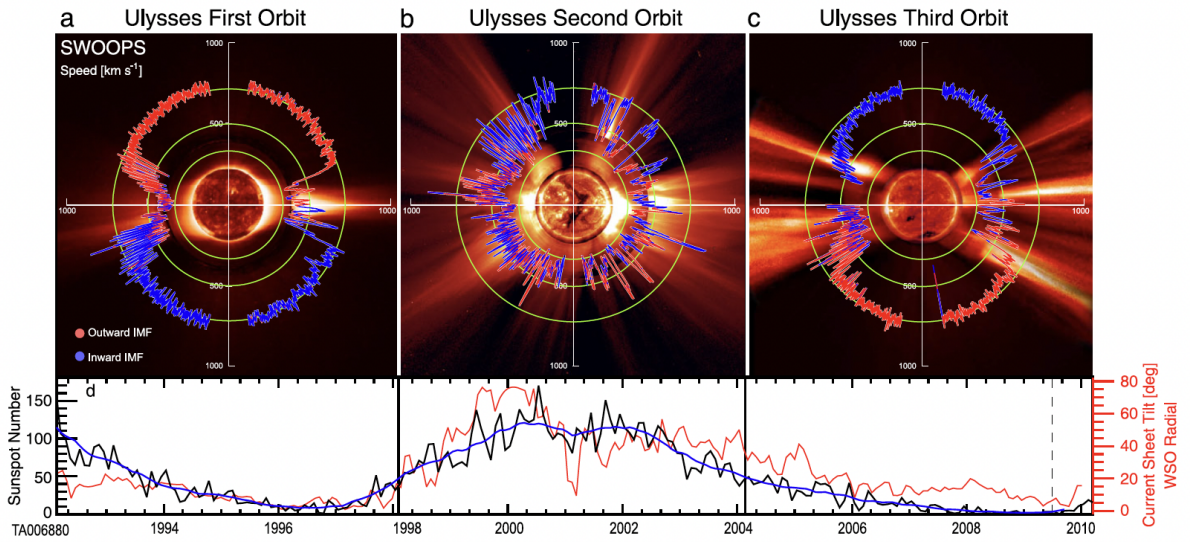

Figure 1.12: Solar wind speed as a function of heliographic latitude illustrating the relationship between the structure of the solar wind and coronal structure at solar minimum (a, c) and solar maximum (b). Ulysses SWOOPS solar wind data are superposed on composite solar images obtained with the SOHO EIT and LASCO C2 instruments and with the Mauna Loa K-coronameter. (d) Solar cycle evolution. Figure taken from (Fox et al., 2016) and originally adopted from (McComas et al., 2003)

Parker-like, filled with compressible fluctuations and transients. During solar maximum, on the other hand, the fast wind streams can be found at all latitudes and the streams are often the mix of solar wind outflows that have different origins.

One of the key challenge in *in situ* observations of the solar wind is that it is extremely difficult to confirm the source region of the solar wind stream. This is because the solar corona is highly magnetic, i.e. with very low plasma β ($\lesssim 0.01$), and hence the plasma motion is controlled by the topology of the magnetic field lines. For example, numerous plumes are seen during solar maximum in Figure 1.11. They can be traced back to a relatively small open field lines region on the coronal graph, i.e. coronal hole. In addition, for missions that are far away from the sun, different solar wind streams with different speed typically are mixed together, making it extremely hard to confirm the source region of the *in situ* time series. The commonly used method to trace the plasma parcel back to the solar surface is through the Potential Field Source Surface modeling (PFSS) (Badman et al., 2020; Panasenco et al., 2020; Badman et al., 2023). To track the

plasma parcel back to the sun, the location of PSP is first ballistically projected back to the source surface (SS) using the measured solar wind speed. The magnetic field lines are assumed to be radial at the SS, and the altitude is *a posteriori* chosen to match the *in situ* the heliospheric current sheet crossings seen by PSP (typically at $R_{SS} = 2.5R_{\odot}$).

The magnetic field is then integrated from the solar surface using magnetograms from Helioseismic and Magnetic Imager (HMI) on board of the Solar Dynamics Observatory (SDO) spacecraft (Pesnell et al., 2012) to the source surface. This method relies on the inputs of the magnetograms that are only refreshed every 6-hour and hence can only contextualize the *in situ* time series in a statistical sense. In addition, it has been shown by (Badman et al., 2023) that by tweaking the parameters in the PFSS modeling and by adopting different extrapolation models, the resultant source regions can seldom reach a consensus. Consequently, it is of great interest to seek features in the *in situ* time series that can provide self-contextualization. In Chapter 4, we provide the *in situ* evidence of the coronal structures from the Gaussianity of magnetic magnitude.

1.2.4 Reflection and Tunneling of Alfvén Waves

As the Alfvén waves propagates upwards in the chromosphere above the canopy, it will face a steep exponential profile of Alfvén speed due to the exponential decrease of density as a function of altitude. It should be noted that, however, when calculating the Alfvén speed:

$$v_A = |B|/\sqrt{\mu_0 \rho} \tag{1.7}$$

the density ρ is the total density of both neutral hydrogen and protons. This is because, even though in the chromosphere the plasma is only partially ionized due to low temperature ($\sim 10^4 K$), the typical Alfvén wave period is about several minutes, and the corresponding frequency is much lower than the ion-neutral collision frequency. Consequently, the neutral hydrogen atoms will be "glued" with the protons, resulting in a higher density in calculating the Alfvén speed. If super-radial expansion of the flux tube

is ignored, the scale height of Alfvén speed h_A is twice the scale height density h_ρ. However, see e.g. Figure 1.6, the magnetic canopy, by definition, is the location where the flux tubes expand significantly. And thus the actual scale height of Alfvén speed is larger than $2h_\rho$. Nevertheless, it is reasonable to assume an exponential profile of v_A from the canopy up to the transition region.

A natural result of the exponential profile of v_A is the filtering effect of the low frequency Alfvén waves (Velli, 1993; Hollweg et al., 1982; Ulmschneider et al., 1991; Hollweg, 1991). For a given Alfvén wave with a frequency of f_0 and a wave length of l_0, according to the WentzelKramersBrillouin (WKB) approximation, the wave action (quantum) of the Alfvén wave is conserved as long as the wavelength $l \ll h_A$. As the wave propagates upwards, by holding the frequency, the wave length will grow with increased Alfvén speed. The wave will then become non-WKB when the wavelength become comparable to h_A. Reaching this point, the wave action will no longer be conserved, and the Alfvén wave will tunnel through Alfvén speed "barrier" identical to the tunneling effects in quantum mechanics. The transmission coefficient (of wave action) for non-WKB Alfvén waves is (Velli, 1993):

$$T = \frac{4v_{A,L}v_{A,R}}{(v_{A,L} + v_{A,R})^2} \tag{1.8}$$

where $v_{A,L}$ and $v_{A,R}$ are the Alfvén at the left and right of the "barrier". Notably, $v_{A,L} = f_0 l$, where l is the wavelength when the Alfvén wave become non-WKB due to the increased wavelength, which is proportional to h_A. Consequently, the transmission coefficient for low frequency Alfvén waves is proportional to the injected frequency, i.e.

$$T \propto f \tag{1.9}$$

For the waves with high enough frequency, the increased wavelength is not large enough to be comparable to h_A, and hence the transmission coefficient is 100%.

The transition region, on the other hand, is a discontinuity in both temperature

and density, but a continuum for magnetic field. And hence, there is a discontinuity of Alfvén speed crossing through the transition region. The effective scale height of Alfvén speed through this discontinuity is 0, and hence all frequencies become non-WKB. From observations, the density drops about 1/20 over the transition region, which can be translated to an approximate universal transmission coefficient of $T_{TR} \simeq 59.7\%$, consistent with simulation results (Réville et al., 2018).

Reaching the corona, the transmission problem becomes slightly more complicated due to the presence of the accelerating solar wind. For one thing, as been shown by early solar wind models, the basic parker solar wind model (Parker, 1958) is not able to reproduce the tenuous high speed solar wind with a speed surpassing 700 km/s, which are later confirmed to be originated from coronal holes (McComas et al., 2000). Consequently, an additional energy source is necessary to accelerate the wind. The large amplitude Alfvén waves (Belcher, 1971) that were ubiquitously observed in all space missions, due to its unparalleled stability among the MHD eigenmodes, is considered to be most promising candidate for the heating and acceleration of the solar wind (Belcher, 1971; Hollweg, 1973; Belcher and Olbert, 1975). The primary mechanism to accelerate the solar wind is through the wave pressure exerted by the Alfvén wave packet, and consequently, part of the fluctuation energy will be turned into solar wind momentum as the wind accelerates from corona base into the heliosphere.

The non-WKB transmission of the Alfvén waves through the solar corona to the Alfvén surface is defined with regard to the conserved wave action in the WKB limit (Heinemann and Olbert, 1980; Velli, 1993). Results have shown that, albeit the steep profile of v_A in the corona, the presence of the wind can significantly increase the transmission coefficient of the low frequency waves, which are completely reflected otherwise. The asymptotic transmission coefficient is:

$$T_c = \frac{4 v_{A,CB} v_{A,AS}}{(v_{A,CB} + v_{A,AS})^2} \tag{1.10}$$

where $v_{A,CB}$ is the Alfvén speed at corona base, and $v_{A,AS}$ is the Alfvén speed at the

Alfvén surface. This is exactly identical to the transmission solution in the static atmosphere shown in eq (1.8).

The basic summary above is to give a brief introduction of the transmission of Alfvén waves at different layers of the solar atmosphere. This is specifically relevant to Chapter 5 because to justify the correspondence between the *in situ* measured wave signals to the excited waves in the lower solar atmosphere, one has to provide at least some basic explanations of the physics happening in between.

1.2.5 Turbulence in the Solar Wind

Turbulence is a ubiquitous phenomenon in nature, from air currents to water eddies, turbulence can be found almost everywhere in daily life. The necessity of turbulence comes from the mismatch between the energy injection which happens at large scales and the energy dissipation into heat in small scales. This can be clearly explained with the Navier-Stokes equation for incompressible fluid:

$$\frac{\partial \vec{u}}{\partial t} + \vec{u} \cdot \nabla \vec{u} = -\frac{1}{\rho} \nabla p + \nu \nabla^2 \vec{u} \tag{1.11}$$

where ν is the shear kinematic viscosity. Assuming 3D isotropy, we can Fourier transform the equation into wavenumber k space, and thus the dissipation term $\nu \nabla^2 \vec{u}$ becomes $\nu k^2 \tilde{u} \propto k^2$. Therefore, the dissipation can only happens at very small scales. However, the fluctuation energy is usually injected via mechanical processes (like waves) which typically happens at low frequency and hence large scales. Consequently, if the energy is being constantly supplied to the system, the energy has to be transferred to small scales to dissipate into heat without loss in the "intermediate scales". This process is coined "turbulence cascade", and the "intermediate scales" is known as the inertial range. The cascade of energy indicates that the energy flow ϵ (cascade rate) from large to small scales in the inertial range is constant, and with this one can do a simple dimensional analysis to find the scaling of the distribution of energy across the scales. Note that the pressure term is proportional to $\vec{u} \cdot \nabla \vec{u}$ in Fourier space, and we can neglect the dissipation. We

are now left with two terms:

$$\frac{\tilde{u}}{\tau} \sim k\tilde{u}^2 \tag{1.12}$$

where τ is the turn over time for the eddy at scale k. We also know that the energy flow can be written as: $\epsilon \sim \tilde{u}^2/\tau$. Therefore:

$$\epsilon \sim k\tilde{u}^3 \tag{1.13}$$

Now we write the power spectrum density of $\tilde{u}$ as a function of wave number k as $P(k)$. We can now make an assumption that $P(k)$ falls very quickly as a function k, and thus the amplitude $\tilde{u}$ as a given wavenumber k is approximately $\tilde{u} \sim \sqrt{kP(k)}$. This is generally true if $P(k) \sim k^{-\alpha}$ and $\alpha > 1$. We may now finally rewrite the equation for cascade rate *epsilon* as the following:

$$P(k) \sim \epsilon^{2/3} k^{-5/3} \tag{1.14}$$

We can know see *a posteriori* that $P(k) \sim k^{-5/3}$, which agrees with our previous assumption. This is the famous Kolmogorov $-5/3$ law, and is part of the turbulence theory developed in 1941 (henceforth referred as K41) (Kolmogorov, 1941).

The K41 theory made various assumptions: 1. The turbulence is isotropic; 2. The nonlinear eddy turn over time for an eddy at wavenumber k is $1/k\tilde{u}$; 3. The energy transfer happens between adjacent scales. All of these assumptions are questionable when turbulence happens in the magnetized solar wind. To begin with, the presence of magnetic field (especially in low β environment close to the sun) introduce anisotropy to the system, and hence the eddies behaves very differently when considering wavevector parallel or perpendicular to the local magnetic field direction. Moreover, the major fluctuation mode in the solar wind is the large amplitude spherically polarized Alfvén waves with constant $|B|$ (Unti and Neugebauer, 1968; Belcher and Davis, 1971), which is an exact solution of the MHD system (Matteini et al., 2014). Thus, to facilitate the

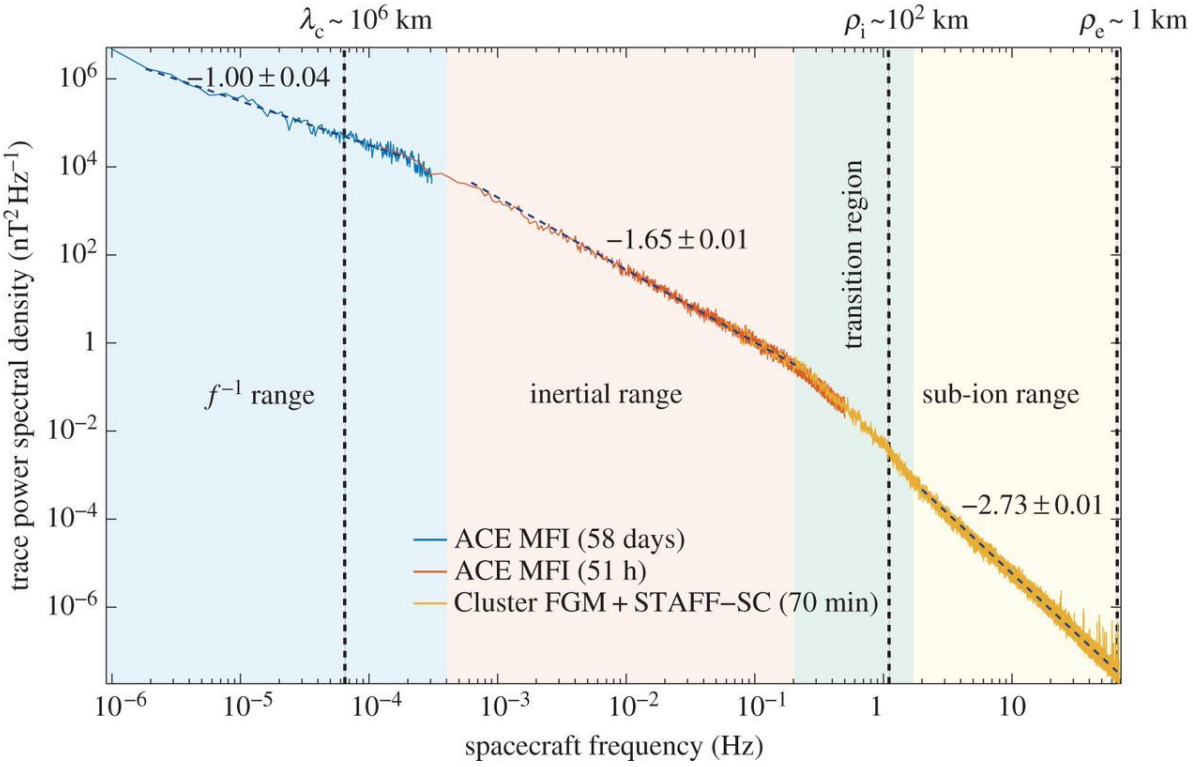

Figure 1.13: Power spectrum of solar wind magnetic field with combined data from ACE (Chiu et al., 1998) and Cluster (Credland et al., 1997) missions . Figure taken from (Kiyani et al., 2015)

turbulence cascade, counter-propagating Alfvén wave packets are necessary (Matthaeus et al., 1996; Chandran and Perez, 2019; Zank et al., 2021), and compared to hydrodynamics turbulence, the nonlinear turn over time should be much larger due to weaker interactions between Alfvén wave packets. Finally, various processes in space plasma can transfer energy across scales (not adjacent scales), for example beam instability. Therefore, over the years, numerous turbulence models have been proposed to explained the turbulence scaling observed in the solar wind (Iroshnikov, 1964; Kraichnan, 1965; Velli et al., 1989; Goldreich and Sridhar, 1995; Boldyrev, 2006; Boldyrev and Perez, 2009).

The majority of the space missions are single spacecraft, and hence the data products are time series of different measurable quantities like vector magnetic field, vector plasma flow speed (first order moments of the ion distribution function), ion density, temperature, etc. However, due to the limited time resolution of the plasma moments, the most commonly used method to derive the turbulence power spectrum density (PSD)

is the trace power spectrum of the three magnetic vector component from fluxgate magnetometer. Adopting this method, a standard picture of solar wind turbulence is shown Figure 1.13. A typical picture of the solar wind turbulence is characterized by an energy injection range with a scaling of $1/f$ in the low frequency range, a close to Kolmogorov scaling in the inertial range, and a steep dissipation range in high frequency. This spectrum is presented in the frequency domain, yet the majority of the turbulence theories are derived in the wavenumber (wavevector if anisotropic) domain. Therefore, most of the studies rely on some assumptions to convert (interpret) the temporal signals into spatial signals. The most commonly used assumption is the Taylor Hypothesis (Taylor, 1938), which assumes that all of the temporal signals in the solar wind are purely created by advection of static structures that are moving with the wind. And hence the frequency spectrum can be converted into wavenumber spectrum via:

$$k = 2\pi f/U \tag{1.15}$$

where U is solar wind speed. In addition, the anisotropy due to the presence of magnetic field can be further classified in a moving window fashion by calculating the local angle between $\vec{U}$ and $\langle\vec{B}\rangle$. This hypothesis, however, is only valid when the local propagation speed of wave packets are much slower than the solar wind speed. As PSP getting closer to the Alfvén surface, the Alfvén speed becomes comparable to solar wind speed by definition. In this scenario, the Taylor Hypothesis is modified (Perez et al., 2021a), and temporal signals are considered to be created by Alfvén waves moving at a phase speed of $U + V_A$ which passes through the spacecraft.

Focus of previous studies (both observational and theoretical) in this field can be approximately classified into three categories: 1. Cascade mechanisms in the inertial range; 2. Energy dissipation mechanisms and the bifurcated behaviors of ions and electrons; 3. Origin and budget of injected energy and its radial evolution. In this dissertation, we are particularly interested in the last category.

Clear energy injection range with scaling of $1/f$ is typically found in fast solar wind

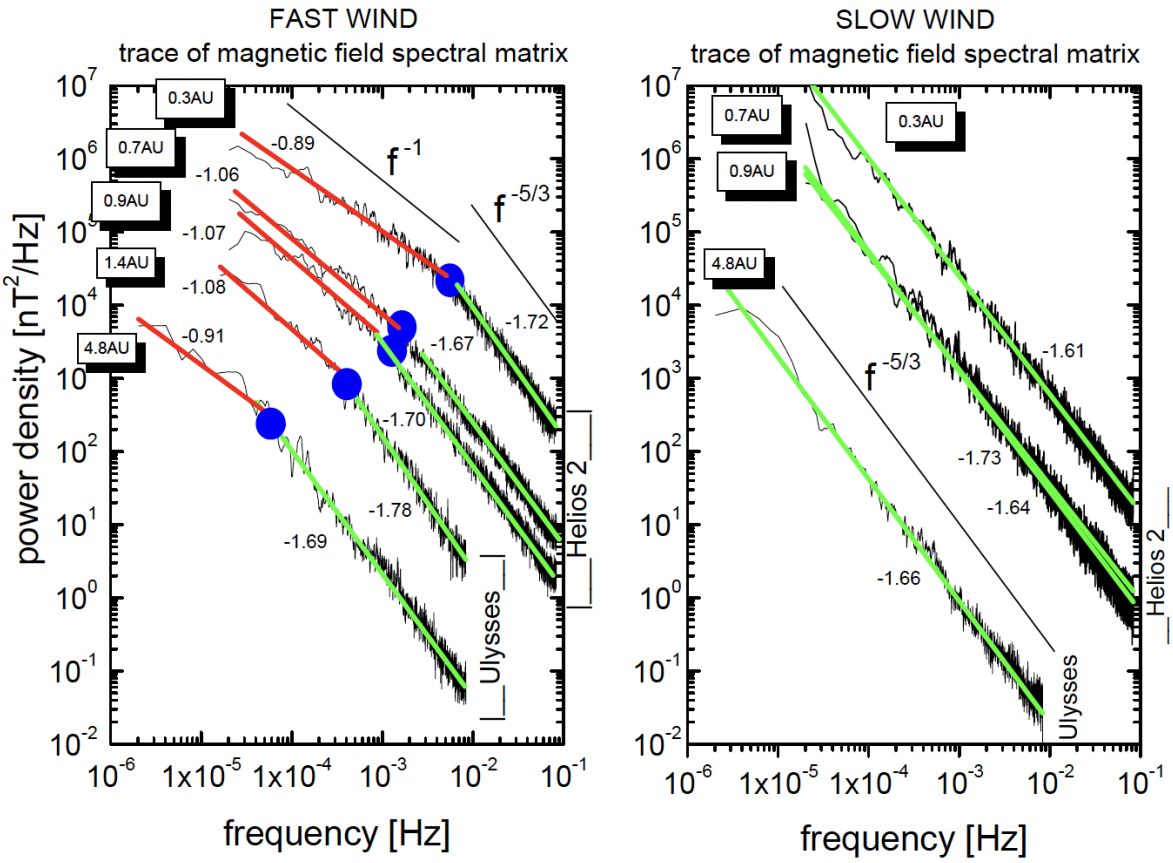

Figure 1.14: Left panel: power density spectra of magnetic field fluctuations observed by Helios 2 between 0.3 and 1 AU within the trailing edge of the same corotating stream shown in Figure 16, during the first mission to the Sun in 1976 and by Ulysses between 1.4 and 4.8 AU during the ecliptic phase. Ulysses observations at 4.8 AU refer to the end of 1991 while observations taken at 1.4 AU refer to the end of August of 2007. While the spectral index of slow wind does not show any radial dependence, the spectral break, clearly present in fast wind and marked by a blue dot, moves to lower and lower frequency as the heliocentric distance increases. Figure taken from (Bruno and Carbone, 2013)

that is commonly believed to originate from corona holes, and hence it is also known as the energy containing range. This is because the integral of $1/f$ is $\ln(f)$, and thus the energy contained in a frequency range from f_1 to f_2 is $\ln(f_2/f_1)$, indicating that the energy distributes evenly across the scales. Therefore, the $1/f$ range can be considered as an energy reservoir which constantly feeds energy into the inertial range, facilitating the turbulence cascade and dissipation. Indeed, observations from Ulysses and Helios in Figure 1.14 shows that the low frequency spectral break between the $1/f$ range and inertial range moves to lower frequency with increasing heliocentric distance, and in the mean time the turbulence energy drops. This is due to two major effects in the solar wind: turbulence dissipation and solar wind expansion.

For the first effect, it is obvious that the energy that is dissipated in the kinetic scales ultimately comes from the energy containing range. Without solar wind expansion, all of the spectra should share the same energy level in the $1/f$ range. And hence, as energy being cascaded and dissipated through the turbulence, it will simultaneously "eats" up the energy containing range, thereby turning the mechanical energy from the energy reservoir into heat. A detailed discussion of this mechanism can be found in Chapter 5.

The latter effect can be easily shown using the conservation of wave action (Velli, 1993) with WKB approximation. The wave action density of an Alfvén wave train in a spherically expanding flux tube with solar wind speed U can be written as:

$$S^+ = \frac{1}{2}\rho R^2 (U + V_A) \frac{(z^+/2)^2}{\omega_0 \frac{V_A}{U+V_A}} \tag{1.16}$$

where $z^+ = v + b$ is the Elsässer variable for outward propagating Alfvén wave component and $b = \delta B/\sqrt{\mu_0 \rho}$. The wave action density is defined as the fluctuation power density divided by the wave frequency in the plasma frame ω, which is doppler shifted from the launched frequency ω_0:

$$\omega = \omega_0 \frac{V_A}{U + V_A} \tag{1.17}$$

because in the plasma frame the source (sun) is moving away at U. The group velocity of the wave train is $U + V_A$, and to normalize the Elsässer variable, an additional $1/2$ factor is introduced. For an purely outward propagating Alfvén wave train, in the limit of negligible Alfvén speed ($V_A \ll U$) and spherically expanding flux tube with purely radial field ($|B| \propto R^{-2}, \rho \propto R^{-2}$), eq (1.16) can be reduced to

$$z^+ \propto R^{-0.5} \tag{1.18}$$

And thus $\delta B \propto R^{-1.5}$ and $\delta B/|B| \propto R^{0.5}$, which are very classical WKB results (Whang, 1973; Hollweg, 1990). Therefore, naturally the turbulence energy will drop with increasing heliocentric distance.

The formation of the energy containing $1/f$ range is topic of great interest in the past three decades, and numerous mechanisms have been proposed: Alfvénic turbulence cascade due to solar wind expansion (Velli et al., 1989), remnants of solar surface fluctuations (Matthaeus and Goldstein, 1986; Matthaeus et al., 2007), phase mixing of Alfvén waves (Magyar and Doorsselaere, 2022), parametric decay instability (Chandran, 2018), and saturation of magnetic fluctuations (Matteini et al., 2018). The $1/f$ noise itself is already of great interest for many fields of studies because it is known as the flicker noise or pink noise. This kind of noise can be found in almost any kind of physical system from economy data to electric currents. One of the focus of this dissertation is to see what the new observations of PSP from close to the sun can inform us about the energy injection range or the $1/f$ range in solar wind turbulence. Chapter 3 provides a systematic search for the $1/f$ range in the first 13 orbits of PSP, and some constraints on the formation mechanisms of the $1/f$ range. Chapter 5, based on the results from Chapter 3, discusses in details what implications the newly found predominant shallow-inertial double power law spectrum can provide for the solar physics community.

For more detailed discussion of the interpretation of the temporal signals from PSP and the transmission of Alfvén waves, please refer to Appendix C.

1.3 Parker Solar Probe

1.3.1 Mission Overview

Parker Solar Probe (PSP) (Fox et al., 2016), launched in November 2018, is the first spacecraft endeavors to travel into the solar atmosphere. As of April 2024 (Figure 1.15), PSP has finished its first 20 orbits and the closest approach to the sun is at 11.4 $R_{\odot}$. PSP will conduct the last planned Venus gravitational assist on Nov 6 2024, and enter its final family of orbits with perihelion at 9.9 $R_{\odot}$. Since 2021, PSP has been providing *in situ* measurements of the upper corona below the Alfvén surface (Kasper et al., 2021).

The primary scientific objectives of PSP are the following: 1. Trace the flow of energy that heats the solar corona and accelerates the solar wind; 2. Determine the structures and dynamics of the plasma and magnetic fields at the sources of the solar wind; 3. Explore mechanisms that accelerate and transport energetic particles. To answer these questions, PSP has four instrument suites on board: 1. the Electromagnetic Fields Investigations (FIELDS) (Bale et al., 2019; Bowen et al., 2020); 2. the Integrated Science Investigation of the Sun, Energetic Particle Instruments (IS⊙IS) (McComas et al., 2016); 3. the Solar Wind Electrons Alphas and Protons Investigation (SWEAP) (Kasper et al., 2016); 4. the Wide Field Imager for Solar Probe Plus (WISPR) (Vourlidas et al., 2016). A summary of the scientific results from the first four years of the mission in solar minimum can be found in this review paper (Raouafi et al., 2023a).

In this dissertation, we aim to provide observational constraints to partially tackle three of the sub-objectives (Fox et al., 2016): 1a. How is the energy from the lower solar atmosphere transferred to, and dissipated in, the corona and solar wind (Chapter 2, Chapter 3, Chapter 5); 2a. How does the magnetic field in the solar wind source regions connect to the photosphere and the heliosphere (Chapter 5, Chapter 4); 2b. Are the sources of the solar wind steady or intermittent (Chapter 4).

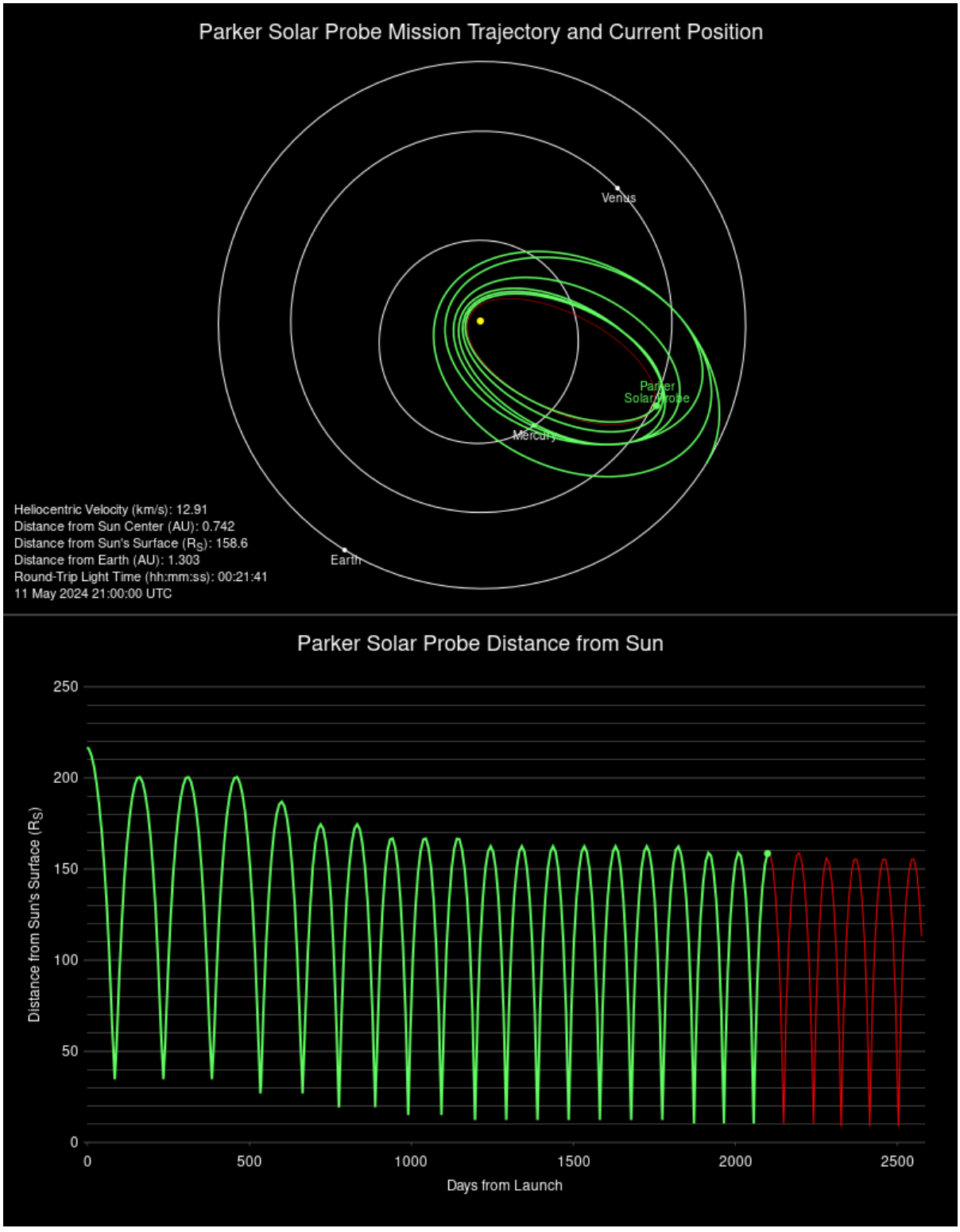

Figure 1.15: Parker Solar Probe orbits. Figure taken from https://parkersolarprobe.jhuapl.edu/The-Mission

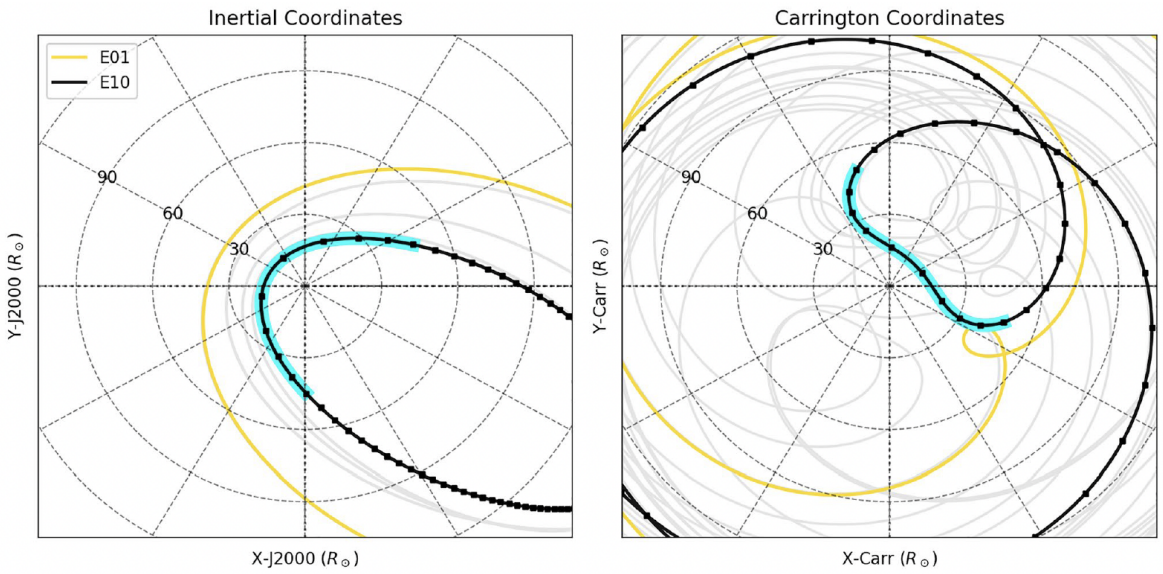

Figure 1.16: Orbital Geometry of the 13.3 R$\odot$orbit family. Parker's E10 orbital track projected into the solar equatorial plane is shown in black with E01 shown in yellow for contrast. Black squares are spaced 24 hr apart. Faint gray curves show the full prime mission trajectory (i.e., 24 orbits). The left-hand panel shows the inertial J2000 reference frame for which the orbit's elliptical nature and decreasing perihelion is clear. The right-hand panel shows the Carrington frame, which is most relevant for source mapping. This frame demonstrates the enormous range of solar longitude traversed by Parker in its latter orbits over just a few days around perihelion. Cyan shading shows the 9-day interval of E10 where Parker co-rotates or super-rotates with respect to the Sun, which is the focus of this study. Figure taken from (Badman et al., 2023)

1.3.2 PSP Orbits and Carrington Rotation

As discussed in section 1.2.3, during solar maximum, the solar corona is extremely complex and the various different structures including the helmet streamer, pseudo-streamer, and corona holes can be found all over the solar disk. In addition to that, PSP is in fact the fastest moving object that has been ever manufactured by humans, with a maximum speed (in solar inertial frame) of 176.46km/s. Consequently, the movement of PSP, especially during perihelion, adds another layer of complexity to explaining the source region of the *in situ* measured plasma and waves.

Right panel of Figure 1.16 shows the orbit of PSP in the solar corotating frame. For example, for the orbit of E10, the spacecraft traversed 60 degrees in Carrington longitude within 24 hours during perihelion, which is the typical apparent size of a equatorial

coronal hole flux tube as shown in Figure 1.11 during solar maximum. However, one will need take into the consideration of the projection effect of the intrinsically 3D structures, and the temporal change of the magnetic field on the sun. In addition, as discussed in (Badman et al., 2023), by adopting different parameters and different magnetic extrapolation techniques, different PFSS models can produce highly bifurcated source region results. Therefore, unless various different models reach consensus on the source region, it is highly questionable whether the magnetic connectivity produced by the models are physically true.

Therefore, in this dissertation, we adapt an alternative approach to tackle the magnetic connectivity problems. Instead of mapping the *in situ* measurements back to somewhere on the solar disk, we seek to explore the intrinsic properties in the data that can provide self-contextualization. In Chapter 4, we discuss some surprising properties of the magnetic magnitude time series measured by PSP around the perihelion and the implications of these properties.

1.4 Outline

The dissertation is organized as follows. In Chapter 2, we present our study concerning the conversion between different MHD eigenmodes. Using an 1D Expanding Box Model, we show that the MHD fast and slow modes are inter-convertible at the region where sound speed equals Alfvén speed without the loss of wave action. In Chapter 3, we provide a statistical study of the energy containing $1/f$ range using data from the first 13 orbits of PSP. In Chapter 4, we present some surprising properties of the magnetic magnitude time series from PSP and their implications on the magnetic connectivity problem. In Chapter 5, based on the finding in Chapter 3, we present a systematic survey of the shallow-inertial double power law found in solar wind turbulence measured by PSP from the first 17 encounters. In Chapter 6, we conclude this dissertation and propose future studies.

CHAPTER 2

Mode Conversion for MHD Waves and the Conservation of Total Wave Action

2.1 Introduction

The heliosphere is permeated by the solar wind, a supersonic and super-Alfvénic plasma flow originating from the solar corona, which continuously expands into the interplanetary medium (Parker, 1958; Velli, 1994). Since the beginning of *in situ* observations, it has been confirmed by various studies (Coleman, 1967, 1968; Belcher, 1971; Belcher and Davis, 1971) that the interplanetary space is filled with Alfvénic MHD turbulence and compressive fluctuations like the Pressure Balanced Structures (PBS) (Marsch, 1991; Tu and Marsch, 1995). Over the years, numerous studies have been conducted on the Alfvénic fluctuations in the solar wind, showing that interplanetary Alfvén waves are "Arc Polarized" or "Spherically Polarized" (Tsurutani et al., 1994; Riley et al., 1995; Tsurutani et al., 1997; Bale et al., 2019; Tenerani et al., 2021), kinetic in Nature (Tsurutani et al., 2018), and exhibit rich nonlinear effects (Hollweg, 1971; Tsurutani et al., 2018; Stefani et al., 2021). On the other hand, magnetosonic waves are more scarce, with some exceptions including in the upstream of interplanetary shocks (Tsurutani et al., 1983), which are likely generated locally by the instabilities associated with upstream beams of energetic ions; proton cyclotron waves generated locally by the kinetic dissipation of the nonlinear Alfvén wave (Tsurutani et al., 2002), which in the low frequency limit becomes slow magnetosonic waves; and in the solar corona [see e.g. (Ofman et al., 1999; Pascoe et al., 2013; Yang et al., 2015)]. Note however, with the plane-wave assumption, the fluctuations in the solar wind have non-negligible magnetosonic waves composition (Chaston

et al., 2020; Zhu et al., 2020). Therefore, the nonlinear evolution of magnetosonic waves in the solar wind remains an interesting topic.

Basic to the understanding of the wave evolution in the highly structured solar wind is the comprehension of the simpler, isotropic case, i.e., that of evolution in a plain, isotropic radial expanding wind. This obviously simple problem is not well-known yet. In the linear case, only the evolution of Alfvén waves is well understood: the Wentzel–Kramers–Brillouin (WKB) approximation predicts a 1/R decrease of the specific energy (Whang, 1973). However, the WKB approximation (as well as the finite frequency approximations, (Heinemann and Olbert, 1980; Velli et al., 1991; Velli, 1993), are not able to cope with the mode mixing introduced by the expansion (Lou, 1993a,b,c). The coupling arises because (a) The characteristics of different degrees of freedom (Alfvénic, Slow, Fast) depends on the plasma $\beta = \frac{2\mu_0 p}{B^2}$ which changes with distance; (b) The d.c. (background) magnetic field $\boldsymbol{B}_0$ and wave vector $\boldsymbol{k}$ change both in direction and modulus due to the expansion, which further modifies the MHD eigenmodes polarization; (c) Different modes tend to decay differently with the expansion, and so does higher degree effects such as wave steepening, and relative strength of wave-coupling.

Moreover, for an infinitely long monochromatic MHD wave train propagating in expanding medium, another underknown effect further complicates the situation. Contrary to common knowledge, the adiabatic invariant of the wave train (Wave Action) (Whitham, 1965; Bretherton, 1968; Dewar, 1970) is not well-conserved if the background conditions evolve close to equi-partition layer (Alfvén speed v_a, Sound speed c_s, wave vector $\vec{k}$, and background magnetic field $\vec{B}_0$ simultaneously satisfy: $v_a = c_s$ and $\vec{k} \parallel \vec{B}_0$) even in the WKB limit. This special condition can be easily achieved if the medium expands, e.g. in the expanding solar wind (see Figure 2.1) where the plasma $\beta \sim 1$. This topic has not been covered thoroughly in past literature, especially for magnetosonic modes, partially because of their dissipative nature. Early studies (Jacques, 1977; Lou, 1993b) on this subject mainly focused on their WKB evolution, i.e. *a priori* assumption of wave action conservation. Some other studies focused more on predicting the magnetogravity mode-conversion rate (Zhugzhda, 1979; Zhugzhda and Dzhalilov, 1981, 1982a,b; Cally,

2001; McDougall and Hood, 2007a,b, 2009). On the other hand, the subject of wave action conservation itself is more of theoretical interest and has only been studied in a general sense by (Hirota and Tokuda, 2010). Therefore, a thorough study of the evolution of simple MHD waves in expanding solar wind is still lacking. Our study aims to provide an intuitive physical picture of the mechanisms behind the violation of conservation law for infinitely long monochromatic wave train.

In this study, we propose a simple model to address the violation of wave action conservation. Our model shows that the violation is due to wave mode conversion, and that the total of wave action summed over all interacting modes (Alfvén, Slow, Fast) is a universally conserved quantity. In addition, we propose three distinctive mechanisms of the mode conversion, i.e. degeneracy, linear mode conversion, and resonance, providing an intuitive physical picture explaining the mode conversion process. By generalizing the conservation law for wave action, our model can serve as an extension of classical wave action conservation theory.

The rest of this chapter is organized as follows: In section 2, we start by reviewing the theory for the conservation of wave action in MHD and propose a simple, intuitive model for wave mode conversion and conservation of total wave action; in section 3, we present complementing simulation results to substantiate our model; in section 4, we discuss the bifurcated behaviors of Alfvén mode and magnetosonic modes; in section 5, we summarize our results.

2.2 Theory

In this section we give a brief overview of the concept of wave action (Whitham, 1965; Bretherton, 1968; Dewar, 1970) with MHD equations, and suggest a possible scenario leads to violation of wave action conservation. And we propose a simple, intuitive model showing that the total of wave action summed over all interacting modes is a universally conserved quantity.

2.2.1 Wave Action

The Lagrangian density for MHD system is (Lundgren, 1963):

$$\mathcal{L} = \frac{1}{2}\rho U^2 - \frac{p}{\gamma - 1} - \frac{B^2}{2\mu_0} \tag{2.1}$$

Where $\rho, \vec{U}, p, \vec{B}, \gamma$ are density, flow velocity, pressure, magnetic field, and adiabatic gas constant. To study the perturbation behaviors of this system, we decompose all fields into the background part plus the perturbation part. In this study, we limit the perturbations to be small compared with background fields. We adopt a WKB style temporal scale separation (wave frequency within the MHD regime but much higher than the effective frequency of expansion time scale). First, expand the Lagrangian density ($\mathcal{L} = \mathcal{L}_0 + \mathcal{L}_1 + \mathcal{L}_2 + o(\delta^2)$); Second, discard the first-order terms because they average to zero (both temporally and spatially); Last, keep the second-order terms [for details, see (Dewar, 1970)]:

$$L = \mathcal{L}_2 = \frac{1}{2}\rho_0(\Delta\vec{u})^2 - \frac{1}{2}\frac{(\Delta p)^2}{c_s^2\rho_0} - \frac{(\Delta\vec{B})^2}{2\mu_0} \tag{2.2}$$

where quantities with subscript "0" are the background fields, and quantities with Δ are the perturbations ($\Delta f = f - f_0$, and $f_0 = \langle f \rangle$). $c_s = \sqrt{\gamma p_0/\rho_0}$ is the sound speed. To proceed, we need to substitute all perturbations with their Fourier-transformed counterpart. The full ideal-MHD equation set with adiabatic closure is:

$$\frac{\partial \rho}{\partial t} + \nabla \cdot (\rho \boldsymbol{u}) = 0 \tag{2.3}$$

$$\rho\left(\frac{\partial \boldsymbol{u}}{\partial t} + \boldsymbol{u} \cdot \nabla \boldsymbol{u}\right) = -\nabla p + \frac{1}{\mu_0}(\nabla \times \boldsymbol{B}) \times \boldsymbol{B} \tag{2.4}$$

$$\frac{\partial \boldsymbol{B}}{\partial t} = \nabla \times (\boldsymbol{u} \times \boldsymbol{B}) \tag{2.5}$$

$$\nabla \cdot \boldsymbol{B} = 0 \tag{2.6}$$

$$\frac{d}{dt}\left(p\rho^{-\gamma}\right) = 0 \tag{2.7}$$

The displacements of three MHD eigenmodes form an orthogonal triad (see Appendix A for derivations), and hence without loss of generality, we write the flow perturbation of mode M as:

$$\Delta\vec{u}_M = \tilde{a}_M \omega_M \hat{e}_M \tag{2.8}$$

After linearization, plug (2.8) into (2.3) and (2.7), we obtain:

$$\Delta p_M = c_s^2 \delta\rho_M = \tilde{a}_M c_s^2 \rho_0 k_M (\hat{k}_M \cdot \hat{e}_M) \tag{2.9}$$

and into (2.5), we obtain:

$$\Delta\vec{B}_M = \tilde{a}_M B_0 k_M \left[\hat{b}(\hat{k}_M \cdot \hat{e}_M) - (\hat{b} \cdot \hat{k}_M)\hat{e}_M\right] \tag{2.10}$$

where $\tilde{a}_M$ is complex amplitude of displacement, ω_M is intrinsic frequency of the wave, $\vec{k}_M$ is wave vector, $\hat{e}_M$ is the unit vector along displacement, and $\hat{k}_M = \vec{k}_M/k_M$, $\hat{b} = \vec{B}_0/B_0$ are unit vectors of wave vector and background magnetic field, all of mode M.

Finally we plug (2.8)-(2.10) into (2.2) and temporally or spatially average it and obtain the averaged Lagrangian Density $\mathscr{L}$:

$$\begin{aligned}
&\mathscr{L}_M(\tilde{a}_M, -\partial_t\theta_M, \nabla_x\theta_M) \\
&\quad = \frac{1}{4}\rho_0 \tilde{a}_M^2 \Big\{\omega_M^2 - c_s^2 k_M^2 (\hat{k}_M \cdot \hat{e}_M)^2 \\
&\qquad - v_a^2 k_M^2 \left[\hat{b}(\hat{k}_M \cdot \hat{e}_M) - (\hat{b} \cdot \hat{k}_M)\hat{e}_M\right]^2\Big\}
\end{aligned} \tag{2.11}$$

where $\theta_M(x,t)$ is the wave phase, hence $-\partial_t\theta_M = \omega_M$ and $\nabla_x\theta_M = \vec{k}_M$. Note that for Alfvén mode ($\delta\rho_A = 0$, $\vec{k}_A \cdot \hat{e}_A = 0$), the Lagrangian density can be reduced to:

$$\begin{aligned}
&\mathscr{L}_A(\tilde{a}_A, -\partial_t\theta_A, \nabla_x\theta_A) \\
&\qquad = \frac{1}{4}\rho_0 \tilde{a}_A^2 \left[\omega_A^2 - v_a^2 k_A^2 (\hat{b} \cdot \hat{k})^2\right]
\end{aligned} \tag{2.12}$$

(Whitham, 1965; Bretherton, 1968) have shown that for a slowly varying (WKB) wavetrain, the local amplitude, frequency, and wavenumber are governed by the variational principle (henceforward we change the notations: $\partial_t\theta \to \theta_t$ and $\nabla_x\theta \to \theta_x$):

$$\delta \int \mathscr{L}(\tilde{a}, -\theta_t, \theta_x) dx dt = 0 \tag{2.13}$$

subject to infinitesimal variations $\delta\tilde{a}(x,t)$, $\delta\theta(x,t)$ which vanish at infinity. Variation with respective to $\tilde{a}$ yields ($\mathscr{L} = \tilde{a}^2\bar{\mathscr{L}}$):

$$\begin{aligned} &\frac{\partial \mathscr{L}}{\partial \tilde{a}} = 2\tilde{a}\bar{\mathscr{L}} = 0 \\ &\Rightarrow \mathscr{L} = 0 \end{aligned} \tag{2.14}$$

which is equivalent to the dispersion relations. Variation with respect to θ on (2.13) yields (see Appendix-A for detailed derivation):

$$\frac{\partial}{\partial t}\left(\frac{\partial \mathscr{L}}{\partial \omega}\right) - \frac{\partial}{\partial x}\left(\frac{\partial \mathscr{L}}{\partial k}\right) = 0 \tag{2.15}$$

This is a conservation equation for the quantity $\partial\mathscr{L}/\partial\omega$ subject to flux $-\partial\mathscr{L}/\partial k$. Now substitute θ with θ_M, k with $\vec{k}_M$, and rewrite ∂_x as ∇, we have:

$$\frac{\partial}{\partial t}\left(\frac{\partial \mathscr{L}_M}{\partial \omega_M}\right) - \nabla \cdot \left(\frac{\partial \mathscr{L}_M}{\partial \vec{k}_M}\right) = 0 \tag{2.16}$$

Considered that the dispersion relations are equivalent to:

$$\mathscr{L}_M = 0 \tag{2.17}$$

and the group velocities are:

$$\vec{v}_{g,M} = -\frac{\partial \mathscr{L}_M}{\partial \vec{k}_M} \Big/ \frac{\partial \mathscr{L}_M}{\partial \omega_M} = \mathscr{L}_{\vec{k},M}/\mathscr{L}_{\omega,M} \tag{2.18}$$

So that the conservation equation turns into:

$$\frac{\partial}{\partial t}\left(\frac{\partial \mathscr{L}_M}{\partial \omega_M}\right) + \nabla \cdot \left(\vec{v}_{g,M}\frac{\partial \mathscr{L}_M}{\partial \omega_M}\right) = 0 \tag{2.19}$$

(2.19) marks the conservation law for wave action density $\mathscr{L}_{\omega,M}$, subject to flux $\vec{v}_{g,M}\mathscr{L}_{\vec{k},M}$. The wave energy density can be further defined as:

$$\begin{aligned} \mathscr{E} &= \omega\mathscr{L}_\omega - \mathscr{L} \\ &= \frac{1}{2}\rho_0\langle(\Delta\vec{u})^2\rangle + \frac{1}{2}\frac{\langle(\Delta p)^2\rangle}{c_s^2\rho_0} + \frac{\langle(\Delta\vec{B})^2\rangle}{2\mu_0} \end{aligned} \tag{2.20}$$

and consider that for waves with small amplitude $\mathscr{L} = 0$, the wave action density h_M for mode M is defined as:

$$h_M = \mathscr{L}_{\omega,M} = \frac{\mathscr{E}_M}{\omega_M} \tag{2.21}$$

where $\mathscr{E}_M$ is the wave energy density and ω_M is the intrinsic frequency of Alfvén, Slow, and Fast wave respectively. And finally we have the **conservation of wave action for monochromatic waves**:

$$\frac{\partial}{\partial t}\left(\frac{\mathscr{E}_M}{\omega_M}\right) + \nabla \cdot \left(\vec{c}_M\frac{\mathscr{E}_M}{\omega_M}\right) = 0 \tag{2.22}$$

Integrating in space and assuming periodicity at the boundary, we get:

$$\hbar_M = \frac{E_M}{\omega_M} = const. \tag{2.23}$$

where $E_M = \int_V \mathscr{E}_M d\nu$ and $\hbar_M$ is the wave action (quantum) for mode M. Note that wave action is the counterpart of adiabatic invariant for waves in fluid system and is independent of the detailed description (e.g. MHD or CGLMHD). The notation $\hbar_M$ is adopted here purposely because it shares the same dimension with the Planck constant $\hbar$ and possess similar physical meaning.

2.2.2 Conservation of Total Wave Action: Theory

In the derivation above, a fundamental assumption is that $\mathscr{L}_A$, $\mathscr{L}_S$, $\mathscr{L}_F$ are independent with each other, which is questionable at equi-partition layer ($c_s = v_a, \vec{k} \parallel \vec{B}_0$). At the equi-partition layer, all three modes (Alfvén, Slow, Fast) propagate at the same phase velocity, and hence wave-wave interaction is possible. Detailed analysis shows that at the equi-partition layer, there are three mode-conversion mechanisms: degeneracy, linear mode conversion, resonance. The first mechanism is degeneracy of magnetosonic modes: At the equi-partition layer, the concept of "Fast" and "Slow" is ill-defined for parallel waves, and hence Fast and Slow waves would be indistinguishable from each other, i.e. an "identity crisis". Passing through the equi-partition layer, the originally "Slow" wave would become "Fast" wave due to the abrupt change of the displacement polarization vector. Note that because this process happens on the $\vec{k} - \vec{B}_0$ plane, degeneracy is only possible for magnetosonic modes. The second mechanism is linear mode conversion [see e.g. (Swanson, 1998, 2003; McDougall and Hood, 2007b)]: at the equi-partition layer, due to the rapid change of eigenvectors, the projection of the disturbance on the each of the two magnetosonic eigenvectors change; Therefore, the initially monochromatic magnetosonic mode would be continuously linearly transformed to the mix of both slow and fast mode, until the background conditions evolve to be sufficiently distant from the equi-partition layer. The third mechanism is resonance: The linearly polarized Alfvén wave would resonate at the equi-partition layer ($c_s = v_a$) to convert the wave energy into sonic modes [see e.g. (Hollweg, 1971; Stefani et al., 2021) and references therein], which is a candidate for chromosphere heating at the magnetic canopy [see (Hollweg et al., 1982; Bogdan et al., 2003)]. For all three mechanisms, the mode conversion processes are transient, and hence dissipation is negligible. Therefore, for Fast (and Slow) mode, the conversion process can be illustrated phenomenologically as:

$$\begin{aligned} \frac{E_F}{\omega_r} \xrightarrow[\text{Linear Mode Conversion}]{\text{Degeneracy}} \frac{E'_F}{\omega_r} + \frac{E'_S}{\omega_r} \\ E_F = E'_F + E'_S \end{aligned} \tag{2.24}$$

where $E_{()}$ and $E'_{()}$ are wave energy before and after equi-partition layer respectively, and ω_r is intrinsic wave frequency at the equi-partition layer. Whereas for Alfvén mode:

$$\begin{aligned} \frac{E_A}{\omega_r} \xrightarrow{\text{Resonance}} \frac{E'_F}{\omega_r} + \frac{E'_S}{\omega_r} + \frac{E'_A}{\omega_r} \\ E_A = E'_F + E'_S + E'_A \end{aligned} \tag{2.25}$$

In the conversion process, the total wave energy is conservatively reallocated among corresponding degrees of freedom (eigenmodes), and hence the exchange of wave action is also conservative. Passing through equi-partition layer, the wave action for each degree of freedom:

$$\hbar'_M = \frac{E'_M}{\omega_M} = const. \tag{2.26}$$

would be independently conserved. And hence the total wave action:

$$\hbar_{tot} = \sum_{M=A,S,F} \frac{E_M}{\omega_M} = \sum_{M=A,S,F} \frac{E'_M}{\omega_M} = const. \tag{2.27}$$

is conserved. In short, we conjecture that for MHD small-amplitude WKB perturbations, the **total of wave action summed over all interacting modes is a universally conserved quantity**.

2.3 Simulation Results

2.3.1 Simulation Setup and Diagnostics

We conduct simulations with Expanding Box Model (EBM) formulated by [(Velli et al., 1992), (Grappin et al., 1993; Grappin and Velli, 1996)] and implemented by [(Shi et al., 2020)]. The code is pseudo-spectral, using Fast Fourier Transform to calculate spatial derivatives and 3rd order explicit Runge-Kutta method to integrate in time. We do not add explicit viscosity or resistivity but adopt a numerical filter that adaptively dissipate shocks formed in the simulations. The simulation setup is illustrated in Figure 2.1. The

simulation domain is 1D with 256 grid points and co-moves with the background solar wind at the speed of $U_0 = 400$ km/s. For each run, we initialize the simulation domain with uniform background magnetic field $\vec{B}_0$, pointing θ_0 w.r.t. the radial direction, and run the simulation from 0.1 AU to 1.0 AU. Velocity has unit $u^* = 150$km/s, length has unit $L^* = 0.012$AU, and number density has unit $n^* = 200\text{cm}^{-3}$, and thus magnetic field has unit of $u^*\sqrt{\mu_0 m_p n^*} = 97.25$nT, where m_p is proton mass. The adiabatic gas constant is chosen to be $\gamma = 5/3$. Different from the regular EBM, the simulation domain in our model is rotated by an initial angle α with respect to the radial direction, i.e., the grid points used in this study are distributed on an axis $\hat{e}_{x'}$ such that the angle between $\hat{e}_r$ (the radial direction) and $\hat{e}_{x'}$ is α initially. As the expansion effect will stretch the plasma volume in the direction perpendicular to $\hat{e}_r$, the axis $\hat{e}_{x'}$ will rotate away from the radial direction, i.e. α will increase with time (see (Shi et al., 2020) for more details).

We initialize simulations with small amplitude monochromatic Alfvén, Slow, and Fast wave with same wavevector $\vec{k}$, and vary only the initial background magnetic field modulus $|\vec{B}_0|$. At each time step, the wave vector is *a priori* determined by linear theory [(Völk and Aplers, 1973)], turning gradually towards radial:

$$\vec{k}(t) = (k_{0x}, k_{0y}/a(t), 0) \tag{2.28}$$

$$a(t) = \frac{R(t)}{R_0} = 1 + \frac{U_0}{R_0} \cdot t \tag{2.29}$$

where $a(t)$ is the expansion factor and $R_0 = 0.1$AU. Then we extract other background quantities including $\rho_0(t)$, $p_0(t)$, and $\vec{B}_0(t)$ by averaging over the simulation domain. It is noteworthy that $\vec{B}_0(t)$, per conservation of magnetic flux, turns gradually away from radial over time (Parker Spiral):

$$\vec{B}_0(t) = (B_{0x}/a(t)^2, B_{0y}/a(t), 0) \tag{2.30}$$

Given $\vec{k}(t)$ and other averaged background quantities, we can derive various useful quan-

tities as diagnostics. The wave energy density is calculated by:

$$\mathscr{E}_w = \frac{1}{2}\langle\rho\rangle\langle(\Delta\vec{u})^2\rangle + \frac{\langle(\Delta p)^2\rangle}{2\langle\rho\rangle c_s^2} + \frac{\langle(\Delta\vec{B})^2\rangle}{2\mu_0} \tag{2.31}$$

where $c_s^2 = \gamma\frac{\langle p\rangle}{\langle\rho\rangle}$, $\langle()\rangle$ is the average of () in the simulation domain, and $\delta() = () - \langle()\rangle$.

After that we need to decompose the wave energy into different degrees of freedom (Alfvén, Slow, and Fast mode). We first decompose the kinetic part of the wave energy density because the eigen-polarization of $\delta\vec{u}$ of the three eigenmodes form an orthogonal triad. And for small amplitude WKB waves, our discussion in section 2.2 shows that $\mathscr{L} = 0$, which indicates equi-partition between the kinetic ($\mathscr{E}_k = \frac{1}{2}\langle\rho\rangle\langle(\Delta\vec{u})^2\rangle$) and potential (elastic+magnetic) ($\mathscr{E}_p + \mathscr{E}_m = \frac{\langle(\Delta p)^2\rangle}{2\langle\rho\rangle c_s^2} + \frac{\langle(\Delta\vec{B})^2\rangle}{2\mu_0}$) energy. Therefore, we can decompose the wave energy density via:

$$\mathscr{E}_{w,(A,S,F)} = \mathscr{E}_{k,(A,S,F)}/\mathscr{E}_k * \mathscr{E}_w \tag{2.32}$$

And with eigen-frequencies $\omega_{A,S,F}$ of each mode, we obtain the wave action for each mode:

$$\hbar_{A,S,F} = \int_{V(t)} \frac{\mathscr{E}_{w,(A,S,F)}}{\omega_{A,S,F}} d\nu = \frac{E_{w,(A,S,F)}}{\omega_{A,S,F}} \tag{2.33}$$

where $V(t)$ is the volume of the "Expanding" simulation domain at time t and $E_{\omega,(A,S,F)}$ is the integrated wave energy enclosed by the simulation domain. Finally, we have the total wave action:

$$\hbar_{tot} = \hbar_A + \hbar_S + \hbar_F \tag{2.34}$$

The conservation of total wave action states that: $\hbar_{tot} = const.$, and thus we diagnose each run with the normalized total wave action $\tilde{\hbar}_{tot}(t)$:

$$\begin{aligned} \tilde{\hbar}_{tot}(t) &= \hbar_{tot}(t)/\hbar_{tot}(0) \\ &= \tilde{\hbar}_A(t) + \tilde{\hbar}_S(t) + \tilde{\hbar}_F(t) \end{aligned} \tag{2.35}$$

This is the primary diagnostic for our simulations.

2.3.2 Conservation of Total Wave Action: Simulation

To prove our conjecture on conservation of total wave action, the initial conditions are carefully selected so that the resonance conditions can be satisfied perfectly or partially in the simulation. Figure 2.2 shows nine simulation runs of monochromatic Alfvén, Slow, and Fast waves with three different initial $|\vec{B}_0|$ (hence Alfvén speed v_a). All runs are initialized with uniform $\vec{B}_0$ with $\delta_0 =< \vec{B}_0, \hat{r} >|_{t=0} = 6°$, and initial wave vector $\vec{k}$ with $\alpha_0 =< \vec{k}, \hat{r} >|_{t=0} = 12°$, both pointing counterclockwise w.r.t. radial $\hat{r}$ ($\alpha =< \vec{k}, \hat{r} >, \delta =< \vec{B}_0, \hat{r} >, \theta =< \vec{k}, \vec{B}_0 >$, also see Figure 2.1). To understand the evolution of monochromatic waves, we show in each panel of Figure 2.2 the normalized total wave action $\tilde{\hbar}_{tot}$ defined in (2.35) and its composition in three different colors: $\tilde{\hbar}_A$ (Alfvén, Blue), $\tilde{\hbar}_S$ (Slow, Orange), $\tilde{\hbar}_F$ (Fast, Green). The resonance criteria, c_s/v_a and $\theta =< \vec{k}, \vec{B}_0 >$ are shown in the top row, and resonant windows are highlighted with red and cyan bars, also overlaid in all panels to indicate the same periods.

As shown in Figure 2.1(c), $\vec{B}_0$ turns gradually away from radial, whereas $\vec{k}$ turns gradually towards radial over time, and thus with our setup ($\alpha_0 > \delta_0$), two vectors will coincide as the wave propagating outwards. The three different initial $|\vec{B}_0|$ are carefully selected to represent perfect equi-partition layer passing ($c_s = v_a, \vec{k} \parallel \vec{B}_0$ are perfectly satisfied simultaneously), partial equi-partition layer passing (Both $c_s = v_a, \vec{k} \parallel \vec{B}_0$ are satisfied, but not simultaneously), and miss (one of the resonant criteria is not satisfied), shown respectively in column 1-3 in Figure 2.2.

Results show that all runs start with conserved wave action (only one color is presented at a given time step, vertical intersection), and some of the runs (S1, S2, F1, F2) subsequently convert to other modes. Specifically, run S1 passes through the equi-partition layer perfectly (overlapping red and cyan overhead bars) at around 0.1 AU and hence converts completely from Slow mode (orange) to Fast mode (green), and vice versa for run F1. On the other hand, run S2 passes through the equi-partition layer

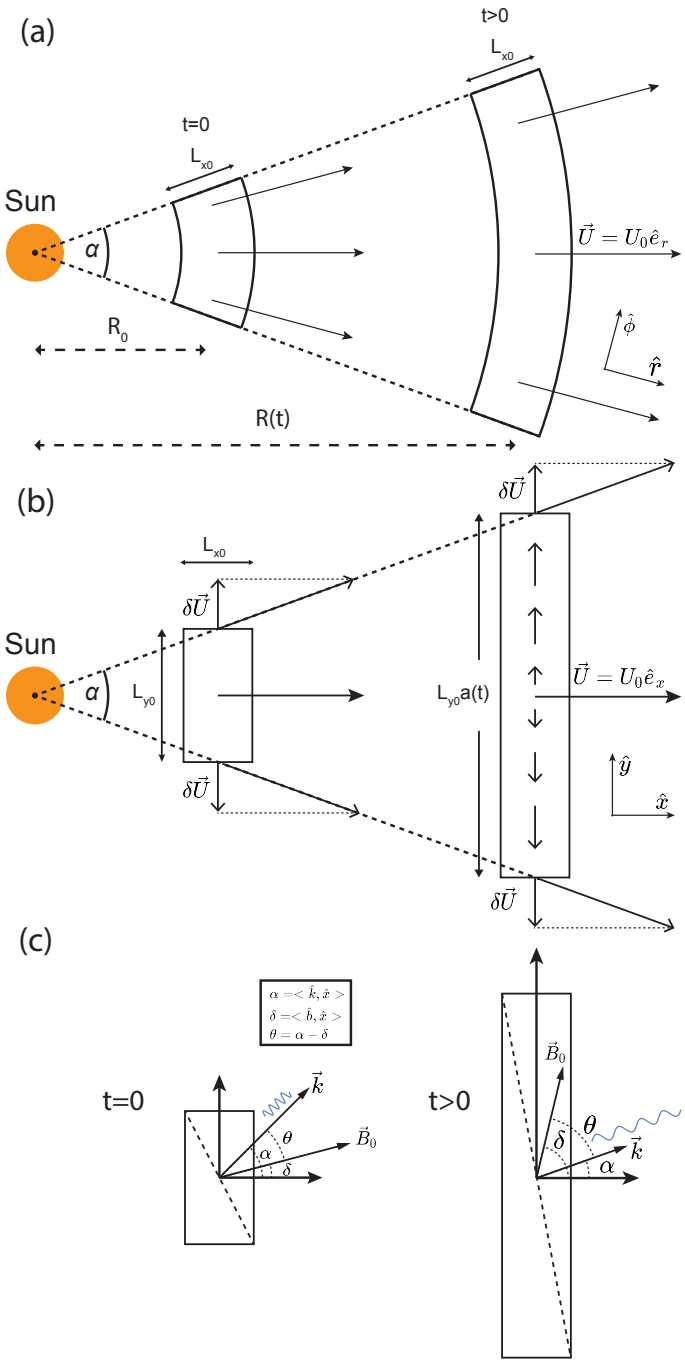

Figure 2.1: Sketch of the evolution of a plasma volume advected by a spherical wind with constant speed. (a) Exact evolution, (b) approximate evolution in the limit of small angular size (Expanding Box Model), and (c) transformation of a parallel wave ($\vec{k} \parallel \vec{B}_0$) into an oblique wave. $\vec{B}_0$ turns away from radial, whereas $\vec{k}$ turns towards radial.

semi-perfectly, and thus run S2 converts partially from Slow mode to Fast mode, and vice versa for run F2. Most importantly, all of the four runs, albeit having mode conversion, maintain an almost constant total wave action all over the evolution. Especially for run S2 and F2, after the transient mode conversion phase, the slow mode and fast mode part of the wave coexist, and the wave action for both modes are independently conserved.

Other runs (A1-A3, S3, F3) present no sign of mode conversion and therefore maintain a constant total (albeit monochromatic) wave action. One may notice that for runs S1 and S3, the total wave action decreases significantly towards the end (R $>$ 0.5 AU). This is due to dissipation of shock formed via wave steepening.

2.4 Discussion

In this section we give a short discussion on the stability of Alfvén wave and the mechanisms of mode-conversion seen in the magnetosonic modes.

2.4.1 Stability of Alfvén Wave

As shown in Figure 2.2, Alfvén wave appears to be more stable than magnetosonic waves. A simple explanation to this is that Alfvén wave is a transverse wave and hence per Burgers' equation, Alfvén wave does not resonates with itself. More specifically, the inviscid Burgers' equation is written as:

$$\frac{\partial \vec{u}}{\partial t} + \vec{u} \cdot \nabla \vec{u} = 0 \tag{2.36}$$

For Alfvén mode, as a transverse wave, the convective term is zero:

$$\vec{u} \cdot \nabla \vec{u} = 0 \tag{2.37}$$

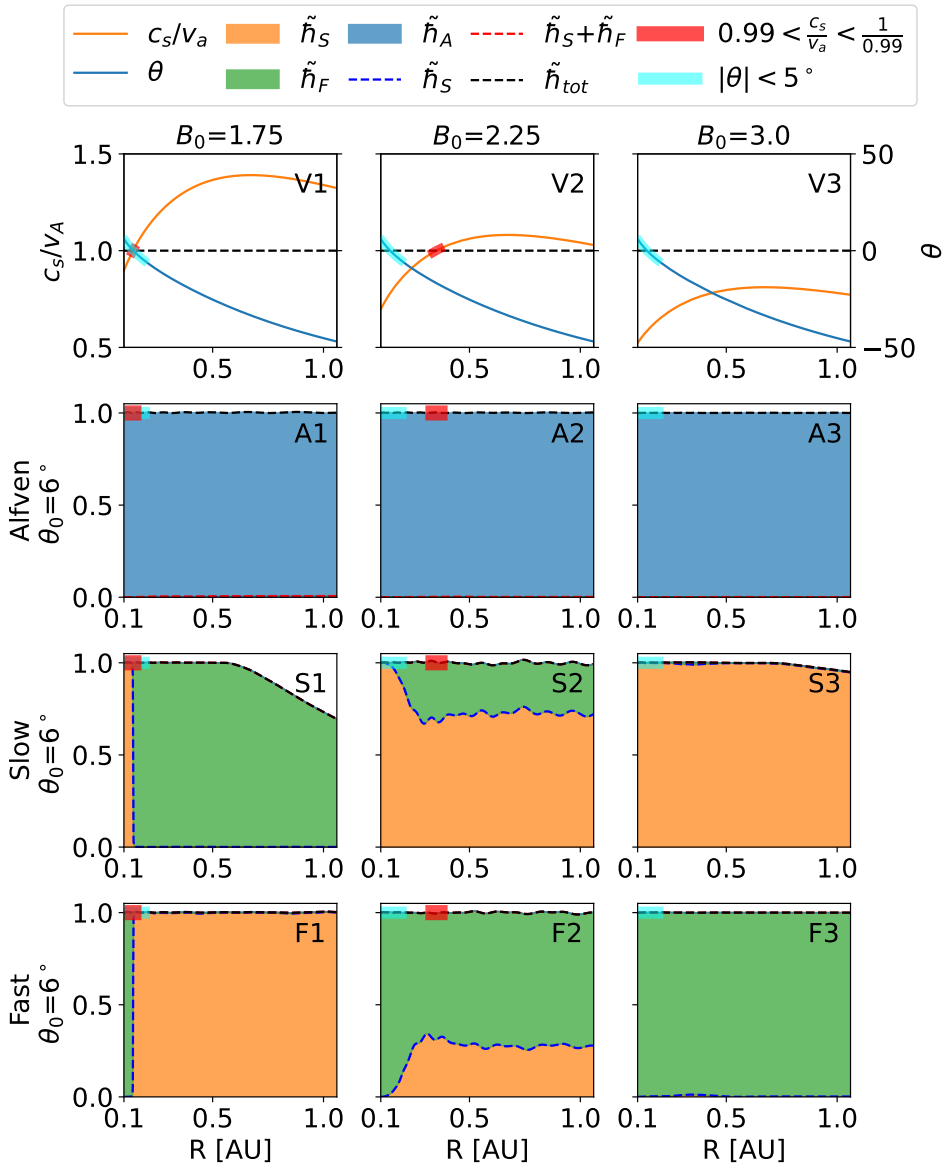

Figure 2.2: The evolution of normalized total wave action with initial monochromatic Alfvén (A1-A3), Slow (S1-S3), and Fast wave (F1-F3) in expanding box simulation, together with resonance/degeneracy condition (V1-V3). All runs are initialized with $\delta_0 =< \vec{B}_0, \hat{r} >|_{t=0} = 6°$, $\alpha_0 =< \vec{k}, \hat{r} >|_{t=0} = 12°$, and $\theta_0 = \alpha_0 - \delta_0$, varying only $|\vec{B}_0|$. The evolution of plasma parameters c_s/v_a and $\theta =< \vec{B}_0, \vec{k} >$ are plotted in the top row with orange and blue lines, and the region close to resonance are highlighted with overlaid red and cyan bar on all panels. Rows 2-4 show the radial evolution of normalized wave actions with different colors, respectively initialized with monochromatic Alfvén, Slow, and Fast wave. The color in the panels indicate the normalized wave action for Alfvén/Slow/Fast mode denoted with $\tilde{\hbar}_A/\tilde{\hbar}_S/\tilde{\hbar}_F$, and they are stacked together, as indicated by dashed lines ($\tilde{\hbar}_S$,$\tilde{\hbar}_S + \tilde{\hbar}_F$), and finally into the normalized total wave action $\tilde{\hbar}_{tot}$.

Hence no self-resonance is present for Alfvén wave. Moreover, the displacement vector of Alfvén wave is perpendicular to the $\vec{k} - \vec{B}_0$ plane. It is hence extremely hard for Alfvén wave to convert to the two magnetosonic modes with linear mode conversion. Therefore, the only viable mechanism in our setup for Alfvén wave to convert to other magnetosonic modes is through Alfvén resonance [(Hollweg, 1971; Stefani et al., 2021)]. The effectiveness of the resonance is proportional to both wave amplitude and interaction time. It is hence very hard for Alfvén wave to exhibit observable nonlinear effect if the wave amplitude is small and is propagating in expanding medium. On the other hand, if we abandon the expansion effects and run the simulation without expansion effect, or increase the wave amplitude, we may achieve significant mode conversion for the Alfvén wave. Therefore, it is interesting to see whether the total wave action is a better-conserved quantity than single-mode wave action with the presence of significant mode-conversion for Alfvén wave.

Figure 2.3 demonstrates two simulation runs, showing respectively small-amplitude Alfvén wave without expansion effect (R1), and large-amplitude Alfvén wave with expansion effect (R2). Simulation results show that both abandoning expansion effect and increasing amplitude can induce significant mode-conversion (resonance). Moreover, the normalized total wave action plots (R1, R2) clearly show that, albeit with significant resonance, the total wave action remains almost constant until shock dissipation intensify.

2.4.2 Magnetosonic Wave Mode Resonance

The mode conversion processes of magnetosonic waves in Figure 2.2, panel S2/F2 are significantly different from the complete mode conversion in panel S1/F1. In fact, they exemplify two distinct mode conversion mechanisms, i.e. degeneracy and linear mode conversion [see e.g. (Zhugzhda, 1979; Zhugzhda and Dzhalilov, 1981, 1982a,b; Cairns and Lashmore-Davies, 1983; Swanson, 1998; Cally, 2001; Swanson, 2003; McDougall and Hood, 2007b,a) and references therein]. Degeneracy happens only when equi-partition layer ($c_s = v_a, \vec{k} \parallel \vec{B}_0$) passing is perfect, and hence is very rare. Linear mode conversion

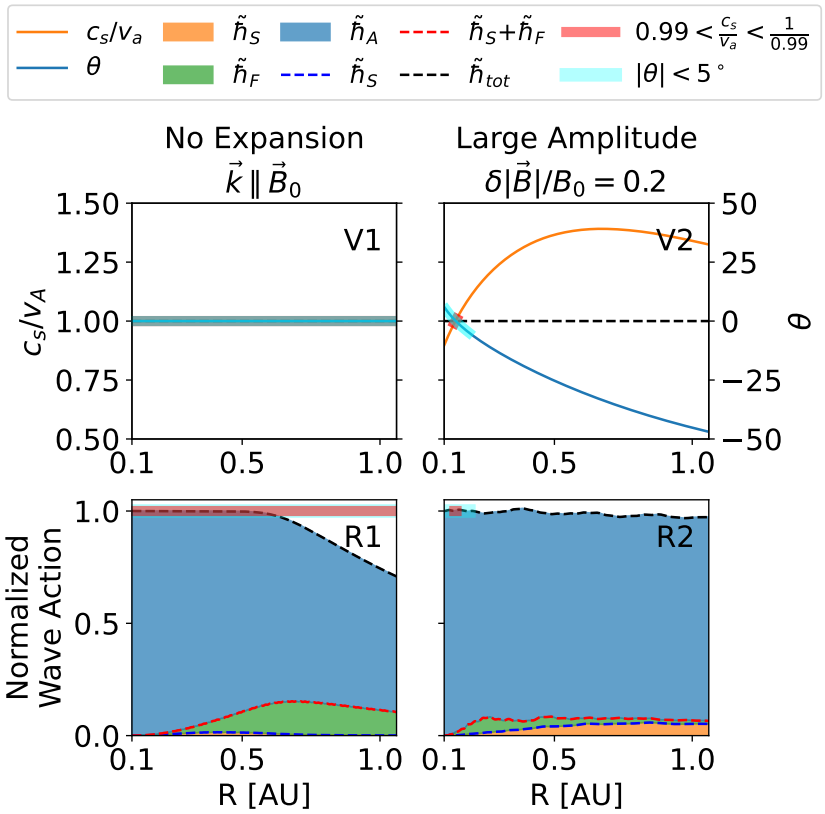

Figure 2.3: The evolution of normalized total wave action with initial monochromatic Alfvén waves. Run R1: small amplitude, always resonant, and has no expansion; Run R2: large amplitude, transient perfect resonant, and has expansion. Resonant conditions are shown in V1/V2. All legends are identical to Figure 2.2. The total wave action is conserved for both runs.

happens within a small region around the equi-partition layer, where the dispersion relation of Slow and Fast mode coincides, and hence is more universal.

The complete conversion in panels S1/F1 can be simply explained by the sudden change of the displacement polarization upon passing through the equi-partition layer, i.e. degeneracy of wave modes. The detailed evolution of run F1 is shown in Figure 2.4. Two wave profiles at two time steps adjacent to the mode conversion point are shown for comparison. Before entering the equi-partition layer, the displacement vector's trajectory (Lissajous curve) from edge to edge in the simulation domain (dark dashed close loop, radar plot, panel b) is parallel to the fast mode displacement polarization (red arrow); and in the meantime the wave vector (blue arrow) and the background magnetic field

(orange dashed arrow) are very closely aligned with each other. Passing through the equi-partition layer (see the slight change of $< \vec{B}_0, \vec{k} >$ before and after the equi-partition layer), the wave profile is hardly modified (panel b/c blue, orange, green, and red dashed line), but the polarization vectors have an abrupt change (sudden change of red/blue vectors in panel b/c, radar plot) because the meaning of "Fast" and "Slow" switches at equi-partition layer, and hence the projection of the displacement vector's trajectory (dark dashed line, radar plot) on the two polarization vector (red/blue vectors, radar plot) has an abrupt change.

For comparison, the detailed evolution of run F2 is shown in Figure 2.5. As we can see in panel b and c, the linearly polarized Fast wave started to convert to slow mode via linear mode conversion (see panel a in Figure 2.5, the growing ratio of orange area (slow mode) from 0.1 AU and 0.3 AU). Such linear mode conversion happens because around the equi-partition layer, the eigen-vectors of magnetosonic modes are changing rapidly, and therefore the system becomes non-WKB. The rapid change of the eigen-vectors changes the mixing ratio of slow and fast mode (see the radar plots in panel b and c, depicting the wave profiles at two time steps indicated by two red vertical dashed line in panel a). Subsequently, because of the phase speed difference between two modes, the Lissajous curve of the wave change from an linearly polarized wave (thin dashed black close loop in radar plot, panel b) to a circularly polarized wave (oval-like dashed black close loop in radar plot, panel c). Note that the oval-like Lissajous curve indicates that the two wave modes have similar frequencies, further confirming the mode conversion process is linear (or else would transport wave energy to higher wave number).

2.5 Summary

Half a century ago, the theory of wave action conservation is devised to describe the nonlinear evolution of WKB waves [see (Whang, 1973), (Whitham, 1965), (Bretherton, 1968), (Dewar, 1970)]. However, the classical theory fails to predict the mode-conversion happening close to the MHD equi-partition layer ($c_s = v_a, \vec{k} \parallel \vec{B}_0$). In this chapter,

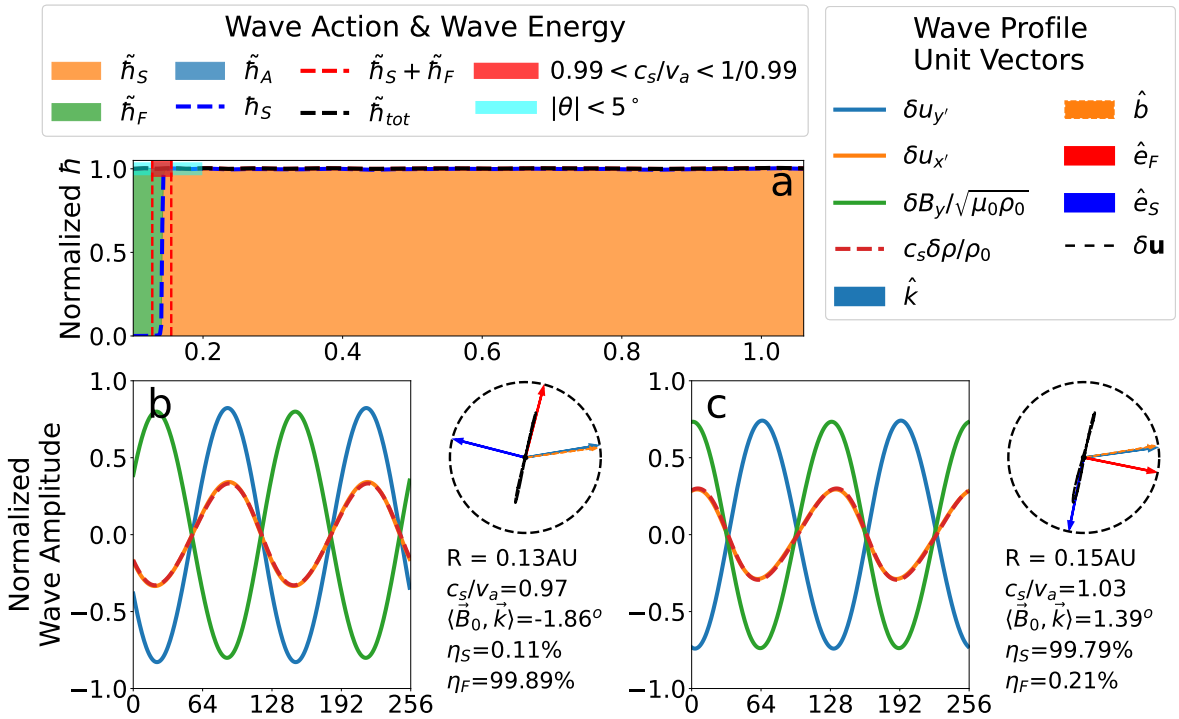

Figure 2.4: The detailed evolution of run F1 with wave profile is shown here. Panel a is identical to panel F1 in Figure 2.2; x axis is radial distance to sun (R [AU]). Panel b and c are the wave profile at two time steps indicated by the two red, vertical dashed line in panel a; x axis is grid points. The legends of panel a are identical to legends in Figure 2.2. The blue, orange solid line in panel b and c are flow speed fluctuation (displacement) amplitude along x' (parallel to $\vec{k}$) and y' (coplanar with $\vec{k}$ and $\vec{B}_0$) direction; green solid line is the normalized magnetic fluctuation amplitude; and the red dashed line is the density fluctuation amplitude. In the radar-like arrow plot, all arrows are unit vectors: the light blue arrow is the wave vector $\vec{k}$; the orange dashed arrow is the background magnetic field $\vec{B}_0$; the red and deep blue arrows are unit vectors of displacement of Fast and Slow mode respectively. The black dashed closed loop is the trajectory of displacement from edge to edge in the simulation domain (trajectory of the blue and orange line in corresponding wave profile panel on the left). The texts in panel b and c are important information of the time frame, where $\eta_{S/F} = \epsilon_{w,S/F}/(\epsilon_{w,S} + \epsilon_{w,F})$ is the ratio of the wave energy belongs to either Slow or Fast mode. For example, in panel b, the black dashed closed loop is parallel to the red arrow, indicating that the wave is pure fast mode; whereas in panel c, the loop is parallel to the blue arrow, indicating that the wave is pure slow mode. By checking both the radar plot and the value of $\eta_{S/F}$, from panel b to c, we clearly witness a mode degeneracy of magnetosonic modes.

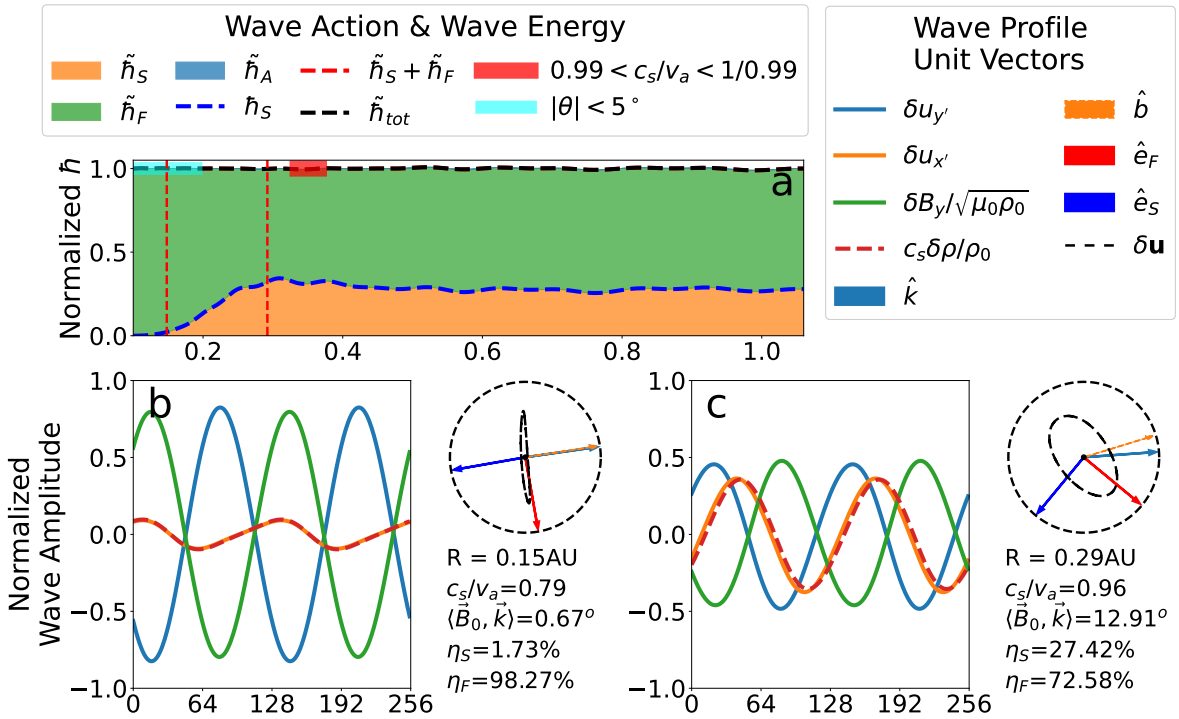

Figure 2.5: The detailed evolution of run F2 with wave profile shown. Panel a is identical to panel F2 in Figure 2.2. All legends are identical to Figure 2.4. Note that the black dashed loop in panel b and c are trajectory of displacement vector from edge to edge in the simulation domain. In panel b, the loop is mostly parallel to the red arrow, indicating that the wave is mostly pure fast wave (also see the time step indicated by the first red, vertical dashed line in panel a, is almost all green); in panel c, the loop has projection on both red and blue vector, indicating that the wave is a mixed slow and fast wave (also see the time step indicated by the second red, vertical dashed line in panel a, is mixed green and orange). Moreover, by comparing the value of $\eta_{S/F}$ in panel b and c, we obviously witness a magnetosonic linear mode conversion from panel b to c.

we have shown that although mode conversion violates the conservation of wave action for infinitely long monochromatic MHD wave trains propagating in the expanding solar wind, the total of wave action summed over all interacting modes (Alfvén, Slow and Fast) remains a universally conserved quantity. 1D MHD simulation with the Expanding Box Model (EBM) [(Velli et al., 1992), (Grappin et al., 1993), (Grappin and Velli, 1996), (Shi et al., 2020)] demonstrate this and further reveal that there are three distinct mode conversion mechanisms: degeneracy, linear mode conversion and resonance. A simple physical picture is that, due to the expansion of the medium, wave vector $\vec{k}$ turns towards radial, and background magnetic field $\vec{B}_0$ turns away from radial per Parker Spiral. Hence

with special setup, when the two vectors align with each other and in the mean time sound speed c_s and Alfvén speed v_a becomes nearly identical, all three mode conversion mechanisms become possible.

Degeneracy is due to the fact that the concepts of "Fast" and "Slow" become ill-defined at the equi-partition layer for parallel waves, and hence passing through the equi-partition layer, the originally "Slow" wave can become "Fast" due to the abrupt change of the displacement polarization vector (see Figure 2.4). Therefore, degeneracy can only happen for magnetosonic modes, and is not applicable to Alfvén mode. Linear mode conversion on the other hand is more universal for magnetosonic waves [see e.g. (Zhugzhda, 1979; Zhugzhda and Dzhalilov, 1981, 1982a,b; Cally, 2001; McDougall and Hood, 2007a,b, 2009) for similar linear mode conversion for magnetogravity waves at the magnetic canopy in solar chromosphere]. Finally, resonance can happen for Alfvén mode, where the well-known Alfvén resonance can generate secondary Slow and Fast waves [see (Hollweg, 1971) or Appendix-A, and simulation in Figure 2.3]. In short, the mode conversion process and the conservation of total wave action can be summarized as:

$$\frac{E_M}{\omega_r} \xrightarrow[\text{Resonance}]{\text{Degeneracy}} \sum_M \frac{E'_M}{\omega_r} \tag{2.38}$$

where E_M and E'_M are wave energy before and after resonance/degeneracy of mode M, and ω_r is resonance frequency.

We believe our proposed physical model is generally applicable to any fluid system because: (a) wave action is a universal concept, regardless of system description; (b) our mathematical description on conservation of total wave action is general, without concerning the details of MHD; (c) All three mode-conversion mechanisms are universal phenomena regardless of fluid description. Hence by providing simple, intuitive physical picture for mode conversion, our model generalizes the classical theory of wave action conservation.

CHAPTER 3

New Observations of the Energy Containing $1/f$ Range from Parker Solar Probe

3.1 Introduction

The trace magnetic power spectrum (PSD) in the solar wind is often characterized by a double power law from intermediate to large scales, with power spectral exponents in the inertial range around -5/3 (or closer to -3/2 in the inner heliosphere) and -1 at larger scales, respectively. This double power law is usually found in the fast wind (Bavassano et al., 1982; Denskat and Neubauer, 1982; Burlaga and Goldstein, 1984), and recently in very long intervals of slow wind (Bruno et al., 2019), and also in extremely long interval without regard to wind speed (Matthaeus and Goldstein, 1986). The low frequency (or large scale in configuration space, converted with modified Taylor Hypothesis Taylor (1938); Perez et al. (2021a)) range of the spectrum has been considered as the energy reservoir that facilitates the turbulence cascade in the solar wind. The origin and formation mechanism of the $1/f$ range of the PSD is still not well-understood and under active debate (see e.g. Matthaeus and Goldstein (1986); Velli et al. (1989); Dmitruk and Matthaeus (2007); Bemporad et al. (2008); Verdini et al. (2012); Matteini et al. (2018); Chandran (2018); Magyar and Doorsselaere (2022)). It is worth noting that the $1/f$ range of the spectrum is indicative of a scale-independent fluctuation energy distribution, i.e. equi-partition of energy over all scales (Keshner, 1982). Moreover, $1/f$ spectrum is also seen in plasma density fluctuations from *Ulysses* at similar frequencies, especially in the high latitudes intervals (Matthaeus et al., 2007).

The majority of the models proposed for the double power law were built on an *a*

priori assumption of the existence of $1/f$ spectrum at low frequency. For example (Velli et al., 1989) proposed that the secondary incoming waves generated by linear coupling of the dominant outgoing waves to the large scale solar wind inhomogeneity could facilitate a quasi-stationary self-similar cascade, resulting in a $1/k$ scaling. (Montroll and Shlesinger, 1982; Matthaeus and Goldstein, 1986) suggest that the $1/f$ spectrum results from the superposition of uncorrelated samples of solar surface turbulence that have log-normal distributions of correlation lengths corresponding to a scale-invariant distribution of correlation times over an appropriate range of parameters. The scale invariance originates in the dynamo and manifests in the photospheric magnetic field.

There are however few notable exceptions. For example it has been pointed out by (Chandran, 2018) (henceforth denoted as C18) that in Fig 2-2 of (Tu and Marsch, 1995), the low frequency z^+ (Elsässer variables: $z^\pm = \boldsymbol{V} \mp \boldsymbol{B}/\sqrt{\mu_0 \rho}$) spectrum were as shallow as $f^{-0.5}$ in the low frequency range, which C18 referred as 'infrared' range. C18 used this as an input to the model and the parametric decay induced inverse cascade of outward propagating Alfvén wave would eventually produce a triple power law z^+ spectrum with $1/f$ in the middle frequency range between 'infrared' range and the inertial range.

Another example would be the conjecture proposed by (Matteini et al., 2018) (henceforth denoted as M18) which tried to build a connection between spectral properties and magnetic compressibility. In particular, there's a paradox between an arbitrary power law index and low magnetic compressibility at all scales. Their conjecture shows that, for turbulence with low magnetic compressibility, if the magnetic fluctuations fully saturate over the scales, i.e. $\langle \delta B \rangle = \langle \delta \boldsymbol{B} \rangle \sim |B| = B$, we have $\langle \delta B/B \rangle \sim \langle \delta B \rangle / B \sim 1$. According to the well-known relation which connects the slope in the power spectrum $P(k) \propto k^\alpha$, and the exponent in the second order structure function $\delta B^2 \propto l^{-2\beta}$ via: $\alpha = 2\beta - 1$, $-3 < \alpha < -1$ (see e.g. (Monin and Jaglom, 1987), and here we translate the frequency f in to wavenumber k with Taylor Hypothesis, and scale $l \sim 1/k$), we see that when $\langle \delta B/B \rangle \sim 1$ for sufficiently large scales (Note that $\langle \delta B/B \rangle$ is a function of temporal increment τ or scales l in configuration space.), we have $\beta \sim 0$, and hence $\alpha \gtrsim -1$, for the same scale range. Consequently, $1/f$ is the steepest possible realization

of power spectrum when magnetic fluctuations fully saturate to the $\langle \delta B/B \rangle \sim 1$ state. In addition, their result leads to a straightforward connection between the scale l_0 at which magnetic field fluctuations fully saturate (i.e. $\langle \delta B/B \rangle \sim 1$) and the spectral breakpoint f_B of the double power law in PSD. M18 argued that closer to the sun, unless the $1/f$ range is formed in the solar corona and advected outwards preserving its shape, it should gradually disappear moving closer to the sun where $\delta B/B < 1$.

Previous observations with *Ulysses*, *Helios*, *WIND* have only explored the heliosphere beyond 0.3 AU. It is well known that due to solar wind expansion, B decreases like R^{-2} radially per conservation of magnetic flux (or Parker Spiral (Parker, 1958), because the field is mostly radial close to the sun) and δB decreases like $R^{-1.5}$ per WKB theory (see e.g. (Whang, 1973; Heinemann and Olbert, 1980; Velli et al., 1991; Tu and Marsch, 1995; Huang et al., 2022)), where R is heliocentric distance. And hence $\langle \delta B/B \rangle$ is expected to increase radially as $R^{0.5}$ from Alfvén critical point (where $\delta B^2, \delta V^2 \propto V_{sw} V_A/(V_A + V_{sw})^2$ reaches its absolute maximum per WKB theory. However, the peak is expected to locate inside the Alfvén point due to non-WKB effects, see e.g. (Cranmer and Ballegooijen, 2005; Verdini and Velli, 2007; Chen et al., 2020; Bandyopadhyay et al., 2022)) until it reaches its full saturation at 1 around 0.3 AU. Therefore, closer to the sun, based on the WKB prediction, we expect to see magnetically incompressible intervals with partial saturation ($\langle \delta B/B \rangle \sim const, const < 1$), or without saturation ($\langle \delta B/B \rangle$ keeps increasing over scales but smaller than 1). It is hence important to validate the connection between $1/f$ spectrum and low magnetic compressibility with solar wind closer to the sun where full magnetic fluctuations saturation is not achieved.

As a consequence, with new observations much closer to the sun from Parker Solar Probe (PSP) (Fox et al., 2016), there are two major questions to be investigated: 1. What are the statistics and radial evolution of low frequency power spectral exponents; 2. With the new evidence from closer to the sun, what new constraints can be applied to the existing models of $1/f$ spectrum. To answer these questions we perform a systematic search for magnetically incompressible ($\delta|\boldsymbol{B}|/|\boldsymbol{B}| \ll 1$) solar wind intervals that are characterized by a double power law with PSP data from Encounter 1 to Encounter 13.

The rest of the chapter is organized as follows: In section 2, we explain the data selection and analysis procedure; In section 3, we show the main results; In section 4, we discuss the implications from new observations on (Matteini et al., 2018) and (Chandran, 2018); In section 5, we conclude and summarize the main results.

3.2 Data and Analysis Procedures

In order to study the low frequency spectral properties of magnetically incompressible solar wind observed by PSP, we performed a systematic search for magnetically incompressible turbulence intervals from E1 (Nov 2018) to E12 (Jun 2022). We mainly use high-resolution vector magnetic field measurements from FIELDS instruments (Bale et al., 2016) to calculate the magnetic turbulence spectrum, and proton measurements from SWEAP instruments (Kasper et al., 2016) and Quasi Thermal Noise (QTN) electron density measurements (Moncuquet et al., 2020; Pulupa et al., 2017) to support interval selection.

3.2.1 Interval Selection

Our selection of magnetically incompressible solar wind intervals is based on the evaluation of the scale-dependent magnetic compressibility $\eta_B(T)$:

$$\eta_B(T) = \left\langle \frac{|B| - \langle |B| \rangle_T}{\langle |B| \rangle} \right\rangle \tag{3.1}$$

where $\langle \rangle_T$ is the ensemble average at scale T, and $\langle \rangle$ is the ensemble average throughout the interval. For all intervals, we ensure that η_B is smaller than 0.1 for any given scale T. Moreover, due to the rapid movement of the spacecraft around perihelia, careful selection is needed to ensure that the spacecraft stays within the same type of solar wind over the selected interval. Therefore secondary parameters, including solar wind speed $V_{sw} = |\boldsymbol{V}|$, thermal speed $V_{th} = \sqrt{2k_BT/m_p}$, normalized cross helicity $\sigma_c = (z^{+2} - z^{-2})/(z^{+2} + z^{-2})$,

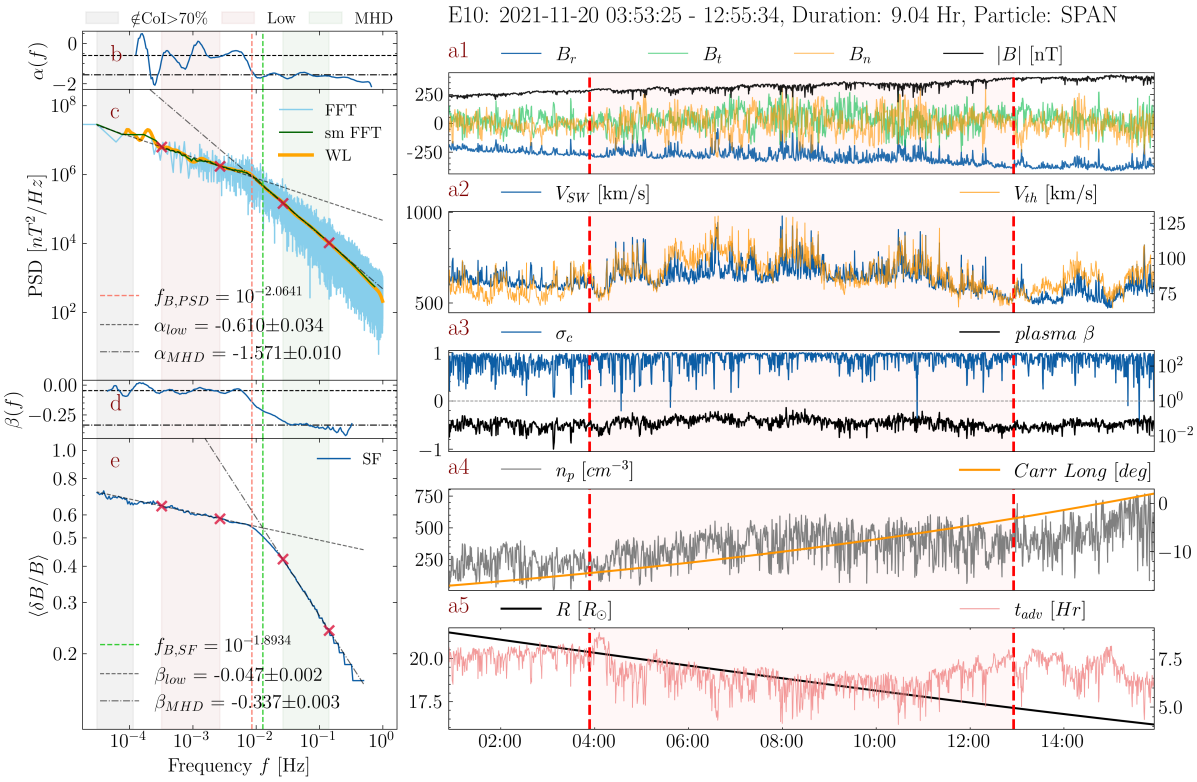

Figure 3.1: Example of a magnetically incompressible solar wind interval from PSP Encounter 10, close to the perihelion. The particle data of this interval are provided by SPAN (Livi et al., 2022). (a1-a5) show time series of magnetic field B_{rtn} in RTN coordinates; solar wind speed V_{SW} and solar wind thermal speed V_{th}; cross helicity σ_c and plasma beta β; proton density n_p and Carrington longitude; and heliocentric distance R in solar radii $R_\odot$ and advection time $t_{adv} = R/V_{SW}$, respectively. The selected interval is indicated with the red shaded area enclosed by two red dashed lines. (b) Power law fitting index α as a function of frequency f of trace PSD. (c) Fast Fourier Transformation (FFT) is plotted in blue as background, smoothed FFT PSD is the green line, and Morlet Wavelet Transformation (WL) PSD is the orange line. The two pairs of red crosses accompanied with red and green shaded areas indicate the ranges of frequency over which the power-law fits are applied, and the two fitted lines are shown in dashed and dashed-dot lines. The gray shaded area is the frequency range where more than 70% of points fall out of the Cone of Influence (CoI) of wavelet transformation. The red dashed line indicates the intersect of two fitted lines, interpreted as the low frequency break point. (d) Power law fitting index β as a function of frequency f of the normalized structure function SF. (e) Normalized first order structure function $\langle \delta B/B \rangle$ as a function of frequency $f = 1/(2 * \Delta t)$, where Δt is the temporal increment. Two fits are applied to the same frequency ranges from (c), which produce a similar low frequency break point, indicated by the green dashed line.

plasma $\beta = 2\mu_0 P/B^2$, proton density n_p, Carrington longitude, Heliocentric distance R, and advection time $t_{adv} = R/V_{sw}$ are examined to differentiate different solar types (see Figure 3.1 panels a1-a5). With our selection criteria, we ended up with 109 non-overlapping magnetically incompressible solar wind intervals observed by PSP from E1 to E13, with total 1500 hours worth of data (see Figure 3.2c for histogram of interval lengths). Note that the jets in the solar wind speed in panel a2, which are accompanied with partial or total reversal of B_r in panel a1 are known as switchbacks, and have been studied by numerous recent studies (see e.g. (Bale et al., 2019; Dudok de Wit et al., 2020; Tenerani et al., 2020; Farrell et al., 2020; Mozer et al., 2020; Woolley et al., 2020; Bourouaine et al., 2020; Martinović et al., 2021; Larosa et al., 2021; Tenerani et al., 2021; Hernández et al., 2021; Laker et al., 2021; Meng et al., 2022; Shi et al., 2022b; Huang et al., 2023a) and references therein). They are known as large amplitude or spherically polarized Alfvén wave (Mallet et al., 2021; Mallet and Chandran, 2021) with almost constant magnetic modulus.

3.2.2 Diagnostics: Magnetic Trace Power Spectrum and Structure Function

For each interval, the following two diagnostics are calculated: trace power spectrum density (PSD) and normalized first-order structure function (SF) for vector magnetic field. To produce a reliable low frequency turbulence spectrum, for each interval, we calculate the trace power spectrum density (PSD) with both Morlet Wavelet Transformation (WL) and Fast Fourier Transformation (FFT). For FFT, we smooth the spectrum by averaging over a sliding window of a factor of 2 in the frequency domain (sm-FFT). The smooth spectra calculated with the two methods (WL and sm-FFT) generally overlap with each other perfectly in the high frequency range but gradually deviate from each other at the low frequency end. Therefore, we keep the spectrum up to the frequency where more than 70% of points fall out of the Cone of Influence (CoI) of the WL spectrum, and we trust only the frequency range where WL overlap with sm-FFT. We calculate the power law fit index α by fitting on the WL PSD unless specified otherwise, and henceforth referred simply as PSD.

We follow the steps described in M18 to calculate the normalized first-order structure function for vector magnetic field. We apply 200 logarithmically spaced lags Δt as temporal increment of vector magnetic field $\delta \boldsymbol{B}(t, \Delta t) = \boldsymbol{B}(t) - \boldsymbol{B}(t + \Delta t)$ within the range ($1s$, $length\ of\ interval/2$). The normalized first-order structure function is then calculated by:

$$SF(\Delta t) = SF_{norm}(\Delta t) = \left\langle \frac{|\delta \boldsymbol{B}(t, \Delta t)|}{B(t, \Delta t)} \right\rangle_t \tag{3.2}$$

where we denote $|\delta \boldsymbol{B}|$ as δB and $|\boldsymbol{B}|$ as B, and $\langle \rangle_t$ is average with regard to t for scale Δt. Note that the intervals we select are magnetically incompressible, and hence B can be considered as scale-independent and can be taken out of the averaging window $\langle \rangle_t$. The resultant $SF(\Delta t)$ in the temporal domain is finally converted to $SF(f)$ in the frequency domain via $f = 1/(2 \cdot \Delta t)$ because twice the period in the absolute fluctuation corresponds to the one period in the non-absolute one.

To extract spectral information from PSD, we apply power law fit on PSD in both low and MHD inertial frequency ranges where the spectrum stabilize visually (red and green shaded area in Figure 3.1c), and we obtain two power law fits with indices α_{Low} and α_{MHD} (black dashed line and dashed dotted line in Figure 3.1c). The intersect of the two fit lines is interpreted as the low frequency break point ($f_{B,PSD}$, red dashed line). To compare the spectral properties of PSD and SF, we apply power law fit in the same frequency ranges to SF (extended shaded area in Figure 3.1e), and the intersect of two fit lines is also interpreted as the low frequency break point ($f_{B,SF}$, green dashed line). Clearly the two break frequencies $f_{B,PSD}$ and $f_{B,SF}$ are very close to each other, consistent with M18. The small deviation may be attributed to spectral leakage of the structure function, which leads to a spectrum smoother than the wavelet or PSD result. For completeness, two moving fits $\alpha(f)$ and $\beta(f)$ with window size of 1/3 decade on PSD and SF are shown in Figure 3.1b and 3.1d.

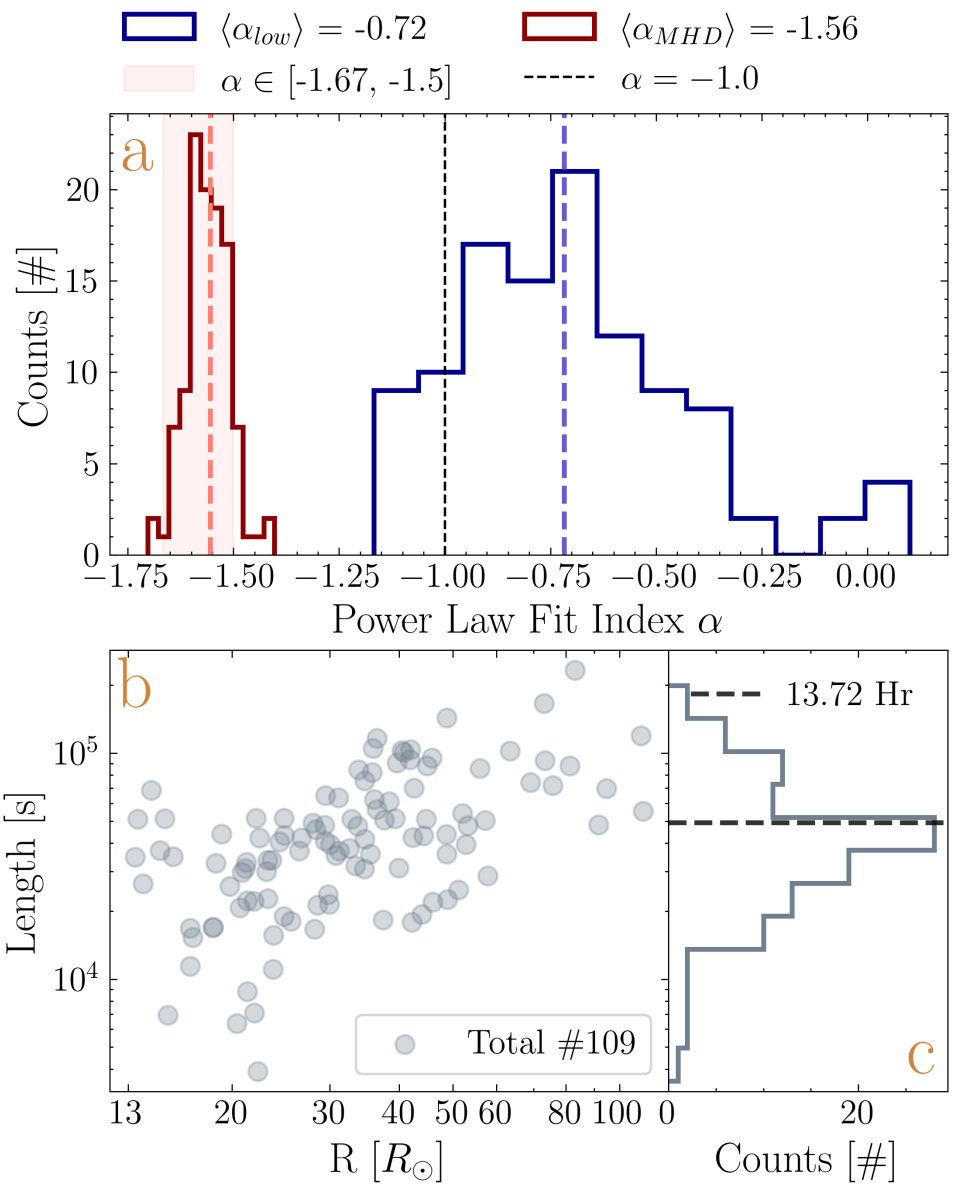

Figure 3.2: (a) Histograms of power law fit index α of low frequency (blue) and MHD frequency (red) ranges. The averaged index values are indicated with corresponding dashed lines and are shown in the legends. The expected power spectral exponent value range from various phenomenologies is indicated with red shaded area. (b) Statistics of length and mean radial distance of the selected 109 intervals. (c) Histogram of interval lengths. The average length is 13.72 hours (shown as legend with accompanied with dashed line), with minimum of 1.08 hours and maximum of 64.70 hours.

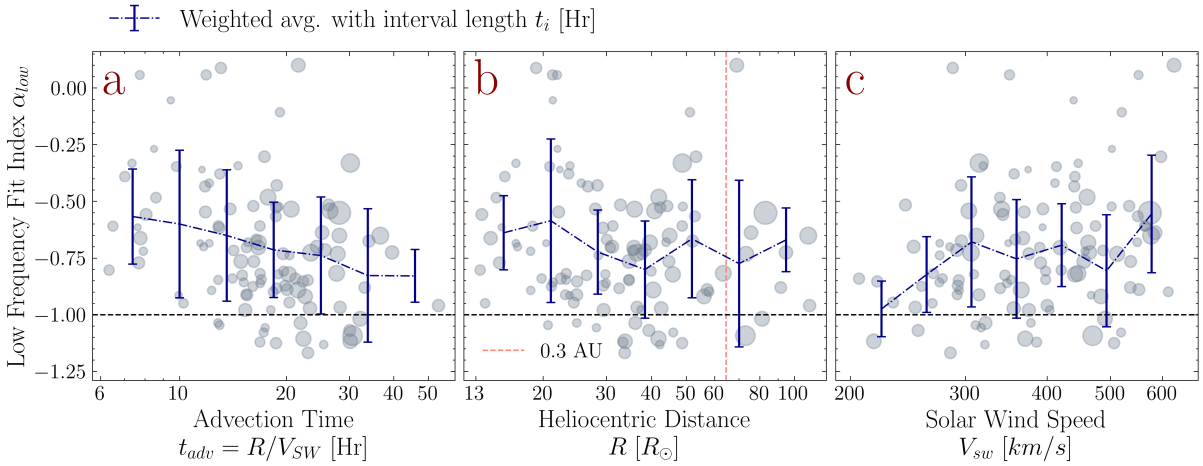

Figure 3.3: (a) Radial evolution of low frequency power law fit index α_{Low}, sorted with advection time ($t_{adv} = R/V_{SW}$). The sizes of the circles indicate the interval length (weight), and the line plot is the binned weighted average of α_{Low}. The errorbars are one standard error of α_{Low} from each bin. (b) Radial evolution of α_{Low} sorted with Heliocentric distance R. (c) Dependence of α_{Low} on solar wind speed V_{SW}.

3.3 Results

3.3.1 Statistics of Power Spectral Exponents

For the 109 intervals, power law fit is applied to both high frequency (MHD/inertial) and low frequency ranges with the method described in section 3.2.2. The primary statistical results are presented in Figure 3.2a, in a style similar to Figure 6 in (Bruno et al., 2019). The histogram of power law fit index in the MHD inertial range α_{MHD} is shown in dark red. Most of the intervals have an inertial range spectral exponent that falls within the expected value range [-1.67, -1.5], predicted by many existing phenomenologies (Kolmogorov, 1941; Iroshnikov, 1964; Kraichnan, 1965; Sridhar and Goldreich, 1994; Goldreich and Sridhar, 1997; Boldyrev, 2005, 2006), consistent with recent observations (see e.g. (Chen et al., 2020; Telloni et al., 2021; Shi et al., 2021; Kasper et al., 2021; Zank et al., 2022; Sioulas et al., 2023a,b; Raouafi et al., 2023a)). However, for the low frequency range fit index (α_{Low}, dark blue), the spectral exponents have an unexpectedly wide distribution, and the majority of them are larger than -1, i.e. the corresponding low frequency spectra are shallower than $1/f$.

3.3.2 Radial Evolution and Dependence on Solar Wind Speed

The radial evolution of power law fit index of PSD in the low frequency range α_{Low} is shown in Figure 3.3, sorted with advection time $t_{adv} = R/V_{SW}$ in 3.3a and heliocentric distance R in 3.3b. To display the trend of evolution, a binned average weighted with interval length is plotted on top of the scatters. When we sort the intervals with advection time t_{adv}, a clear asymptotic evolution from shallower spectrum towards $1/f$ spectrum is seen. However, when sorted with heliocentric distance R, no clear trend is found, and instead α_{Low} is scattered in a wide range of values below 0.3 AU. For completeness, the dependence of α_{Low} on solar wind speed is shown in panel c. For intervals with very low solar wind speed ($\sim$ 200 km/s), which are typically observed very close to the sun, α_{Low} are mostly close to -1, i.e. very close to $1/f$ spectrum. For intervals with higher solar wind speed, no obvious trend is observed. Therefore, for the very low speed streams, it is possible that the $1/f$ spectrum originated from the solar corona (see e.g. (Matthaeus and Goldstein, 1986)).

However, substantial solar wind acceleration has been observed below 0.3 AU (see e.g. (Shi et al., 2021; Sioulas et al., 2022; Shi et al., 2022a)). In other words, the solar wind speed is a radially varying parameter even for the same stream, and hence the dependence of α_{Low} on solar wind speed should be taken with caution. Moreover, it should be also noted that the actual advection time is an integrated quantity, and thus the t_{adv} used here can be merely considered as a proxy to the real advection time. And the interval length systematically grows with advection time and heliocentric distance, and hence α_{low} is acquired from lowering frequency range with increasing t_{adv} and R. The radial evolution of α_{low} could be associated with the change in fitting frequency range.

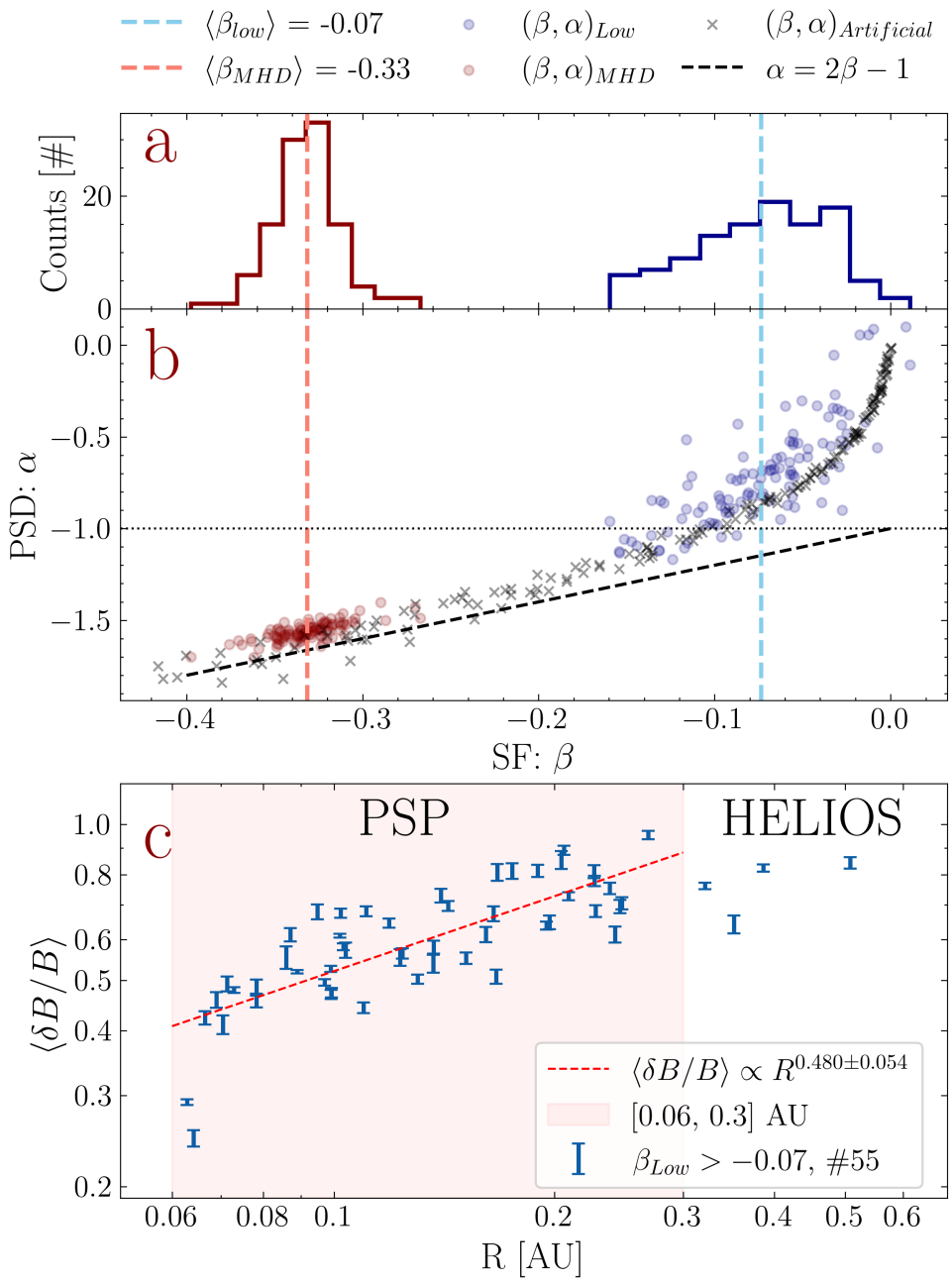

Figure 3.4: (a) Histogram of power law fit index β of the normalized first order structure function SF from both low (blue) and MHD (red) frequency ranges. The averages are indicated with corresponding dashed lines. (b) Scatters of power law fit index pairs (α,β) of trace PSD and SF from both low (blue) and MHD (red) frequency ranges. The (α,β) pairs from artificial data are also shown with black crosses, and the theoretical relation $\alpha = 2\beta - 1$ is indicated with black dashed line. (c) Dependence of $\langle\delta B/B\rangle$ from the saturated intervals ($\beta_{Low} > -0.07$) on Heliocentric distance R. The value ranges of $\langle\delta B/B\rangle$ in the low frequency range are indicated with errorbars. The newly explored Heliosphere radial range ($R < 0.3$ AU) is indicated with red shaded area.

3.4 Discussions

3.4.1 Implications on Matteini2018

M18 tried to build a connection between low magnetic compressibility and $1/f$ spectrum via the well-known relation: $\alpha = 2\beta - 1,\ -1 > \alpha > -3$, where α is the spectral exponent of the PSD, and β is the power law index of the first order structure function (here expressed in terms of frequency). Due to low magnetic compressibility, $\langle \delta B/B \rangle$ can be considered as first order structure function δB normalized by its own constant modulus. Therefore the fully saturated magnetic fluctuations, i.e. $\delta B/B \sim 1$, can be translated to $\beta \sim 0$, and therefore $\alpha \gtrsim -1$. In other words, $1/f$ is the steepest possible realization of the low frequency spectrum when magnetic field fluctuations fully saturates. It has also been proposed by M18 that "unless the 1/f range is formed in the corona and just advected in interplanetary space preserving its shape, it should gradually disappear, moving closer to the Sun where $\delta B/B < 1$."

It is therefore interesting to examine the behaviors of α_{Low} and β_{Low} closer to the sun where $\delta B/B < 1$. There are roughly two possible behaviors of $\langle \delta B/B \rangle$ in the low frequency range: 1. Partial saturation, i.e. $\delta B/B \sim const$, $\beta \sim 0$; 2. No saturation, $\beta < 0$. Figure 3.4a shows the histogram of the β_{Low} and β_{MHD} in both low and MHD frequency ranges. The histogram of β_{Low} clearly shows that substantial portion of intervals have no saturation ($\beta \lesssim -0.1$). However, the scatter plot of (β_{Low}, α_{Low}) in Figure 3.4b shows that the low frequency PSD of these intervals are close to $1/f$. In fact for those intervals with partial saturation ($\beta_{Low} \gtrsim -0.1$), the scatter plot shows that the corresponding α_{Low} are much greater than -1, i.e. the low frequency PSD are much shallower than $1/f$.

Figure 3.4b further reveals that in the inertial range, the observed (β, α) pairs follow the relation $\alpha = 2\beta - 1$ pretty well (black dashed line), with a slight systematic shift towards shallower α, but in the low frequency range deviate significantly. To understand such deviation, we generate 1-D artificial time series with different power spectral exponent α_0. For each α_0, we generate an artificial time series $A(t; \alpha_0)$ formed with sinusoidal

fluctuations with random phases and amplitudes following power law:

$$A(t;\alpha_0) = \sum_{i}^{N} \omega_i^{(\alpha_0+1)/2} \sin[2\pi(\omega_i t + \phi_i)] \tag{3.3}$$

where ω_i is i^{th} frequency log-linearly spaced from 10^{-5} Hz to 1 Hz, ϕ_i is random phase in range of $(0, 2\pi)$, and N is set to 10000. For each $A(t;\alpha_0)$, we calculate the power law fitting index for the PSD (α) and SF (β) from the same frequency range $(10^{-2.5}, 10^{-1})$ Hz.

The scatter plot of $(\alpha,\beta)_{Artificial}$ pairs are shown in Figure 3.4b as gray crosses. $(\alpha,\beta)_{Artificial}$ catch well the trend of the observed (α,β) pairs, especially in the MHD frequency range, and also deviate significantly from the relation $\alpha = 2\beta - 1$. Such systematic deviation is possibly due to the spectral leakage effect, because contrary to FFT and wavelet transformation, the structure function has a broad-band response. Therefore, cautions should be taken when one is trying to relate $1/f$ spectrum with magnetic fluctuations saturation (regardless of full or partial). For completeness, shown in Figure 3.4c, for those 55 intervals with partially saturated magnetic fluctuations (here defined as $\beta > -0.07$), we see the radial evolution of saturation values $\langle \delta B/B \rangle$ follows well with the WKB prediction of $R^{0.5}$.

In summary, one should be careful when relating magnetic fluctuations saturation ($\langle \delta B/B \rangle \sim const$) to $1/f$ spectrum, because of the spectral leakage effect. And closer to the sun where $\delta B/B < 1$, we see low frequency spectra much shallower than $1/f$ with partially saturated magnetic fluctuations. One good example has already been shown in Figure 3.1. Therefore, according to M18, it is possible that some of these low frequency range spectra originated from the solar corona (see also (Matthaeus et al., 1982, 2007; Bemporad et al., 2008) for the coronal origin of $1/f$ spectrum.)

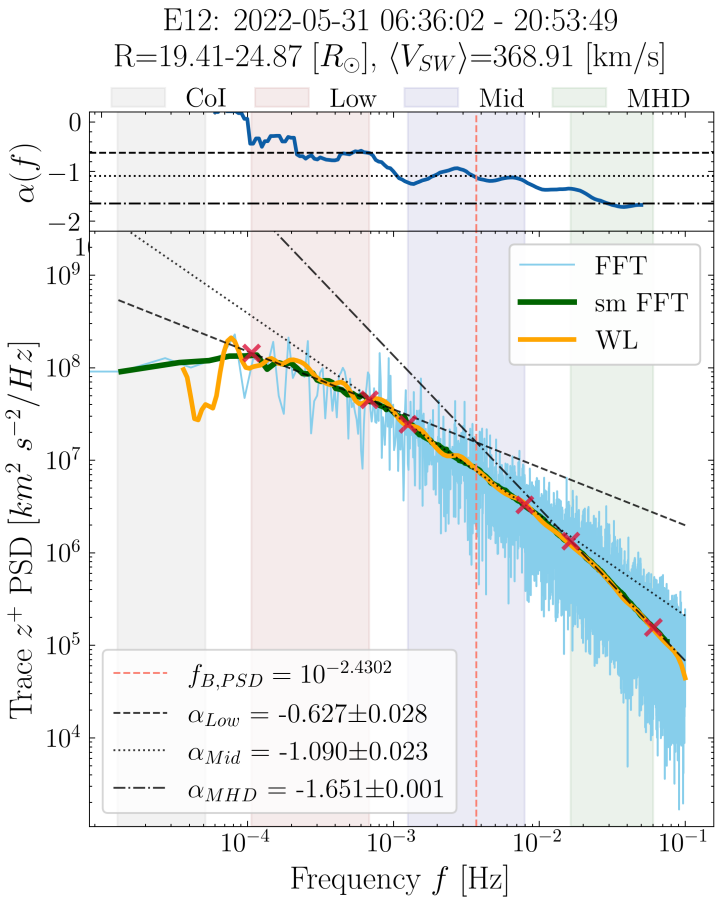

Figure 3.5: Example of C18 type of trace z^+ spectrum. The FFT spectrum is shown with blue line as background, the smoothed FFT is the green line, and the trace Morlet Wavelet (WL) PSD is the orange line. The gray shaded area indicates that more than 70% of points fall out of the Cone of Influence (CoI) of wavelet transformation. The power law fit is conducted on the smoothed FFT, and the moving window fit $\alpha(f)$ (window sized 1/3 decade) is shown in the overhead panel. The trace PSD is separated into three distinct frequency ranges (Low, Mid, MHD), each possesses a quasi-steady power law range, indicated with red (Low), blue (Mid), and green (MHD) shaded areas. Power law fits are applied to each of the ranges and the fit indices $\alpha_{Low/Mid/MHD}$ are shown in the legends. A "low frequency break" is found as the intersect between the power law fits from low frequency and MHD inertial range, indicated with orange dashed line.

3.4.2 Implications on Chandran2018

C18 proposed that the $1/f$ spectrum is formed by inverse cascade of Alfvén waves facilitated by parametric decay within the context of weak-turbulence theory. The author initialize the simulation with primarily outward propagating Alfvén waves, i.e. $e^+ \gg e^-$, where $e^\pm$ are the frequency (f) spectra of Alfvén waves propagating in opposite directions along the magnetic field lines. If the initial e^+ has a peak frequency f_0 (where fe^+ is maximized), and an 'infrared' scaling f_p at smaller f with $-1 < p < 1$, then e^+ acquires an f^{-1} scaling throughout a range of frequencies that spreads out in both directions from f_0. The final state of their model evolution is a triple power law with 'infrared' scaling in the low frequency, $1/f$ in the intermediate frequency range, and f^{-2} scaling in the inertial range (the inertial range is initialized with the critical-balanced parallel spectrum of $k_\parallel^{-2}$, see e.g. (Goldreich and Sridhar, 1995; Podesta, 2009; Forman et al., 2011)).

Therefore it is interesting to explore the magnetically incompressible (yet weakly compressible, plasma $\beta \ll 1$, and $\delta\vec{B} \sim |B|$ to allow parametric decay (Fu et al., 2018)), Alfvénic turbulence (primarily outward propagating Alfvén waves, i.e. $|\sigma_c| \sim 1$) intervals close to the sun, to see if there exists the triple power law z^+ spectrum. Among the 109 intervals, there are 4 intervals displaying clear triple power law in trace z^+ PSD with stable intermediate frequency range. One of the best examples is shown in Figure 3.5, which is an interval from E12, with $\langle\sigma_c\rangle = 0.82$. Note that due to the low resolution particle data, the time series is resampled to 5s, and hence the WL spectrum is very wavy. To acquire a better moving fit $\alpha(f)$ profile, the moving power law fit with window size of 1/3 decade is applied to the smoothed FFT PSD (green line).

In the low frequency range, we see a stable 'infrared' spectrum with $f^{-0.627}$. In the intermediate range, the spectrum is very close to $1/f$. And in the inertial range, the scaling (can be converted to configuration space with Taylor Hypothesis, (Taylor, 1986; Perez et al., 2021b)) is agreeable with the perpendicular spectrum of $k_\perp^{-5/3}$ from the critical balance theory, which would mask the steeper parallel spectrum because we are observing the trace z^+ PSD. This is also supported by (Cuesta et al., 2022; Sioulas

et al., 2023b), which has shown that when considering turbulence anisotropy, for fast streams ($V_{sw} \gtrsim 400km/s$) close to the sun, the low frequency spectrum is dominated by parallel fluctuations, and in the inertial range, the perpendicular spectrum has a $f^{-5/3}$ scaling. This is also consistent with the simulation by (Verdini et al., 2012), where at higher frequencies the steep parallel spectral slope (-2) is masked by the more energetic perpendicular spectrum (slope -5/3). In summary, this triple power law is consistent with the simulation result from C18, and further provide evidence for the presence of parametric decay instability in the solar wind (see e.g. (Matteini et al., 2010; Tenerani and Velli, 2013; Zanna et al., 2015; Tenerani et al., 2017; Shi et al., 2017; Bowen et al., 2018; Réville et al., 2018)).

It should also be noted that due to the existence of the triple power law, the concept of 'low frequency break point' is now questionable. For example the orange dashed line in Figure 3.5 is obtained as the intersect between the low frequency 'infrared' spectrum and the MHD spectrum, and interpreted as the low frequency break point $f_{B,PSD}$. However, any frequencies in between these two ranges should be considered as the 'break frequency'. Therefore, the low frequency break point obtained with this method would have a unacceptably large uncertainty. For this reason, we have not shown any statistics of $f_{B,PSD}$ in this study.

3.5 Conclusions and Summary

In this chapter we have selected 109 magnetically incompressible intervals with total 1500 hours worth of data from Parker Solar Probe encounter 1 to 13. All of the intervals display double power law in the intermediate to large scales in their trace magnetic power spectrum density (PSD). Traditionally, the double power law in PSD is characterized by power indices $-5/3$ and -1 at the two scale ranges respectively, and there are many models in the literatures to explain the origin of the $1/f$ range (e.g. (Matthaeus and Goldstein, 1986; Velli et al., 1989; Dmitruk and Matthaeus, 2007; Verdini et al., 2012; Matteini et al., 2018; Chandran, 2018; Magyar and Doorsselaere, 2022)). Previous ob-

servations from *Ulysses, Helios, WIND* have only explored the heliosphere beyond 0.3 AU. In this study, we aim to use the latest observations from PSP to provide constraints on the origin of the $1/f$ range.

From the statistics of the 109 intervals, we found that within 0.3 AU, the majority the intervals display spectra that are much shallower than $1/f$ in the low frequency range. And as advection time $t_{adv} = R/V_{SW}$ increases, the low frequency power law fit index α_{Low} asymptotically approach -1. This suggests a dynamical formation of such range from the Alfvén point up to 0.3 AU. However when sorted with heliocentric distance, no obvious evolution of α_{Low} is observed. Moreover, for those extremely slow solar wind streams which were observed very close to sun, the low frequency spectra scaling are very close to $1/f$. Therefore we can not rule out the possibility that the $1/f$ originated from the corona and are advected out (Matthaeus and Goldstein, 1986). Moreover, it should be noted that such $1/f$ scaling is also present at the density spectrum from *Ulysses* observations (Matthaeus et al., 2007), which appeared to have latitudinal dependence at 1AU. At solar mid-latitudes, such scaling matches reasonably well with the longitudinal spectra of photospheric magnetic field (Nakagawa and Levine, 1974).

Unlike other models, (Matteini et al., 2018) and (Chandran, 2018) allow the low frequency spectrum to be shallower than $1/f$. In fact, as has been pointed out by (Chandran, 2018), it has been reported by (Tu and Marsch, 1995) that in the low frequency range, z^+ have spectrum as shallow as $f^{-0.5}$. The new observations provide evidence inconsistent with the conjecture by (Matteini et al., 2018) because closer to the sun where $\delta B/B < 1$ the low frequency spectrum does not gradually disappear, but instead they are omnipresent. On the other hand, some Alfvénic intervals display clear triple power law in the z^+ spectra with $1/f$ scaling in the intermediate frequency range, and therefore provide some evidence for the model from (Chandran, 2018).

The new observations from Parker Solar Probe encounter 1 to 13 provide abundant new evidence for the origin of the low frequency trace magnetic $1/f$ spectrum. Unfortunately, up to this point, the existing models have had difficulty covering all of the observed behaviors of the $1/f$ scaling in trace magnetic PSD. In fact, it is not even ap-

propriate to call this part of the spectrum '$1/f$' spectrum because of the omnipresent shallower spectra observed closer to the sun. However, based on this study, the new evidence indicates that for different intervals from different solar wind conditions, the low frequency spectrum might have different formation mechanisms. Therefore we need to accumulate more observations from future PSP orbits to obtain a clearer picture of the low frequency turbulence spectrum.

CHAPTER 4

Solar Wind Structures from the Gaussianity of Magnetic Magnitude

4.1 Introduction

The solar atmosphere is highly structured both spatially and temporally (Bale et al., 2019; Kasper et al., 2019). Recent studies have successfully established connections between PSP *in situ* observations (Fox et al. (2016) and see Raouafi et al. (2023a) for a review for results of the first four years of the mission) and solar atmospheric structures including mid-latitude coronal holes (Badman et al., 2023; Davis et al., 2023), pseudostreamers (Kasper et al., 2021), and supergranulation (Bale et al., 2021; Fargette et al., 2021; Bale et al., 2023), even though alternative explanations remain (Shi et al., 2022b). Recent advances in remote sensing provide strong support for the minutes long small-scale jetting activity from magnetic reconnection ("jetlets") as a major source of the solar wind (Raouafi et al., 2023b). In addition, EUV observations from Solar Orbiter (Müller et al., 2020) unveiled ubiquitous brightening termed "picoflare" (Chitta et al., 2023) with associated jets that last only a few tens of seconds, suggesting the solar wind source might be highly intermittent. However, magnetic footpoint mapping methods (Badman et al., 2020; Panasenco et al., 2020; Badman et al., 2023) use photospheric magnetic field observations over the whole visible disk that are refreshed at best once every six hours and lack, of course, any real temporal reliability for the far side. Therefore, such methods are hardly able to reliably contextualize and explain the boundaries of the highly structured solar wind *in situ* time series, except perhaps in a statistical sense.

Using a data mining approach, this chapter starts from reporting an unexpected

property of the solar wind. We find that when the magnetic magnitude B is normalized by a power law fit with regard to the heliocentric distance, it occasionally exhibits a perfect Gaussian distribution. Based on this discovery, we introduce a novel time series visualization method named Gaussianity Scalogram (GS) to visualize the scale-dependent Gaussianity of B. Applying this method to data from PSP and Ulysses, we successfully identified characteristics of *in situ* remnants of coronal holes (Badman et al., 2023; Davis et al., 2023) and switchback patches (Bale et al., 2021; Shi et al., 2022b; Bale et al., 2023). Additionally, we discovered structures that are temporally compatible with small-scale jetting activities, including "jetlets" and "picoflares" (Raouafi et al., 2023b; Chitta et al., 2023). The rest of the chapter is structured as follows: In the next section, we describe the helio-radial power law fit and the construction of GS; In section 3, we present some applications of GS; In section 4, we discuss the computer simulation of Gaussianization of B in MHD turbulence and the major implications; In section 5, we conclude and summarize our results.

4.2 Helioradial Dependence of B and the Gaussianity Scalogram

Two of the most interesting yet overlooked features of the time series of the solar wind magnetic field magnitude B are that: 1. Sometimes B displays a surprisingly stable power law dependence on the heliocentric distance R; 2. By applying a helio-radial power law fit between B and R, i.e. $B \propto R^{-s}$, the fit normalized magnetic magnitude $B^* = B(R/R_0)^s$ sometimes displays a near-perfect Gaussian distribution. This is illustrated in Figure 4.3 (a-c), where the selected interval is highlighted with a golden bar in panel (a) and the helio-radial power law fit (fit index $s = 1.86$) is shown in the inset figure. The histogram of B is shown in blue in panel (b) and the normalized B^* is shown in red. To illustrate the close proximity of the probability density function of B^* (PDF_{B^*}) to a Gaussian distribution ($\mathcal{N}$), a standard Gaussian curve is overplotted in panel (c) (shifted with the mean value $\langle B^* \rangle$ and scaled with the standard deviation σ_{B^*}). The Jensen-

Shannon Distance (JSD) of base e (a statistical distance metric between probability density functions (Lin, 1991)) is calculated between PDF_{B^*} and $\mathcal{N}$, and the value is $JSD(PDF_{B^*}, \mathcal{N}) = 10^{-1.431}$, indicating considerable closeness between two distribution functions (for benchmark, see Appendix B). In addition, this highly Gaussian B^* interval coincides with the radial solar wind speed profile which is visualized with radial colored lines in panel (a) and Figure 4.2 (c) (compiled with SPAN-ion from SWEAP suite (Kasper et al., 2016)). From Nov-17 to Nov-20, the spacecraft was immersed in the high speed solar wind, indicating its coronal hole origin. The JSD produced by this process is represented as one pixel (tip of the green pyramid) in the Gaussianity Scalogram (GS) shown in panel (d3), and the scalogram for the corresponding helio-radial power law fit index s is displayed in panel (d4).

Each pixel in the GS is characterized by a timestamp (t_{mid}) and window size (win), similar to wavelet scalogram. Uniquely in GS, the step size in win (vertical axis) is chosen to be twice the step size in t_{mid} (horizontal axis), and thus the time range covered by one pixel corresponds to the same time range covered by three pixels in the following row, and so on towards the smallest scales. Therefore, if an interval and the nested sub-intervals possess similar characteristics (e.g. relatively small JSD regardless of t_{mid} and win within the interval), a pyramidal structure is expected from the GS, and the base of the pyramid indicates the start and end time of the interval. One example is highlighted by the green dashed pyramid in panel (d3), where the tip of the pyramid is in fact selected *a posteriori* as the local minimum in the GS (PDF_{B^*} being closest to Gaussian among the surrounding time and scales). Ample information can be inferred from the GS: 1. A semi-crossing of the heliospheric current sheet (HCS) at noon of Nov-22 is visualized as an inverted black pyramid. This is because the rapid drop of B during HCS crossing can significantly destroy its Gaussianity; 2. It has been confirmed recently by (Badman et al., 2023) that the solar wind can be traced back to a single mid-latitude coronal hole from Nov-17 to the end of Nov-20, and from another coronal hole for the whole day of Nov-21 (see also (Bale et al., 2023; Panasenco et al., 2020; Badman et al., 2020)). The coronal holes are naturally visualized here as two white pyramids (green and

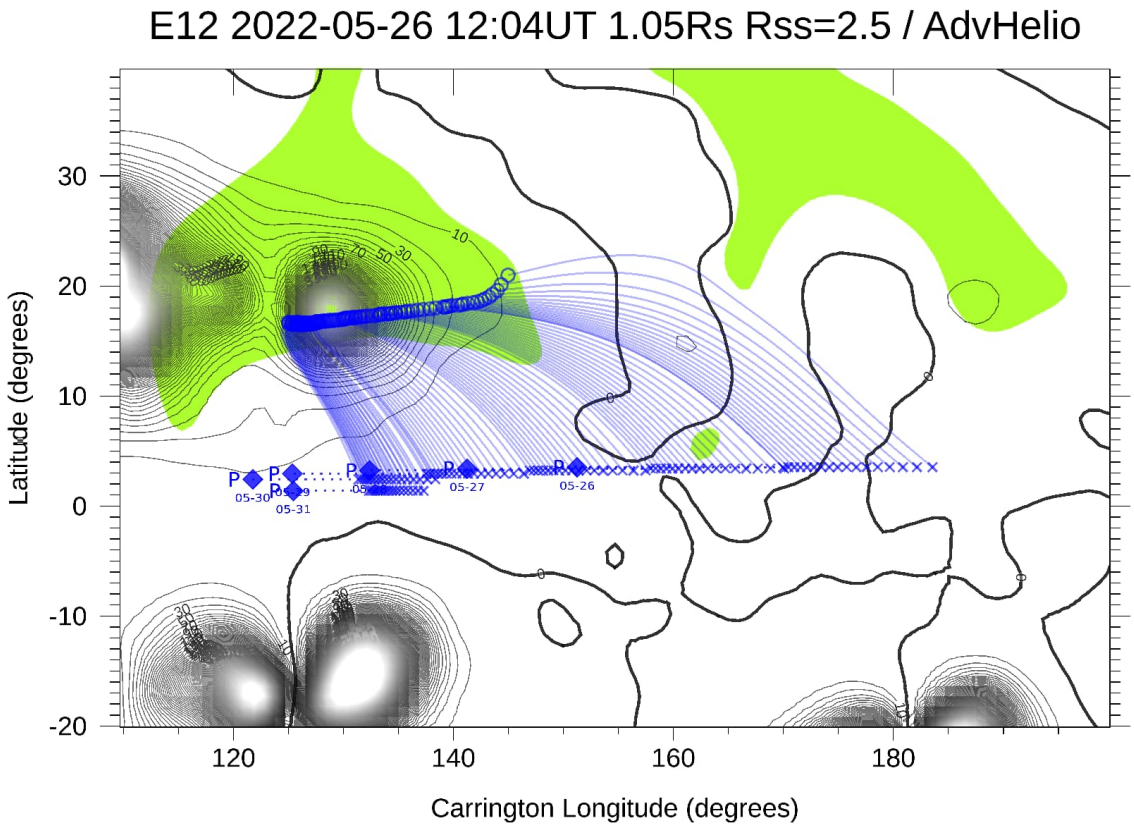

Figure 4.1: Magnetic field connectivity with the solar sources during inbound of PSP encounter 12. The thick black lines are the model neutral lines. Black contours indicate magnetic field pressure at 1.05 R_s. The ballistic projection of the PSP trajectory (blue diamonds) on the source surface (blue crosses) and down to the solar wind source regions (blue circles) is calculated for source surfaces $R_{ss}/R_s = 2.5$ (see (Panasenco et al., 2020) for details) and measured in situ solar wind speed $\pm$80 km s1. Open magnetic field regions are shown in blue (negative) and green (positive).

red dashed lines) separated by a dark region around the mid-night of Nov-20; 3. The helio-radial power law fit index s is unexpectedly stable regardless of locations and scales and systematically deviates from R^{-2} ($s \simeq 1.87 \pm 0.02$) (see also (Bale et al., 2019)).

The clear correspondence between the white pyramid and coronal hole encourages us to predict intervals of solar wind originating from coronal holes with GS compiled from PSP data. Among the first 14 encounters (Nov-2018 to Dec-2022), we only identified one more (for a total of 2) long intervals ($>$ 3 days) characterized by high Gaussianity in B^*. A panoramic view of these two long intervals is shown in Figure 4.2. The newly

found interval from the inbound of E12, shown in Figure 4.4 and Figure 4.2 (d), is characterized by a 5-day long highly Gaussian B^* time series. For illustration purpose, the green pyramid in Figure 4.4 (d3) is selected as the deepest local minimum in GS for $win > 3$ days. The histogram of B^* is remarkably concentrated (panel (b)) and aligns with Gaussian almost perfectly within 4 standard deviation (panel (c)). Similar to Figure 4.3 (c), the non-Gaussian part of PDF_{B^*} has a systematic bias towards magnetic holes (weaker magnetic magnitudes, for recent studies using PSP data see e.g. (Yu et al., 2021, 2022)), and the helio-radial power law fit index scalogram also shows a systematic deviation from $s = 2$, similarly $s \simeq 1.87 \pm 0.02$. To validate this prediction, independent results from Potential Field Source Surface (PFSS) modeling is shown in Figure 4.1 (see (Panasenco et al., 2020) for more details), which indicates that the selected interval is indeed magnetically connected to a mid-latitude coronal hole.

4.3 Fractal Gaussian Structures in the Solar Wind

To substantiate the applications of GS, here we demonstrate several examples that visualize the fractal Gaussian structures in the solar wind (Due to the rapid movement of PSP around perihelia, the structures in the *in situ* time series can be categorized into two kinds. Spatial: longitudinal structures traversed by PSP; Temporal (radial): radial structures advected by the solar wind and/or propagation of Alfvén waves) based on Taylor Hypothesis (Perez et al., 2021a). From the largest scales: Ulysses, years-long polar coronal hole (McComas et al., 2003), towards the smaller scales: hour-long switchback patches (Bale et al., 2021; Fargette et al., 2021; Shi et al., 2022b; Bale et al., 2023); minute-long structures compatible with "jetlets" (Raouafi et al., 2023b); and second-long structures compatible with "picoflare" (Chitta et al., 2023).

Figure 4.5 shows the GS of the first Ulysses orbit, and the colorbar in panel (b) is enhanced compared to Figure 4.3 (d3) for illustration purposes. The solar latitude and wind speed profile in panel (a) indicate that the spacecraft was in southern and northern polar coronal holes in the whole year of 1994, and from 1995 to 1997 (see also (McComas

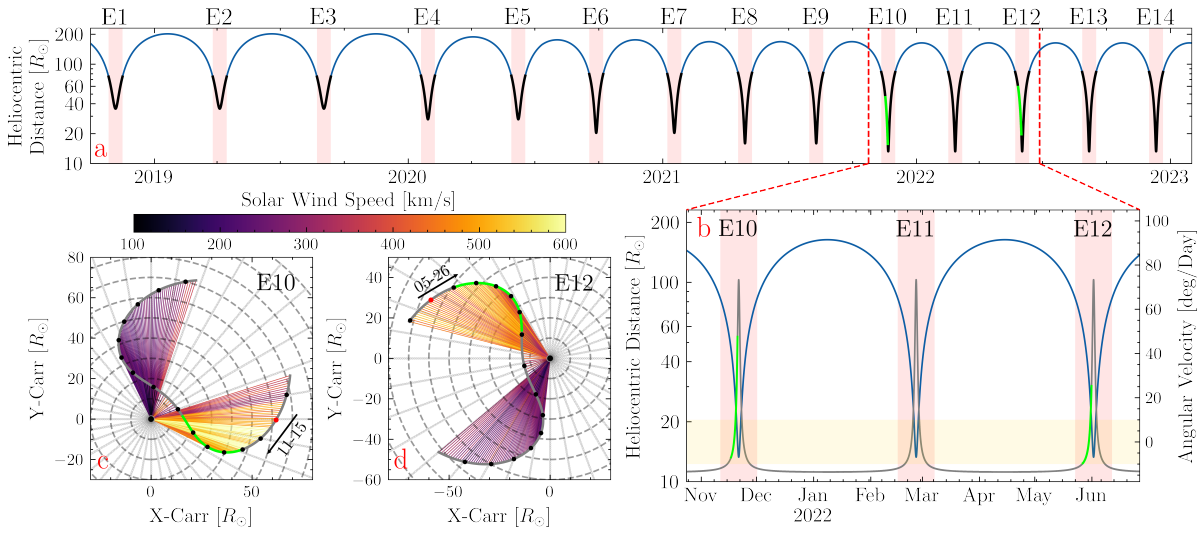

Figure 4.2: Panoramic plot of the data considered in this chapter. (a): This panel shows the heliocentric distance of the spacecraft from encounter 1 to 14. The data analyzed in this chapter is from ± 10 days around the perihelia, which are highlighted with black lines and pink shaded areas. The two normally distributed long intervals under investigation are represented by the two green segments. (b): This panel provides a detailed illustration of E10 to E12, with the spacecraft's angular velocity in the Carrington corotation frame displayed on the twin axis. The corotating periods ($\omega < 10$ $[deg/Day]$) are marked with golden shaded areas, and the selected intervals are highlighted in green on top of the angular velocity profile. (c) and (d): These panels provide a synopsis plot of E10 and E12 spacecraft trajectories from ± 8 days around the perihelion in the Carrington corotating frame. The starts of each day are indicated by black dots, and the two arrows show the spacecraft's entering directions, with the corresponding dates highlighted by red circles. The solar wind streamlines are colored according to the 10-minute averaged solar wind speed and are plotted every 2 hours. The two selected intervals are also highlighted in green.

et al., 2003)). The two large white pyramids in the GS clearly correspond to the two polar coronal holes. Notably, the boundary observed in panel (b) results from an artificial cut-off in the helio-radial power law fit, as shown in panel (c). The cut-off value is chosen to be $R_{max}/R_{min} = 1.5$, below which the spacecraft is considered stationary, and B is not normalized to B^* using helio-radial power law fit prior to the calculation of Gaussianity. However, the Gaussianity is much weaker in the polar coronal holes compared to the mid-latitude coronal holes observed by PSP at much smaller heliocentric distance, and the histograms of magnetic magnitude show much more significant fat tail towards the magnetic holes side (not shown here). This indicates that the Gaussianity of magnetic

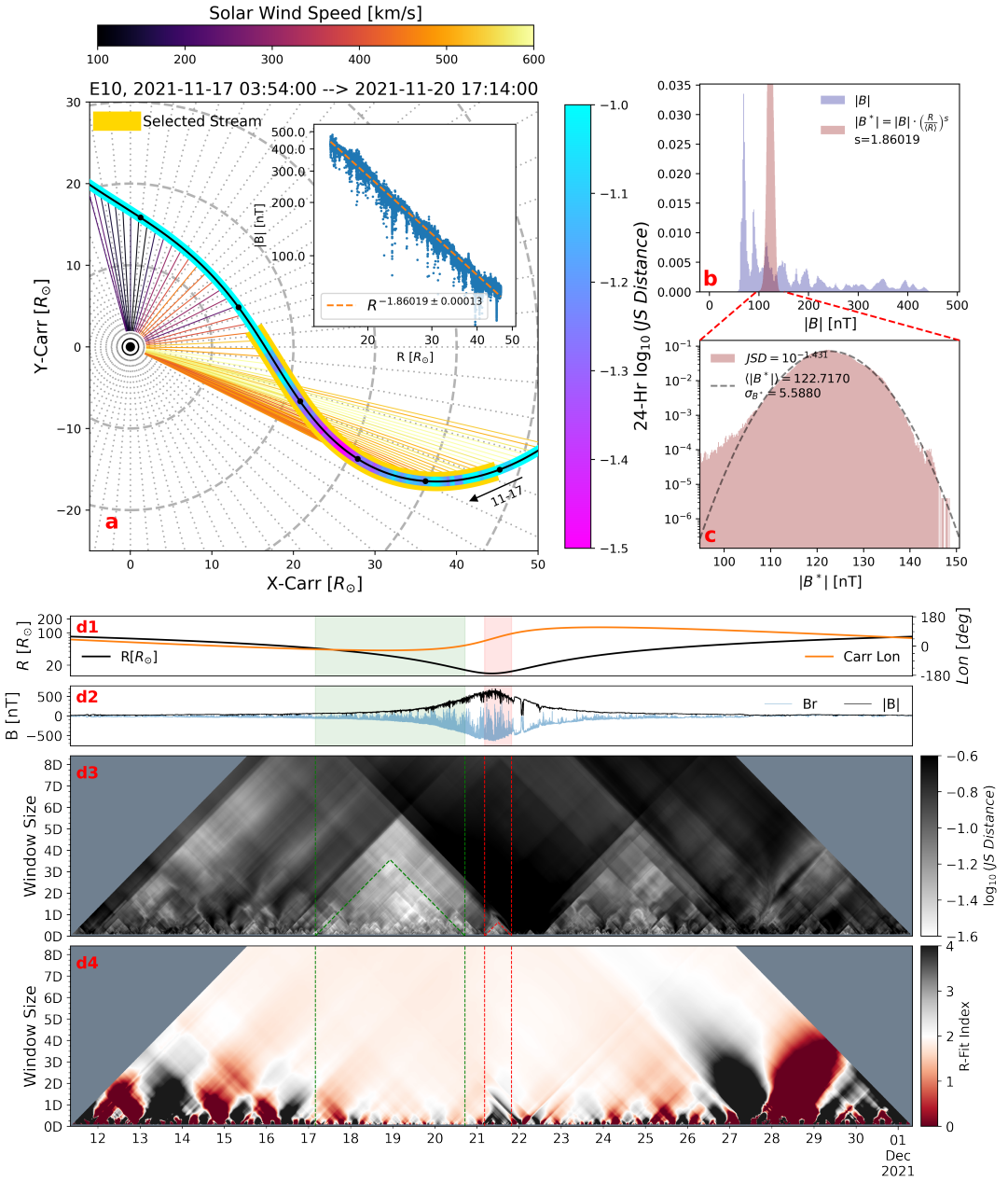

Figure 4.3: Selected interval from November 2021, encounter 10 of Parker Solar Probe. (a): This panel presents the spacecraft trajectory in the Carrington corotating frame from the afternoon of November 16, 2021, to the afternoon of November 22, 2021. Each day's start is indicated with black circles. The ballistic solar wind streamlines are plotted at a 2-hour cadence and colored according to the 10-minute averaged solar wind speed profile from SPAN-ion moment. The selected interval is emphasized with a golden bar, and the 24-Hour window Jensen-Shannon Distance (JSD) of normalized magnetic magnitude B^* is represented by the colored band. An inset displays the helio-radial power law dependence of B. (b): The histogram of B and B^* from the selected interval. (c): The histogram of B^* and $JSD(PDF_{B^*})$. (d1): Spacecraft heliocentric distance (black) and Carrington longitude (orange). (d2): Magnetic field radial component B_r and magnitude B. (d3):Gaussianity Scalogram (Scalogram of JSD). The selected interval is highlighted with the green pyramid. (d4): Helio-radial power law fit index scalogram of B.

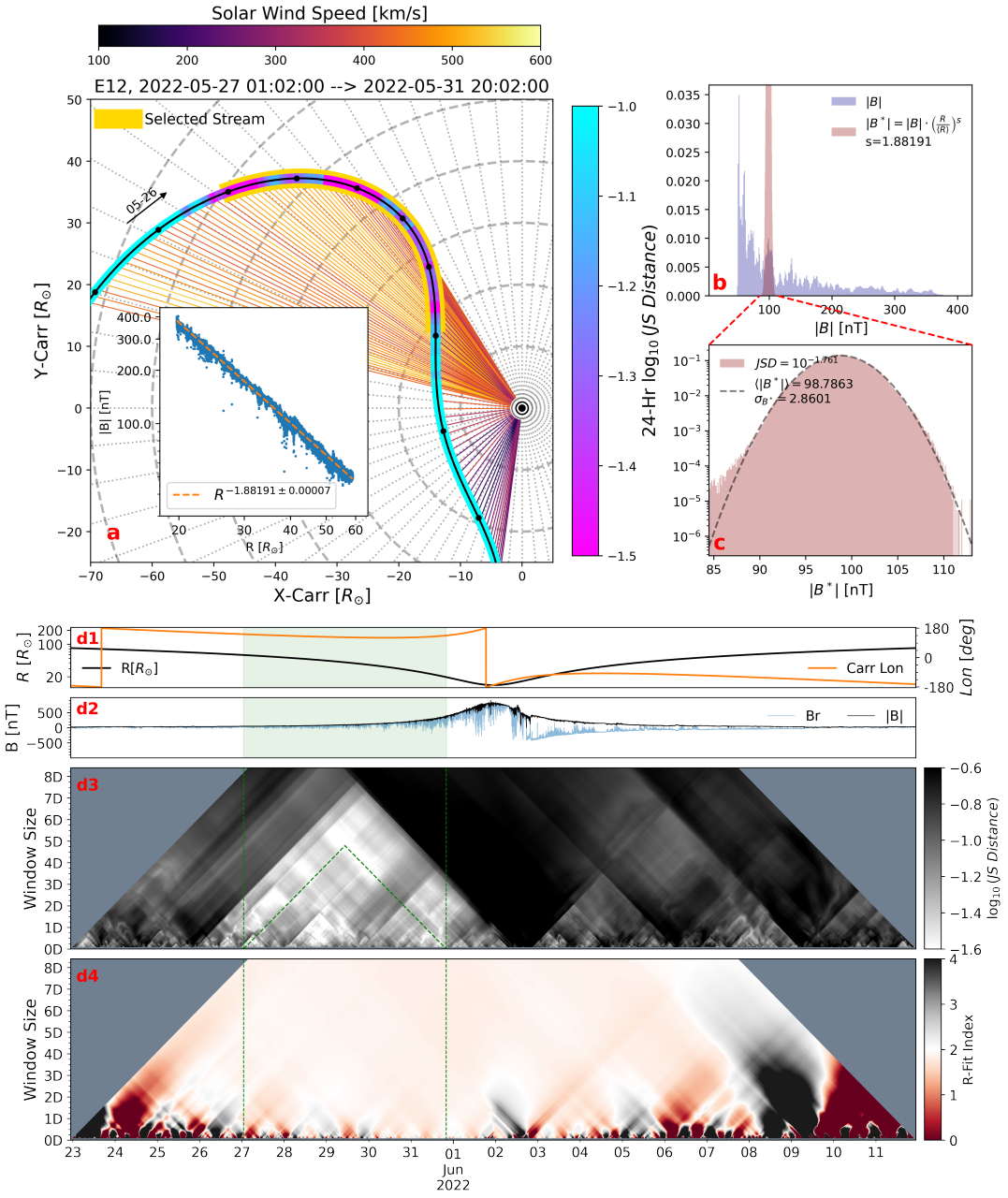

Figure 4.4: Selected interval from E12.

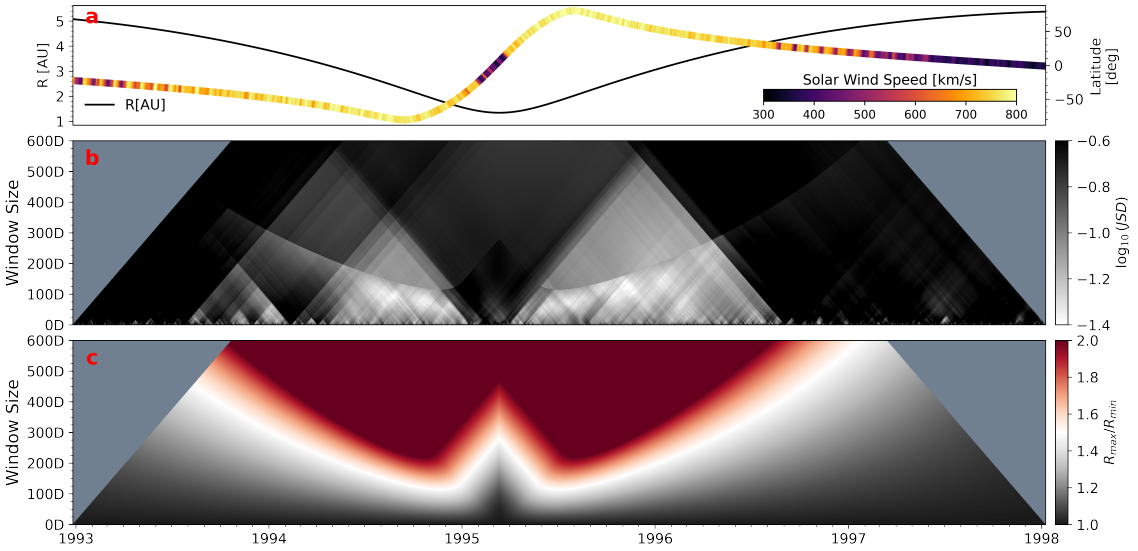

Figure 4.5: Gaussianity Scalogram from Ulysses first orbit from 1993 to 1998. (a): Ulysses heliocentric distance R (black line) and heliographic latitude colored with local 48-hour averaged solar wind speed. (b): GS compiled from magnetic magnitude B (lower half) and helio-radial power law normalized magnitude B^* (upper half). (c): R_{max}/R_{min} of each interval (pixel), the cut-off value is chosen to be $R_{max}/R_{min} = 1.5$, beyond which B is normalized into B^* using helio-radial power law fit before calculating the Gaussianity.

magnitudes decreases with increasing heliocentric distance, possibly due to the transition from low-β to high-β environment ($\beta = 2\mu_0 P/B^2$ is the ratio between plasma thermal pressure P and magnetic pressure $B^2/2\mu_0$), and the plasma thermal pressure hence has a larger influence on the distribution of B. Additionally this also indicates that magnetic holes are much more preferred than spikes in the solar wind plasma.

Figure 4.6 shows the hour-long switchback patches from a single mid-latitude coronal hole in PSP E10, which have been recently proposed to be the remnants of the supergranulations in the solar atmosphere (Bale et al., 2021; Fargette et al., 2021; Bale et al., 2023). To indicate the spacecraft movement, the Carrington longitude of PSP is plotted every one degree on the top bars of both panels (a) and (b), and the color indicates spacecraft angular velocity in the corotating frame (blue: prograde, red: retrograde, see also Figure 4.3 for PSP trajectory in the corotating frame at the same perihelion). The magnetic magnitude is normalized with a universal helio-radial power law fit index ($s = 1.87$) and the GS is compiled with the high-resolution fluxgate magnetic data ($\sim$ 292 Hz, see (Bale

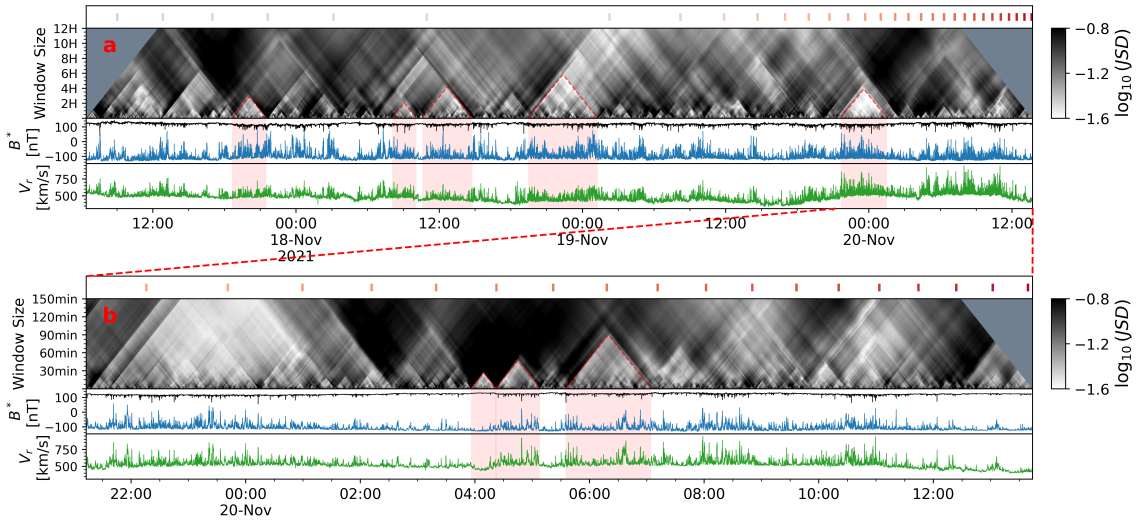

Figure 4.6: Gaussianity scalogram of Parker Solar Probe E10 inbound mid-latitude coronal hole. (a): From top to bottom: Carrington longitude plotted with 1 degree cadence colored with spacecraft angular velocity in the corotating frame (blue: prograde, red: retrograde); JS scalogram with 1-minute resolution; Normalized magnetic magnitude B^* and radial component B^*_r; Radial solar wind speed V_r; (b): Expanded view of panel (a) with 10-second resolution.

et al., 2016; Bowen et al., 2020)). The red dashed pyramids in panel (a) and (b) are drawn to highlight the B^* intervals with high level of Gaussianity. The selected intervals in panel (a) show that the GS effectively captures some of the switchback patches. When these are compared with the Carrington longitude, it becomes evident that some of the structures align with the size of supergranulation, as discussed in (Bale et al., 2023). However, other structures, which are smaller in angular size and likely temporal in nature, could be more accurately attributed to the 'breathing' phenomenon of the solar wind, as explained in (Berger et al., 2017; Shi et al., 2022b). After the "fast radial scan" phase on Nov-18, the spacecraft began to rapidly retrograde on Nov-19 and Nov-20 (see Figure 4.3 (a) for the spacecraft trajectory in the corotating frame). For better comparison, an expanded view is shown in panel (b). The second and third pyramids also show decent capability of capturing the switchback patches, whereas the first pyramid seems to capture a boundary between the patches. Starting from 7:00 on Nov-20, the remaining patches consistently exhibit a high level of Gaussianity across all scales and locations, resulting in indistinct boundaries between them.

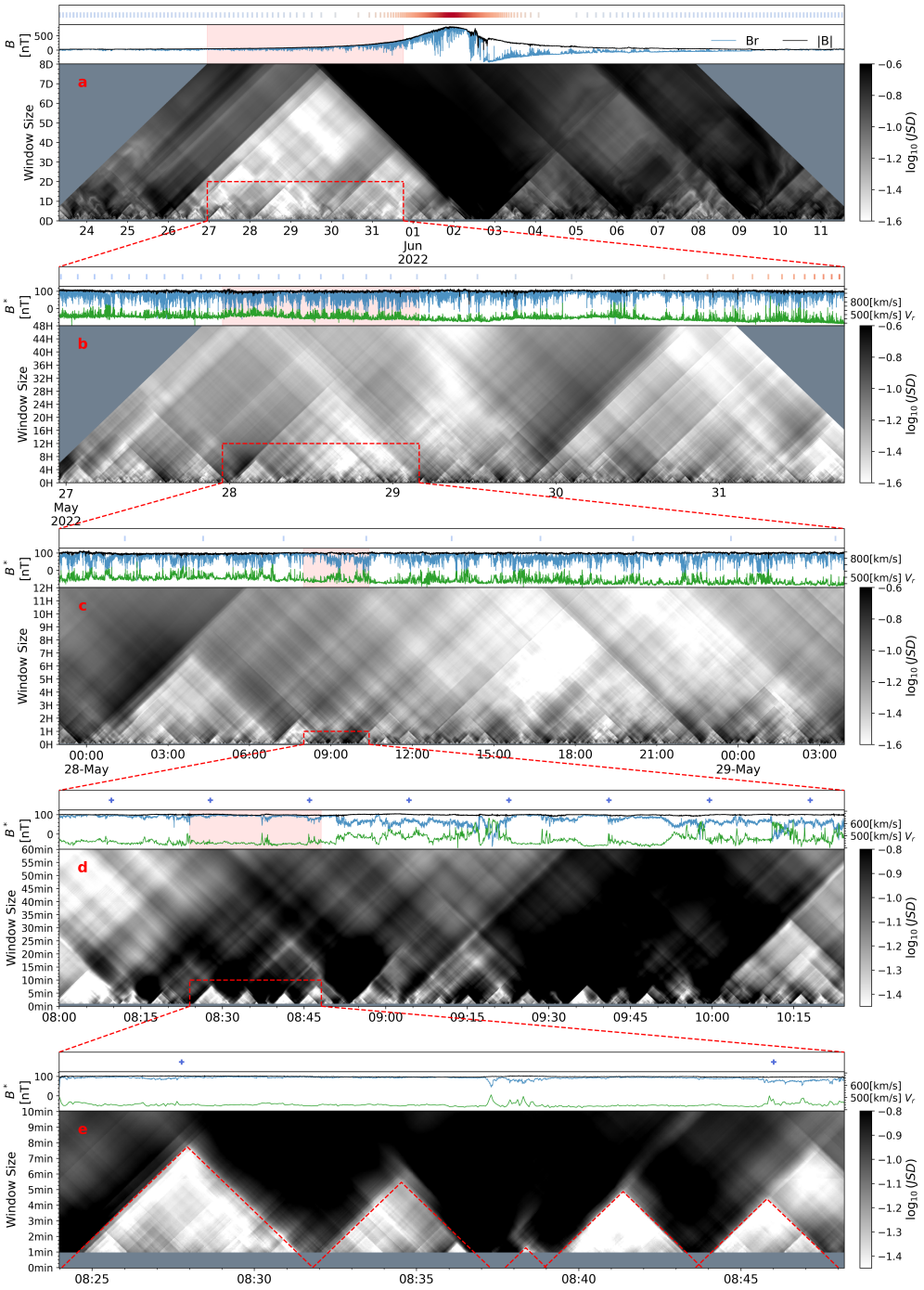

Figure 4.7: Hierarchic multi-scale Gaussianity Scalogram illustration of mid-latitude coronal hole from PSP encounter 12 inbound. For all subplots, the Carrington longitude of the spacecraft is shown in the top panel. For subplots (a) to (c), the bars are plotted every 1 degree, with colors indicating the heliocentric angular velocity in the solar corotating frame (blue: progradation, red: retrogradation). For subplots d and e, the crosses are plotted every 0.1 degree. The corresponding magnetic field magnitude B and radial component B_r are shown in the second panel of each subplot; and except for subplot (a), the magnetic field is normalized with helio-radial power law fit. The radial solar wind speed V_r is also shown in subplot (b) to (e).

Figure 4.7 presents a hierarchic GS of the mid-latitude coronal hole from the inbound of PSP E12. In panels (d) and (e), focusing on the smallest scales resolvable by the JSD (approximately 1 minute, corresponding to around 20,000 data points for the shortest interval. For details on how the number of data points influences this analysis, see Appendix B), we observe a surprising number of structures with distinct boundaries. In fact, these structures, typically lasting 1-10 minutes, are omnipresent in the Alfvénic solar wind for all PSP encounters. Notably, they are not limited to winds with a clear coronal hole origin, such as those in the outbound paths of E12 (for more details, see the supplementary video in Appendix 4). These structures are typically separated (interrupted) by radial jets (i.e. individual switchbacks), and these separations are frequently accompanied by close to kinetic scale ($\lesssim$ 5 seconds) fluctuations that are bursty and short-lived in all three components of magnetic field. For further illustration, refer to the https://www.youtube.com/watch?v=L8gH4luCao8 (skewness scalogram video). Unlike the spatial structures shown in panels (a), (b), and (c) (as well as in Figure 4.3 and Figure 4.5), the longitude change of the spacecraft for each structure in panel (d) and (e) is less than 0.1 degree, as indicated by the crosses plotted every 0.1 Carrington longitude in the top bar. Therefore, these structures are likely temporal, i.e. advected by the solar wind. All of these features are highly compatible with the "jetlets" observed in equatorial coronal holes (Raouafi et al., 2023b), and therefore could potentially be the "building blocks" of the solar wind. In fact, even finer structures can be found with the normalized standard deviation ($\sigma_{B^*}/\langle B^* \rangle$) scalogram and skewness scalogram shown in Figure 4.9. For example, the small white pyramid around 8:36 in Figure 4.7e has two 30-seconds long substructures nested beneath in Figure 4.9. These seconds-long structures are intervals with smaller standard deviation compared to the surroundings, and their interruptions are temporally compatible with the "picoflare" (Chitta et al., 2023).

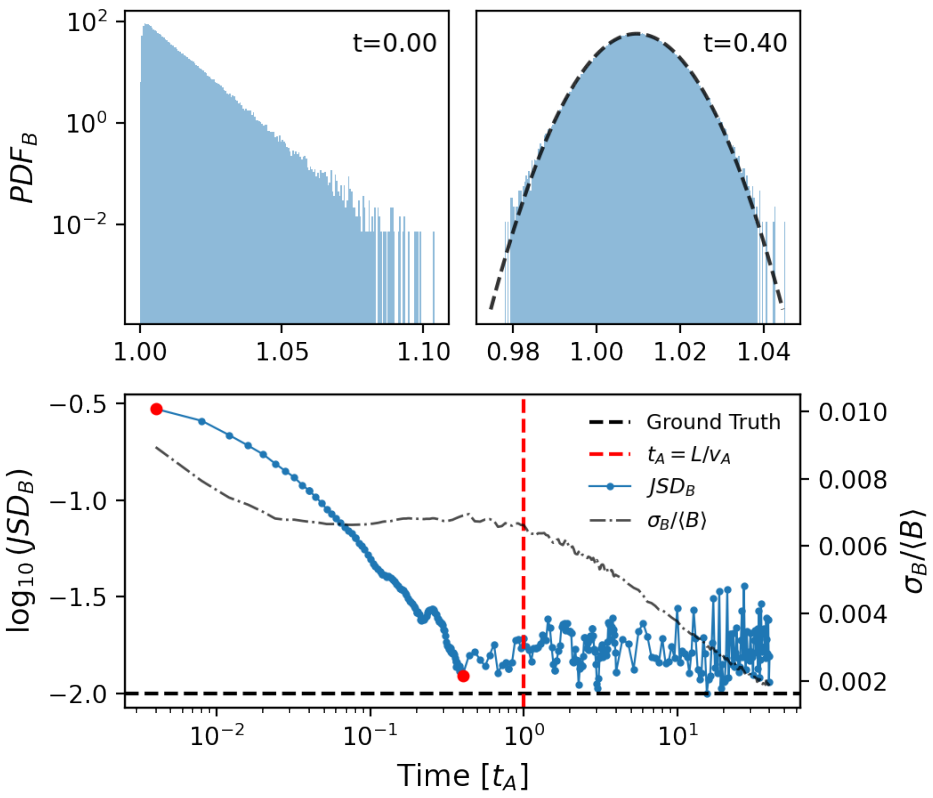

Figure 4.8: Relaxation of magnetic magnitude B in Alfvénic MHD turbulence simulation. Upper panels: (Left) Probability distribution of B (PDF_B) at $t = 0.00\ t_A$, where $t_A = L/v_A$ is the Alfvén time and L is the size of simulation box, v_A is the Alfvén speed; (Right) PDF_B at $t = 0.40\ t_A$. Lower panel: Time evolution of the Jensen-Shannon Distance between PDF_B and Gaussian Distribution (blue line), and the normalized standard deviation of B (dash dotted line). The time axis is normalized with the Alfvén time t_A. The simulation time step of the upper left and right panels are highlighted with two red circles in the lower panel.

4.4 Discussion

These observations indicate that the Alfvénic solar wind is permeated with highly Gaussian magnetic magnitude intervals that are often interrupted by radial jets (switchbacks) every 1-10 minutes. In addition, the magnetic fluctuations inside the intervals often resemble the small amplitude outward propagating linear Alfvén waves. It is therefore reasonable to model the system using small amplitude Alfvénic MHD turbulence. Figure 4.8 shows the temporal evolution of the $JSD(PDF_B, \mathcal{N})$ of a 3D MHD small amplitude Alfvénic turbulence simulation (Shi et al., 2023). The simulation is run with 512^3 periodic

box, and is initialized with unidirectional small amplitude linearly polarized Alfvén waves with isotropic wave vector spectrum (see Appendix B for more details). At $t = 0.00\ t_A$ (Alfvén crossing time $t_A = L/v_A$, where L is the simulation box size), PDF_B deviates significantly from a Gaussian distribution due to the small amplitude shear Alfvén wave initialization (fluctuations in B are positive definite). The corresponding JSD is highlighted as the first red dot in the lower panel and is much larger than 0. Surprisingly, within one Alfvén crossing time at $t = 0.40\ t_A$, the distribution of B rapidly relaxes to a near-perfect Gaussian distribution, and the JSD rapidly drops towards the ground truth value (see Appendix B). As the simulation evolves, the JSD remains considerably small and thus the distribution of B remains very close to Gaussian. The simulation indicates that Gaussian is the natural relaxation state for magnetic magnitude in small amplitude Alfvénic turbulence, consistent with the ubiquitous 1-10 minutes Gaussian intervals found in the solar wind. However, a 3D analytical model of a switchback with constant magnetic magnitude and fully open field lines is not yet available (see (Tenerani et al., 2020; Squire and Mallet, 2022; Shi et al., 2024; Matteini et al., 2024) for recent progress on switchback modeling). Therefore, our simulation can not reproduce the realistic physical condition of the solar wind turbulence in which large amplitude spherically polarized Alfvénic fluctuations dominate.

Nevertheless, the simulation suggests that information is fully exchanged within the system, as it propagates at Alfvén speed throughout the simulation box. This allows B to relax to a Gaussian distribution, which occurs within about 0.5 t_A, i.e. the time it takes for Alfvén waves to carry information from the center of the simulation box to its edges. However, in observations, it is not reasonable to assume that the information is fully exchanged for the hours, days or even months long structures shown in Figures 4.3, 4.5 and 4.6, due to the super-Alfvénic nature of the solar wind close to the sun and the longitudinal movement of the spacecraft. Beyond the Alfvén surface (Kasper et al., 2021), the information can only propagate radially outwards in the solar wind. Moreover, the structures that last an hour or longer are likely spread spatially and longitudinally. However, Alfvén waves, along with the information they carry, are guided

by the background magnetic field, which predominantly points radially outwards around PSP perihelia. Therefore, alternative explanations are necessary for the observed hour-long (and longer) Gaussian structures. The simplest explanation for the Gaussian B structures originating from coronal holes (mid-latitude coronal holes from E10 and E12, and polar coronal holes from Ulysses) is the pressure balance between the open coronal field lines. Close to the sun, the solar wind originating from the coronal holes is mostly magnetic dominant (plasma $\beta = 2\mu_0 P/B^2 \ll 1$, see e.g. (Kasper et al., 2021)). Therefore, to maintain pressure balance, the open field lines from the same coronal hole tend to evolve to a state in which the magnetic pressure $P_B = B^2/2\mu_0$ is mostly uniform for a given cross section of the magnetic flux tube. In Figure 4.3, the helio-radial power law normalization of B essentially maps the magnetic field line density, which is effectively the magnetic flux density due to the spherical polarization of the Alfvén waves, from various radial distances and transverse locations to a single cross-section of the flux tube (for more details of spherical polarization of Alfvén waves, see Appendix B and (Matteini et al., 2014, 2015)). As a support of this idea, from the PSP observations of E10 and E12 (Figure 4.3 and Figure 4.4), the helio-radial power law normalization of B effectively collapses the histogram of B into a delta-function-like histogram of B^*. This is indicative of identical field line density within a single coronal hole due to the magnetic pressure balance. The detailed distribution of B^* is hence the feature of the noise in magnetic magnitude within a single coronal hole, which can be considered as a one-dimensional random walk (continuous addition of small amplitude random fluctuations that can be considered as samples drawn from the same stochastic source throughout its passage from the base of the corona to the spacecraft). Therefore, the Gaussian distribution of B^* can be easily explained as the result of the stopped random walk according to central limit theorem. Nevertheless, difficulties remain for the physical origin of the hour-long structures. They may be the manifestation of the denser field line density originating from a single supergranulation based on its connection with switchback patches, but a more detailed discussion lies beyond the scope of this dissertation.

Finally, the existence of a stable power law dependence of B with regard to heliocentric

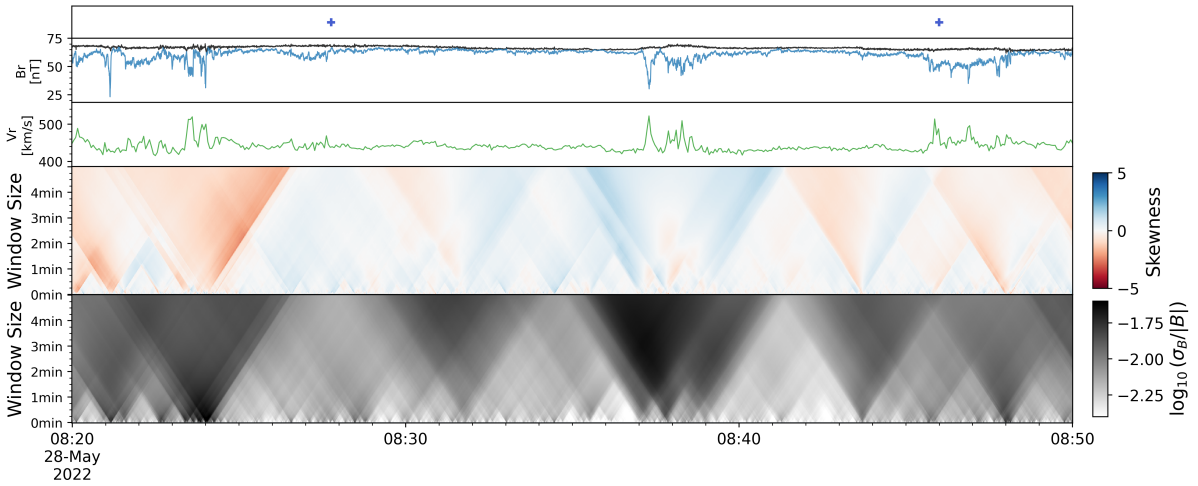

Figure 4.9: Skewness and normalized standard deviation scalogram. From top to bottom: spacecraft carrington longitude plotted with 0.1 degree cadence; magnetic magnitude (B, black) and radial component (B_r, blue); radial solar wind speed (V_r); skewness scalogram of B; normalized standard deviation scalogram of B

distance R itself already sheds light on the physics of the solar wind originating from coronal holes. As solar activities ramp up for solar cycle 25, 4 out of the 5 recent encounters (E10, E11, E12, E14) of PSP show systematic preference for a single helio-radial power law index, which consistently deviates from R^{-2}. However, the R^{-2} power law, expected only from the dominant radial component B_r as a result of the Parker Spiral (conservation of magnetic flux in spherical expansion), is not strictly applicable to B, especially for PSP, due to the ubiquitous switchbacks. Due to the relation between B and the local magnetic flux density, this is indicative of a stable expansion rate for the magnetic flux tube in the magnetic dominant wind ($\beta \ll 1$) close to the sun. Such an expansion rate is crucial for the estimation of the WKB evolution of the fluctuation quantities like the magnetic and velocity field (Hollweg, 1973; Heinemann and Olbert, 1980; Velli et al., 1991; Huang et al., 2022). It should be noted that the fit indices of B coincide with the helio-radial dependence of the electron density compiled from Quasi Thermal Noise (Kruparova et al., 2023; Moncuquet et al., 2020), indicating that the deviation from R^{-2} could be the evidence of active acceleration of the solar wind.

4.5 Conclusion and Summary

Compiled from the almost featureless magnetic magnitude time series from the solar wind, the Gaussianity Scalogram (GS) unveiled a striking number of fractal magnetic structures spanning across over seven orders of magnitude in time. These structures include spatial structures like polar coronal holes (McComas et al., 2003), mid-latitude coronal holes (Badman et al., 2023), and switchback patches (Bale et al., 2023). They also include temporal structures compatible with "jetlets" (Raouafi et al., 2023b) and "picoflare" (Chitta et al., 2023), which are often interrupted by the radial jets (switchbacks). In addition, three-dimensional MHD simulations have shown that Gaussian is the natural relaxation state for small amplitude unidirectional Alfvénic turbulence. The minute-long structures are hence likely to be the natural products of Alfvénic MHD turbulence. Thus, it is now clear that the Alfvénic solar wind is permeated with these intermittent Gaussian B structures, which are self-similarly organized from seconds to years, and are possibly the remnants of the magnetic structures on the solar surface (Uritsky and Davila, 2012; Aschwanden, 2011; Aschwanden et al., 2016; Bale et al., 2023; Raouafi et al., 2023b; Chitta et al., 2023). This chapter reveals just a fraction of the rich structures uncovered by the GS from the solar wind time series. The GS proves to be a versatile tool, essential not only for deciphering the structure and dynamics of plasma and magnetic fields, one of the key objectives of the PSP mission (Fox et al., 2016), but also for revitalizing decades-old solar wind data from missions like Helios, Ulysses, and WIND. These efforts unveil new physics previously hidden within these data sets. Additionally, the GS applicability may extend beyond solar wind analysis, potentially serving other kinds of high resolution stochastic time series data.

CHAPTER 5

3-Minute Oscillations in the Upper Corona: Evidence from PSP

5.1 Introduction

The heliosphere is created by the supersonic plasma flow originating from the Sun known as the solar wind. Parker (1958) successfully predicted the existence of the supersonic wind, which was later confirmed by *in situ* observations from the Luna 2 (Gringauz et al., 1962) and Mariner II spacecraft (Neugebauer and Snyder, 1966). However, it was quickly realized (Parker, 1965) that thermal conduction is not capable of accelerating the solar wind to high speed ($\gtrsim$ 700 km/s, see e.g. observations from Ulysses (McComas et al., 2000)), and therefore additional injection of momentum and energy at substantial distances from the sun are necessary to heat and accelerate fast solar wind streams (Leer and Holzer, 1980).

Large amplitude Alfvén waves are ubiquitous in the solar wind (Unti and Neugebauer, 1968; Belcher and Davis, 1971). Interplanetary Alfvénic fluctuations are characterized by a quasi-constant magnetic magnitude $|B|$, hence the magnetic field vector tip appears to undergo a random walk on a sphere (Barnes and Hollweg, 1974; Tsurutani et al., 1997; Matteini et al., 2014, 2024). Constant $|B|$ states are an exact solution of the Magnetohydrodynamics (MHD) equations, and can propagate without much damping. Consequently, Alfvénic fluctuations are considered to be a prime candidate for the heating and acceleration of the solar wind (Belcher, 1971; Belcher and Olbert, 1975; Alazraki and Couturier, 1971; Shi et al., 2022a) (For a review, see (Hansteen and Velli, 2012)).

The origin of Alfvénic fluctuations in the solar wind remains debated. It has been conjectured that they may be generated by magnetic reconnection in the lower solar corona (Bale et al., 2021; Drake et al., 2021; Bale et al., 2023); others argue that Alfvén waves originate deeper in the solar atmosphere (Jess et al., 2009, 2015; Morton et al., 2023): either from the transition region and chromosphere (Tian et al., 2014; De Pontieu et al., 2007; Kuridze and Zaqarashvili, 2008), or directly from the photosphere where they are generated by convective motions (Cally, 2012; Hansen and Cally, 2012; Morton et al., 2013; Cally, 2017; Morton et al., 2019; Kuniyoshi et al., 2023) or motions and shocks associated with G-band bright points (Cranmer and Ballegooijen, 2005). It is well-known that the solar convection zone acts as a resonance chamber and the resultant fluctuations concentrate around 5-minute frequency, known as the p-mode (pressure-mode) oscillations (Ulrich, 1970; Foukal, 2004). In the chromosphere, the primary fluctuation frequency drifts slightly higher becoming the well studied chromospheric 3-minute oscillations (Fleck and Schmitz, 1991; Jess et al., 2012). Entering the upper chromosphere and transition region, the primary fluctuation frequency can become larger but the measured values, around 100-500s, are still debated (De Pontieu et al., 2007; Morton et al., 2012). Recently, numerous time-evolving filamentary substructures termed 'plumelets' were found within coronal plumes, and they possess a characteristic frequency of 3.3 mHz, commensurate with the p-mode (Uritsky et al., 2021). (Kumar et al., 2022) showed evidence of quasiperiodic jets with 3-5 min period and energy release (EUV brightenings) at the base of plumes, and predicted that these jets could be the sources of the switchbacks in the solar wind. Later, (Kumar et al., 2023) analyzed the the coronal hole outflow in PSP E10 and discovered distinct period peaks at around 3, 5, 10 and 20 minutes, consistent with the period peaks in emission intensity of the jetlets at the base of coronal hole plumes and plumelets, validating their hypothesis. In addition, higher frequency waves, known as decayless oscillations, are observed in coronal loops (Mandal et al., 2022; Zhong et al., 2023; Shrivastav et al., 2023). For recent reviews, see (Mathioudakis et al., 2013; Van Doorsselaere et al., 2020; Banerjee et al., 2021). It is therefore of interest to examine whether in-situ observations provide any evidence of fluctuation energy concentration in

a certain range of frequencies in the upper corona.

Parker Solar Probe (PSP), launched in late 2018 (Fox et al., 2016), has been providing *in situ* observations of the magnetic-dominated solar corona since 2021 (Kasper et al., 2021). The unprecedented *in situ* measurements from the near-sun heliosphere has ushered in a new era of space plasma studies (see e.g. (Chen et al., 2020; Adhikari et al., 2020; Shi et al., 2021; Matthaeus, 2021; Sioulas et al., 2022; Zank et al., 2022; Chen, 2022; Zhang et al., 2022; Sioulas et al., 2023b,a; Dunn et al., 2023; Larosa et al., 2023; McIntyre et al., 2023), and see (Raouafi et al., 2023a) for a recent review). Notably, new observations from PSP have shown that the $1/f$ range in standard solar wind turbulence model (Bruno and Carbone, 2013) appears to be absent closer to the sun, and instead shallower ($\sim f^{-0.5}$) spectra are found around the Alfvén surface, and it has been statistically evidenced that the $1/f$ range forms dynamically around 0.2 AU (Huang et al., 2023c; Davis et al., 2023; Chandran, 2018). The $1/f$ range is also known as the energy containing range because the integrated fluctuation energy $\ln(f_2/f_1)$ is independent of the specific frequencies considered, and instead dependent only on the size of the frequency range. Therefore, close to the sun, the majority of the solar wind turbulence energy concentrates in a small range of frequencies around the "bend" between the shallow low frequency range ($\sim f^{-0.5}$) and the inertial range ($\sim f^{[-1.67,-1.5]}$, see e.g. (Chen et al., 2020; Sioulas et al., 2023a; McIntyre et al., 2023)).

In addition, the fluctuations in the solar wind turbulence were launched at the base of the corona (or deeper in the solar atmosphere), where the plasma is relatively stationary. Consequently, the frequency power spectrum measured by PSP can be considered as the real frequency spectrum launched at the base of the corona, and are subsequently modified by nonlinear interactions. Additionally, there is a Doppler shift resulting from the relative motion between the spacecraft and the solar wind (the radial doppler shift can be considered negligible because $V_{psp,r} \lesssim 100$ km/s at perihelia, and the phase velocity of outward propagating Alfvén waves $V_{phase} = V_A + V_{SW} \sim 1000$ km/s $\gg V_{psp,r}$, but the perpendicular doppler shift could contaminate the frequency spectrum at perihelion. For detailed discussions, refer to Appendix C). As a result, the frequency of the "bend",

i.e. the center frequency of the fluctuation energy f_{mid}, can be considered as the proxy to the primary fluctuation frequency at the source of the fluctuations (corona base or deeper), assuming such frequency is not significantly altered by nonlinear interactions (which however is subject to future scrutiny). In this study, we report the first *in situ* observational evidence that the magnetic fluctuations energy in upper solar corona universally concentrates around 3-minute. The rest of the chapter is organized as follows: In the next section, we introduce the data and the relevant statistical methods; In section 3, we report the primary statistical results of center fluctuation frequency f_{mid} as a function of solar wind advection time $\tau_{adv} = (R - R_{\odot})/V_r$; In section 4, we discuss the source of the Alfvén waves and the turbulence properties; In section 5, we conclude and summarize our results.

5.2 Data and Methods

The magnetic field data is obtained from the fluxgate magnetometer in the FIELDS instrument suite (Bale et al., 2016) and the plasma measurements are acquired from the Faraday cup (SPC) and SPAN-ion from the SWEAP instrument suite (Kasper et al., 2019). Electron density data compiled from Quasi-Thermal-Noise (QTN) (Kruparova et al., 2023) is used as a proxy for proton density in the solar wind.

An example interval is shown in Figure 5.1. The trace power spectrum density (PSD_{FFT}) of magnetic field is shown in panel (b) in blue. The PSD is the trace sum of the squared amplitudes of the Fast Fourier Transformation (FFT) of the three magnetic vector components. To obtain a smoother spectrum, the PSD is smoothed using a window with a frequency factor of 2, and is shown in the green dashed line (sm-PSD_{FFT}). However, due to the rapid movement of PSP, the time series is naturally non-stationary, violating the fundamental assumptions of Fourier Transformation. Therefore, wavelet transformation is compiled for comparison, which is shown as orange line (PSD_{WL}). In general, we found that for frequencies where more than 50% of the PSD_{WL} falls within the Cone of Influence (CoI, shown as the gray shaded area), the PSD_{WL} and sm-PSD_{FFT}

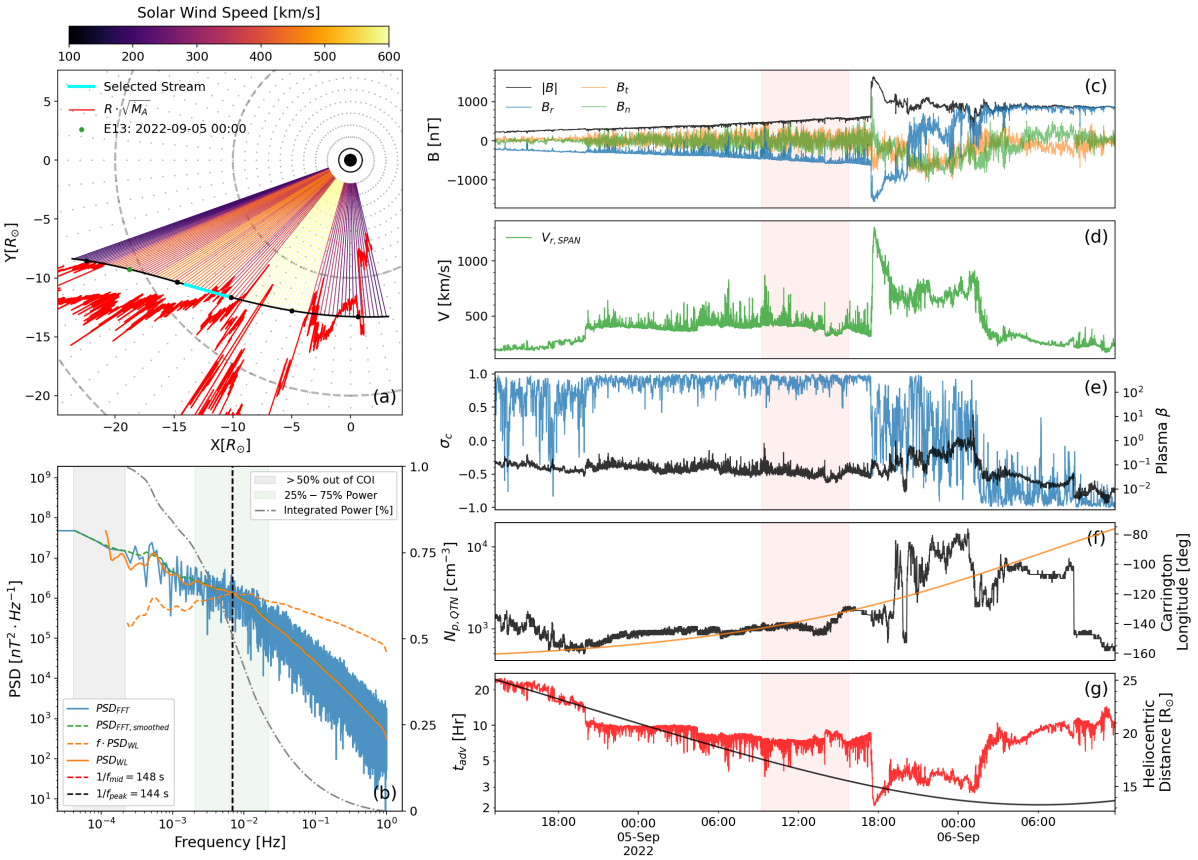

Figure 5.1: (a) Trajectory of PSP in the solar corotating frame with radial lines colored with local 10-minute average of solar wind speed. Black dots are plotted every 8 hours and the green dot indicates the entering direction. The red line is an illustration of the Alfvén mach number $M_A = V_r/V_A$. If the wind is super-Alfvénic, the red line falls out of the spacecraft trajectory (black line), and falls below the trajectory if the wind is sub-Alfvénic. The selected interval is highlighted with the cyan bar. (b) Trace magnetic power spectrum density (PSD) of the selected interval compiled from various methods. Blue: Fast Fourier Transformation (PSD_{FFT}). Green dashed: smoothed PSD_{FFT}. Orange: Wavelet Transformation (PSD_{WL}). Orange dashed: PSD_{WL} compensated with reference spectrum $1/f$. Gray area: frequency range where more than 50% of points fall out of the Cone of Influence (CoI) of the wavelet transformation (i.e. with too strong boundary effects). Dotted-dashed: Normalized integration of PSD_{WL} (orange line), i.e. normalized fluctuation energy, twin y-axis. Green area: frequency range over which the normalized fluctuation energy grows from 25% to 75%. Vertical dark dashed: middle frequency of the green area. Vertical red dashed: peak frequency of the compensated PSD_{WL} (orange dashed line). (c) R, T, N components and magnitude of the magnetic field. The selected interval is highlighted with the vertical pink area. (d) Radial solar wind speed from SPAN-ion and Alfvén speed $V_A = |B|/\sqrt{n_p m_p \mu_0}$. Proton density n_p is acquired from electron density from quasi-thermal-noise, and alpha particle and other heavier elements composition are ignored. (e) Cross helicity σ_c (left, blue) and plasma $\beta = 2\mu_0 P/B^2$ (right, black). (f) Proton density n_p (left, black) and Carrington Longitude (right, orange) (g) Advection time $\tau_{adv} = (R - R_\odot)/V_r$ (left, red) and Helio-radial distance R of the spacecraft (right, black).

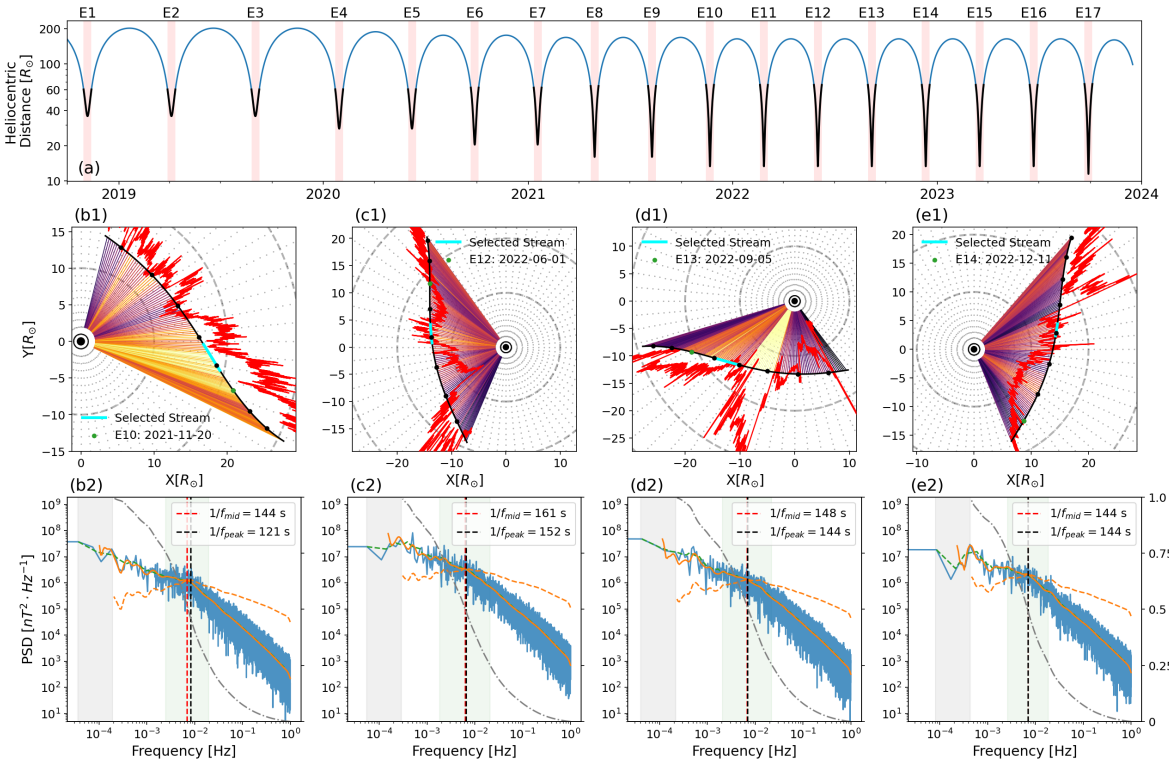

Figure 5.2: (a) Helio-radial distance of PSP by the end of 2023. The intervals considered in this study are highlighted with the black lines. (b1-e1) Trajectory of PSP (black line), Selected interval (cyan bar), Solar wind speed (colored radial lines), Illustration of Alfvén Mach number M_A ($R \cdot \sqrt{M_A}$, R is the radial distance of PSP, red line). Black dots are plotted every 8 hours and the green dot indicates the entering direction. (b2-e2) Trace magnetic power spectrum density (PSD) compiled from various methods: FFT (blue), smoothed FFT (green dashed), wavelet (orange), wavelet compensated with $1/f$ (orange dashed). Gray area: frequency range ignored due to Cone of influence. Green area: frequency range over which 50% (from 25% to 75%) of fluctuation energy resides. Red dashed: center of the green area. Black dashed: peak of the orange dashed line. Refer to Figure 5.1 for a colorbar for solar wind speed and detailed explanation for various lines.

overlap almost perfectly with each other, and hence we entrust the overlapping frequency range. In this study, we consider the PSD_{WL} outside of the CoI range (part of the orange line that is outside of the gray area in panel (b)) as the primary power spectrum density of the magnetic field, and will henceforth refer to PSD_{WL} as PSD for simplicity. For detailed discussion of CoI, please refer to Chapter 3.

The normalized integrated power of the PSD is shown with the dashed-dotted line in the twin axis. The frequency range that contains 50% (from 25% to 75%) of the total fluctuation energy is highlighted with the green shaded area, and the center of the frequency range f_{mid} is shown with the red dashed line ($1/f_{mid} = 148s$). If the PSD scales as $1/f$, the energy distribution is independent of the specific frequency considered because the integrated power from f_1 to f_2 is $\ln(f_2/f_1)$. As a result, $1/f$ is the *de facto* "unity" reference spectrum, i.e. if the spectrum is steeper than $1/f$, the energy concentrate at the low frequency end, whereas if the spectrum is shallower than $1/f$, the energy concentrate at the high frequency end. In Chapter 3 we have shown that, close to the sun, the PSD is characterized by a double power law where the low frequency range is shallower than $1/f$, and the inertial range is steeper, similar to Figure 5.1(b). Therefore, we compensate the spectrum with f, and the resultant compensated spectrum is shown with the orange dashed line. The compensated spectrum obviously shows a peak ($1/f_{peak} = 144s$), and we consider this as the "peak" frequency of the PSD, or the real location of the "bend".

Traditionally, the location of the low frequency spectral break is obtained from power law fit on both ranges of the PSD (see e.g. (Bruno and Carbone, 2013) and references therein). However, the turbulence spectrum measured by PSP close the sun (shallow-inertial) differ significantly from standard turbulence model ($1/f$-inertial), and sometimes displays a triple power law (shallow-$1/f$-inertial). Consequently, obtaining the low frequency spectral break locations from power law fits is highly unreliable. Thus we consider the f_{mid} defined above as a proxy to the low frequency spectral break, which turns out to be surprisingly accurate when the spectrum has a shallow-inertial double power law.

In this study, we systematically surveyed the *in situ* solar wind time series from $\pm$

7 days around the first 17 perihelia and they are summarized in Figure 5.2(a). We scan the date ranges with fixed window sizes of 2, 3, 4, 6, 8 and 12-Hour, with a fixed step size of 15-minute. We compile the wavelet PSD for each of the intervals, and calculate the center frequency of the frequency range where 50% of fluctuation energy resides (f_{mid}). We also calculate the averaged properties for each interval, including the mean solar wind speed, Alfvén mach number, and advection time ($\tau_{adv} = (R - R_{\odot})/V_r$, R is the heliocentric distance of PSP, and V_r is the local radial solar wind speed). Whenever possible, we prioritize using V_r from SPAN-ion and electron density from QTN as a proxy for proton density due to the limited field of view of both SPAN-ion and SPC. Moreover, to better understand the radial evolution, we also focused on two extended intervals from inbounds of E10 and E12 that have been confirmed to be originated from single mid-latitude coronal holes (Badman et al., 2023; Huang et al., 2023b). Additionally, results from Chapter 4 have shown that the Gaussianity of $|B|$ can be used as a simple indicator for the wind originated from coronal holes, and hence a strong correlation to the Alfvénicity of solar wind. Therefore, in this study, besides an unbiased statistical survey, we also apply a simple threshold of Jensen Shannon Distance (JSD) smaller than 0.1 to filter the intervals with high level of Gaussianity in $|B|$, and thereby with high level of Alfvénicity.

5.3 Results

5.3.1 Case Studies: Pristine Alfvénic Solar Wind

Figure 5.1 shows an example interval from E13 where the PSD is characterized by a shallow-inertial double power law. This phenomenon is among one of the unexpected discoveries of PSP (Huang et al., 2023c; Davis et al., 2023) and differs significantly from the standard solar wind turbulence model where the inertial range ends with an energy containing $1/f$ range (see e.g. (Bavassano et al., 1982; Denskat and Neubauer, 1982; Burlaga and Goldstein, 1984) and (Bruno and Carbone, 2013; Tu and Marsch, 1995) for reviews). Because of the shallow-inertial double power law, the majority of the fluctuation

energy (dotted-dashed line) concentrates around the low frequency spectral break (or "bend") at around $1/f_{mid} = 148s$.

This interval is typical and interesting because : 1. It is (accelerating) fast Alfvénic wind, and thus likely originated from coronal hole. This can be seen from panel (d) that the baseline $V_r \gtrsim 450km/s$ and from panel (e) that the normalized cross helicity $\sigma_c \simeq 1$; 2. It sits right at the Alfvén surface where the Alfvén Mach number $M_A = V_r/V_A$ ($V_A = |B|/\sqrt{\mu_0 n_p m_p}$) become unity, and therefore PSP is making *in situ* measurements in the upper corona. This can be seen from panel (a) where the red line ($R\cdot\sqrt{M_A}$) crosses the spacecraft trajectory towards the end of the interval and from panel (d) where the Alfvén speed V_A passes the radial solar wind speed V_r; 3. The radial distance of this interval is $R \sim 17R_\odot$ with advection time $\tau_{adv} \lesssim 8Hr$, and if we consider the group velocity ($V_g = V_A + V_r \gtrsim 1000$km/s) of the Alfvén waves, the real propagation time $t_p \lesssim 3.1Hr$. Thus, this interval is one of the most pristine solar wind streams measured by PSP. Note that the primary physical carriers of the fluctuation energy in the temporal domain are the so-called magnetic switchbacks, i.e. large amplitude spherically polarized outward propagating Alfvén waves (Bale et al., 2019; Squire et al., 2020; Dudok de Wit et al., 2020; Shoda et al., 2021; Rasca et al., 2021; Mozer et al., 2021; Bale et al., 2023; Drake et al., 2021; Tenerani et al., 2021; Shi et al., 2022b; Huang et al., 2023a; Larosa et al., 2023; Toth et al., 2023; Jagarlamudi et al., 2023; Bizien et al., 2023). Due to the polarization and the unidirectional outward propagation, these waves are accompanied by radial jets on the order of local Alfvén speed (Matteini et al., 2014) shown in both panel (a) and panel (d).

Figure 5.2 panels (b-e) show three more typical cases from E10, E12 and E14 where the PSD is characterized by a shallow power law (panel (d) is almost identical to Figure 5.1). All cases are Alfvénic fast wind that have not been thoroughly accelerated and the selected streams sit right at the Alfvén surface. In addition, the "bend" frequencies, or the center frequencies ($1/f_{mid}$) for fluctuation energy all concentrate at around 3-minute. It should be noted here that the selected streams from panel (b) and (c) (E10 and E12) have been confirmed by previous studies using Potential Field Source Surface modeling

(Badman et al., 2020; Panasenco et al., 2020) to both originate from single mid-latitude coronal hole (Badman et al., 2023; Huang et al., 2023b).

The cases shown above indicate that the fluctuation energy concentrates around 3-minute for the pristine Alfvénic solar wind. Notably, if one assumes the spacecraft remains stationary (see Appendix C for discussion of the doppler effects from PSP movement), and the time series are created solely by the advection of the solar wind, the frequency spectrum measured by PSP should be identical to the frequency spectrum at the source of the wind (corona base or deeper), provided that nonlinear effects are insignificant. Therefore, it is of great interest to conduct a systematic survey for the statistical behaviors of magnetic fluctuations in the solar wind to study the radial evolution of $1/f_{mid}$. One may expect that $1/f_{mid}$ evolves towards 3-minute with decreasing advection time τ_{adv}.

5.3.2 Statistical Results: E1-E17

Figure 5.3 shows the statistical results of $1/f_{mid}$ from a systematic scan with 6-Hour fixed window and 15-minute step size of $\pm$ 7 days around the first 17 PSP perihelia. The intervals whose $\sigma_{\tau_{adv}}/\langle\tau_{adv}\rangle > 20\%$ are discarded (about 6.5% of all intervals), and we ends up with 20975 intervals. The results are presented as a function of advection time $\tau_{adv} = (R - R_\odot)/V_r$, where R is the mean heliocentric distance of each interval and V_r is the interval averaged radial solar wind speed. τ_{adv} can be considered as a proxy to the "age" of the solar wind plasma because the solar wind speed increases exponentially from corona base to the Alfvén surface. Panel (a) shows the statistics of all of the 20975 intervals. Evidently, $1/f_{mid}$ trends nicely with τ_{adv} and seems to gradually stabilizes around 3-minute for the "youngest" solar wind. However the scatters are spread because the fixed 6 hour long window does not discriminate large scale structures in the solar wind like Heliospheric current sheet (HCS) crossings, Coronal Mass Ejections (CME) or ICME, and magnetic holes. Albeit being intrinsic components of the solar wind, these structures are usually not considered part of the solar wind turbulence. In order to better

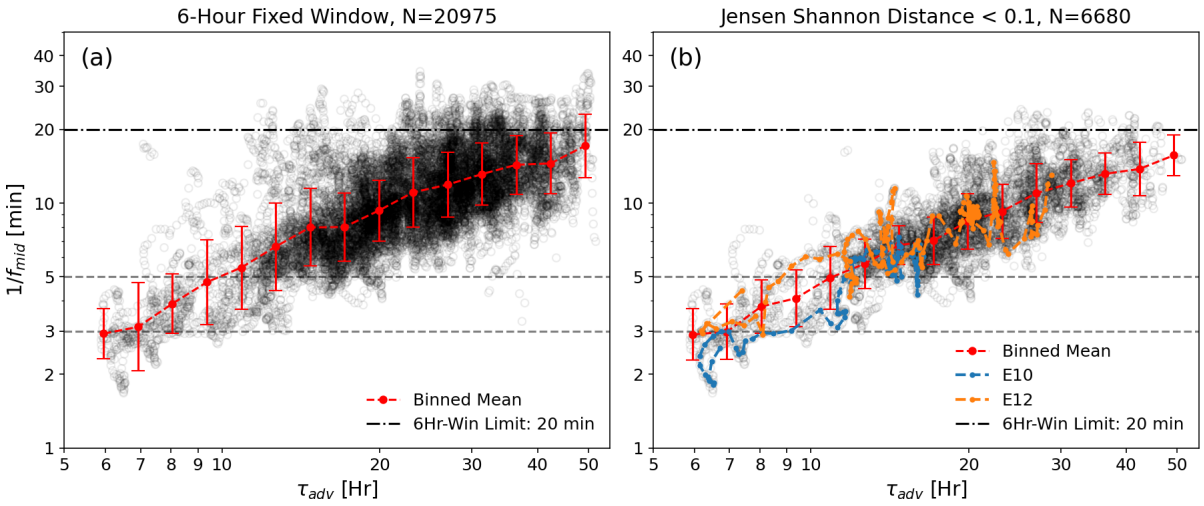

Figure 5.3: (a) Statistics of the center frequency of the fluctuation energy $1/f_{mid}$ of total 20975 intervals with fixed 6-hour window as a function of advection time $\tau_{adv} = (R - R_\odot)/V_r$, where V_r is the interval mean radial solar wind speed and R is the mean heliocentric distance of the interval. The red line is the binned mean of the scatters with errorbars indicating one standard deviation of the points within each bin. The dotted dashed line indicates the upper limit of $1/f_{mid}$ for the 6-hour window size assuming a Kolmogorov $f^{-5/3}$ spectrum. (b) Statistics of the 6680 intervals filtered with Jensen-Shannon Distance of $|B|$ smaller than 0.1, i.e. $|B|$ is highly Gaussian. This criterion filters out intervals with high level of Alfvénicity and indicates coronal hole origin of the streams. The radial evolution within two confirmed coronal holes from inbounds of E10 and E12 are highlighted with the blue and orange lines.

understand the radial evolution of f_{mid} for Alfvénic turbulence, it is beneficial to filter the Alfvénic wind.

In Chapter 4 we discovered a simple connection between the Gaussianity of magnetic magnitude $|B|$ and the coronal hole origin of the wind. High level of Gaussianity in $|B|$ indicates constancy of $|B|$ and hence high level of Alfvénicity. Based upon this simple relation, we select the intervals with highly Gaussian $|B|$ using the Jensen-Shannon Distance threshold of 0.1, and 6680 intervals survived. The statistical results of the filtered intervals are shown in panel (b). The filtered intervals are clearly more concentrated with the majority of the outliers removed (HCS crossing, CME and magnetic holes can significantly destroy the Gaussianity of $|B|$). Similarly, $1/f_{mid}$ stabilizes around 3-minute for the most pristine solar wind, and the binned mean line remains largely consistent. To better understand the radial evolution of $1/f_{mid}$ inside of coronal holes, the intervals

from the two extended time range with confirmed mid-latitude coronal hole origin are highlighted (blue: E10, orange: E12). The points are connected with dashed lines based on their interval averaged heliocentric distance R to indicate the order of measurement. The trend is clear: as τ_{adv} decreases, $1/f_{mid}$ gradually decrease until it saturates at 3-minute and stays around the saturation value even though the helio-radial distance R continue to decrease.

Additionally, τ_{adv} in fact significantly over-estimates the "age" of the Alfvén waves because from the energy perspective the "age" is determined by the integral of the group velocity from corona base to PSP. Adopting a typical Alfvén speed V_A and solar wind speed V_r profile, e.g. Figure 1 in (Verdini et al., 2012), the group velocity in the frame of the static sun $V_g = V_A + V_r$ is almost always larger than $1000km/s$, translating to an "age" smaller than 2.01 hours for an interval measured at 11.4 $R_\odot$. Therefore, the "age" of the Alfvén waves is actually much younger than the τ_{adv} shown in Figure 5.3, especially for the intervals with small τ_{adv} values that are located on the left side of panels (a) and (b) whose Alfvén speed is comparable to solar wind speed. This has two major implications: 1. Future orbits of PSP can at best measure intervals with "age" $\simeq$ 1.72 hours assuming perihelion distance $R = 9.9R_\odot$ and a mean group velocity of $V_g = 1000km/s$; 2. Referring to the evolution of $1/f_{mid}$ in Figure 5.3, a half-hour change in τ_{adv} makes marginal difference in $1/f_{mid}$. Therefore, our results are representative of the measurement limit in terms of PSP orbit design.

Notably, during the perihelion, the perpendicular speed of PSP can reach up to $V_{inertial,\phi} \simeq$ 200km/s in the inertial frame and can reach up to $V_{carr,\phi} \simeq$ 100km/s in the co-rotating frame. The Alfvén waves are guided by the background magnetic field, which is mostly radial around perihelion. For the solar wind plasma measured by PSP around perihelion, typically $|B|$ is quasi-constant ($\delta|B|/|B| \lesssim 0.01$), and plasma β is very small ($\beta < 0.1$). Consequently, in the MHD regime, there is no information carrier in the ϕ direction, and hence the perturbations can be considered causally unrelated. Adopting $V_\phi \simeq$ 100km/s in the co-rotating frame, 3-minute can be translated into 18Mm at $12R_\odot$, and thus 1500km at the corona base assuming a radial expansion of the coronal hole

flux tube. Using a modest super-radial expansion factor of 3 from photosphere to corona base, the physical size can be mapped to 500km at the photosphere, about 1/3 the size of the granule (for V_ϕ in the inertial frame, about 2/3 the size of a granule). Assuming that the perturbation as a function of perpendicular spatial coordinates can be written as power spectrum density with power law dependence $P(k_\phi) \propto k_\phi^{-\alpha}$, and $\alpha > 1$. In this scenario, the wave number spectrum can 'contaminate' the frequency spectrum via doppler shift:

$$2\pi f = k_\phi V_\phi \tag{5.1}$$

Due to the steep power law dependence ($\alpha > 1$), the 'contamination' becomes strongest when V_ϕ reaches its maximum right at the perihelion (for the same f, it corresponds to smaller k, and thus higher energy level). Even though we have no information on the $P(k_\phi)$ at the Alfvén surface, due to the causal independence of the perturbation in the ϕ direction, we can refer to the perpendicular spectrum in the photosphere. Based on Solar Optical Telescope observations (Rieutord et al., 2010), the perpendicular power spectrum density follows $P(k_\perp) \propto k_\perp^{-10/3}$ for the sub-granular scales, and reaches a peak at the Granulation scale of 1700 km. Due to the steepness of the spectrum, one would only expect strong 'contamination' in the frequency spectrum when V_ϕ is large. However, both $V_{inertial,\phi}$ and $V_{carr,\phi}$ changes significantly over a small range of radial distance around the perihelion. This could be the reason why we see a upper trend in $1/f_{mid}$ in Figure C.2(b) as PSP approaches perihelion for both coronal hole intervals from inbounds of E10 and E12. Consequently, the real primary oscillation frequency in upper corona could be closer to 2-minute than 3-minute. Nevertheless, here we decided to present the original statistics for the sake of clearness and reproductivity. For more detailed discussion on the doppler shift, please refer to Appendix C.

In summary, together with case studies and statistical scans, we have provided strong evidence that the magnetic fluctuation energy concentrates around 3-minute for the most pristine solar wind that are measured *in situ* around the Alfvén surface.

5.4 Discussion

5.4.1 The Source of the Alfvén Waves

A well-established physical picture of the source of the Alfvén waves in the corona (Morton et al., 2023) is that the fluctuations originate from the 5-minute p-mode (pressure-mode) in the photosphere where $\beta \gg 1$, i.e. sound speed c_s is much greater than Alfvén speed v_A. Going up into the middle of the chromosphere lies the magnetic canopy, i.e. layer where $c_s = v_A$ ($\beta \sim 1$, introduced by (Rosenthal et al., 2002; Bogdan et al., 2003)), within which linear mode conversion between the two magnetosonic modes is possible. Below the canopy, $c_s > v_A$, the fast mode is sonic (compressive) and isotropic, and hence $\delta\vec{v} \parallel \vec{k}$, where $\delta\vec{v}$ is the velocity perturbation and $\vec{k}$ is the wave vector. On the contrary, the slow mode is magnetic and guided by the background magnetic field $\vec{B}_0$. In addition, due to the high β environment, the motion of the magnetic field lines are largely controlled by the plasma motion. On the other hand, above the canopy where $c_s < v_A$, the slow mode becomes the pure sonic mode but is highly anisotropic, i.e. guided by $\vec{B}_0$, and the fast mode is now magnetic and isotropic. Moreover, due to the low β environment, the plasma is being controlled by the magnetic field. Consequently, mode conversion from the sonic fluctuations below the canopy (fast mode) to magnetic fluctuations above the canopy (fast mode) is possible when the eigen perturbation $\delta\vec{v}$ of both modes are not orthogonal. This linear mode conversion has been shown by numerous simulation studies (Spruit and Bogdan, 1992; Cally and Bogdan, 1997; Cally, 2000; Crouch and Cally, 2003; Bogdan et al., 2003), and has also been shown in Chapter 2 that the mode conversion conserves wave action. Passing through the magnetic canopy, the fast magnetosonic mode will face a steep Alfvén speed profile and hence be refracted. Around the height of the refraction, the fast mode linearly couples with the Alfvén mode and is hence partially converted (Cally and Hansen, 2011; Cally, 2017; Khomenko and Cally, 2019). The mode conversion from p-mode in the photosphere to Alfvén mode in the upper chromosphere and transition region is termed "double mode-conversion" (Khomenko and Cally, 2012) and is expected to allow 30% of the p-mode flux to pass through the

transition region carrying an energy flux of 800 Wm^{-2} in the 3-5 mHz frequency band (3-5 minutes) (Hansen and Cally, 2012). 1D simulation from (Réville et al., 2018) also indicates that for Alfvén wave with 3-minute period, the transmission coefficient through the transition layer is about 50%.

From the corona base to the spacecraft at Alfvén surface, one should be careful about the non-WKB effects of Alfvén wave due to steep Alfvén speed profile, i.e. reflection (Heinemann and Olbert, 1980; Hollweg, 1990; Velli et al., 1991; Velli, 1993). Here we use a Heliosphere model which includes the transition from static atmosphere to propagating solar wind from (Velli et al., 1991):

$$\rho = \rho_0 \frac{\exp\{-\alpha/2 \cdot [1 - (R_\odot/R)]\}}{\{1 + \beta[(R/R_\odot - 1)]\}^2} \tag{5.2}$$

$$V_a = V_{a0} \left(\frac{R_\odot}{R}\right)^2 \left(\frac{\rho_0}{\rho}\right)^{1/2} \tag{5.3}$$

$$U = \frac{U_\infty}{\beta^2} \exp(-\alpha/2) \left(\frac{R}{R_\odot}\right)^2 \left(\frac{V_a}{V_{a0}}\right)^2 \tag{5.4}$$

where V_{a0} is the initial Alfvén speed at the corona base, U_∞ is the asymptotic solar wind speed at infinity, and α and β are free parameters. To find a typical transmission coefficient for the 3-minute ($\simeq$5.5 mHz) wave, we adopt some reasonable values: $\alpha = 0, \beta = 5, V_{a0} = 2000\text{km/s}, U_\infty = 700\text{km/s}$, and this produces a Alfvén surface at a realistic distance of $15.09R_\odot$. Following (Velli, 1993), the transmission coefficient (with respect to the conserved wave action/quantum in the WKB limit) of frequency 5.5 mHz is calculated to be $T(5.5\text{mHz}) \approx 99.8\%$, which is effectively perfect transmission. One can of course play with different α, β, V_{a0} and U_∞, but as long as the parameters are consistent with realistic fast wind conditions, the transmission coefficient for 5.5 mHz wave will be almost always close to 100%, i.e. very close to the ideal WKB range. Thus, as least within 1-D model, the 3-minute Alfvén wave can be safely considered as WKB from the corona base to Alfvén surface. In fact, as been discussed in (Velli, 1993), the existence of the wind can significantly increase the transmission for the low frequency waves, which

are completely reflected otherwise, and the asymptotic transmission coefficient is:

$$T_c = \frac{4V_{A0}V_{Ac}}{(V_{A0} + V_{Ac})^2} \tag{5.5}$$

where V_{A0} is the Alfvén speed at the corona base and V_{Ac} is the Alfvén speed at the Alfvén (critical) surface. Consequently, the steep Alfvén speed profile from corona base to the Alfvén surface can at most insignificantly reflect the injected energy, if not negligibly. For more detailed discussions, please refer to Appendix C.

The concentration of turbulence fluctuation energy around 3-minute at the Alfvén surface and upper corona is therefore particularly interesting because it is not only in favor with the aforementioned Alfvén wave generation mechanisms, but is also compatible with various remote sensing observations made at lower corona (Morton et al., 2016, 2019, 2023), transition region (Tian et al., 2014), and chromosphere (De Pontieu et al., 2007). It is well known from observations that the fluctuations from below the transition region is strong enough to power the fast solar wind (which needs $\gtrsim 100W/m^2$) even assuming a weakest transmission coefficient of 3% at the transition layer (De Pontieu et al., 2007). Previous *in situ* studies of the solar wind turbulence on the energy injection range have predominantly shown that the low-frequency spectral breaks between the inertial range and $1/f$ range lie at very low frequencies ($\lesssim 10^{-3}Hz \sim 3Hr$, see e.g. (Wu et al., 2020, 2021b; Bruno and Carbone, 2013; Bruno et al., 2019; Bavassano et al., 1982; Denskat and Neubauer, 1982; Burlaga and Goldstein, 1984; Tu and Marsch, 1995)), perhaps with only one exception from the single fast solar wind interval from Helios 2 (see Figure 1 in (Wu et al., 2021a) and Figure 29 in (Bruno and Carbone, 2013)) where the low frequency spectral break occurred at around $10^{-2}Hz$. Note that this specific interval measured at 0.29AU has also been previously recognized and analyzed by (Chandran, 2018) from Fig 2-2(c) of (Tu and Marsch, 1995) as a shallow-inertial double power law, and in fact it is a very typical shallow-$1/f$-inertial triple power law. Nevertheless, it should be noted that the $1/f$ range indicates a scale-independent distribution of fluctuation energy, and hence the central frequency of fluctuation energy for that specific interval from Helios 2

is located at a much lower frequency than the spectral break. Therefore, the existence of the shallow ($f^{-\alpha}, \alpha < 1$) and steep ($\alpha > 1$) double power law spectra that were first observed by PSP (Huang et al., 2023c; Davis et al., 2023) provide the first evidence that the Alfvén wave power concentrates around a specific small frequency range. The purpose of this study is to show it is statistically true that in the upper solar corona and around the Alfvén surface, the primary frequency of magnetic fluctuations concentrates around 3-minute, thereby consistent with both numerical modeling and remote sensing observations.

It should be noted, however, that, our results pose yet no preference for either of the two primary coronal heating mechanisms, i.e. AC (waves heating) and DC (reconnection/nano-flare heating) (see e.g. (Hansteen and Leer, 1995; McComas et al., 2007; Velli et al., 2015; Van Doorsselaere et al., 2020; Banerjee et al., 2021)). As has been pointed out by (Parker, 1991), to maintain the million degree solar corona, much of the energy has to be deposited at the first few solar radii above the transition region, which however, has been proven to be difficult for Alfvén waves due to its stability (see e.g. simulation by (Tenerani et al., 2020)). Nevertheless, our study can serve as an example for future studies to constrain the coronal heating mechanisms using *in situ* observations from PSP.

5.4.2 $1/f$ Range, Turbulence Cascade and Dissipation

Figure 5.3 also illustrates an active turbulence cascade and dissipation. From both panels we see clear trends that f_{mid} moves to much lower frequency as the advection time increases (or as the solar wind grows "older"). However, the trend of f_{mid} with regard to τ_{adv} should be interpreted with caution because it results from the combination of multiple processes: 1. The energy containing $1/f$ range is being dynamically created as the radial distance of PSP increases (Huang et al., 2023c; Davis et al., 2023); 2. The active turbulence cascade and dissipation "eat-up" the energy containing range and move the low frequency spectral break between $1/f$ and inertial to low frequency (see models e.g.

(Tu and Marsch, 1993, 1995) and observations (Bruno and Carbone, 2013; Chen et al., 2020; Wu et al., 2021a; Sioulas et al., 2022)); 3. Our method of compiling f_{mid} using the normalized integrated energy curve can only capture the location of low frequency break when the spectrum has a clear shallow-inertial double power law (e.g. the four spectra in Figure 5.2). However it can not capture of the location of the low frequency spectral break when the spectrum becomes a triple power law (shallow-$1/f$-inertial) or the classical double power law ($1/f$-inertial), and it will instead produce a value with slightly lower frequency. All of the aforementioned caveats will be obvious when one views a video of Figure 5.1 produced using a sliding window (see supplementary video (`https://www.youtube.com/watch?v=snnLKmt-qhA`)).

The supplementary video therefore provide some evidence that the energy containing $1/f$ range is dynamically created after the solar wind leave the Alfvén surface and the fluctuation energy subsequently "spread-out" from its concentration around 3-minute, creating a triple power law (shallow-$1/f$-inertial). This phenomenon has been predicted based on a turbulence model (Chandran, 2018) and been found in a turbulence simulation (Meyrand et al., 2023). However, detailed discussion of the formation mechanism of $1/f$ range lies beyond the scope of this study and it is a topic of active debates (see e.g. (Keshner, 1982; Montroll and Shlesinger, 1982; Bak et al., 1987; Velli et al., 1989; Matthaeus and Goldstein, 1986; Matthaeus et al., 2007; Bemporad et al., 2008; Dmitruk et al., 2011; Verdini et al., 2012; Matteini et al., 2018; Chandran, 2018; Magyar and Doorsselaere, 2022; Meyrand et al., 2023)).

For completeness, here we provide an order of magnitude estimate of solar wind heating rate from our statistical results shown in Figure 5.3(a) using the equation (C.25). We may assume that the low frequency spectrum scales like $1/f$ and the inertial range scales like $f^{-5/3}$ or $f^{-3/2}$ and hence $\alpha_0 = 1$ and $\alpha_1 = 5/3$. Adopting a typical spectrum intensity at the spectral break to be $C_0 f_c^{-\alpha_0} = (10^{-5}\ \mathrm{nT^2 \cdot Hz^{-1}})/\mu_0$, and the near sun change of f_c from panel (a) to be $df_c/dt = (1/3\mathrm{min} - 1/6\mathrm{min})/(12\mathrm{Hr} - 7\mathrm{Hr})$, finally the solar wind heating rate is estimated to be: $-\epsilon(t) \simeq 1.23 \times 10^{-14}\mathrm{W \cdot m^{-3}}$. This value is consistent with the results from (Wu et al., 2020).

5.5 Summary and Conclusion

In this study, we conducted a systematic survey of the solar wind magnetic fluctuations for the first 17 perihelia of PSP. Our results have shown that as PSP gets closer to the Alfvén surface, the turbulence power spectrum density (PSD) is often characterized by a shallow-inertial double power law: in the energy injection range, the spectrum is shallower than $1/f$, and in the inertial range, the spectrum is steeper than $1/f$. Consequently, the energy concentrates around the "bend" (low frequency power spectral break). This phenomenon differs significantly from traditional solar wind turbulence models, and shows strong indication that close to the sun (around the Alfvén surface), there exists a primary frequency for the magnetic fluctuations in the solar wind.

Our thorough scan of the data has shown that the primary frequency (or the center frequency of fluctuation power, f_{mid}) trends almost perfectly with advection time $\tau_{adv} = (R - R_\odot)/V_r$, where R is the heliocentric distance and V_r is the radial solar wind speed, and it stablizes at around 3-minute for the "youngest" solar wind streams, compatible with the famous chromospheric 3-minute oscillations, which is considered to be driven by the photosphere 5 minute p-mode oscillations. Therefore, our results provide a strong evidence that the fluctuations in the solar wind (whose primary physical carriers are the magnetic switchbacks, i.e. large amplitude spherically polarized outward propagating Alfvén waves) are sourced from the lower solar atmosphere, possibly ultimately driven by the resonance chamber on the sun.

Parker Solar Probe will enter its final orbits with perihelion at 9.9 $R_\odot$ in December 2024 amid the climax of solar cycle 25, and hence can potentially observe Alfvénic solar wind with $\tau_{adv} \lesssim 4Hr$ (assuming $R - R_\odot = 8.9R_\odot$ and $V_r \simeq 450km/s$). The future measurements may provide stronger evidence that $1/f_{mid}$ actually stablizes at 3-minute or prove otherwise. Nevertheless, one should be reminded that $\tau_{adv} \simeq 6Hr$ is already extremely "young" for Alfvénic solar wind originated from coronal holes. Our results therefore serve as the first *in situ* evidence that there exists an energy concentration of magnetic fluctuations close to 3-minute frequency at around the Alfvén surface and in

the upper solar corona.

Case List

Here we provide a list of cases where the trace magnetic PSD can be characterized by a clear shallow double power law and the center frequency of fluctuation energy $1/f_{mid} \simeq$ 3-minute. The "$1/f_{min}$" column indicates the minimum frequency in minutes considered trustworthy for each PSD, i.e. the right edge of the grey area in Figure 5.1(b). The "$\Delta\phi$" column lists the minimum and maximum angular velocity for each intervals times the "$1/f_{min}$", indicating the possible value range of Carrington longitude change for the lowest frequencies. The M_A column shows the interval averaged Alfvén mach number ($M_A = V_r/V_A$), where $M_A > 1$ indicates that PSP is in the solar wind and $M_A < 1$ indicates that PSP is inside of the solar corona. The "$1/f_{mid}$" column shows the middle frequency of the magnetic fluctuation energy defined in the main text.

#	Enc	Start	Size	$1/f_{min}$[min]	$\Delta\phi$[deg]	V_r[km/s]	$R[R_\odot]$	τ_{adv}[Hr]	M_A	$1/f_{mid}$[s]
1	10	2021-11-19 20:00	07:15	82.8	(0.80, 1.26)	541.58	22.00	7.55	1.54	186
2	10	2021-11-20 03:45	03:15	36.9	(0.58, 0.70)	545.93	19.82	6.74	1.44	148
3	10	2021-11-20 06:30	07:30	86.0	(1.59, 2.41)	537.39	18.06	6.20	1.37	144
4	10	2021-11-20 12:45	07:45	89.4	(2.35, 3.42)	460.93	15.97	6.34	1.20	136
5	10	2021-11-21 05:00	06:00	68.3	(3.39, 3.48)	421.17	13.30	5.75	1.05	161
6	11	2022-02-25 15:30	04:45	54.2	(2.64, 2.76)	378.80	13.36	6.45	0.79	161
7	11	2022-02-26 03:15	03:15	36.9	(1.24, 1.43)	371.27	15.25	7.64	1.04	132
8	12	2022-06-01 05:45	04:00	45.6	(1.37, 1.66)	344.98	15.75	8.31	0.60	161
9	12	2022-06-01 12:30	05:00	57.4	(2.35, 2.74)	418.20	14.02	6.08	0.87	161
10	13	2022-09-05 03:45	03:30	39.8	(0.72, 0.88)	442.01	18.90	7.91	1.30	157
11	13	2022-09-05 09:15	06:30	73.7	(1.82, 2.54)	410.37	16.51	7.36	0.93	148
12	13	2022-09-05 14:00	03:15	36.9	(1.17, 1.36)	368.76	15.57	7.70	0.97	128
13	14	2022-12-11 23:15	03:15	36.9	(1.34, 1.53)	362.07	14.82	7.45	0.85	144
14	15	2023-03-17 13:30	04:00	45.6	(2.09, 2.27)	427.18	13.59	5.74	0.98	136
15	15	2023-03-17 15:45	03:15	36.9	(1.78, 1.87)	411.73	13.41	5.93	0.94	124
16	15	2023-03-17 23:30	03:30	39.8	(1.86, 1.99)	403.94	13.56	6.21	0.90	152
17	15	2023-03-18 02:15	03:30	39.8	(1.70, 1.89)	337.81	13.96	7.48	0.86	144
18	16	2023-06-21 10:00	03:15	36.9	(1.07, 1.26)	241.82	16.07	12.29	1.19	144
19	16	2023-06-21 16:00	04:30	51.1	(1.97, 2.32)	281.35	14.34	9.28	1.02	161
20	17	2023-09-27 14:30	03:15	36.9	(1.91, 2.20)	352.44	12.31	6.33	0.92	114

Table 5.1: List of shallow-inertial double power law intervals

CHAPTER 6

Summary and Implications

In this dissertation, we first explored in Chapter 2 the linear propagation problem of the MHD waves in expanding medium. Albeit being a classical problem, we found a surprising phenomenon that as the magnetosonic waves pass the equi-partition layer ($c_s = v_A$), the wave action of a single wave mode is not conserved. Through simulations, we eventually understood that this is due to the linear mode conversion between the two magnetosonic modes as a result of the mode degeneracy at the layer. This problem was *a posteriori* realized to be trivial since it is a simple linear conversion between wave modes and hence the total 'number' of quanta is by definition conserved, and this process is also well-studied as part of the double mode conversion mechanism happening around the magnetic canopy. Nevertheless, this study serves as a good foundation for the understanding of the source of Alfvén waves in the solar atmosphere.

Parker Solar Probe was launched in November 2018. For the first few years (2018-2021) of the mission, the activity of solar cycle 25 remained relatively low, and hence the *in situ* measurements from PSP for the first 9 encounters were primarily solar wind originated from the edge of the polar coronal holes or the traditional slow wind from the Helmet streamer. However, solar activities began to build up starting from E10 (November-2021), and for the first time, we were able to capture solar wind that is directly sourced from low-latitude coronal holes right at the Alfvén critical surface. This provides an invaluable chance to both discover new phenomena and finding new constraints for existing theories. Indeed, new data from new environment using cutting-edge instruments can always bring surprising and exciting scientific results.

In Chapter 3, we found for the first time that close to the sun, contrary to the

traditional solar wind turbulence model where the spectrum has a $1/f$-inertial double power law in the energy injection and inertial range, the low frequency turbulence spectra are dominated by a 'shallower' scaling close to $f^{-0.5}$, violating the 'energy containing' picture of the famous $1/f$ range.

In Chapter 4, adopting a data mining approach, we found that the magnetic magnitude B follows perfect helio-radial power laws around the perihelion and the fit index significantly deviates from the expected value of spherical expansion. Even more surprisingly, we found that the helio-radial normalized magnetic magnitude B^* has a perfect Gaussian distribution when the spacecraft is inside of a coronal hole. Exploiting this idea, we invented a novel visualization method named 'Gaussianity Scalogram', and revealed numerous interesting structures in the solar wind, including coronal holes, switchback patches, and ubiquitous minutes-long Gaussian structures.

In Chapter 5, following the work in Chapter 3, we realized that the shallow-inertial double power law is a manifestation of the concentration of fluctuation energy around the 'bend'. Consequently, we exploited this characteristic and showed that the fluctuation energy concentrates around 3 minutes as PSP dives into the Alfvén critical surface, i.e. upper corona. For the first time, we are able to provide *in situ* evidence in the upper corona that the local fluctuation frequency is consistent with the famous chromosphere 3-minute oscillations.

These new observational results lead to a much clear picture for the evolution of Alfvén waves and turbulence in the solar wind (originated from coronal holes): The primary source of the fluctuation energy are the photosphere granulations. The fluctuations are then trapped within the resonance chamber bounded by the tachocline and the photosphere, resulting in a legion of resonant modes with frequencies concentrated around 5 minutes. The 5-minute p-mode fluctuations are then leaked into chromosphere. Due to the steep density profile, only waves with frequency above the acoustic cut-off frequency ($P \approx 180s$) are allowed to penetrate. Consequently, the primary fluctuation period in the chromosphere is observed to be 3 minutes. Going higher into the chromosphere, the rapid drop in density leads to a gradual dominance of the magnetic field. Therefore, in

the middle of the chromosphere lies the boundary separating the thermally and magnetically dominant plasma, i.e. the magnetic canopy ($c_s = v_A$ or $\beta \simeq 1$). Due to the mode degeneracy at the canopy, the acoustic fast mode from below can linearly convert to the magnetic fast mode above the canopy. The magnetic fast mode will then propagate upwards and again transfer a significant portion of energy to Alfvén mode through linear coupling, finishing the double mode conversion. Due to the low-β environment, the open field lines in magnetic flux tube then act as a wave guide for the Alfvén waves, which will heat and accelerate the coronal plasma into solar wind. The heating is primarily achieved with plasma turbulence which cascade fluctuation energy from large scales (low frequencies) and dissipate them into heat in small scales (high frequencies). The acceleration, on the other hand, is achieved mainly through the wave pressure of the Alfvén waves. From observations, we now know *a posteriori* that the short propagation time from corona base to the Alfvén surface ($\sim$ 2 Hours) might not be enough for nonlinear effects (turbulence cascade and wave-wave interactions) to modify the turbulence frequency spectrum to a substantial degree. Consequently, it is highly likely that the propagation of Alfvén waves from the corona base to the Alfvén surface can be regarded as WKB from the energy perspective. Passing the Alfvén critical surface, the coronal plasma becomes super-Alfvénic solar wind, and the nonlinear effects start to make substantial modification to the Alfvén waves (turbulence) spectrum. For one thing, wave-wave interactions (likely parametric decay instability (PDI)) will induce inverse cascade of the otherwise concentrated Alfvén waves, and gradually create a evenly distributed, energy containing $1/f$ spectrum in low frequencies. Additionally, the turbulence cascade will transfer energy from low frequencies (large scales) to high frequencies (small scales), and eventually dissipate the energy via wave-particle interactions (likely ion-cyclotron resonance). The cascade and dissipation can consume energy from the $1/f$ energy reservoir and hence gradually move the low frequency spectral break to lower frequencies.

These novel observations presented in this dissertation will lay the groundwork for several intriguing open questions. Here, we list three prospective projects that build upon the work completed in this dissertation:

In Chapter 4, we have shown that Gaussian distribution is the natural relaxation state for small amplitude Alfvénic turbulence. The relaxation from non-Gaussian to Gaussian is extremely rapid, which happens within one Alfvén crossing time. This newly discovered MHD turbulence phenomenon is thus of great interest to plasma physics itself. For one thing, the Alfvén waves are guided by the background field $\vec{B}_0$ in the simulation. Therefore, it remains unclear whether Alfvén waves are the main driver in the Gaussianization process or the induced magnetosonic modes are more dominant. Furthermore, the detailed mechanism of the Gaussianization is also unresolved. The linear propagation of Alfvén waves is not capable of modifying the distribution of B, and hence the Gaussianization is achieved with nonlinearity. In future work, we plan investigate in detail how and under what conditions the Gaussianization of B can happen in MHD turbulence, using different plasma parameters and simulation box shapes.

In Chapter 3 and Chapter 5, we have provided strong evidence that the energy containing $1/f$ range is formed dynamically around the Alfvén surface, and is possibly the result of PDI. Nevertheless, the $1/f$ range deserves a series of more dedicated studies to differentiate the handful of formation mechanisms proposed in the past four decades. Additionally, the origin of the low frequency shallow scaling $\sim f^{-0.5}$ remains unclear. Even though it is tempting to apply the $T \propto f$ tunneling transmission profile to the MHD inertial scaling of $f^{-1.5}$, this approach is surely problematic: The primary energy source of the Alfvén waves is likely the 5-minute p-mode oscillations, making it improbable that the fluctuation energy in Alfvénic turbulence is injected at $\sim 10^{-4}$ Hz. Moreover, even if the Alfvén waves were launched with a developed spectrum starting at 10^{-4} Hz, the accurate transmission values compiled from realistic Alfvén speed profile such as Figure 1.10 will nevertheless produce a filtered spectrum which is inconsistent with the $f^{-0.5}$ scaling. This is because the limited number of v_A scale heights from the canopy to the transition region. Consequently, future works are necessary to understand the origin of the low frequency shallow scaling up to 10^{-4} Hz. More specifically, to investigate whether the $f^{-0.5}$ scaling is the result of unknown filtering effects from the photosphere to the chromosphere using remote-sensing frequency spectrum from space-borne instruments

such as VIRGO experiment on board of Solar and Heliospheric Observatory (SOHO) spacecraft (Andersen, 1991).

Of course, the most exciting prospective work remains: determining, through our observations in Chapter 5, whether we can establish constraints on the two major flavors of coronal heating mechanisms: wave heating (AC) and reconnection heating (DC). Now we have shown that the primary fluctuation mode in the coronal open flux tubes might be the 3-minute oscillations driven by their lower boundaries. The primary question now becomes that whether the observed fluctuations at the Alfvén surface, once mapped back to the corona base assuming WKB, are enough to maintain the million degree corona. The future orbits of PSP will likely provide more abundant evidence on this question. In addition, our sun is ultimately an ordinary star in the universe. It is hence of great interest to explore whether PSP, as a heliophysics mission, can cross-fertilize stellar physics, especially the physics of stellar chromosphere and corona.

In summary, the work completed in this dissertation was primarily inspired by the exciting new observations made by PSP in the previously unexplored regions of the solar corona and heliosphere. We believe that these captivating novel phenomena will open up several intriguing avenues for future studies.

APPENDIX A

Magnetohydrodynamics Waves

A.1 Linear Eigenmodes

The ideal-MHD equation set with adiabatic closure is:

$$\frac{\partial \rho}{\partial t} + \nabla \cdot (\rho \vec{u}) = 0 \tag{A.1}$$

$$\rho \left(\frac{\partial \vec{u}}{\partial t} + \vec{u} \cdot \nabla \vec{u} \right) = -\nabla p + \frac{1}{\mu_0} (\nabla \times \vec{B}) \times \vec{B} \tag{A.2}$$

$$\frac{\partial \vec{B}}{\partial t} = \nabla \times (\vec{u} \times \vec{B}) \tag{A.3}$$

$$\nabla \cdot \vec{B} = 0 \tag{A.4}$$

$$\frac{d}{dt}(p\rho^{-\gamma}) = 0 \tag{A.5}$$

where γ is the adiabatic gas constant.

The linearized MHD equations read, assuming fluctuations of the type $\exp\left(i\left(\vec{k}\cdot\vec{x} - \omega \cdot t\right)\right)$:

$$-\omega\rho_1 + \rho_0 \left(\vec{k} \cdot \vec{u}_1\right) = 0 \tag{A.6}$$

$$-\omega\vec{B}_1 + \vec{B}_0 \left(\vec{k} \cdot \vec{u}_1\right) = \left(\vec{B}_0 \cdot \vec{k}\right) \vec{u}_1 \tag{A.7}$$

$$-\omega\vec{u}_1 = -c_s^2 \vec{k} \frac{\rho_1}{\rho_0} - \frac{1}{\mu_0 \rho_0} \cdot \left(\vec{k}\left(\vec{B}_0 \cdot \vec{B}_1\right) - \left(\vec{k} \cdot \vec{B}_0\right)\vec{B}_1\right) \tag{A.8}$$

We solve for $\vec{u}_1$ and get

$$\left[\left(C^2 - \mu^2 v_A^2\right)\underline{\underline{1}} - \left(c_s^2 + v_A^2\right)\hat{k}\hat{k} + \mu v_A^2 \left(\hat{b}\hat{k} + \hat{k}\hat{b}\right)\right] \cdot \vec{u}_1 = \underline{\underline{M}} \cdot \vec{u}_1 = 0 \tag{A.9}$$

with $C = \frac{\omega}{k}$, $\hat{k} = \frac{\vec{k}}{k}$, $\hat{b} = \frac{\vec{B}_0}{B_0}$, $\mu = \hat{k} \cdot \hat{b}$, $v_A = \frac{B_0}{\sqrt{\mu_0 \rho_0}}$, $c_s^2 = \left(\frac{\partial p}{\partial \rho}\right)_s$. An important property of the matrix $\underline{\underline{M}}$ is, that it is invariant against the replacements $\hat{k} \to -\hat{k}$ or $\hat{b} \to -\hat{b}$. By introducing an orthogonal system

$$\underline{e}_z = \hat{k} \tag{A.10}$$

$$\underline{e}_x = \hat{k} \times \hat{b} / \sqrt{1 - \mu^2} \tag{A.11}$$

$$\underline{e}_y = \left(\mu \hat{k} - \hat{b}\right) / \sqrt{1 - \mu^2} \tag{A.12}$$

we arrive at

$$\underline{\underline{M}} = \left(C^2 - C_A^2\right) \underline{e}_x \underline{e}_x + \underline{\underline{A}} \tag{A.13}$$

with $C_A^2 = \mu^2 v_A^2$ and

$$\underline{\underline{A}} = \underbrace{\left(C^2 - \mu^2 v_A^2\right)}_{A} \underline{e}_y \underline{e}_y + \underbrace{\left[\left(C^2 + \mu^2 v_A^2\right) - \left(c_s^2 + v_A^2\right)\right]}_{B} \underline{e}_z \underline{e}_z \underbrace{-\mu v_A^2 \sqrt{1 - \mu^2}}_{\tilde{C}} \left(\underline{e}_y \underline{e}_z + \underline{e}_z \underline{e}_y\right) \tag{A.14}$$

In order to get non-vanishing eigenvectors for $\vec{u}_1$, the determinante of $\underline{\underline{M}}$ must vanish. This implies $\det \underline{\underline{A}} = 0$, which leads to

$$C_{f,s}^2 = \frac{c_s^2 + v_A^2}{2} \pm \sqrt{\left(\frac{c_s^2 + v_A^2}{2}\right)^2 - \mu^2 c_s^2 v_A^2} \tag{A.15}$$

as phase-velocities for a fast (f) or a slow (s) magnetosonic wave. Their polarisation-vectors $\underline{e}_f$ and $\underline{e}_s$ are eigenvectors of the symmetric matrix $\underline{\underline{A}}$. We can get them by a simple rotation of the angle β:

$$\left.\begin{aligned} \underline{e}_y &= \cos\beta \underline{e}_s + \sin\beta \underline{e}_f \\ \underline{e}_z &= -\sin\beta \underline{e}_s + \cos\beta \underline{e}_f \end{aligned}\right\} \Leftrightarrow \left\{\begin{aligned} \underline{e}_s &= \cos\beta \underline{e}_y - \sin\beta \underline{e}_z \\ \underline{e}_f &= \sin\beta \underline{e}_y + \cos\beta \underline{e}_z \end{aligned}\right. \tag{A.16}$$

By insertion we get

$$\begin{aligned}\underline{\underline{A}} = &\underbrace{\left(A \cdot \cos^2\beta + B \cdot \sin^2\beta - \tilde{C}\sin 2\beta\right)}_{X} \underline{e}_s\underline{e}_s + \\ &+ \underbrace{\left(A \cdot \sin^2\beta + B \cdot \cos^2\beta + \tilde{C} \cdot \sin 2\beta\right)}_{Y} \underline{e}_f\underline{e}_f + \\ &+ \left[\frac{1}{2}(A-B)\sin 2\beta + \tilde{C}\cos 2\beta\right]\left(\underline{e}_s\underline{e}_f + \underline{e}_f\underline{e}_s\right) \end{aligned} \tag{A.17}$$

This is a diagonal matrix for $\sin 2\beta = \frac{-\tilde{C}}{\sqrt{\frac{1}{4}(B-A)^2+\tilde{C}^2}}$ and $\cos 2\beta = \frac{\frac{1}{2}(A-B)}{\sqrt{\frac{1}{4}(B-A)^2+\tilde{C}^2}}$. This choice guarantees that β is positive for a positive μ. By applying the formulaes $\cos^2\beta = \frac{1}{2}(1+\cos 2\beta)$ and $\sin^2\beta = 1-\cos^2\beta$, we get $\mid \cos\beta \mid = \sqrt{\frac{C_f^2-C_A^2}{C_f^2-C_s^2}}$, $\mid \sin\beta \mid = \sqrt{\frac{C_A^2-C_s^2}{C_f^2-C_s^2}}$, $X = C^2 - C_s^2$ and $Y = C^2 - C_f^2$. When 2β ranges from 0 to 2π, β ranges from 0 to π. Therefore, $\sin\beta$ is ever positive. If 2β reaches π, $\sin 2\beta$ turns negative and β reaches $\frac{\pi}{2}$, so that $\cos\beta$ also turns negative. So, the sign of $\cos\beta$ is the same as the sign of $\sin 2\beta = \text{sign}(\mu)$. $\Rightarrow$ $\sin\beta = \sqrt{\frac{C_A^2-C_s^2}{C_f^2-C_s^2}}$, $\cos\beta = \text{sign}(\mu)\cdot\sqrt{\frac{C_f^2-C_A^2}{C_f^2-C_s^2}}$. It follows that β jumps from 0^0 to π when μ changes sign. So, there is a 180^0-turn of $\underline{e}_s$ and $\underline{e}_f$ at $\mu = 0$. Therefore, we get $\vec{u}_1 = u_1 \cdot \text{sign}(\mu)\underline{e}_{s/f}$ and $\vec{u}_1 = u_1 \cdot \underline{e}_A$ with $\underline{e}_A = \underline{e}_x$ for slow and fast magnetosonic waves and for Alfvén-waves. Now, let $\hat{b} = (\cos\delta, \sin\delta)$, $\hat{k} = (\cos\alpha, \sin\alpha)$. By expressing everything in this coordinate-system, which is the coordinate-system of

the expanding box, $u_1 = u_0 \cdot \cos(x')$ and x' a coordinate along $\hat{k}$, we arrive at

$$\left\{ \begin{array}{c} u_{1x,slow} \\ u_{1x,fast} \end{array} \right\} = u_0 \cdot \cos(x') \cdot \left[\left\{ \begin{array}{c} \cos\beta \\ \sin\beta \end{array} \right\} (-\sin\alpha) \cdot \mathrm{sign}\left[\sin(\alpha-\delta)\right] + \right.$$
$$\left. + \left\{ \begin{array}{c} -\sin\beta \\ \cos\beta \end{array} \right\} \cdot \cos\alpha \right] \tag{A.18}$$

$$\left\{ \begin{array}{c} u_{1y,slow} \\ u_{1y,fast} \end{array} \right\} = u_0 \cdot \cos(x') \cdot \left[\left\{ \begin{array}{c} \cos\beta \\ \sin\beta \end{array} \right\} \cdot \cos\alpha \cdot \mathrm{sign}\left[\sin(\alpha-\delta)\right] + \right.$$
$$\left. + \left\{ \begin{array}{c} -\sin\beta \\ \cos\beta \end{array} \right\} \cdot \sin\alpha \right] \tag{A.19}$$

$$\left\{ \begin{array}{c} B_{1x,slow} \\ B_{1x,fast} \end{array} \right\} = \left\{ \begin{array}{c} \frac{1}{C_s} \\ \frac{1}{C_f} \end{array} \right\} (-1) B_{mod} u_0 \cos(x') \left(\sqrt{1-\mu^2} \left\{ \begin{array}{c} -\sin\beta \\ \cos\beta \end{array} \right\} + \right.$$
$$\left. + \mu \left\{ \begin{array}{c} \cos\beta \\ \sin\beta \end{array} \right\} \right) \cdot (-\sin\alpha) \cdot \mathrm{sign}\left[\sin(\alpha-\delta)\right] \tag{A.20}$$

$$\left\{ \begin{array}{c} B_{1y,slow} \\ B_{1y,fast} \end{array} \right\} = \left\{ \begin{array}{c} \frac{1}{C_s} \\ \frac{1}{C_f} \end{array} \right\} (-1) B_{mod} u_0 \cos(x') \left(\sqrt{1-\mu^2} \left\{ \begin{array}{c} -\sin\beta \\ \cos\beta \end{array} \right\} + \right.$$
$$\left. + \mu \left\{ \begin{array}{c} \cos\beta \\ \sin\beta \end{array} \right\} \right) \cdot \cos\alpha \cdot \mathrm{sign}\left[\sin(\alpha-\delta)\right] \tag{A.21}$$

$$\left\{ \begin{array}{c} \rho_{1,slow} \\ \rho_{1,fast} \end{array} \right\} = \left\{ \begin{array}{c} \frac{1}{C_s} \\ \frac{1}{C_f} \end{array} \right\} \cdot \rho_0 \cdot u_0 \cdot \cos(x') \cdot \left\{ \begin{array}{c} -\sin\beta \\ \cos\beta \end{array} \right\} + \rho_0 \tag{A.22}$$

$$u_{1z,Alfvén} = u_0 \cdot \cos(x') \tag{A.23}$$

$$B_{1z,Alfvén} = -\sqrt{\mu_0 \rho_0} \cdot u_{1z,Alfvén} \tag{A.24}$$

for slow and fast magnetosonic waves and for the Alfvén waves, if we restrict ourselves to $\mu \geq 0$ in order to avoid the discontinuity in the formulae. If $\mu < 0$ then it is $-\pi \leq \alpha - \delta < -\frac{\pi}{2}$ or $\frac{\pi}{2} < \alpha - \delta \leq \pi$ and because of $\vec{u}_1(-\vec{k}) = \vec{u}_1(\vec{k})$, $\vec{B}_1(-\vec{k}) = -\vec{B}_1(\vec{k})$, $(\rho_1 - \rho_0)(-\vec{k}) = -(\rho_1 - \rho_0)(\vec{k})$ according to (A.6) ff, we can apply (A.18) ff for $\alpha + \pi$ or $\alpha - \pi$ and replacing $C_{s,f}$ by $-C_{s,f}$ in (A.18) ff. For the Alfvén-waves we have to change

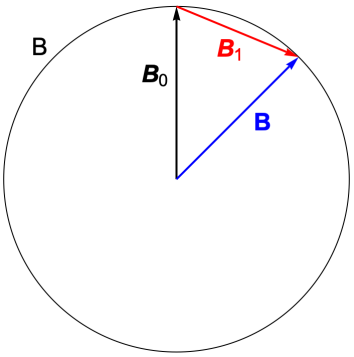

Figure A.1: Spherical Polarization of Alfvén waves

$B_{1z,Alfvén} = +\sqrt{\mu_0 \rho_0} \cdot u_{1z,Alfvén}$.

A.2 Spherical Polarization of Large Amplitude Alfvén Waves

Although the spherical (arc) polarization of observed Alfvén waves is well-known (Del Zanna, 2001; Riley et al., 1996; Vasquez and Hollweg, 1996; Tsurutani et al., 1994; Wang et al., 2012; Erofeev, 2019; Johnston et al., 2022; Hollweg, 1974; Squire and Mallet, 2022), we provide here a description here for spherically polarized Alfvén waves in a magnetically dominated plasma (plasma $\beta = 2\mu_0 P/B^2 \lesssim 0.1$, typical for Alfvénic solar wind measured by PSP around perihelion (Kasper et al., 2021)). Similar to (Matteini et al., 2014), this consider the background magnetic field $\vec{B}_0$ to have the same constant magnetic magnitude B, differently from (Hollweg, 1974) where $\vec{B}_0$ is calculated as the spatial average $\langle \vec{B} \rangle$, yielding a smaller field magnitude than the radius of the sphere B.

For a fluctuation-free magnetic flux tube originating from a coronal hole, the magnetic field is pointing mostly radially in the high corona and solar wind close to the sun. The spherically polarized Alfvén waves can therefore be considered as a perturbation to this otherwise quiet system. To maintain the constant B state observed in the solar wind, the additive magnetic perturbation has to "switchback" on top of the radial background field. This scenario is depicted in Figure 4 in (Matteini et al., 2014). The constant magnetic magnitude B is shown as the radius of the circle and the static radial field from coronal hole is $\boldsymbol{B}_0$. To maintain the constant B state, the perturbation to the system $\boldsymbol{B}_1$

is restricted to the semi-circle, and the resultant magnetic vector $\boldsymbol{B} = \boldsymbol{B}_0 + \boldsymbol{B}_1$ can thus fluctuate on a constant sphere of B. Following this setup, the magnetically dominant ($p \ll B^2/2\mu_0$) incompressible MHD equations can be rewritten as follows ($\rho = const$, $p = const$, $B^2 = const$, $\vec{B} = \vec{B}_0 + \vec{B}_1$):

$$\frac{\partial \vec{u}}{\partial t} = \vec{b} \cdot \nabla \vec{b} - \vec{u} \cdot \nabla \vec{u} \tag{A.25}$$

$$\frac{\partial \vec{b}}{\partial t} = \vec{b} \cdot \nabla \vec{u} - \vec{u} \cdot \nabla \vec{b} \tag{A.26}$$

where $\vec{b} = \vec{B}/\sqrt{\mu_0 \rho} = \vec{B}_0/\sqrt{\mu_0 \rho} + \vec{B}_1/\sqrt{\mu_0 \rho} = \vec{b}_0 + \vec{b}_1$. Assuming the frame is co-moving with the bulk flow and the perturbations are Alfvénic, i.e. $\vec{u} = \vec{u}_1$ and $\vec{u}_1 = \pm \vec{b}_1$, the equations can be further reduced into a wave equation:

$$\frac{\partial^2 \vec{b}_1}{\partial t^2} = (\vec{v}_a \cdot \nabla)^2 \vec{b}_1 \tag{A.27}$$

where $\vec{v}_a = \vec{b}_0 = \vec{B}_0/\sqrt{\mu_0 \rho}$. This equation is identical to the circularly polarized Alfvén wave equation, except that $\vec{B}_1$ can be large but restricted to the sphere defined by B_0 and the Alfvén phase velocity $\vec{v}_a$ is precisely defined (not defined with time-averaged field).

This model leads to some important implications: 1. The spherically polarized Alfvén wave is an exact solution and is mathematically identical to the small amplitude shear Alfvén mode; 2. If a radial jet is present in the system, i.e. $\vec{u}_{1r} \parallel \vec{B}_0$, in accordance with the observed "switchbacks", the spherically polarized Alfvén waves can only be outward-propagating. This is because to maintain the constant B state, the only possible polarization is $\vec{u}_1 = -\vec{B}_1/\sqrt{\mu_0 \rho}$; 3. There exists a well-defined background field $\vec{B}_0$ for the constant B state, and hence the constant magnetic magnitude B can be regarded as a good proxy for the local $\vec{B}_0$, i.e. the local magnetic flux density.

In fact, the reversal of the magnetic field line (switchback) does not increase the number of field lines (thus field line density) and the Alfvén wave, being a solenoidal mode, does not change the local magnetic flux density. This establishes a connection between the magnetic magnitude (magnetic field line density) and the local magnetic

flux density within the magnetically dominated coronal holes close to the sun. The helio-radial normalization of B in the main text can therefore be regarded as mapping the magnetic flux density measured at different radial distances and longitudinal locations back to a cross section of the magnetic flux tube originating from the coronal hole.

APPENDIX B

Clarifications on Gaussianity Scalogram

B.1 Jensen-Shannon Distance, Gaussianity scalogram and Benchmark

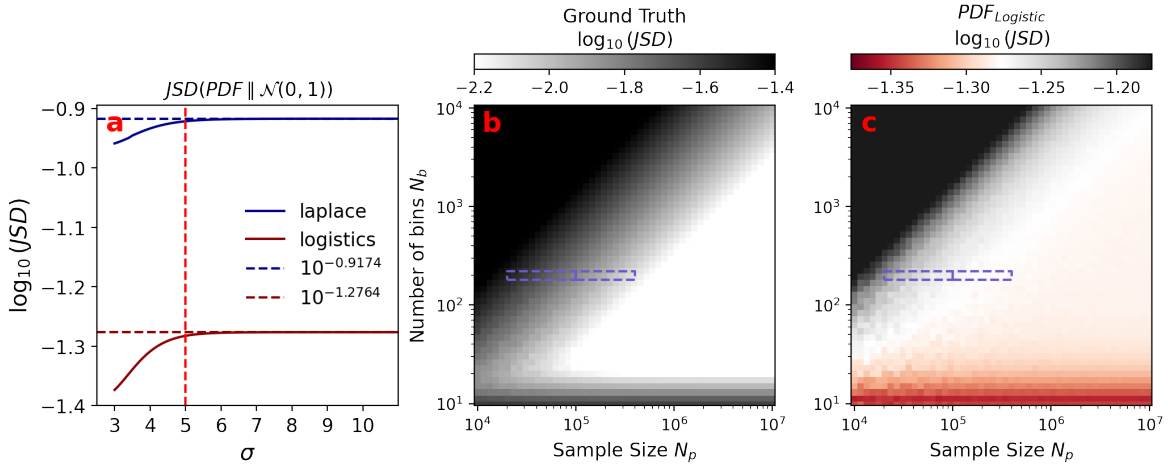

Figure B.1: Benchmark of all three free parameters: number of standard deviation σ, number of bins, and number of points. Panel (a): the Jensen-Shannon distance between a given probability distribution function and the standard Gaussian distribution $\mathcal{N}(0,1)$; Panel (b): the "Ground Truth" values, i.e. the JS distance of the histogram with N_b number of bins estimated from N_p number of points from $\mathcal{N}(0,1)$; Panel (c): the same x and y bins as panel (b), with values of $JSD(PDF_{Logistic} \parallel \mathcal{N}(0,1))$.

The Jensen-Shannon Distance is the square root of Jensen-Shannon Divergence (Lin, 1991) which is the symmetrized and smoothed version of KullbackLeibler Divergence (Kullback and Leibler, 1951). Due to its symmetry and smoothness, Jensen-Shannon Distance is an ideal metric for the similarity between the observed magnetic field magnitude distribution and the Gaussian distribution. For two discrete probability distribution functions P and Q defined in the same space $\mathcal{X}$, the Jensen-Shannon Divergence is cal-

culated as following:

$$\mathrm{JSD}(P\|Q) = \frac{1}{2}D_{\mathrm{KL}}(P\|M) + \frac{1}{2}D_{\mathrm{KL}}(Q\|M) \tag{B.1}$$

where $M = (P+Q)/2$ is the mixture distribution of P and Q, and $D_{\mathrm{KL}}(P\|Q)$ is the KullbackLeibler Divergence:

$$D_{\mathrm{KL}}(P\|Q) = \sum_{x\in\mathcal{X}} P(x)\log\left(\frac{P(x)}{Q(x)}\right) \tag{B.2}$$

In this study, we use `scipy.spatial.distance.jensenshannon` (Virtanen et al., 2020) to calculate the Jensen-Shannon Distance. This program uses natural base logarithm in KullbackLeibler Divergence, and therefore the final Jensen-Shannon distance is bounded by $[0, \sqrt{ln(2)}]$.

The Gaussianity scalogram (GS) is a map where the vertical axis is window size (win) and the horizontal axis is the central time of each interval (t_{mid}), together forming a scalogram of Jensen-Shannon distance between the normalized probability density function of a given interval $PDF(t_{mid}, win)$ and the standard Gaussian distribution $\mathcal{N}(0,1)$, i.e. $JSD(PDF(t_{mid}, win), \mathcal{N}(0,1))$, or simply $JSD(PDF, \mathcal{N})$. To calculate $PDF(t_{mid}, win)$ from the ensemble of samples from a given interval, there are three controlling parameters: sample size N_p, number of bins N_b, and number of standard deviation considered σ. In addition, for benchmark purposes, it is necessary to calculate the JSD between some well-known symmetric distributions and standard Gaussian distribution. The summary of the influence of the controlling parameters and the comparison with well-known distributions are shown in Figure B.1.

The JSD between Laplace and Logistic distributions and Gaussian distribution as a function of standard deviation range considered is shown in panel (a). The JSD value stablizes approximately at 5 σ, and therefore for all GS shown in this dissertation, the PDF are all compiled for $\pm 5\sigma$. To see how N_p and N_b control the JSD value, samples are repeated drawn from a true Logistic distribution to calculate $JSD(Logistic, \mathcal{N}|N_p, N_b)$.

In panel (c), we see a much stablized region for large enough N_p and not-too-large N_b (The stable region is orange-ish because theoretical value at 5 σ is slightly smaller than the true value shown in panel (a) as dark red horizontal dashed line). Two purple dashed regions are highlighted in panel (c), where the right one indicates the parameter space used for low resolution GS shown in Figure 4.3 and 4.4, and the left one corresponds to the high resolution version shown in Figure 4.7 (c-e).

In addition, N_p and N_b also influence the ground truth value, i.e. the Jensen-Shannon distance between an ensemble statistically drawn from Gaussian generator and the real Gaussian PDF, which is not available in closed form (Nielsen, 2019). To obtain the ground truth value, the PDF is a histogram of equally spaced N_b bins located within $\pm$ 5 σ compiled from N_p independent samples drawn from a standard Gaussian source `numpy.random.randn` (Harris et al., 2020), and then the JSD is the averaged distance between the statistically calculated PDF(N_p, N_b) (repeated 30 times for each N_p and N_b) and the true Gaussian PDF. The standard deviation is found to be small for a given tuple of N_p and N_b. The resulting N_p-N_b map is shown in panel (b), and the two parameter space considered are also shown as purple dashed regions. Even for the poorest case ($N_p \sim 20000$), the ground truth value is still sufficiently away from JSD($Logistic, \mathcal{N}$).

B.2 PSP and Ulysses Data Analysis

The Gaussianity scalograms are compiled from magnetic magnitude time series of PSP and Ulysses. The fluxgate magnetometer of PSP (Bale et al., 2016; Bowen et al., 2020) offers two versions of level-2 data in RTN coordinates: mag_rtn_4_per_cyc and mag_rtn. The GS for intervals longer than one day are compiled with the low resolution (4 samples per 0.874 second) data product and the rest are compiled with the high resolution (256 samples per 0.874 second) mag_rtn. All magnetic magnitude data points for each interval are treated as independent samples drawn from a stochastic source and therefore the invalid (NaN) values are discarded and no interpolation is applied. The Ulysses magnetic field data is treated the same way.

B.3 Three-Dimensional MHD Alfvénic Turbulence Simulation

The simulation is conducted using a 3D Fourier-transform based pseudo-spectral MHD code (Shi et al., 2020). MHD equation set in conservation form is evolved with a third-order Runge-Kutta method. A detailed description of the simulation set-up and normalization units can be found in (Shi et al., 2023). Here we briefly summarize the key parameters.

The domain of the simulation is a rectangular box with the length of each side being $L = 5$. The number of grid points along each dimension is 512. To ensure numerical stability, explicit resistivity and viscosity $\eta = \nu = 2 \times 10^{-5}$ are adopted besides a de-aliasing.

For the initial configuration, uniform density, magnetic field and pressure are added: $\rho_0 = B = 1$, $P_0 = 0.1006$. The magnetic field has a small angle (8.1°) with respect to x-axis, and it is inside $x - y$ plane. On top of the background fields, we add correlated velocity and magnetic field fluctuations, i.e. the fluctuations are Alfvénic, with 3D isotropic power spectra. The reduced 1D spectra roughly follow $|k|^{-1.3}$. The strength of the fluctuations is $b_{rms}/B \approx 0.14$ where b_{rms} is the root-mean-square of the magnetic field fluctuation.

B.4 Fluxgate Magnotometer Noise and Zeros-Drift

There are several sources of error in the PSP fluxgate magnetometer measurements (Bale et al., 2016), including the instrumental noise as well as uncertainty in the zero offsets which drift in time (Bowen et al., 2020). The instrumental noise of each vector component is approximated as Gaussian white noise with a standard deviation $\sigma \simeq 0.05nT$, and together produce a noise with a standard deviation of $\sigma_{noise} \sim 0.1nT$ for the magnetic magnitude. σ_{noise} is usually much smaller than the standard deviation of the *in situ* measured σ_B for all scales that we are interested in. Nevertheless, the GS of a ground measured one-hour magnetic field time series for calibration is shown in Figure B.2. The

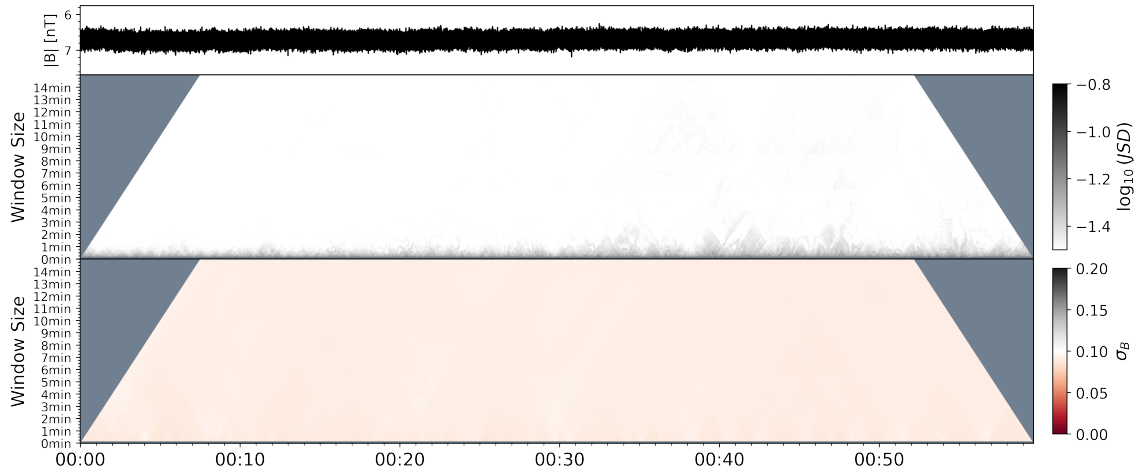

Figure B.2: Gaussianity Scalogram of magnetic magnitude from the fluxgate magnetometer noise. From top to bottom: magnetic magnitude B time series; GS of B; standard deviation scalogram of B.

distribution of the noise signal is universally Gaussian regardless of scales and location, and the standard deviations are unanimously small. Therefore, most of the Gaussian structures we show in the dissertation are real signals rather than instrument noise.

The error from drifting spacecraft offsets is a significantly larger contribution to the error as the approximated zero-offsets drift over time and are calibrated each day (Bowen et al., 2020). The drift of the spacecraft offsets, which is thought to occur due to slowly varying currents on the spacecraft is not well constrained and varies over time. This error is not Gaussian in nature, but should introduce small offsets in the measured field from the real background magnetic field. Spacecraft rolls are used to determine zero-offsets in both the inbound and outbound phases of each orbit, and are updated daily through optimizing the measurements to ensuring that spherically polarized magnetic field intervals maintain a constant magnitude. Typical offset values drift about $0.5nT$/day. Due to the continuous drift and non-Gaussian nature, the sub-day ($\lesssim 5Hr$) structures are not strongly affected by the zeros-drift. And the days-long structures are also not affected because of the instrument calibration of the zeros-offset.

B.5 Supplementary Materials

This manuscript contains one supplementary video:

`gaussianity_skewness_scalogram_E12.mp4` (https://www.youtube.com/watch?v=L8gH4luCao8).

It shows the Gaussianity scalogram and normalized standard deviation scalogram of magnetic magnitude with window sized from 30 second to 15 minutes for the whole Parker Solar Probe E12. This video aims to show the self-similar magnetic structures revealed by GS and the corresponding sub-structures from the normalized standard deviation scalogram. For the first one minute, the GS looks different because of the low sampling rate of the fluxgate magnetometer. It also shows the Skewness scalogram and normalized standard deviation scalogram of magnetic magnitude with window sized from 1 second to 5 minutes for the whole Parker Solar Probe E12. This video aims to show the systematic tendency for magnetic holes in the magnetic magnitude distributions.

APPENDIX C

Interpretation of Temporal Signals

The data provided by PSP are time series of different measurable quantities from single spacecraft measurements, such as vector magnetic field, vector proton velocities, proton densities, etc. Consequently, different studies interpret the raw temporal signals using different assumptions. Partially due to the predominant dependence on wavevector in most of the turbulence theories and models, a significant portion of the observational studies interpret the temporal signals as wind-advected spatial structures in order to make comparisons. To convert the temporal signals into spatial signals, Taylor Hypothesis (TH) (Taylor, 1938) is used:

$$k \cdot U = 2\pi f \tag{C.1}$$

where k is the wavenumber, U is the local solar wind speed, and f is the given frequency from the observed data. k is considered created by the advection of the solar wind at speed U, and hence $\vec{k} \parallel \vec{U}$ locally. In addition, locally averaged vector magnetic field $\langle \vec{B} \rangle$ is compiled at the given temporal window $1/f$ in a sliding window fashion to represent the local "parallel" direction in the turbulence anisotropy theory. And the temporal signal can be interpreted via windowed-FFT or wavelet transformation as a 2D anisotropic power spectrum density $P(k_\perp, k_\parallel)$ (or even 3D depending on the specific turbulence theory one choose to compare to).

Partially due to the stability of the Alfvén mode (see e.g. (Hollweg, 1971)), the Alfvén speed $V_A = |B|/\sqrt{\mu_0 \rho}$ is often considered as the representation of the information propagation speed in solar wind plasma. In the near-Earth solar wind, solar wind speed

$U \simeq 400$km/s is much larger than the typical Alfvén speed $V_A \simeq 50$km/s, and hence (C.1) is accurate with an error around 10% at 1AU, thereby being the common approach. However, as PSP gets closer to the sun, especially around the Alfvén surface (Kasper et al., 2021) where U becomes comparable to V_A by definition, (C.1) needs to be modified. The commonly used modification is that:

$$\vec{k} \cdot (\vec{U} + \vec{V}_A) = 2\pi f \tag{C.2}$$

where $\vec{V}_A$ has a scale-dependent direction determined by the local average magnetic field direction, and similarly $\vec{k}$ is assumed to align with $\vec{U} + \vec{V}_A$. This modified TH makes an extremely important assumption: All of the temporal signals in the solar wind measured by PSP are propagating Alfvén waves. This assumption is of course questionable since all types of transients exists in the solar wind: Heliospheric Current Sheets (HCS), Coronal Mass Ejections (CME), and discontinuities (tangential, shocks, etc.). Nevertheless, this assumption can be justified for PSP data with two major reasons: 1. The solar wind measured by PSP around the perihelion ($\pm$7 days) is Alfvénic (high $\vec{V}$ and $\vec{B}$ correlation) most of the time ($> 80\%$), signifying unidirectional outward propagating Alfvén waves; 2. For turbulence studies, the large scale transients (HCS or CME) are usually removed prior to statistical analysis in order to make meaningful comparisons with theories.

However, instead of invoking TH and converting the temporal signals into spatial signals, one can resort to a more straightforward approach: make the same assumption that PSP is measuring unidirectional outward propagating Alfvén waves and directly analyze the frequency spectrum compiled from the temporal signals.

C.1 Transmission of Alfvén Waves

To justify the aforementioned approach, one needs to consider the propagation properties of Alfvén waves in the solar wind which experiences significant expansion and acceleration from the coronal base to PSP. The transmission coefficient of Alfvén waves in the solar

wind is defined in terms of the total wave action (quantum) flux for an expanding flux tube starting from the coronal base (Heinemann and Olbert, 1980; Velli, 1993):

$$S^{\pm} = \frac{1}{2}\rho \frac{(z^{\pm}/2)^2}{\omega_0 \frac{V_A}{U+V_A}} \cdot (U \pm V_A) \cdot A \tag{C.3}$$

where $\vec{z}^{\pm} = \vec{v} \pm \vec{b}$ is the Elsässer variable, and $\vec{b} = \frac{\delta \vec{B}}{\sqrt{\mu_0 \rho}}$ is the normalized magnetic perturbation in the system. Here we defined z^+ as the outward-propagating Alfvén waves and hence S^+ is the wave action density of the outward component, and *vice versa* for z^- and S^-. A is the cross section area of the flux tube as a function of radial distance, and in the case of spherical expansion $A(R) \propto R^2$. Notably, ω_0 is the launch angular frequency of the wave at the coronal base, and it is doppler shifted to ω_1 in the plasma frame (for simplicity, z^+ will be used as an example):

$$\omega_1 = \omega_0 \frac{V_A}{U + V_A} \tag{C.4}$$

because from the perspective of the wave in the plasma frame, the source is moving away at the speed of U. And hence here:

$$\frac{1}{2}\rho(z^+/2)^2$$

is the fluctuation energy density of the Alfvén wave packet, and:

$$\frac{1}{2}\rho \frac{(z^+/2)^2}{\omega_1} = \frac{1}{2}\rho \frac{(z^+/2)^2}{\omega_0 \frac{V_A}{U+V_A}}$$

is the wave action density of the Alfvén wave packet, which is an adiabatic invariant for a propagating wave when the wavelength is much shorter than the typical spatial scale of the medium (Bretherton, 1968; Dewar, 1970). This is also called the wave quantum because it has exactly the same definition as a photon. For a given frequency, if the wave is adiabatic, we can regard the wave packet as a particle, and speed of the particle in

inertial frame is the group velocity $U + V_A$, and thus:

$$\frac{1}{2}\rho\frac{(z^+/2)^2}{\omega_0\frac{V_A}{U+V_A}}\cdot(U+V_A) \tag{C.5}$$

is the wave action flux density, and together with the cross section area A of the flux tube at a given radial distance R, making (C.3) the total wave action flux as a function of R. Evidently, when the outward propagating wave is adiabatic, S^+ is a perfectly conserved quantity, i.e. the total number of 'Alfvénton' being a constant for any given cross section of the flux tube. This is also termed as being WKB (Wentzel-Kramers-Brillouin) (Whang, 1973; Hollweg, 1990). However, due to the spatial gradient of U, V_A, ρ and A, low frequency waves can become non-WKB and be partially reflected (and partially tunnelled). The transmission problem is then phrased in terms of the WKB value of the total wave action flux, thereby producing a frequency-dependent transmission coefficient profile. The key point to solve the transmission problem of $z^\pm$ is that from the corona base (source) to infinity, the net flux of the outward propagating Alfvén waves is constant:

$$S^+ - S^- = S_\infty \tag{C.6}$$

where S_∞ is the total wave action flux at infinity. The transmission coefficient for a given launch angular frequency ω_0 is hence defined as:

$$T = S_\infty / S_0^+ \tag{C.7}$$

where S_0^+ is the total wave action flux at the corona base. The propagation of Alfvén waves is governed by the following equation:

$$\frac{\partial z^\pm}{\partial t} + (\vec{U} \pm \vec{V}_A)\cdot\nabla z^\pm + z^\mp\cdot\nabla(\vec{U}\mp\vec{V}_A) + \frac{1}{2}(z^\mp - z^\pm)\nabla\cdot(\vec{V}_A \mp \frac{1}{2}\vec{U}) = 0 \tag{C.8}$$

The first two terms describe the wave propagation; the third term describes the reflection of the waves by gradient of the Alfvén speed, which vanishes for a vertical field in a planar atmosphere, but is different from zero in the more realistic spherically or supraspherically expanding flux tube; the fourth term describes the WKB losses and the isotropic part of the reflection. To solve this problem, we assume the temporal part for each wave can be written as $\tilde{Z}^{\pm}\exp(-i\omega t)$ ($\tilde{Z}^{\pm}$ is the complex amplitude) in the plasma frame (ω is doppler shifted from the launch frequency ω_0 due to the presence of the wind), and hence we can apply Fourier transformation, and integrate in spatial coordinate:

$$-i\omega z^{\pm} + (\vec{U} \pm \vec{V}_A)\cdot\nabla z^{\pm} + z^{\mp}\cdot\nabla(\vec{U} \mp \vec{V}_A) + \frac{1}{2}(z^{-} - z^{+})\nabla\cdot(\vec{V}_A \mp \frac{1}{2}\vec{U}) = 0 \quad \text{(C.9)}$$

Note that this inertial frame is the same frame as the solar inertial frame, and thus $\omega = \omega_0$, the launch angular frequency of the wave. Intuitively, this can be explained using double doppler shifts with three frames involved: solar inertial frame S_0, solar wind plasma frame P, and the stationary (relative to the sun) spacecraft frame S. In S_0, the frequency of the wave is ω_0. It is doppler shifted to a lower frequency ω_1 in P, shown in (C.4), because the wave sources moves away with respective to an observer in the frame. The frequency is then shifted back to ω_0 in S because, for an observer in S, the receiver is moving at U with respect to the source, and hence:

$$\omega = \omega_1\frac{U + V_A}{V_A} = \omega_0 \quad \text{(C.10)}$$

However, integrating (C.9) is quite tricky because one needs to set a boundary condition, but we have no information on the relations between z^{+} and z^{-} either at the corona base or infinity. Luckily, the Alfvén surface where $U = V_A$, acts as a natural singular point in this system, because the z^{-} equation in (C.9) reduces to:

$$-i\omega z^{-} + \frac{1}{2}(z^{-} - z^{+})\nabla\cdot(\vec{V}_A + \frac{1}{2}\vec{U}) = 0 \quad \text{(C.11)}$$

and given a radial profile of $V_A(R)$ and $U(R)$, one obtains a linear relation between z^{+}

and z^- at the Alfvén surface. In addition, the group velocity for the inward waves is zero at the Alfvén surface, and hence the net total wave action flux S_∞ is:

$$S_\infty = S_c^+ - S_c^- = S_c^+ \tag{C.12}$$

where $S_c^\pm$ is the total wave action flux for $z^\pm$ at the Alfvén (critical) surface. Now combining (C.9), (C.11) and (C.12), we can integrate the equations for both z^+ and z^- from the Alfvén surface back to the corona base and obtain a transmission coefficient profile from the corona base to the Alfvén surface. As an example, here we use the solar wind and Alfvén speed profile from (Velli et al., 1991):

$$\rho = \rho_0 \frac{\exp\{-\alpha/2 \cdot [1 - (R_\odot/R)]\}}{\{1 + \beta[(R/R_\odot - 1)]\}^2} \tag{C.13}$$

$$V_A = V_{A0} \left(\frac{R_\odot}{R}\right)^2 \left(\frac{\rho_0}{\rho}\right)^{1/2} \tag{C.14}$$

$$U = \frac{U_\infty}{\beta^2} \exp(-\alpha/2) \left(\frac{R}{R_\odot}\right)^2 \left(\frac{V_A}{V_{A0}}\right)^2 \tag{C.15}$$

where V_{A0} is the initial Alfvén speed at the corona base, U_∞ is the asymptotic solar wind speed at infinity, and α and β are free parameters. To find a typical transmission coefficient for the 3-minute ($\simeq$5.5 mHz) wave, we adopt some reasonable values: $\alpha = 0, \beta = 5, V_{A0} = 2000\text{km/s}, U_\infty = 700\text{km/s}$, and this produces a Alfvén surface at a observational compatible distance of $15.09R_\odot$. The resulting solar wind and Alfvén speed profile is shown in the left panel of Figure C.1, and in the right panel we show the transmission coefficient as a function of launch frequency $f_0 = \omega_0/2\pi$. From the graph we can see that for an Alfvén wave packet with a period of 3 minute, the transmission coefficient from the corona base to the Alfvén surface is 99.6%, very close to perfect transmission. And for the ultra-low frequency waves, asymptotic transmission coefficient is tunnelling value determined solely by the Alfvén speed at the corona base V_{A0} and at the Alfvén (critical) surface V_{Ac}:

$$T_c = 4\frac{V_{A0}V_{Ac}}{(V_{A0} + V_{Ac})^2} \tag{C.16}$$

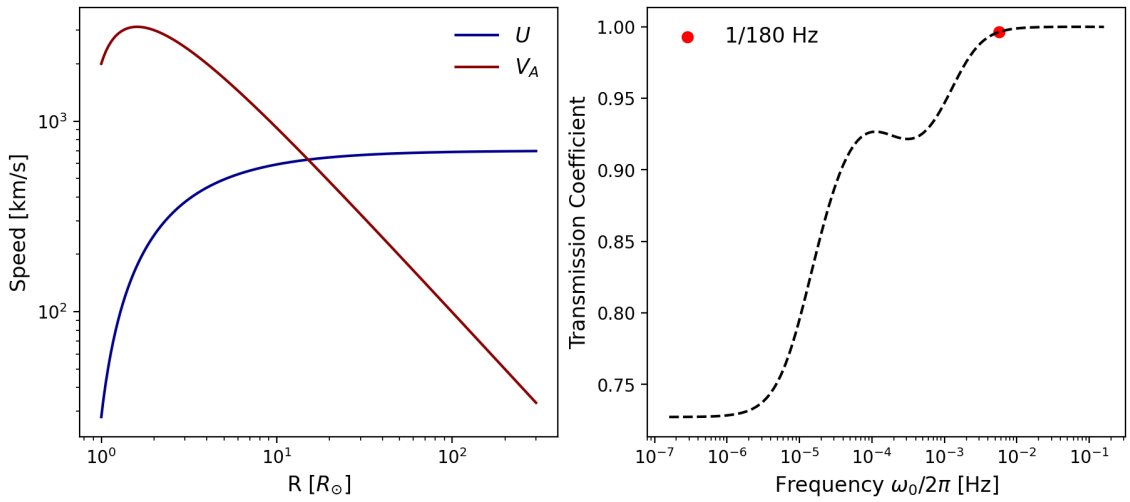

Figure C.1: Left: Solar wind and Alfvén speed profile. Right: Transmission coefficient of Alfvén waves as a function of launch frequency.

The transmission is much enhanced compared to the case of static atmosphere with exponential Alfvén speed profile, where the ultra-low frequency waves are completely reflected. Notably, the transmission coefficient value for a 3-minute wave is not sensitive to the specific profile of U and V_A as long as the given profiles are realistic. In addition, for the frequency range that we are dealing with in this study ($f \gtrsim 10^{-4}$ Hz), the transmission coefficient is generally larger than 90%, and hence can be safely considered as quasi-WKB. For more in depth discussion of the transmission problem, please refer to (Velli, 1993).

C.2 Doppler Effects

Through the discussion in the previous section we have shown that for the frequency range we studied in this work, the linear theory dictates a perfect transmission, in other words, negligible modification to the frequency spectrum except for the systematic decay in energy from WKB evolution. However, PSP is the fastest moving human-made object, and hence especially during the perihelion, doppler effects resulting from the spacecraft movement can be significant. Again, we emphasize our fundamental assumption that PSP is measuring unidirectional outward propagating Alfvén waves, and therefore the doppler

effects can be separated into two scenarios (PSP orbit is mostly within the ecliptic plane with very little θ variations): radial velocity of PSP $V_{PSP,r}$ and perpendicular velocity of PSP $V_{PSP,\phi}$.

C.2.1 Radial Doppler Shift

Treating the radial doppler shift is trivial, we can simply incorporate the spacecraft velocity in (C.10):

$$f = f_1 \frac{U + V_A + V_{PSP,r}}{V_A} = f_0 \frac{U + V_A + V_{PSP,r}}{U + V_A} \tag{C.17}$$

where f_0 is the launch frequency, f_1 is the doppler shifted frequency in the solar wind plasma frame, and f is the frequency of the wave in the spacecraft frame. Here we select the sign of $V_{PSP,r}$ to be positive when the spacecraft is moving radially inward. Around perihelion, $V_{PSP,r} \simeq 100$km/s, whereas $U + V_A \gtrsim 1000$km/s, and hence $f/f_0 < 10\%$. To visualize this effect, the radial doppler shift is removed for the coronal hole interval from E12, and the comparison is shown in Figure C.2 (b). Obviously the effect makes little change to the raw values of $1/f_{mid}$ and hence we decided to keep the original data of $1/f_{mid}$ in the statistical results shown in Figure 5.3. In summary, the radial doppler effects from the radial movements of PSP are marginal for all intervals considered in this study.

C.2.2 Perpendicular Doppler Shift

The perpendicular doppler shift, on the other hand, is much less straightforward. It is well-known that Alfvén waves are guided by the background field $\vec{B}_0$, and the group velocity is perfectly aligned with $\vec{B}_0$. Consequently, Alfvén waves packets hardly interact with each other in the perpendicular direction in large scales. Therefore, the perturbation of $\delta\vec{B}$ in the ϕ direction is an unknown function of spatial coordinates, which can be expressed as a unknown wavenumber power spectrum density in ϕ direction $P(k_\phi)$. As PSP approaches the perihelion, its velocity $V_{PSP,\phi}$ can reach to around 170km/s, or

100km/s in the Carrington corotating frame. And hence the wavenumber spectrum (spatial signals) can be doppler shifted to frequency spectrum via:

$$2\pi f = k_\phi \cdot V_{PSP,\phi} \tag{C.18}$$

The doppler shifted spectrum can then be considered as a "contamination" of the real frequency spectrum of the outward propagating Alfvén waves. Notably, $V_{PSP,\phi}$ change significantly around the perihelion over a relatively small range of radial distance, especially in the solar corotating frame. Assuming a power law dependence $P(k_\phi) \propto k^{-\alpha}$ and $\alpha > 1$, smaller k (larger scales) indicates stronger fluctuation energy. In this scenario, as PSP approaches perihelion, $V_{PSP,\phi}$ increases rapidly, and hence for the same frequency f, it corresponds to progressively smaller k, and hence increasingly higher fluctuation energy. Therefore, the "contamination" grows rapidly as PSP approaches perihelion, and reaches its maximum right at the perihelion. This could be reason why we see an upward trend in $1/f_{mid}$ right at the perihelion for the coronal hole interval from the inbound section of E12 shown in Figure C.2 (and similarly for E10 coronal hole shown in Figure 5.3). Therefore, the actual $1/f_{mid}$ in the upper corona could be closer to 2-minute than 3-minute if the contamination is removed. Nevertheless, we decided to keep the original statistics to maintain reproductivity and generality of our study.

C.3 Nonlinear Effects: Parametric Decay Instability and Turbulence Cascade

Based on the discussion in the previous section, we have shown that for the frequency range of interest, the reflection of Alfvén waves are negligible. Therefore, nonlinear effects are necessary in order to change the frequency spectrum of the Alfvén waves. There are two major nonlinear effects that is believed to be significant in the solar wind at PSP distance: parametric decay instability (PDI) and turbulence cascade. However, instead of discussing the details of the two nonlinear effects, one can estimate the propagation

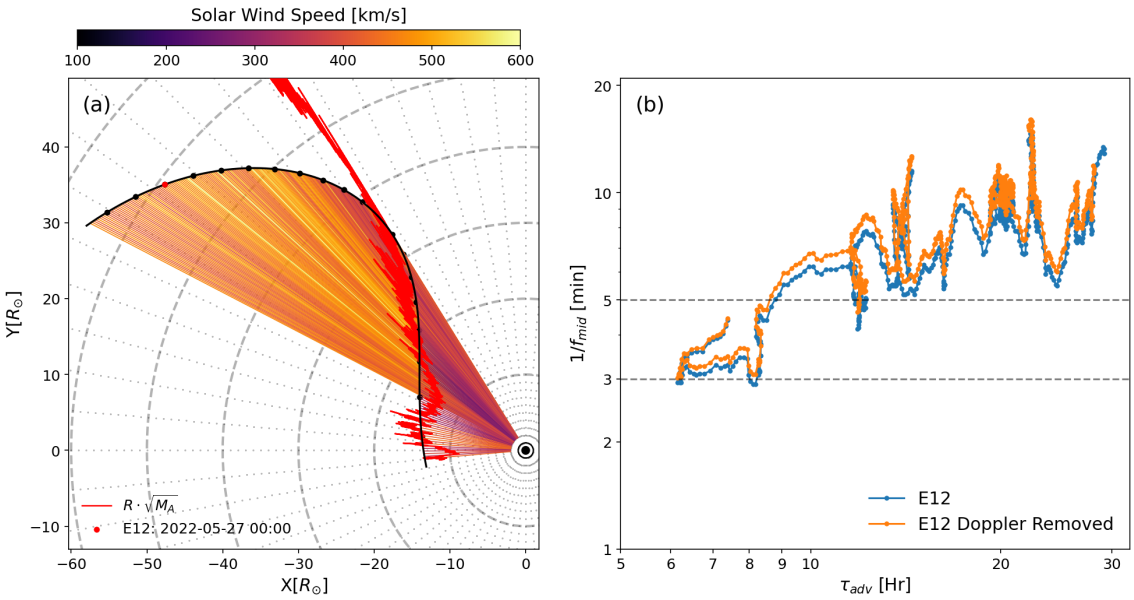

Figure C.2: (a) Trajectory of PSP for the inbound section of E12 from 2022-05-26 02:15:00 to 2022-06-01 21:45:00. This interval has confirmed origin from a coronal using PFSS model in Chapter 4. The black dots on the trajectory are plotted every 8 hours, and the date of the red dot is shown in the legend to indicate the spacecraft's entering direction. The helio-radial lines are colored with locally averaged solar wind speed. The red line is an illustration of Alfvén Mach number $M_A = V_r/V_A$, and is plotted as $R \cdot \sqrt{M_A}$. (b) An illustration of Doppler effects from the spacecraft motion. Blue: $1/f_{mid}$ with doppler effects; Orange: doppler effects are removed.

time of the Alfvén waves from the corona base to Alfvén surface using the group velocity $U + V_A$. Assuming a radially expanded flux tube (which slightly underestimates the real length of the field line because the plume lines in during solar eclipse clearly show super-radial expansion), the propagation time compiled from the profile in Figure C.1 is 1.55 hours, much shorter than the 'age' of plasma estimated from the advection time $\tau_{adv} = R/U$ shown in Figure 5.3.

The main effect of PDI from model (Chandran, 2018) is 'spreading' the energy at the bend to lower frequencies through inverse cascade of Alfvén waves. Even though this mechanisms is still being debated, the predicted processes have gained some evidence from recent observations (Davis et al., 2023) and from the supplemental video (`https://www.youtube.com/watch?v=snnLKmt-qhA`) of this work. A detailed discussion of this mechanism is beyond the scope of this study. Nevertheless, the fact that we identified

a systematic collection of the shallow-inertial double power law spectrum around the perihelion indicates that parametric decay instability might not have made significant modification to the spectrum yet when they are captured by PSP. The turbulence cascade, on the other hand, is much slower. We have already provided in depth discussion of this effect in the main text, and thus will be skipped here.

C.4 Turbulence Anisotropy

For completeness, here we provide a discussion on the 'sampling-bias' in the turbulence anisotropy. It has been shown in (Sioulas et al., 2023b) that the 'parallel' spectrum dominates the large scale (small k) part of the anisotropic PSD. Here the concept of 'parallel' and 'perpendicular' are defined w.r.t. the angle between the local solar wind speed and the scale-dependent background magnetic field. At low frequency (large scale from Taylor Hypothesis), the background field is almost perfectly radial, and hence parallel to the solar wind, and thereby creating a 'sampling-bias' in the anisotropic PSD.

As been discussed in the previous sections, this study choose an alternative yet equal approach: Instead of invoking Taylor Hypothesis and converting the temporal signals into spatial signals, we interpret the temporal signals measured by PSP as it is, and directly analyze the frequency spectrum. Ultimately, the choice between either approaches is dependent on whether one believes that the perturbations in the solar wind are waves or turbulence. Our justification for the prior is the following: The majority of the perturbation energy are carried by the so called switchbacks, or large amplitude spherically polarized Alfvén waves, which are very clearly radially propagating outwards along the quasi-radial background field. It is true that at smaller scales, the waves are guided by the locally perturbed magnetic field, but by definition, these waves are energetically less significant. Additionally, for the perturbations at 3-minute period, at Alfvén surface, it can be translated to 0.26 $R_\odot$ in spatial scale assuming a 1000km/s group velocity. Applying this spatial scale to the ϕ direction, due to the lack of perpendicular information carrier, we are almost sure that the two signals separated by this distance are causally

unrelated. Therefore, following the discussions in the previous section, perturbations created by PSP perpendicular movements at this spatial scales should be considered as 'contamination' to the temporal signals.

C.5 Movement of the Low Frequency Spectral Break in Expanding Solar Wind

Suppose a well-developed turbulence whose power spectrum consists of two parts:

$$P(f,\tau) = \begin{cases} C_0(\tau) f^{-\alpha_0}, & f \le f_c(\tau) \\ C_1(\tau) f^{-\alpha_1}, & f \ge f_c(\tau) \end{cases} \tag{C.19}$$

Where τ is the "age" of the turbulence starting from a reference point, satisfying that $\tau \gg 1/f_{min}$. f_{min} is the lowest frequency that is considered credible in the spectrum due to the Cone of Influence (CoI), and for a 6-hour fixed window, it is about 80 minutes. Obviously, there should be:

$$C_0(\tau) f_c^{-\alpha_0} = C_1(\tau) f_c^{-\alpha_1} \tag{C.20}$$

at any given moment. Here we have assumed that the energy containing range is decaying due to the solar wind expansion, otherwise $C_0(\tau)$ should be a constant.

The total energy in the system at moment t is:

$$\mathcal{E}(\tau) = \int_0^{+\infty} P(f,\tau) df = \int_0^{f_c(\tau)} C_0(\tau) f^{-\alpha_0} df + \int_{f_c(\tau)}^{+\infty} C_1(\tau) f^{-\alpha_1} df \tag{C.21}$$

At a later time $t + \Delta\tau$, the total energy is:

$$\begin{aligned}\mathcal{E}(\tau+\Delta\tau) &= \int_0^{+\infty} P(f,\tau+\Delta\tau)df \\ &= \int_0^{f_c(\tau+\Delta\tau)} C_0(\tau+\Delta\tau)f^{-\alpha_0}df + \int_{f_c(\tau+\Delta\tau)}^{+\infty} C_1(\tau+\Delta\tau)f^{-\alpha_1}df \\ &\simeq \int_0^{f_c(\tau)+\Delta f_c} \left[C_0(\tau)+\frac{dC_0}{dt}\Delta\tau\right] f^{-\alpha_0}df + \int_{f_c(\tau)+\Delta f_c}^{+\infty} \left[C_1(\tau)+\frac{dC_1}{dt}\Delta\tau\right] f^{-\alpha_1}df\end{aligned} \tag{C.22}$$

From equation (C.20), we can see that:

$$\frac{dC_1}{dt} = \frac{dC_0}{dt} f_c^{\Delta\alpha} + \Delta\alpha C_0 f_c^{\Delta\alpha-1}\frac{df_c}{dt} \tag{C.23}$$

where $\Delta\alpha = \alpha_1 - \alpha_0$. Here the first r.h.s term is the change of the inertial range energy due to the solar wind expansion, and the second term is the change of the inertial range energy due to the movement of the low frequency spectral break f_c. Thus, we get:

$$\begin{aligned}\mathcal{E}(\tau+\Delta\tau) = &\int_0^{f_c(\tau)+\Delta f_c} C_0 f^{-\alpha_0}df + \int_{f_c(\tau)+\Delta f_c}^{+\infty} C_1 f^{-\alpha_1}df \\ &+ \Delta\alpha C_0 f_c^{\Delta\alpha-1}\frac{df_c}{dt}\Delta\tau \cdot \int_{f_c(\tau)+\Delta f_c}^{+\infty} f^{-\alpha_1}df \\ &+ \frac{dC_0}{dt}\Delta\tau\left[\int_0^{f_c(\tau)+\Delta f_c} f^{-\alpha_0}df + f_c^{\Delta\alpha}\cdot\int_{f_c(\tau)+\Delta f_c}^{+\infty} f^{-\alpha_1}df\right]\end{aligned} \tag{C.24}$$

It is obvious that the first line is equal to $\mathcal{E}(\tau)$. The second line is the change of total energy due to the movement of the low frequency spectral break due to turbulence dissipation. The third line is the change of total energy due to solar wind expansion. We can hence write the energy dissipation rate as $\epsilon(\tau)$:

$$\begin{aligned}-\epsilon(\tau) = \frac{\mathcal{E}(\tau+\Delta\tau)-\mathcal{E}(\tau)}{\Delta\tau} &= \Delta\alpha C_0 f_c^{\Delta\alpha-1}\frac{df_c}{dt}\cdot\int_{f_c(\tau)+\Delta f_c}^{\infty} f^{-\alpha_1}df \\ &\approx \left(\frac{\alpha_1-\alpha_0}{\alpha_1-1}\right) C_0 f_c^{-\alpha_0}\frac{df_c}{dt}\end{aligned} \tag{C.25}$$

One may use (C.25) to evaluate the energy cascade rate $\epsilon(\tau)$ from the change of $f_c(\tau)$

over time.

C.6 Window Limit

Figure C.3 is an illustration of the window limit of 20 minute for the 6 hour window (the dotted dashed line in Figure 5.3). For a Kolmogorov $f^{-5/3}$ spectrum, the fluctuation power concentrates at the low frequency end. Therefore, the normalized integrated energy (dotted dashed line in Figure C.3) grows slowly at high frequencies and quickly at low frequencies. If we similarly ignore the frequency range where more than 50% of points fall out of the Cone of Influence (CoI) of the wavelet transformation (gray area), the resultant frequency range that contains 50% of fluctuation energy (from 25% to 75%) is highlighted with the green area, and the center frequency is $1/f_{mid}$ = 20 minute. This frequency can be considered as the saturation frequency because as the solar wind propagates outwards (τ_{adv} and R increases), the low frequency spectral break is known to move to lower frequencies (Tu and Marsch, 1993, 1995). And for a fixed 6 hour window, the low frequency break can move well into the grey area, or even fall out of the resolvable frequency range (in this case, <1/6Hr$\simeq 10^{-4.3}$Hz). Consequently, the frequency range of interest (right of gray area) is only left with the inertial range, which is often very close to Kolmogorov $f^{-5/3}$ in the solar wind.

The window limit is of course dependent on the window size, and in this case is 6 hour. In this study, we thoroughly scanned the solar wind with windows of different sizes. For shorter window sizes, the window limit become smaller, and hence making it harder to capture the radial evolution of $1/f_{mid}$. On the other hand, longer window can capture the radial evolution nicely, but may fail to resolve the elementary solar wind streams, i.e. tend to mix different streams. This is because PSP retrogrades extremely rapidly at the perihelia, often exceeding 60 deg Carrington Longitude per day (i.e. 2.5 deg/Hr, see e.g. Figure 5.2(c1)). And hence the *in situ* time series measured at perihelia are often mixtures of very different solar wind streams. For example in Appendix 5.5, the majority of the intervals with clear shallow power law is shorter than 6 hours. From

our experience, 6 hour is a good trade-off window size to balance these two effects, and therefore we choose 6 hour window to illustrate our statistical results. Nevertheless, the primary conclusion is not sensitive to the choice of the window size.

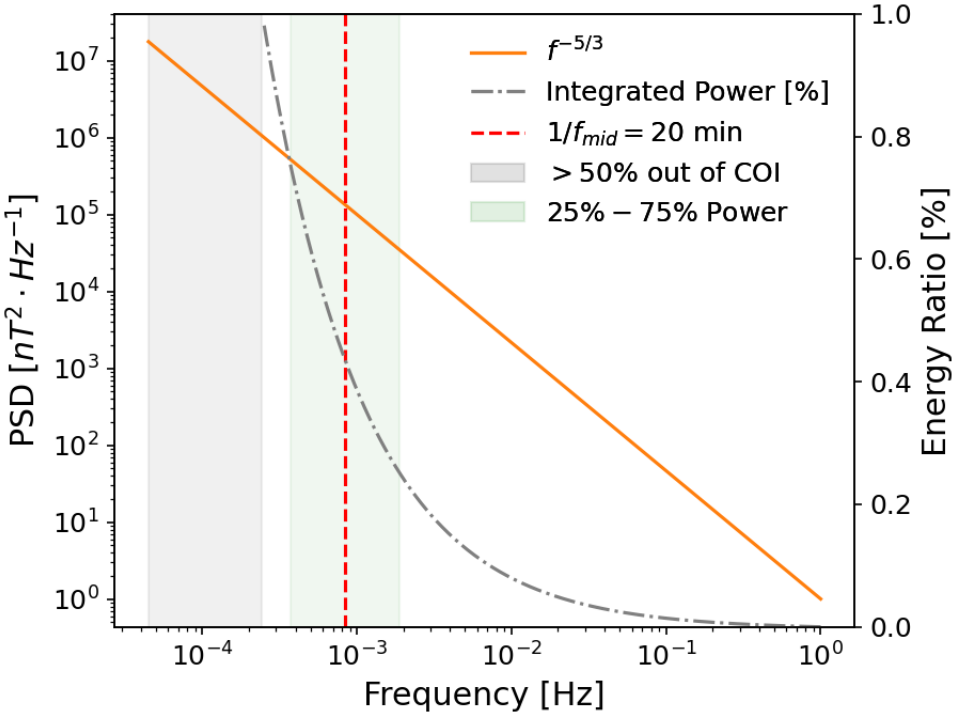

Figure C.3: Illustration of the saturation value of $1/f_{mid}$ from a 6 hour window. Orange: Fake Kolmogorov $f^{-5/3}$ spectrum; Dotted dashed: Normalized integrated power of $f^{-5/3}$, twin axis; Gray area: Frequency range where >50% of points are out of the Cone of Influence; Green area: frequency range that contains 50% of fluctuation energy (from 25% to 75%).

BIBLIOGRAPHY

Adhikari, L., Zank, G. P., Zhao, L.-L., Kasper, J. C., Korreck, K. E., Stevens, M., Case, A. W., Whittlesey, P., Larson, D., Livi, R., and Klein, K. G. (2020). Turbulence Transport Modeling and First Orbit Parker Solar Probe (PSP) Observations. *The Astrophysical Journal Supplement Series*, 246(2):38. Publisher: The American Astronomical Society. 89

Alazraki, G. and Couturier, P. (1971). Solar wind accejeration caused by the gradient of Alfven wave pressure. *Astronomy and Astrophysics, Vol. 13, p. 380 (1971)*, 13:380. ISBN: 0004-6361. 87

Andersen, B. N. (1991). Virgo-solar irradiance and radiance monitoring on SOHO. *Advances in Space Research*, 11(4):93–102. 112

Aschwanden, M. (2011). *Self-Organized Criticality in Astrophysics: The Statistics of Nonlinear Processes in the Universe*. Springer Berlin Heidelberg, Berlin, Heidelberg. 86

Aschwanden, M. J., Crosby, N. B., Dimitropoulou, M., Georgoulis, M. K., Hergarten, S., McAteer, J., Milovanov, A. V., Mineshige, S., Morales, L., Nishizuka, N., Pruessner, G., Sanchez, R., Sharma, A. S., Strugarek, A., and Uritsky, V. (2016). 25 Years of Self-Organized Criticality: Solar and Astrophysics. *Space Science Review*, 198:47–166. _eprint: 1403.6528. 86

Badman, S. T., Bale, S. D., Oliveros, J. C. M., Panasenco, O., Velli, M., Stansby, D., Buitrago-Casas, J. C., Réville, V., Bonnell, J. W., Case, A. W., Wit, T. D. d., Goetz, K., Harvey, P. R., Kasper, J. C., Korreck, K. E., Larson, D. E., Livi, R., MacDowall, R. J., Malaspina, D. M., Pulupa, M., Stevens, M. L., and Whittlesey, P. L. (2020). Magnetic Connectivity of the Ecliptic Plane within 0.5 au: Potential Field Source Surface Modeling of the First Parker Solar Probe Encounter. *The Astrophysical Journal Supplement Series*, 246(2):23. Publisher: The American Astronomical Society. 16, 70, 72, 96

Badman, S. T., Riley, P., Jones, S. I., Kim, T. K., Allen, R. C., Arge, C. N., Bale, S. D., Henney, C. J., Kasper, J. C., Mostafavi, P., Pogorelov, N. V., Raouafi, N. E., Stevens, M. L., and Verniero, J. L. (2023). Prediction and Verification of Parker Solar Probe Solar Wind Sources at 13.3 R? *Journal of Geophysical Research: Space Physics*, 128(4):e2023JA031359. _eprint: https://onlinelibrary.wiley.com/doi/pdf/10.1029/2023JA031359. 16, 17, 29, 30, 70, 71, 72, 86, 94, 96

Bak, P., Tang, C., and Wiesenfeld, K. (1987). Self-organized criticality - An explanation of 1/f noise. *Physical Review Letters*, 59:381–384. 104

Bale, S. D., Badman, S. T., Bonnell, J. W., Bowen, T. A., Burgess, D., Case, A. W., Cattell, C. A., Chandran, B. D. G., Chaston, C. C., Chen, C. H. K., Drake, J. F.,

de Wit, T. D., Eastwood, J. P., Ergun, R. E., Farrell, W. M., Fong, C., Goetz, K., Goldstein, M., Goodrich, K. A., Harvey, P. R., Horbury, T. S., Howes, G. G., Kasper, J. C., Kellogg, P. J., Klimchuk, J. A., Korreck, K. E., Krasnoselskikh, V. V., Krucker, S., Laker, R., Larson, D. E., MacDowall, R. J., Maksimovic, M., Malaspina, D. M., Martinez-Oliveros, J., McComas, D. J., Meyer-Vernet, N., Moncuquet, M., Mozer, F. S., Phan, T. D., Pulupa, M., Raouafi, N. E., Salem, C., Stansby, D., Stevens, M., Szabo, A., Velli, M., Woolley, T., and Wygant, J. R. (2019). Highly structured slow solar wind emerging from an equatorial coronal hole. *Nature*, pages 1–6. 27, 31, 57, 70, 73, 95

Bale, S. D., Drake, J. F., McManus, M. D., Desai, M. I., Badman, S. T., Larson, D. E., Swisdak, M., Horbury, T. S., Raouafi, N. E., Phan, T., Velli, M., McComas, D. J., Cohen, C. M. S., Mitchell, D., Panasenco, O., and Kasper, J. C. (2023). Interchange reconnection as the source of the fast solar wind within coronal holes. *Nature*, 618(7964):252–256. Number: 7964 Publisher: Nature Publishing Group. 70, 71, 72, 74, 78, 79, 86, 88, 95

Bale, S. D., Goetz, K., Harvey, P. R., Turin, P., Bonnell, J. W., Dudok de Wit, T., Ergun, R. E., MacDowall, R. J., Pulupa, M., Andre, M., Bolton, M., Bougeret, J. L., Bowen, T. A., Burgess, D., Cattell, C. A., Chandran, B. D. G., Chaston, C. C., Chen, C. H. K., Choi, M. K., Connerney, J. E., Cranmer, S., Diaz-Aguado, M., Donakowski, W., Drake, J. F., Farrell, W. M., Fergeau, P., Fermin, J., Fischer, J., Fox, N., Glaser, D., Goldstein, M., Gordon, D., Hanson, E., Harris, S. E., Hayes, L. M., Hinze, J. J., Hollweg, J. V., Horbury, T. S., Howard, R. A., Hoxie, V., Jannet, G., Karlsson, M., Kasper, J. C., Kellogg, P. J., Kien, M., Klimchuk, J. A., Krasnoselskikh, V. V., Krucker, S., Lynch, J. J., Maksimovic, M., Malaspina, D. M., Marker, S., Martin, P., Martinez-Oliveros, J., McCauley, J., McComas, D. J., McDonald, T., Meyer-Vernet, N., Moncuquet, M., Monson, S. J., Mozer, F. S., Murphy, S. D., Odom, J., Oliverson, R., Olson, J., Parker, E. N., Pankow, D., Phan, T., Quataert, E., Quinn, T., Ruplin, S. W., Salem, C., Seitz, D., Sheppard, D. A., Siy, A., Stevens, K., Summers, D., Szabo, A., Timofeeva, M., Vaivads, A., Velli, M., Yehle, A., Werthimer, D., and Wygant, J. R. (2016). The FIELDS Instrument Suite for Solar Probe Plus. Measuring the Coronal Plasma and Magnetic Field, Plasma Waves and Turbulence, and Radio Signatures of Solar Transients. *ßr*, 204(1-4):49–82. 55, 78, 90, 122, 123

Bale, S. D., Horbury, T. S., Velli, M., Desai, M. I., Halekas, J. S., McManus, M. D., Panasenco, O., Badman, S. T., Bowen, T. A., Chandran, B. D. G., Drake, J. F., Kasper, J. C., Laker, R., Mallet, A., Matteini, L., Phan, T. D., Raouafi, N. E., Squire, J., Woodham, L. D., and Woolley, T. (2021). A Solar Source of Alfvénic Magnetic Field Switchbacks: In Situ Remnants of Magnetic Funnels on Supergranulation Scales. *The Astrophysical Journal*, 923(2):174. Publisher: American Astronomical Society. 70, 71, 74, 78, 88

Bame, S. J., McComas, D. J., Barraclough, B. L., Phillips, J. L., Sofaly, K. J., Chavez, J. C., Goldstein, B. E., and Sakurai, R. K. (1992). The Ulysses solar wind plasma experiment. *Astronomy and Astrophysics Supplement Series (ISSN 0365-0138), vol.*

92, no. 2, Jan. 1992, p. 237-265. Research supported by DOE., 92:237–265. ISBN: 0365-0138. 14

Bandyopadhyay, R., Matthaeus, W. H., McComas, D. J., Chhiber, R., Usmanov, A. V., Huang, J., Livi, R., Larson, D. E., Kasper, J. C., Case, A. W., Stevens, M., Whittlesey, P., Romeo, O. M., Bale, S. D., Bonnell, J. W., Wit, T. D. d., Goetz, K., Harvey, P. R., MacDowall, R. J., Malaspina, D. M., and Pulupa, M. (2022). Sub-Alfvénic Solar Wind Observed by the Parker Solar Probe: Characterization of Turbulence, Anisotropy, Intermittency, and Switchback. *The Astrophysical Journal Letters*, 926(1):L1. Publisher: The American Astronomical Society. 54

Banerjee, D., Krishna Prasad, S., Pant, V., McLaughlin, J. A., Antolin, P., Magyar, N., Ofman, L., Tian, H., Van Doorsselaere, T., De Moortel, I., and Wang, T. J. (2021). Magnetohydrodynamic Waves in Open Coronal Structures. *Space Science Reviews*, 217(7):76. 88, 103

Barnes, A. and Hollweg, J. V. (1974). Large-amplitude hydromagnetic waves. *Journal of Geophysical Research*, 79(16):2302–2318. 87

Bavassano, B., Dobrowolny, M., Fanfoni, G., Mariani, F., and Ness, N. F. (1982). Statistical properties of MHD fluctuations associated with high-speed streams from Helios-2 observations. *Solar Physics*, 78(2):373–384. 52, 94, 102

Belcher, J. W. (1971). ALFVÉNIC Wave Pressures and the Solar Wind. *Astrophysical Journal, vol. 168, p.509.* 19, 31, 87

Belcher, J. W. and Davis, L. (1971). Large-amplitude Alfvén waves in the interplanetary medium, 2. *Journal of Geophysical Research*, 76(16):3534–3563. 21, 31, 87

Belcher, J. W. and Olbert, S. (1975). Stellar winds driven by Alfvén waves. *The Astrophysical Journal*, 200:369–382. ISBN: 0004-637X. 19, 87

Bemporad, A., Matthaeus, W. H., and Poletto, G. (2008). Low-Frequency Lyα Power Spectra Observed by UVCS in a Polar Coronal Hole. *The Astrophysical Journal*, 677(2):L137. 52, 64, 104

Berger, T., Hillier, A., and Liu, W. (2017). Quiescent Prominence Dynamics Observed with the Hinode Solar Optical Telescope. II. Prominence Bubble Boundary Layer Characteristics and the Onset of a Coupled Kelvin–Helmholtz Rayleigh–Taylor Instability. *The Astrophysical Journal*, 850(1):60. Publisher: The American Astronomical Society. 79

Bizien, N., Wit, T. D. d., Froment, C., Velli, M., Case, A. W., Bale, S. D., Kasper, J., Whittlesey, P., MacDowall, R., and Larson, D. (2023). Are Switchback Boundaries Observed by Parker Solar Probe Closed? *The Astrophysical Journal*, 958(1):23. Publisher: The American Astronomical Society. 95

Bogdan, T. J., Hansteen, M. C. V., McMurry, A., Rosenthal, C. S., Johnson, M., Petty-Powell, S., Zita, E. J., Stein, R. F., McIntosh, S. W., and Nordlund, Å. (2003). Waves in the Magnetized Solar Atmosphere. II. Waves from Localized Sources in Magnetic Flux Concentrations. *The Astrophysical Journal*, 599(1):626. Publisher: IOP Publishing. 12, 38, 100

Boldyrev, S. (2005). On the Spectrum of Magnetohydrodynamic Turbulence. *The Astrophysical Journal*, 626(1):L37–L40. Publisher: American Astronomical Society. 60

Boldyrev, S. (2006). Spectrum of Magnetohydrodynamic Turbulence. *Physical Review Letters*, 96(11):115002. 22, 60

Boldyrev, S. and Perez, J. C. (2009). Spectrum of Weak Magnetohydrodynamic Turbulence. *Physical Review Letters*, 103(22):225001. Publisher: American Physical Society. 22

Borovikov, S. N. and Pogorelov, N. V. (2014). VOYAGER 1 NEAR THE HELIOPAUSE. *The Astrophysical Journal Letters*, 783(1):L16. Publisher: The American Astronomical Society. 8

Bourouaine, S., Perez, J. C., Klein, K. G., Chen, C. H. K., Martinović, M., Bale, S. D., Kasper, J. C., and Raouafi, N. E. (2020). Turbulence Characteristics of Switchback and Nonswitchback Intervals Observed by Parker Solar Probe. *apjl*, 904(2):L30. _eprint: 2010.00936. 57

Bowen, T. A., Badman, S., Hellinger, P., and Bale, S. D. (2018). Density Fluctuations in the Solar Wind Driven by Alfvén Wave Parametric Decay. *The Astrophysical Journal*, 854(2):L33. 67

Bowen, T. A., Bale, S. D., Bonnell, J. W., Dudok de Wit, T., Goetz, K., Goodrich, K., Gruesbeck, J., Harvey, P. R., Jannet, G., Koval, A., MacDowall, R. J., Malaspina, D. M., Pulupa, M., Revillet, C., Sheppard, D., and Szabo, A. (2020). A Merged Search-Coil and Fluxgate Magnetometer Data Product for Parker Solar Probe FIELDS. *Journal of Geophysical Research: Space Physics*, 125(5):e2020JA027813. _eprint: https://onlinelibrary.wiley.com/doi/pdf/10.1029/2020JA027813. 27, 79, 122, 123, 124

Bretherton, F. P. (1968). Wavetrains in inhomogeneous moving media. *Proceedings of the Royal Society of London. Series A. Mathematical and Physical Sciences*, 302(1471):529–554. 32, 33, 36, 48, 128

Bruno, R. and Carbone, V. (2013). The Solar Wind as a Turbulence Laboratory. *Living Reviews in Solar Physics*, 10(1):2. 24, 89, 93, 94, 102, 104

Bruno, R., Telloni, D., Sorriso-Valvo, L., Marino, R., Marco, R. D., and D'Amicis, R. (2019). The low-frequency break observed in the slow solar wind magnetic spectra. *Astronomy & Astrophysics*, 627:A96. Publisher: EDP Sciences. 52, 60, 102

Burlaga, L. F. and Goldstein, M. L. (1984). Radial variations of large-scale magnetohydrodynamic fluctuations in the solar wind. *Journal of Geophysical Research: Space Physics*, 89(A8):6813–6817. _eprint: https://onlinelibrary.wiley.com/doi/pdf/10.1029/JA089iA08p06813. 52, 94, 102

Cairns, R. A. and Lashmore-Davies, C. N. (1983). A unified theory of a class of mode conversion problems. *The Physics of Fluids*, 26(5):1268–1274. Publisher: American Institute of Physics. 46

Cally, P. (2000). Modelling p-Mode Interaction with a Spreading Sunspot Field. *Solar Physics*, 192(1):395–401. 12, 100

Cally, P. S. (2001). Note on an Exact Solution for Magnetoatmospheric Waves. *The Astrophysical Journal*, 548(1):473–481. Publisher: American Astronomical Society. 32, 46, 51

Cally, P. S. (2012). Alfvén Reflection and Reverberation in the Solar Atmosphere. *Solar Physics*, 280(1):33–50. 88

Cally, P. S. (2017). Alfvén waves in the structured solar corona. *Monthly Notices of the Royal Astronomical Society*, 466(1):413–424. 88, 100

Cally, P. S. and Bogdan, T. J. (1997). Simulation of f- and p-Mode Interactions with a Stratified Magnetic Field Concentration. *The Astrophysical Journal*, 486(1):L67. 12, 100

Cally, P. S. and Hansen, S. C. (2011). BENCHMARKING FAST-TO-ALFVÉN MODE CONVERSION IN A COLD MAGNETOHYDRODYNAMIC PLASMA. *The Astrophysical Journal*, 738(2):119. Publisher: The American Astronomical Society. 100

Chandran, B. D. G. (2018). Parametric instability, inverse cascade and the range of solar-wind turbulence. *Journal of Plasma Physics*, 84(1). Publisher: Cambridge University Press. 26, 52, 53, 55, 67, 68, 89, 102, 104, 135

Chandran, B. D. G. and Perez, J. C. (2019). Reflection-driven magnetohydrodynamic turbulence in the solar atmosphere and solar wind. *Journal of Plasma Physics*, 85(4):905850409. Publisher: Cambridge University Press. 22

Chaston, C. C., Bonnell, J. W., Bale, S. D., Kasper, J. C., Pulupa, M., Wit, T. D. d., Bowen, T. A., Larson, D. E., Whittlesey, P. L., Wygant, J. R., Salem, C. S., MacDowall, R. J., Livi, R. L., Vech, D., Case, A. W., Stevens, M. L., Korreck, K. E., Goetz, K., Harvey, P. R., and Malaspina, D. M. (2020). MHD Mode Composition in the Inner Heliosphere from the *Parker Solar Probe* 's First Perihelion. *The Astrophysical Journal Supplement Series*, 246(2):71. 31

Chen, C. H. K. (2022). A new way for turbulence to heat the corona. *Nature Astronomy*, 6(6):637–638. Number: 6 Publisher: Nature Publishing Group. 89

Chen, C. H. K., Bale, S. D., Bonnell, J. W., Borovikov, D., Bowen, T. A., Burgess, D., Case, A. W., Chandran, B. D. G., Wit, T. D. d., Goetz, K., Harvey, P. R., Kasper, J. C., Klein, K. G., Korreck, K. E., Larson, D., Livi, R., MacDowall, R. J., Malaspina, D. M., Mallet, A., McManus, M. D., Moncuquet, M., Pulupa, M., Stevens, M. L., and Whittlesey, P. (2020). The Evolution and Role of Solar Wind Turbulence in the Inner Heliosphere. *The Astrophysical Journal Supplement Series*, 246(2):53. 54, 60, 89, 104

Chitta, L. P., Zhukov, A. N., Berghmans, D., Peter, H., Parenti, S., Mandal, S., Aznar Cuadrado, R., Schühle, U., Teriaca, L., Auchère, F., Barczynski, K., Buchlin, É., Harra, L., Kraaikamp, E., Long, D. M., Rodriguez, L., Schwanitz, C., Smith, P. J., Verbeeck, C., and Seaton, D. B. (2023). Picoflare jets power the solar wind emerging from a coronal hole on the Sun. *Science*, 381(6660):867–872. Publisher: American Association for the Advancement of Science. 70, 71, 74, 81, 86

Chiu, M., Von-Mehlem, U., Willey, C., Betenbaugh, T., Maynard, J., Krein, J., Conde, R., Gray, W., Hunt, J., Mosher, L., McCullough, M., Panneton, P., Staiger, J., and Rodberg, E. (1998). ACE Spacecraft. *Space Science Reviews*, 86(1):257–284. 22

Coleman, Paul J., J. (1968). Turbulence, Viscosity, and Dissipation in the Solar-Wind Plasma. *apj*, 153:371. 31

Coleman, P. J. (1967). Wave-like phenomena in the interplanetary plasma: Mariner 2. *Planetary and Space Science*, 15(6):953–973. 31

Cram, L. E. (1978). High resolution spectroscopy of the disk chromosphere. VI. Power, phase and coherence spectra of atmospheric oscillations. *Astronomy and Astrophysics, Vol. 70, p. 345 (1978)*, 70:345. ISBN: 0004-6361. 10

Cranmer, S. R. and Ballegooijen, A. A. v. (2005). On the Generation, Propagation, and Reflection of Alfven Waves from the Solar Photosphere to the Distant Heliosphere. *The Astrophysical Journal Supplement Series*, 156(2):265–293. Publisher: American Astronomical Society. 54, 88

Credland, J., Mecke, G., and Ellwood, J. (1997). THE CLUSTER MISSION: ESA'S SPACEFLEET TO THE MAGNETOSPHERE. *Space Science Reviews*, 79(1):33–64. 22

Crouch, A. and Cally, P. (2003). Mode Conversion of Solar p Modes in non-Vertical Magnetic Fields – i. two-Dimensional Model. *Solar Physics*, 214(2):201–226. 12, 100

Cuesta, M. E., Chhiber, R., Roy, S., Goodwill, J., Pecora, F., Jarosik, J., Matthaeus, W. H., Parashar, T. N., and Bandyopadhyay, R. (2022). Isotropization and Evolution of Energy-Containing Eddies in Solar Wind Turbulence: Parker Solar Probe, Helios 1, ACE, WIND, and Voyager 1. *The Astrophysical Journal Letters*, 932(1):L11. arXiv:2205.00526 [astro-ph, physics:physics]. 66

Davis, N., Chandran, B. D. G., Bowen, T. A., Badman, S. T., Wit, T. D. d., Chen, C. H. K., Bale, S. D., Huang, Z., Sioulas, N., and Velli, M. (2023). The Evolution

of the 1/f Range within a Single Fast-solar-wind Stream between 17.4 and 45.7 Solar Radii. *The Astrophysical Journal*, 950(2):154. Publisher: The American Astronomical Society. 70, 71, 89, 94, 103, 135

De Pontieu, B., McIntosh, S. W., Carlsson, M., Hansteen, V. H., Tarbell, T. D., Schrijver, C. J., Title, A. M., Shine, R. A., Tsuneta, S., Katsukawa, Y., Ichimoto, K., Suematsu, Y., Shimizu, T., and Nagata, S. (2007). Chromospheric Alfvénic Waves Strong Enough to Power the Solar Wind. *Science*, 318(5856):1574–1577. Publisher: American Association for the Advancement of Science. 10, 88, 102

DeForest, C. E., Howard, T. A., and McComas, D. J. (2014). INBOUND WAVES IN THE SOLAR CORONA: A DIRECT INDICATOR OF ALFVÉN SURFACE LOCATION. *The Astrophysical Journal*, 787(2):124. Publisher: The American Astronomical Society. 7

Del Zanna, L. (2001). Parametric decay of oblique arc-polarized Alfvén waves. *Geophysical Research Letters*, 28(13):2585–2588. _eprint: https://onlinelibrary.wiley.com/doi/pdf/10.1029/2001GL012911. 117

Denskat, K. U. and Neubauer, F. M. (1982). Statistical properties of low-frequency magnetic field fluctuations in the solar wind from 0.29 to 1.0 AU during solar minimum conditions: HELIOS 1 and HELIOS 2. *Journal of Geophysical Research: Space Physics*, 87(A4):2215–2223. _eprint: https://onlinelibrary.wiley.com/doi/pdf/10.1029/JA087iA04p02215. 52, 94, 102

Deubner, F.-L. (1974). Some properties of velocity fields in the solar photosphere. *Solar Physics*, 39(1):31–48. 10

Dewar, R. L. (1970). Interaction between Hydromagnetic Waves and a Time-Dependent, Inhomogeneous Medium. *Physics of Fluids*, 13(11):2710. 32, 33, 34, 48, 128

Dmitruk, P. and Matthaeus, W. H. (2007). Low-frequency $1/f$ fluctuations in hydrodynamic and magnetohydrodynamic turbulence. *Physical Review E*, 76(3):036305. Publisher: American Physical Society. 52, 67

Dmitruk, P., Mininni, P. D., Pouquet, A., Servidio, S., and Matthaeus, W. H. (2011). Emergence of very long time fluctuations and $1/f$ noise in ideal flows. *Physical Review E*, 83(6):066318. Publisher: American Physical Society. 104

Drake, J. F., Agapitov, O., Swisdak, M., Badman, S. T., Bale, S. D., Horbury, T. S., Kasper, J. C., MacDowall, R. J., Mozer, F. S., and Phan, T. D. (2021). Switchbacks as signatures of magnetic flux ropes generated by interchange reconnection in the corona. *Astronomy & Astrophysics*, 650:A2. ISBN: 0004-6361 Publisher: EDP Sciences. 88, 95

Dudok de Wit, T., Krasnoselskikh, V. V., Bale, S. D., Bonnell, J. W., Bowen, T. A., Chen, C. H. K., Froment, C., Goetz, K., Harvey, P. R., Jagarlamudi, V. K., Larosa, A., MacDowall, R. J., Malaspina, D. M., Matthaeus, W. H., Pulupa, M., Velli, M., and

Whittlesey, P. L. (2020). Switchbacks in the Near-Sun Magnetic Field: Long Memory and Impact on the Turbulence Cascade. *The Astrophysical Journal Supplement Series*, 246(2):39. 57, 95

Dunn, C., Bowen, T., Mallet, A., Badman, S., and Bale, S. (2023). Effect of Spherical Polarization on the Magnetic Spectrum of the Solar Wind. arXiv:2305.09763 [astro-ph, physics:physics]. 89

Elliott, I. (1969). Power spectra of Hα Doppler shifts. *Solar Physics*, 6(1):28–40. 10

Erofeev, D. V. (2019). Characteristics of Arc-Polarized Alfvén Waves in the Near-Earth Solar Wind. *Geomagnetism and Aeronomy*, 59(8):1081–1087. 117

Fargette, N., Lavraud, B., Rouillard, A. P., Réville, V., Wit, T. D. D., Froment, C., Halekas, J. S., Phan, T. D., Malaspina, D. M., Bale, S. D., Kasper, J. C., Louarn, P., Case, A. W., Korreck, K. E., Larson, D. E., Pulupa, M., Stevens, M. L., Whittlesey, P. L., and Berthomier, M. (2021). Characteristic Scales of Magnetic Switchback Patches Near the Sun and Their Possible Association With Solar Supergranulation and Granulation. *The Astrophysical Journal*, 919(2):96. Publisher: The American Astronomical Society. 70, 74, 78

Farrell, W. M., MacDowall, R. J., Gruesbeck, J. R., Bale, S. D., and Kasper, J. C. (2020). Magnetic Field Dropouts at Near-Sun Switchback Boundaries: A Superposed Epoch Analysis. *The Astrophysical Journal Supplement Series*, 249:28. ADS Bibcode: 2020ApJS..249...28F. 57

Fleck, B. and Schmitz, F. (1991). The 3-min oscillations of the solar chromosphere-A basic physical effect? *Astronomy and Astrophysics (ISSN 0004-6361), vol. 250, no. 1, Oct. 1991, p. 235-244.*, 250:235–244. ISBN: 0004-6361. 10, 88

Forman, M. A., Wicks, R. T., and Horbury, T. S. (2011). DETAILED FIT OF "CRITICAL BALANCE" THEORY TO SOLAR WIND TURBULENCE MEASUREMENTS. *The Astrophysical Journal*, 733(2):76. 66

Foukal, P. (2004). *Solar astrophysics*. Wiley-VCH, Weinheim, 2nd rev. ed edition. 88

Fox, N. J., Velli, M. C., Bale, S. D., Decker, R., Driesman, A., Howard, R. A., Kasper, J. C., Kinnison, J., Kusterer, M., Lario, D., Lockwood, M. K., McComas, D. J., Raouafi, N. E., and Szabo, A. (2016). The Solar Probe Plus Mission: Humanity's First Visit to Our Star. *Space Science Reviews*, 204(1-4):7–48. 6, 8, 16, 27, 54, 70, 86, 89

Fu, X., Li, H., Guo, F., Li, X., and Roytershteyn, V. (2018). Parametric Decay Instability and Dissipation of Low-frequency Alfvén Waves in Low-beta Turbulent Plasmas. *The Astrophysical Journal*, 855(2):139. Publisher: The American Astronomical Society. 66

Gary, G. A. (2001). Plasma Beta above a Solar Active Region: Rethinking the Paradigm. *Solar Physics*, 203(1):71–86. 11

Goldreich, P. and Sridhar, S. (1995). Toward a Theory of Interstellar Turbulence. II. Strong Alfvenic Turbulence. *The Astrophysical Journal*, 438:763. 22, 66

Goldreich, P. and Sridhar, S. (1997). Magnetohydrodynamic Turbulence Revisited. *apj*, 485(2):680–688. _eprint: astro-ph/9612243. 60

Grappin, R. and Velli, M. (1996). Waves and streams in the expanding solar wind. *Journal of Geophysical Research: Space Physics*, 101(A1):425–444. 39, 50

Grappin, R., Velli, M., and Mangeney, A. (1993). Nonlinear wave evolution in the expanding solar wind. *Physical Review Letters*, 70(14):2190–2193. Publisher: American Physical Society. 39, 50

Gringauz, K. I., Bezrukikh, V. V., Ozerov, V. D., and Rybchinskii, R. E. (1962). The study of interplanetary ionized gas, high-energy electrons and corpuscular radiation of the sun, employing three-electrode charged particle traps on the second Soviet space rocket. *Planetary and Space Science*, 9:103–107. ADS Bibcode: 1962P&SS....9..103G. 87

Gurnett, D. A. and Kurth, W. S. (2019). Plasma densities near and beyond the heliopause from the Voyager 1 and 2 plasma wave instruments. *Nature Astronomy*, 3(11):1024–1028. Publisher: Nature Publishing Group. 8

Hansen, S. C. and Cally, P. S. (2012). BENCHMARKING FAST-TO-ALFVÉN MODE CONVERSION IN A COLD MHD PLASMA. II. HOW TO GET ALFVÉN WAVES THROUGH THE SOLAR TRANSITION REGION. *The Astrophysical Journal*, 751(1):31. Publisher: The American Astronomical Society. 88, 101

Hansteen, V. H. and Leer, E. (1995). Coronal heating, densities, and temperatures and solar wind acceleration. *Journal of Geophysical Research: Space Physics*, 100(A11):21577–21593. _eprint: https://onlinelibrary.wiley.com/doi/pdf/10.1029/95JA02300. 103

Hansteen, V. H. and Velli, M. (2012). Solar Wind Models from the Chromosphere to 1 AU. *Space Science Reviews*, 172(1-4):89–121. 87

Harris, C. R., Millman, K. J., van der Walt, S. J., Gommers, R., Virtanen, P., Cournapeau, D., Wieser, E., Taylor, J., Berg, S., Smith, N. J., Kern, R., Picus, M., Hoyer, S., van Kerkwijk, M. H., Brett, M., Haldane, A., del Río, J. F., Wiebe, M., Peterson, P., Gérard-Marchant, P., Sheppard, K., Reddy, T., Weckesser, W., Abbasi, H., Gohlke, C., and Oliphant, T. E. (2020). Array programming with NumPy. *Nature*, 585(7825):357–362. Number: 7825 Publisher: Nature Publishing Group. 122

Heinemann, M. and Olbert, S. (1980). Non-WKB Alfvén waves in the solar wind. *Journal of Geophysical Research: Space Physics*, 85(A3):1311–1327. 19, 32, 54, 85, 101, 128

Hernández, C. S., Sorriso-Valvo, L., Bandyopadhyay, R., Chasapis, A., Vásconez, C. L., Marino, R., and Pezzi, O. (2021). Impact of Switchbacks on Turbulent Cascade and Energy Transfer Rate in the Inner Heliosphere. *The Astrophysical Journal Letters*, 922(1):L11. 57

Hirota, M. and Tokuda, S. (2010). Wave-action conservation law for eigenmodes and continuum modes. *Physics of Plasmas*, 17(8):082109. 33

Hollweg, J. V. (1971). Density fluctuations driven by Alfvén waves. *Journal of Geophysical Research (1896-1977)*, 76(22):5155–5161. Publisher: John Wiley & Sons, Ltd. 31, 38, 46, 51, 126

Hollweg, J. V. (1973). Alfvén waves in the solar wind: Wave pressure, poynting flux, and angular momentum. *Journal of Geophysical Research (1896-1977)*, 78(19):3643–3652. _eprint: https://onlinelibrary.wiley.com/doi/pdf/10.1029/JA078i019p03643. 19, 85

Hollweg, J. V. (1974). Transverse Alfvén waves in the solar wind: Arbitrary k, v 0, B 0, and $|\delta B|$. *Journal of Geophysical Research (1896-1977)*, 79(10):1539–1541. _eprint: https://onlinelibrary.wiley.com/doi/pdf/10.1029/JA079i010p01539. 117

Hollweg, J. V. (1990). On WKB expansions for Alfvén waves in the solar wind. *Journal of Geophysical Research: Space Physics*, 95(A9):14873–14879. Edition: Hollweg, J. V. (1990), On WKB expansions for Alfvén waves in the solar wind, J. Geophys. Res., 95(A9), 14873-14879, doi:10.1029/JA095iA09p14873. Place: United States Publisher: Blackwell Publishing Ltd. 26, 101, 129

Hollweg, J. V. (1991). Alfvén Waves. In Ulmschneider, P., Priest, E. R., and Rosner, R., editors, *Mechanisms of Chromospheric and Coronal Heating*, pages 423–434, Berlin, Heidelberg. Springer. 18

Hollweg, J. V., Jackson, S., and Galloway, D. (1982). Alfvén waves in the solar atmosphere. *Solar Physics*, 75(1):35–61. 13, 18, 38

Huang, J., Kasper, J. C., Fisk, L. A., Larson, D. E., McManus, M. D., Chen, C. H. K., Martinović, M. M., Klein, K. G., Thomas, L., Liu, M., Maruca, B. A., Zhao, L., Chen, Y., Hu, Q., Jian, L. K., Verniero, J. L., Velli, M., Livi, R., Whittlesey, P., Rahmati, A., Romeo, O., Niembro, T., Paulson, K., Stevens, M., Case, A. W., Pulupa, M., Bale, S. D., and Halekas, J. S. (2023a). The Structure and Origin of Switchbacks: Parker Solar Probe Observations. *The Astrophysical Journal*, 952(1):33. Publisher: The American Astronomical Society. 57, 95

Huang, Z., Shi, C., Sioulas, N., and Velli, M. (2022). Conservation of Total Wave Action in the Expanding Solar Wind. *The Astrophysical Journal*, 935(1):60. Publisher: American Astronomical Society. 54, 85

Huang, Z., Shi, C., Velli, M., Sioulas, N., Panasenco, O., Bowen, T., Matteini, L., Xia, M., Shi, X., Huang, S., Huang, J., and Casillas, L. (2023b). In situ Remnants of

Solar Surface Structures from Jensen-Shannon Scalogram. Publisher: arXiv Version Number: 1. 94, 96

Huang, Z., Sioulas, N., Shi, C., Velli, M., Bowen, T., Davis, N., Chandran, B. D. G., Matteini, L., Kang, N., Shi, X., Huang, J., Bale, S. D., Kasper, J. C., Larson, D. E., Livi, R., Whittlesey, P. L., Rahmati, A., Paulson, K., Stevens, M., Case, A. W., Wit, T. D. d., Malaspina, D. M., Bonnell, J. W., Goetz, K., Harvey, P. R., and MacDowall, R. J. (2023c). New Observations of Solar Wind 1/f Turbulence Spectrum from Parker Solar Probe. *The Astrophysical Journal Letters*, 950(1):L8. Publisher: The American Astronomical Society. 89, 94, 103

Iroshnikov, P. S. (1964). Turbulence of a Conducting Fluid in a Strong Magnetic Field. *sovast*, 7:566. 22, 60

Jacques, S. (1977). Momentum and energy transport by waves in the solar atmosphere and solar wind. *Astrophysical Journal*, 215(3):942–951. Place: United States. 32

Jagarlamudi, V. K., Raouafi, N. E., Bourouaine, S., Mostafavi, P., Larosa, A., and Perez, J. C. (2023). Occurrence and Evolution of Switchbacks in the Inner Heliosphere: Parker Solar Probe Observations. *The Astrophysical Journal Letters*, 950(1):L7. Publisher: The American Astronomical Society. 95

Jess, D. B., Mathioudakis, M., Erdélyi, R., Crockett, P. J., Keenan, F. P., and Christian, D. J. (2009). Alfvén Waves in the Lower Solar Atmosphere. *Science*, 323(5921):1582–1585. Publisher: American Association for the Advancement of Science. 88

Jess, D. B., Moortel, I. D., Mathioudakis, M., Christian, D. J., Reardon, K. P., Keys, P. H., and Keenan, F. P. (2012). THE SOURCE OF 3 MINUTE MAGNETOACOUSTIC OSCILLATIONS IN CORONAL FANS. *The Astrophysical Journal*, 757(2):160. Publisher: The American Astronomical Society. 88

Jess, D. B., Morton, R. J., Verth, G., Fedun, V., Grant, S. D. T., and Giagkiozis, I. (2015). Multiwavelength Studies of MHD Waves in the Solar Chromosphere. *Space Science Reviews*, 190(1):103–161. 88

Johnston, Z., Squire, J., Mallet, A., and Meyrand, R. (2022). On the properties of Alfvénic switchbacks in the expanding solar wind: Three-dimensional numerical simulations. *Physics of Plasmas*, 29(7):072902. 117

Kasper, J. C., Abiad, R., Austin, G., Balat-Pichelin, M., Bale, S. D., Belcher, J. W., Berg, P., Bergner, H., Berthomier, M., Bookbinder, J., Brodu, E., Caldwell, D., Case, A. W., Chandran, B. D. G., Cheimets, P., Cirtain, J. W., Cranmer, S. R., Curtis, D. W., Daigneau, P., Dalton, G., Dasgupta, B., DeTomaso, D., Diaz-Aguado, M., Djordjevic, B., Donaskowski, B., Effinger, M., Florinski, V., Fox, N., Freeman, M., Gallagher, D., Gary, S. P., Gauron, T., Gates, R., Goldstein, M., Golub, L., Gordon, D. A., Gurnee, R., Guth, G., Halekas, J., Hatch, K., Heerikuisen, J., Ho, G., Hu, Q., Johnson, G., Jordan, S. P., Korreck, K. E., Larson, D., Lazarus, A. J., Li, G., Livi,

R., Ludlam, M., Maksimovic, M., McFadden, J. P., Marchant, W., Maruca, B. A., McComas, D. J., Messina, L., Mercer, T., Park, S., Peddie, A. M., Pogorelov, N., Reinhart, M. J., Richardson, J. D., Robinson, M., Rosen, I., Skoug, R. M., Slagle, A., Steinberg, J. T., Stevens, M. L., Szabo, A., Taylor, E. R., Tiu, C., Turin, P., Velli, M., Webb, G., Whittlesey, P., Wright, K., Wu, S. T., and Zank, G. (2016). Solar Wind Electrons Alphas and Protons (SWEAP) Investigation: Design of the Solar Wind and Coronal Plasma Instrument Suite for Solar Probe Plus. *ßr*, 204(1-4):131–186. 27, 55, 72

Kasper, J. C., Bale, S. D., Belcher, J. W., Berthomier, M., Case, A. W., Chandran, B. D., Curtis, D. W., Gallagher, D., Gary, S. P., and Golub, L. (2019). Alfvénic velocity spikes and rotational flows in the near-Sun solar wind. *Nature*, 576(7786):228–231. ISBN: 0028-0836 Publisher: Nature Publishing Group UK London. 70, 90

Kasper, J. C., Klein, K. G., Lichko, E., Huang, J., Chen, C. H. K., Badman, S. T., Bonnell, J., Whittlesey, P. L., Livi, R., Larson, D., Pulupa, M., Rahmati, A., Stansby, D., Korreck, K. E., Stevens, M., Case, A. W., Bale, S. D., Maksimovic, M., Moncuquet, M., Goetz, K., Halekas, J. S., Malaspina, D., Raouafi, N. E., Szabo, A., MacDowall, R., Velli, M., Dudok de Wit, T., and Zank, G. P. (2021). Parker Solar Probe Enters the Magnetically Dominated Solar Corona. *Physical Review Letters*, 127(25):255101. Publisher: American Physical Society. 27, 60, 70, 83, 84, 89, 117, 127

Keshner, M. (1982). 1/f noise. *Proceedings of the IEEE*, 70(3):212–218. Conference Name: Proceedings of the IEEE. 52, 104

Khomenko, E. and Cally, P. S. (2012). NUMERICAL SIMULATIONS OF CONVERSION TO ALFVÉN WAVES IN SUNSPOTS. *The Astrophysical Journal*, 746(1):68. Publisher: The American Astronomical Society. 12, 100

Khomenko, E. and Cally, P. S. (2019). Fast-to-Alfvén Mode Conversion and Ambipolar Heating in Structured Media. II. Numerical Simulation. *The Astrophysical Journal*, 883(2):179. Publisher: The American Astronomical Society. 100

Kiyani, K. H., Osman, K. T., and Chapman, S. C. (2015). Dissipation and heating in solar wind turbulence: from the macro to the micro and back again. *Philosophical Transactions of the Royal Society A: Mathematical, Physical and Engineering Sciences*, 373(2041):20140155. Publisher: Royal Society. 22

Kobanov, N. I., Chelpanov, A. A., and Kolobov, D. Y. (2013). Oscillations above sunspots from the temperature minimum to the corona. *Astronomy & Astrophysics*, 554:A146. Publisher: EDP Sciences. 9

Kolmogorov, A. (1941). The Local Structure of Turbulence in Incompressible Viscous Fluid for Very Large Reynolds' Numbers. *Akademiia Nauk SSSR Doklady*, 30:301–305. 21, 60

Kraichnan, R. (1965). Inertial-Range Spectrum of Hydromagnetic Turbulence. 22, 60

Kruparova, O., Krupar, V., Szabo, A., Pulupa, M., and Bale, S. D. (2023). Quasi-thermal Noise Spectroscopy Analysis of Parker Solar Probe Data: Improved Electron Density Model for Solar Wind. *The Astrophysical Journal*, 957(1):13. 85, 90

Kullback, S. and Leibler, R. A. (1951). On Information and Sufficiency. *The Annals of Mathematical Statistics*, 22(1):79–86. Publisher: Institute of Mathematical Statistics. 120

Kumar, P., Karpen, J. T., Uritsky, V. M., Deforest, C. E., Raouafi, N. E., and DeVore, C. R. (2022). Quasi-periodic Energy Release and Jets at the Base of Solar Coronal Plumes. *The Astrophysical Journal*, 933(1):21. Publisher: The American Astronomical Society. 88

Kumar, P., Karpen, J. T., Uritsky, V. M., Deforest, C. E., Raouafi, N. E., DeVore, C. R., and Antiochos, S. K. (2023). New Evidence on the Origin of Solar Wind Microstreams/Switchbacks. *The Astrophysical Journal Letters*, 951(1):L15. arXiv:2305.06914 [astro-ph, physics:physics]. 88

Kuniyoshi, H., Shoda, M., Morton, R. J., and Yokoyama, T. (2023). Can the solar p-modes contribute to the high-frequency transverse oscillations of spicules? Publisher: arXiv Version Number: 1. 88

Kuridze, D. and Zaqarashvili, T. (2008). Resonant energy conversion of 3-min intensity oscillations into Alfvén waves in the solar atmosphere. *Journal of Atmospheric and Solar-Terrestrial Physics*, 70(2-4):351–355. 88

Laker, R., Horbury, T. S., Bale, S. D., Matteini, L., Woolley, T., Woodham, L. D., Badman, S. T., Pulupa, M., Kasper, J. C., Stevens, M., Case, A. W., and Korreck, K. E. (2021). Statistical analysis of orientation, shape, and size of solar wind switchbacks. *Astronomy and Astrophysics*, 650:A1. 57

Larosa, A., Chen, C. H. K., McIntyre, J. R., and Jagarlamudi, V. K. (2023). The relation between magnetic switchbacks and turbulence in the inner heliosphere. arXiv:2312.16521 [astro-ph, physics:physics]. 89, 95

Larosa, A., Krasnoselskikh, V., Wit, T. D. d., Agapitov, O., Froment, C., Jagarlamudi, V. K., Velli, M., Bale, S. D., Case, A. W., Goetz, K., Harvey, P., Kasper, J. C., Korreck, K. E., Larson, D. E., MacDowall, R. J., Malaspina, D., Pulupa, M., Revillet, C., and Stevens, M. L. (2021). Switchbacks: statistical properties and deviations from Alfvénicity. *Astronomy & Astrophysics*, 650:A3. Publisher: EDP Sciences. 57

Leer, E. and Holzer, T. E. (1980). Energy addition in the solar wind. *Journal of Geophysical Research: Space Physics*, 85(A9):4681–4688. _eprint: https://onlinelibrary.wiley.com/doi/pdf/10.1029/JA085iA09p04681. 87

Leibacher, J. and Stein, R. F. (1971). NEW DESCRIPTION OF THE SOLAR FIVE-MINUTE OSCILLATION. *Astrophys. Lett. 7: 191-2(Jan 1971).* Institution: Harvard Coll. Observatory, Cambridge, Mass. 10

Leighton, R. B., Noyes, R. W., and Simon, G. W. (1962). Velocity Fields in the Solar Atmosphere. I. Preliminary Report. *The Astrophysical Journal*, 135:474. Publisher: IOP ADS Bibcode: 1962ApJ...135..474L. 2, 9

Lin, J. (1991). Divergence measures based on the Shannon entropy. *IEEE Transactions on Information Theory*, 37(1):145–151. Conference Name: IEEE Transactions on Information Theory. 72, 120

Linsky, J. L. (1980). Stellar Chromospheres. *International Astronomical Union Colloquium*, 51:248–277. 2

Linsky, J. L. (2017). Stellar Model Chromospheres and Spectroscopic Diagnostics. *Annual Review of Astronomy and Astrophysics*, 55(Volume 55, 2017):159–211. Publisher: Annual Reviews. 2

Livi, R., Larson, D. E., Kasper, J. C., Abiad, R., Case, A. W., Klein, K. G., Curtis, D. W., Dalton, G., Stevens, M., Korreck, K. E., Ho, G., Robinson, M., Tiu, C., Whittlesey, P. L., Verniero, J. L., Halekas, J., McFadden, J., Marckwordt, M., Slagle, A., Abatcha, M., Rahmati, A., and McManus, M. D. (2022). The Solar Probe ANalyzer—Ions on the Parker Solar Probe. *The Astrophysical Journal*, 938(2):138. 56

Lou, Y.-Q. (1993a). Propagation of three-dimensional Alfvén waves and its nonlinear effects in the solar wind. *Journal of Geophysical Research: Space Physics*, 98(A3):3563–3584. _eprint: https://onlinelibrary.wiley.com/doi/pdf/10.1029/92JA02243. 32

Lou, Y.-Q. (1993b). Three-dimensional nonsteady compressible magnetohydrodynamic fluctuations in the solar wind. *Journal of Geophysical Research: Space Physics*, 98(A7):11483–11500. _eprint: https://onlinelibrary.wiley.com/doi/pdf/10.1029/93JA01033. 32

Lou, Y.-Q. (1993c). Three-dimensional steady compressible perturbations in the magnetohydrodynamic solar wind. *Journal of Geophysical Research: Space Physics*, 98(A7):11501–11512. _eprint: https://onlinelibrary.wiley.com/doi/pdf/10.1029/93JA00633. 32

Lundgren, T. S. (1963). Hamilton's Variational Principle for a Perfectly Conducting Plasma Continuum. *Physics of Fluids*, 6(7):898. 34

Magyar, N. and Doorsselaere, T. V. (2022). Phase Mixing and the 1/f Spectrum in the Solar Wind. *The Astrophysical Journal*, 938(2):98. Publisher: The American Astronomical Society. 26, 52, 67, 104

Mallet, A. and Chandran, B. D. G. (2021). Exact nonlinear solutions for three-dimensional Alfvén-wave packets in relativistic magnetohydrodynamics. *Journal of Plasma Physics*, 87(6):175870601. Publisher: Cambridge University Press. 57

Mallet, A., Squire, J., Chandran, B. D. G., Bowen, T., and Bale, S. D. (2021). Evolution of Large-amplitude Alfvén Waves and Generation of Switchbacks in the Expanding

Solar Wind. *The Astrophysical Journal*, 918(2):62. Publisher: American Astronomical Society. 57

Mandal, S., Chitta, L. P., Antolin, P., Peter, H., Solanki, S. K., Auchère, F., Berghmans, D., Zhukov, A. N., Teriaca, L., Cuadrado, R. A., Schühle, U., Parenti, S., Buchlin, É., Harra, L., Verbeeck, C., Kraaikamp, E., Long, D. M., Rodriguez, L., Pelouze, G., Schwanitz, C., Barczynski, K., and Smith, P. J. (2022). What drives decayless kink oscillations in active-region coronal loops on the Sun? *Astronomy & Astrophysics*, 666:L2. Publisher: EDP Sciences. 10, 88

Marsch, E. (1991). MHD Turbulence in the Solar Wind. In Schwenn, R. and Marsch, E., editors, *Physics of the Inner Heliosphere II: Particles, Waves and Turbulence*, Physics and Chemistry in Space, pages 159–241. Springer, Berlin, Heidelberg. 31

Martinović, M. M., Klein, K. G., Huang, J., Chandran, B. D. G., Kasper, J. C., Lichko, E., Bowen, T., Chen, C. H. K., Matteini, L., Stevens, M., Case, A. W., and Bale, S. D. (2021). Multiscale Solar Wind Turbulence Properties inside and near Switchbacks Measured by the Parker Solar Probe. *The Astrophysical Journal*, 912:28. ADS Bibcode: 2021ApJ...912...28M. 57

Mathioudakis, M., Jess, D. B., and Erdélyi, R. (2013). Alfvén Waves in the Solar Atmosphere. *Space Science Reviews*, 175(1):1–27. 88

Matteini, L., Horbury, T. S., Neugebauer, M., and Goldstein, B. E. (2014). Dependence of solar wind speed on the local magnetic field orientation: Role of Alfvénic fluctuations. *Geophysical Research Letters*, 41:259–265. ADS Bibcode: 2014GeoRL..41..259M. 21, 84, 87, 95, 117

Matteini, L., Horbury, T. S., Pantellini, F., Velli, M., and Schwartz, S. J. (2015). ION KINETIC ENERGY CONSERVATION AND MAGNETIC FIELD STRENGTH CONSTANCY IN MULTI-FLUID SOLAR WIND ALFVÉNIC TURBULENCE. *The Astrophysical Journal*, 802(1):11. 84

Matteini, L., Landi, S., Del Zanna, L., Velli, M., and Hellinger, P. (2010). Parametric decay of linearly polarized shear Alfvén waves in oblique propagation: One and two-dimensional hybrid simulations. *Geophysical Research Letters*, 37:L20101. ADS Bibcode: 2010GeoRL..3720101M. 67

Matteini, L., Stansby, D., Horbury, T. S., and Chen, C. H. K. (2018). On the $1/f$ Spectrum in the Solar Wind and Its Connection with Magnetic Compressibility. *The Astrophysical Journal*, 869(2):L32. 26, 52, 53, 55, 67, 68, 104

Matteini, L., Tenerani, A., Landi, S., Verdini, A., Velli, M., Hellinger, P., Franci, L., Horbury, T. S., Papini, E., and Stawarz, J. E. (2024). Alfvénic fluctuations in the expanding solar wind: Formation and radial evolution of spherical polarization. *Physics of Plasmas*, 31(3):032901. 83, 87

Matthaeus, W. H. (2021). Turbulence in space plasmas: Who needs it? *Physics of Plasmas*, 28(3):032306. Publisher: American Institute of Physics. 89

Matthaeus, W. H., Breech, B., Dmitruk, P., Bemporad, A., Poletto, G., Velli, M., and Romoli, M. (2007). Density and Magnetic Field Signatures of Interplanetary 1/f Noise. *The Astrophysical Journal*, 657(2):L121. Publisher: IOP Publishing. 26, 52, 64, 68, 104

Matthaeus, W. H. and Goldstein, M. L. (1986). Low-Frequency $\frac{1}{f}$ Noise in the Interplanetary Magnetic Field. *Physical Review Letters*, 57(4):495–498. Publisher: American Physical Society. 26, 52, 53, 61, 67, 68, 104

Matthaeus, W. H., Goldstein, M. L., and Smith, C. (1982). Evaluation of Magnetic Helicity in Homogeneous Turbulence. *Physical Review Letters*, 48(18):1256–1259. 64

Matthaeus, W. H., Zank, G. P., and Oughton, S. (1996). Phenomenology of hydromagnetic turbulence in a uniformly expanding medium. *Journal of Plasma Physics*, 56(3):659–675. Publisher: Cambridge University Press. 22

McComas, D. J., Alexander, N., Angold, N., Bale, S., Beebe, C., Birdwell, B., Boyle, M., Burgum, J. M., Burnham, J. A., Christian, E. R., Cook, W. R., Cooper, S. A., Cummings, A. C., Davis, A. J., Desai, M. I., Dickinson, J., Dirks, G., Do, D. H., Fox, N., Giacalone, J., Gold, R. E., Gurnee, R. S., Hayes, J. R., Hill, M. E., Kasper, J. C., Kecman, B., Klemic, J., Krimigis, S. M., Labrador, A. W., Layman, R. S., Leske, R. A., Livi, S., Matthaeus, W. H., McNutt, R. L., Mewaldt, R. A., Mitchell, D. G., Nelson, K. S., Parker, C., Rankin, J. S., Roelof, E. C., Schwadron, N. A., Seifert, H., Shuman, S., Stokes, M. R., Stone, E. C., Vandegriff, J. D., Velli, M., von Rosenvinge, T. T., Weidner, S. E., Wiedenbeck, M. E., and Wilson, P. (2016). Integrated Science Investigation of the Sun (ISIS): Design of the Energetic Particle Investigation. *Space Science Reviews*, 204(1):187–256. 27

McComas, D. J., Barraclough, B. L., Funsten, H. O., Gosling, J. T., Santiago-Muñoz, E., Skoug, R. M., Goldstein, B. E., Neugebauer, M., Riley, P., and Balogh, A. (2000). Solar wind observations over Ulysses' first full polar orbit. *Journal of Geophysical Research: Space Physics*, 105(A5):10419–10433. _eprint: https://onlinelibrary.wiley.com/doi/pdf/10.1029/1999JA000383. 14, 19, 87

McComas, D. J., Elliott, H. A., Schwadron, N. A., Gosling, J. T., Skoug, R. M., and Goldstein, B. E. (2003). The three-dimensional solar wind around solar maximum. *Geophysical Research Letters*, 30(10). _eprint: https://onlinelibrary.wiley.com/doi/pdf/10.1029/2003GL017136. 14, 16, 74, 86

McComas, D. J., Velli, M., Lewis, W. S., Acton, L. W., Balat-Pichelin, M., Bothmer, V., Dirling Jr., R. B., Feldman, W. C., Gloeckler, G., Habbal, S. R., Hassler, D. M., Mann, I., Matthaeus, W. H., McNutt Jr., R. L., Mewaldt, R. A., Murphy, N., Ofman, L., Sittler Jr., E. C., Smith, C. W., and Zurbuchen, T. H. (2007). Understanding coronal heating and solar wind acceleration: Case for in situ near-Sun measurements. *Reviews of Geophysics*, 45(1). _eprint: https://onlinelibrary.wiley.com/doi/pdf/10.1029/2006RG000195. 103

McDougall, A. M. D. and Hood, A. W. (2007a). MHD mode conversion in a stratified atmosphere. *Proceedings of the International Astronomical Union*, 3(S247):296–302. Publisher: Cambridge University Press. 33, 46, 51

McDougall, A. M. D. and Hood, A. W. (2007b). A New Look at Mode Conversion in a Stratified Isothermal Atmosphere. *Solar Physics*, 246(1):259–271. 33, 38, 46, 51

McDougall, A. M. D. and Hood, A. W. (2009). MHD Mode Conversion around a 2D Magnetic Null Point. *AIP Conference Proceedings*, 1094(1):752–755. Publisher: American Institute of Physics. 33, 51

McIntyre, J. R., Chen, C. H., and Larosa, A. (2023). Properties underlying the variation of the magnetic field spectral index in the inner solar wind. *The Astrophysical Journal*, 957(2):111. Publisher: IOP Publishing. 89

Meng, M.-M., Liu, Y. D., Chen, C., and Wang, R. (2022). Analysis of the Distribution, Rotation and Scale Characteristics of Solar Wind Switchbacks: Comparison between the First and Second Encounters of Parker Solar Probe. *Research in Astronomy and Astrophysics*, 22:035018. ADS Bibcode: 2022RAA....22c5018M. 57

Meyrand, R., Squire, J., Mallet, A., and Chandran, B. D. G. (2023). Reflection-driven turbulence in the super-Alfv\'enic solar wind. arXiv:2308.10389 [astro-ph, physics:physics]. 104

Moncuquet, M., Meyer-Vernet, N., Issautier, K., Pulupa, M., Bonnell, J. W., Bale, S. D., Wit, T. D. d., Goetz, K., Griton, L., Harvey, P. R., MacDowall, R. J., Maksimovic, M., and Malaspina, D. M. (2020). First In Situ Measurements of Electron Density and Temperature from Quasi-thermal Noise Spectroscopy with Parker Solar Probe/FIELDS. *The Astrophysical Journal Supplement Series*, 246(2):44. Publisher: The American Astronomical Society. 55, 85

Monin, A. S. and Jaglom, A. M. (1987). *Statistical fluid mechanics. 2.* MIT Pr, Cambridge, Mass., 3. print edition. 53

Montroll, E. W. and Shlesinger, M. F. (1982). On 1/f noise and other distributions with long tails. *Proceedings of the National Academy of Sciences of the United States of America*, 79(10):3380–3383. 53, 104

Morton, R. J., Sharma, R., Tajfirouze, E., and Miriyala, H. (2023). Alfvénic waves in the inhomogeneous solar atmosphere. *Reviews of Modern Plasma Physics*, 7(1):17. 12, 88, 100, 102

Morton, R. J., Tomczyk, S., and Pinto, R. F. (2016). A GLOBAL VIEW OF VELOCITY FLUCTUATIONS IN THE CORONA BELOW 1.3 R? WITH CoMP. *The Astrophysical Journal*, 828(2):89. Publisher: The American Astronomical Society. 102

Morton, R. J., Verth, G., Fedun, V., Shelyag, S., and Erdélyi, R. (2013). EVIDENCE FOR THE PHOTOSPHERIC EXCITATION OF INCOMPRESSIBLE CHROMOSPHERIC WAVES. *The Astrophysical Journal*, 768(1):17. Publisher: The American Astronomical Society. 88

Morton, R. J., Verth, G., Jess, D. B., Kuridze, D., Ruderman, M. S., Mathioudakis, M., and Erdélyi, R. (2012). Observations of ubiquitous compressive waves in the Sun's chromosphere. *Nature Communications*, 3(1):1315. Number: 1 Publisher: Nature Publishing Group. 10, 88

Morton, R. J., Weberg, M. J., and McLaughlin, J. A. (2019). A basal contribution from p-modes to the Alfvénic wave flux in the Sun's corona. *Nature Astronomy*, 3(3):223–229. 10, 88, 102

Mozer, F. S., Agapitov, O. V., Bale, S. D., Bonnell, J. W., Goetz, K., Goodrich, K. A., Gore, R., Harvey, P. R., Kellogg, P. J., Malaspina, D., Pulupa, M., and Schumm, G. (2020). Time Domain Structures and Dust in the Solar Vicinity: *Parker Solar Probe* Observations. *The Astrophysical Journal Supplement Series*, 246(2):50. 57

Mozer, F. S., Bale, S. D., Bonnell, J. W., Drake, J. F., Hanson, E. L. M., and Mozer, M. C. (2021). On the Origin of Switchbacks Observed in the Solar Wind. *The Astrophysical Journal*, 919(1):60. Publisher: The American Astronomical Society. 95

Müller, D., St. Cyr, O. C., Zouganelis, I., Gilbert, H. R., Marsden, R., Nieves-Chinchilla, T., Antonucci, E., Auchère, F., Berghmans, D., Horbury, T. S., Howard, R. A., Krucker, S., Maksimovic, M., Owen, C. J., Rochus, P., Rodriguez-Pacheco, J., Romoli, M., Solanki, S. K., Bruno, R., Carlsson, M., Fludra, A., Harra, L., Hassler, D. M., Livi, S., Louarn, P., Peter, H., Schühle, U., Teriaca, L., del Toro Iniesta, J. C., Wimmer-Schweingruber, R. F., Marsch, E., Velli, M., De Groof, A., Walsh, A., and Williams, D. (2020). The Solar Orbiter mission. Science overview. *åp*, 642:A1. _eprint: 2009.00861. 70

Nakagawa, Y. and Levine, R. H. (1974). Dynamics of the Solar Magnetic Field. II. The Energy Spectrum of Large-Scale Solar Magnetic Fields. *The Astrophysical Journal*, 190:441–446. ADS Bibcode: 1974ApJ...190..441N. 68

Neugebauer, M., Goldstein, B. E., McComas, D. J., Suess, S. T., and Balogh, A. (1995). Ulysses observations of microstreams in the solar wind from coronal holes. *Journal of Geophysical Research: Space Physics*, 100(A12):23389–23395. _eprint: https://onlinelibrary.wiley.com/doi/pdf/10.1029/95JA02723. 14

Neugebauer, M. and Snyder, C. W. (1966). Mariner 2 observations of the solar wind: 1. Average properties. *Journal of Geophysical Research (1896-1977)*, 71(19):4469–4484. _eprint: https://onlinelibrary.wiley.com/doi/pdf/10.1029/JZ071i019p04469. 87

Nielsen, F. (2019). On the Jensen–Shannon Symmetrization of Distances Relying on Abstract Means. *Entropy*, 21(5):485. 122

Noyes, R. W. and Leighton, R. B. (1963). Velocity Fields in the Solar Atmosphere. II. The Oscillatory Field. *The Astrophysical Journal*, 138:631. Publisher: IOP ADS Bibcode: 1963ApJ...138..631N. 2, 9

Ofman, L., Nakariakov, V. M., and DeForest, C. E. (1999). Slow Magnetosonic Waves in Coronal Plumes. *The Astrophysical Journal*, 514(1):441–447. 31

Orrall, F. Q. (1966). Observational Study of Macroscopic Inhomogeneities in the Solar Atmosphere. VIII. Vertical Chromospheric Oscillations Measured in K_{3}. *The Astrophysical Journal*, 143:917. Publisher: IOP ADS Bibcode: 1966ApJ...143..917O. 10

Panasenco, O., Velli, M., D'Amicis, R., Shi, C., Réville, V., Bale, S. D., Badman, S. T., Kasper, J., Korreck, K., Bonnell, J. W., Wit, T. D. d., Goetz, K., Harvey, P. R., MacDowall, R. J., Malaspina, D. M., Pulupa, M., Case, A. W., Larson, D., Livi, R., Stevens, M., and Whittlesey, P. (2020). Exploring Solar Wind Origins and Connecting Plasma Flows from the Parker Solar Probe to 1 au: Nonspherical Source Surface and Alfvénic Fluctuations. *The Astrophysical Journal Supplement Series*, 246(2):54. Publisher: The American Astronomical Society. 16, 70, 72, 73, 74, 96

Parker, E. N. (1958). Dynamics of the Interplanetary Gas and Magnetic Fields. *The Astrophysical Journal*, 128:664. 19, 31, 54, 87

Parker, E. N. (1965). Dynamical theory of the solar wind. *Space Science Reviews*, 4(5):666–708. 87

Parker, E. N. (1991). Heating solar coronal holes. *The Astrophysical Journal*, 372:719. 103

Pascoe, D. J., Nakariakov, V. M., and Kupriyanova, E. G. (2013). Fast magnetoacoustic wave trains in magnetic funnels of the solar corona. *Astronomy & Astrophysics*, 560:A97. Publisher: EDP Sciences. 31

Perez, J. C., Bourouaine, S., Chen, C. H. K., and Raouafi, N. E. (2021a). Applicability of Taylor's hypothesis during Parker Solar Probe perihelia. *Astronomy & Astrophysics*, 650:A22. 23, 52, 74

Perez, J. C., Chandran, B. D. G., Klein, K. G., and Martinović, M. M. (2021b). How Alfvén waves energize the solar wind: heat versus work. *Journal of Plasma Physics*, 87(2):905870218. _eprint: 2103.09365. 66

Pesnell, W. D., Thompson, B. J., and Chamberlin, P. C. (2012). The Solar Dynamics Observatory (SDO). *Solar Physics*, 275:3–15. ADS Bibcode: 2012SoPh..275....3P. 17

Podesta, J. J. (2009). DEPENDENCE OF SOLAR-WIND POWER SPECTRA ON THE DIRECTION OF THE LOCAL MEAN MAGNETIC FIELD. *The Astrophysical Journal*, 698(2):986–999. 66

Pulupa, M., Bale, S. D., Bonnell, J. W., Bowen, T. A., Carruth, N., Goetz, K., Gordon, D., Harvey, P. R., Maksimovic, M., Martínez-Oliveros, J. C., Moncuquet, M., Saint-Hilaire, P., Seitz, D., and Sundkvist, D. (2017). The Solar Probe Plus Radio Frequency Spectrometer: Measurement requirements, analog design, and digital signal processing. *Journal of Geophysical Research: Space Physics*, 122(3):2836–2854. _eprint: https://onlinelibrary.wiley.com/doi/pdf/10.1002/2016JA023345. 55

Raouafi, N. E., Matteini, L., Squire, J., Badman, S. T., Velli, M., Klein, K. G., Chen, C. H. K., Matthaeus, W. H., Szabo, A., Linton, M., Allen, R. C., Szalay, J. R., Bruno, R., Decker, R. B., Akhavan-Tafti, M., Agapitov, O. V., Bale, S. D., Bandyopadhyay, R., Battams, K., Berčič, L., Bourouaine, S., Bowen, T. A., Cattell, C., Chandran, B. D. G., Chhiber, R., Cohen, C. M. S., D'Amicis, R., Giacalone, J., Hess, P., Howard, R. A., Horbury, T. S., Jagarlamudi, V. K., Joyce, C. J., Kasper, J. C., Kinnison, J., Laker, R., Liewer, P., Malaspina, D. M., Mann, I., McComas, D. J., Niembro-Hernandez, T., Nieves-Chinchilla, T., Panasenco, O., Pokorný, P., Pusack, A., Pulupa, M., Perez, J. C., Riley, P., Rouillard, A. P., Shi, C., Stenborg, G., Tenerani, A., Verniero, J. L., Viall, N., Vourlidas, A., Wood, B. E., Woodham, L. D., and Woolley, T. (2023a). Parker Solar Probe: Four Years of Discoveries at Solar Cycle Minimum. *Space Science Reviews*, 219(1):8. 27, 60, 70, 89

Raouafi, N. E., Stenborg, G., Seaton, D. B., Wang, H., Wang, J., DeForest, C. E., Bale, S. D., Drake, J. F., Uritsky, V. M., Karpen, J. T., DeVore, C. R., Sterling, A. C., Horbury, T. S., Harra, L. K., Bourouaine, S., Kasper, J. C., Kumar, P., Phan, T. D., and Velli, M. (2023b). Magnetic Reconnection as the Driver of the Solar Wind. *The Astrophysical Journal*, 945(1):28. Publisher: The American Astronomical Society. 70, 71, 74, 81, 86

Rasca, A. P., Farrell, W. M., MacDowall, R. J., Bale, S. D., and Kasper, J. C. (2021). Near-Sun Switchback Boundaries: Dissipation with Solar Distance. *The Astrophysical Journal*, 916(2):84. Publisher: The American Astronomical Society. 95

Réville, V., Tenerani, A., and Velli, M. (2018). Parametric Decay and the Origin of the Low-frequency Alfvénic Spectrum of the Solar Wind. *The Astrophysical Journal*, 866(1):38. Publisher: American Astronomical Society. 19, 67, 101

Rieutord, M., Roudier, T., Rincon, F., Malherbe, J.-M., Meunier, N., Berger, T., and Frank, Z. (2010). On the power spectrum of solar surface flows. *Astronomy & Astrophysics*, 512:A4. Publisher: EDP Sciences. 99

Riley, P., Sonett, C. P., Balogh, A., Forsyth, R. J., Scime, E. E., and Feldman, W. C. (1995). Alfvenic fluctuations in the solar wind: A case study using Ulysses measurements. *Space Science Reviews*, 72(1):197–200. 31

Riley, P., Sonett, C. P., Tsurutani, B. T., Balogh, A., Forsyth, R. J., and Hoogeveen, G. W. (1996). Properties of arc-polarized Alfvén waves in the ecliptic plane: Ulysses observations. *Journal of Geophysical Research: Space Physics*, 101(A9):19987–19993. ISBN: 0148-0227 Publisher: Wiley Online Library. 117

Rosenthal, C. S., Bogdan, T. J., Carlsson, M., Dorch, S. B. F., Hansteen, V., McIntosh, S. W., McMurry, A., Nordlund, Å., and Stein, R. F. (2002). Waves in the Magnetized Solar Atmosphere. I. Basic Processes and Internetwork Oscillations. *The Astrophysical Journal*, 564(1):508. 12, 100

Shi, C. ., Velli, M., Bale, S. D., Réville, V., Maksimović, M., and Dakeyo, J.-B. (2022a). Acceleration of polytropic solar wind: Parker Solar Probe observation and

one-dimensional model. *Physics of Plasmas*, 29(12):122901. Publisher: American Institute of Physics. 61, 87

Shi, C., Panasenco, O., Velli, M., Tenerani, A., Verniero, J. L., Sioulas, N., Huang, Z., Brosius, A., Bale, S. D., Klein, K., Kasper, J., Wit, T. D. d., Goetz, K., Harvey, P. R., MacDowall, R. J., Malaspina, D. M., Pulupa, M., Larson, D., Livi, R., Case, A., and Stevens, M. (2022b). Patches of Magnetic Switchbacks and Their Origins. *The Astrophysical Journal*, 934(2):152. Publisher: The American Astronomical Society. 57, 70, 71, 74, 79, 95

Shi, C., Sioulas, N., Huang, Z., Velli, M., Tenerani, A., and Réville, V. (2023). Evolution of MHD turbulence in the expanding solar wind: residual energy and intermittency. arXiv:2308.12376 [astro-ph, physics:physics]. 82, 123

Shi, C., Velli, M., Panasenco, O., Tenerani, A., Réville, V., Bale, S. D., Kasper, J., Korreck, K., Bonnell, J. W., de Wit, T. D., Malaspina, D. M., Goetz, K., Harvey, P. R., MacDowall, R. J., Pulupa, M., Case, A. W., Larson, D., Verniero, J. L., Livi, R., Stevens, M., Whittlesey, P., Maksimovic, M., and Moncuquet, M. (2021). Alfv\'enic versus non-Alfv\'enic turbulence in the inner heliosphere as observed by Parker Solar Probe. *Astronomy & Astrophysics*, 650:A21. arXiv: 2101.00830. 60, 61, 89

Shi, C., Velli, M., Tenerani, A., Rappazzo, F., and Réville, V. (2020). Propagation of Alfvén Waves in the Expanding Solar Wind with the Fast–Slow Stream Interaction. *The Astrophysical Journal*, 888(2):68. 39, 40, 50, 123

Shi, C., Velli, M., Toth, G., Zhang, K., Tenerani, A., Huang, Z., Sioulas, N., and Holst, B. v. d. (2024). Analytic Model and Magnetohydrodynamic Simulations of Three-dimensional Magnetic Switchbacks. *The Astrophysical Journal Letters*, 964(2):L28. Publisher: The American Astronomical Society. 83

Shi, M., Li, H., Xiao, C., and Wang, X. (2017). The Parametric Decay Instability of Alfvén Waves in Turbulent Plasmas and the Applications in the Solar Wind. *The Astrophysical Journal*, 842(1):63. Publisher: American Astronomical Society. 67

Shoda, M., Chandran, B. D. G., and Cranmer, S. R. (2021). Turbulent Generation of Magnetic Switchbacks in the Alfvénic Solar Wind. *The Astrophysical Journal*, 915(1):52. Publisher: American Astronomical Society. 95

Shrivastav, A. K., Pant, V., Berghmans, D., Zhukov, A. N., Van Doorsselaere, T., Petrova, E., Banerjee, D., Lim, D., and Verbeeck, C. (2023). A Statistical Investigation of Decayless Oscillations in Small-scale Coronal Loops Observed by Solar Orbiter/EUI. Publisher: arXiv Version Number: 2. 10, 88

Simon, G. W. and Leighton, R. B. (1964). Velocity Fields in the Solar Atmosphere. III. Large-Scale Motions, the Chromospheric Network, and Magnetic Fields. *The Astrophysical Journal*, 140:1120. Publisher: IOP ADS Bibcode: 1964ApJ...140.1120S. 2, 9

Sioulas, N., Huang, Z., Shi, C., Velli, M., Tenerani, A., Bowen, T. A., Bale, S. D., Huang, J., Vlahos, L., Woodham, L. D., Horbury, T. S., Wit, T. D. d., Larson, D., Kasper, J., Owen, C. J., Stevens, M. L., Case, A., Pulupa, M., Malaspina, D. M., Bonnell, J. W., Livi, R., Goetz, K., Harvey, P. R., MacDowall, R. J., Maksimović, M., Louarn, P., and Fedorov, A. (2023a). Magnetic Field Spectral Evolution in the Inner Heliosphere. *The Astrophysical Journal Letters*, 943(1):L8. Publisher: The American Astronomical Society. 60, 89

Sioulas, N., Huang, Z., Velli, M., Chhiber, R., Cuesta, M. E., Shi, C., Matthaeus, W. H., Bandyopadhyay, R., Vlahos, L., Bowen, T. A., Qudsi, R. A., Bale, S. D., Owen, C. J., Louarn, P., Fedorov, A., Maksimović, M., Stevens, M. L., Case, A., Kasper, J., Larson, D., Pulupa, M., and Livi, R. (2022). Magnetic Field Intermittency in the Solar Wind: Parker Solar Probe and SolO Observations Ranging from the Alfvén Region up to 1 AU. *The Astrophysical Journal*, 934(2):143. Publisher: The American Astronomical Society. 61, 89, 104

Sioulas, N., Velli, M., Huang, Z., Shi, C., Bowen, T. A., Chandran, B. D. G., Liodis, I., Davis, N., Bale, S. D., and Horbury, T. S. (2023b). On the evolution of the Anisotropic Scaling of Magnetohydrodynamic Turbulence in the Inner Heliosphere. *The Astrophysical Journal*, 951(2):141. Publisher: IOP Publishing. 60, 66, 89, 136

Spruit, H. C. and Bogdan, T. J. (1992). The conversion of p-modes to slow modes and the absorption of acoustic waves by sunspots. *The Astrophysical Journal*, 391:L109. 12, 100

Squire, J., Chandran, B. D. G., and Meyrand, R. (2020). In-situ Switchback Formation in the Expanding Solar Wind. *The Astrophysical Journal*, 891(1):L2. Publisher: American Astronomical Society. 95

Squire, J. and Mallet, A. (2022). On the construction of general large-amplitude spherically polarised Alfvén waves. *Journal of Plasma Physics*, 88(5):175880503. Publisher: Cambridge University Press. 83, 117

Sridhar, S. and Goldreich, P. (1994). Toward a Theory of Interstellar Turbulence. I. Weak Alfvenic Turbulence. *The Astrophysical Journal*, 432:612. ADS Bibcode: 1994ApJ...432..612S. 60

Stefani, F., Forbriger, J., Gundrum, T., Herrmannsdörfer, T., and Wosnitza, J. (2021). Mode Conversion and Period Doubling in a Liquid Rubidium Alfv\'en-Wave Experiment with Coinciding Sound and Alfv\'en Speeds. *Physical Review Letters*, 127(27):275001. Publisher: American Physical Society. 31, 38, 46

Swanson, D. G. (2003). *Plasma waves*. Series in plasma physics. Institute of Physics Pub, Bristol ; Philadelphia, 2nd ed edition. OCLC: ocm52256959. 38, 46

Swanson, D. G. D. G. (1998). *Theory of mode conversion and tunneling in inhomogeneous plasmas / D.G. Swanson.* Wiley, New York. 38, 46

Tan, B., Huang, J., Zhang, Y., Deng, Y., Chen, L., Liu, F., Fan, J., and Shi, J. (2024). The Non-Thermal Radio Emissions of the Solar Transition Region and the Proposal of an Observational Regime. *Universe*, 10(2):82. Number: 2 Publisher: Multidisciplinary Digital Publishing Institute. 3

Taylor, G. I. (1938). The Spectrum of Turbulence. *Proceedings of the Royal Society of London Series A*, 164(919):476–490. 23, 52, 126

Taylor, J. B. (1986). Relaxation and magnetic reconnection in plasmas. *Rev. Mod. Phys.*, 58(3):741–763. Publisher: American Physical Society. 66

Telloni, D., Sorriso-Valvo, L., Woodham, L. D., Panasenco, O., Velli, M., Carbone, F., Zank, G. P., Bruno, R., Perrone, D., Nakanotani, M., Shi, C., D'Amicis, R., De Marco, R., Jagarlamudi, V. K., Steinvall, K., Marino, R., Adhikari, L., Zhao, L., Liang, H., Tenerani, A., Laker, R., Horbury, T. S., Bale, S. D., Pulupa, M., Malaspina, D. M., MacDowall, R. J., Goetz, K., de Wit, T. D., Harvey, P. R., Kasper, J. C., Korreck, K. E., Larson, D., Case, A. W., Stevens, M. L., Whittlesey, P., Livi, R., Owen, C. J., Livi, S., Louarn, P., Antonucci, E., Romoli, M., O'Brien, H., Evans, V., and Angelini, V. (2021). Evolution of Solar Wind Turbulence from 0.1 to 1 au during the First Parker Solar Probe-Solar Orbiter Radial Alignment. *apjl*, 912(2):L21. 60

Tenerani, A., Sioulas, N., Matteini, L., Panasenco, O., Shi, C., and Velli, M. (2021). Evolution of Switchbacks in the Inner Heliosphere. *The Astrophysical Journal Letters*, 919(2):L31. Publisher: American Astronomical Society. 31, 57, 95

Tenerani, A. and Velli, M. (2013). Parametric decay of radial Alfvén waves in the expanding accelerating solar wind. *Journal of Geophysical Research: Space Physics*, 118(12):7507–7516. _eprint: https://onlinelibrary.wiley.com/doi/pdf/10.1002/2013JA019293. 67

Tenerani, A., Velli, M., and Hellinger, P. (2017). The Parametric Instability of Alfvén Waves: Effects of Temperature Anisotropy. *The Astrophysical Journal*, 851(2):99. 67

Tenerani, A., Velli, M., Matteini, L., Réville, V., Shi, C., Bale, S. D., Kasper, J. C., Bonnell, J. W., Case, A. W., Wit, T. D. d., Goetz, K., Harvey, P. R., Klein, K. G., Korreck, K., Larson, D., Livi, R., MacDowall, R. J., Malaspina, D. M., Pulupa, M., Stevens, M., and Whittlesey, P. (2020). Magnetic Field Kinks and Folds in the Solar Wind. *The Astrophysical Journal Supplement Series*, 246(2):32. Publisher: The American Astronomical Society. 57, 83, 103

Tian, H., DeLuca, E. E., Cranmer, S. R., De Pontieu, B., Peter, H., Martínez-Sykora, J., Golub, L., McKillop, S., Reeves, K. K., Miralles, M. P., McCauley, P., Saar, S., Testa, P., Weber, M., Murphy, N., Lemen, J., Title, A., Boerner, P., Hurlburt, N., Tarbell, T. D., Wuelser, J. P., Kleint, L., Kankelborg, C., Jaeggli, S., Carlsson, M., Hansteen, V., and McIntosh, S. W. (2014). Prevalence of small-scale jets from the networks of the solar transition region and chromosphere. *Science*, 346(6207):1255711. 88, 102

Toth, G., Velli, M., and Holst, B. v. d. (2023). Theory of Magnetic Switchbacks Fully Supported by Parker Solar Probe Observations. *The Astrophysical Journal*, 957(2):95. Publisher: The American Astronomical Society. 95

Tsurutani, B. T., Dasgupta, B., Galvan, C., Neugebauer, M., Lakhina, G. S., Arballo, J. K., Winterhalter, D., Goldstein, B. E., and Buti, B. (2002). Phase-steepened Alfvén waves, proton perpendicular energization and the creation of magnetic holes and magnetic decreases: The ponderomotive force. *Geophysical Research Letters*, 29(24):86–1–86–4. _eprint: https://onlinelibrary.wiley.com/doi/pdf/10.1029/2002GL015652. 31

Tsurutani, B. T., Ho, C. M., Arballo, J. K., Lakhina, G. S., Glassmeier, K.-H., and Neubauer, F. M. (1997). Nonlinear electromagnetic waves and spherical arc-polarized waves in space plasmas. *Plasma Physics and Controlled Fusion*, 39(5A):A237–A250. Publisher: IOP Publishing. 31, 87

Tsurutani, B. T., Ho, C. M., Smith, E. J., Neugebauer, M., Goldstein, B. E., Mok, J. S., Arballo, J. K., Balogh, A., Southwood, D. J., and Feldman, W. C. (1994). The relationship between interplanetary discontinuities and Alfvén waves: Ulysses observations. *Geophysical Research Letters*, 21:2267–2270. ADS Bibcode: 1994GeoRL..21.2267T. 31, 117

Tsurutani, B. T., Lakhina, G. S., Sen, A., Hellinger, P., Glassmeier, K.-H., and Mannucci, A. J. (2018). A Review of Alfvénic Turbulence in High-Speed Solar Wind Streams: Hints From Cometary Plasma Turbulence. *Journal of Geophysical Research: Space Physics*, 123(4):2458–2492. _eprint: https://onlinelibrary.wiley.com/doi/pdf/10.1002/2017JA024203. 31

Tsurutani, B. T., Smith, E. J., and Jones, D. E. (1983). Waves observed upstream of interplanetary shocks. *Journal of Geophysical Research: Space Physics*, 88(A7):5645–5656. _eprint: https://onlinelibrary.wiley.com/doi/pdf/10.1029/JA088iA07p05645. 31

Tu, C.-Y. and Marsch, E. (1993). A model of solar wind fluctuations with two components: Alfvén waves and convective structures. *Journal of Geophysical Research: Space Physics*, 98(A2):1257–1276. _eprint: https://onlinelibrary.wiley.com/doi/pdf/10.1029/92JA01947. 104, 139

Tu, C. Y. and Marsch, E. (1995). MHD structures, waves and turbulence in the solar wind: Observations and theories. *Space Science Reviews*, 73(1):1–210. 31, 53, 54, 68, 94, 102, 104, 139

Ulmschneider, P., Priest, E. R., and Rosner, R. (1991). *Mechanisms of Chromospheric and Coronal Heating: Proceedings of the International Conference, Heidelberg, 5–8 June 1990*. Springer Science & Business Media. 18

Ulrich, R. K. (1970). The Five-Minute Oscillations on the Solar Surface. *The Astrophysical Journal*, 162:993. Publisher: IOP ADS Bibcode: 1970ApJ...162..993U. 2, 9, 88

Unti, T. W. J. and Neugebauer, M. (1968). Alfvén Waves in the Solar Wind. *The Physics of Fluids*, 11(3):563–568. 21, 87

Uritsky, V. M. and Davila, J. M. (2012). Multiscale Dynamics of Solar Magnetic Structures. *Astrophys. J.*, 748:60. _eprint: 1111.5053. 86

Uritsky, V. M., DeForest, C. E., Karpen, J. T., DeVore, C. R., Kumar, P., Raouafi, N. E., and Wyper, P. F. (2021). Plumelets: Dynamic Filamentary Structures in Solar Coronal Plumes. *The Astrophysical Journal*, 907:1. Publisher: IOP ADS Bibcode: 2021ApJ...907....1U. 88

Van Doorsselaere, T., Srivastava, A. K., Antolin, P., Magyar, N., Vasheghani Farahani, S., Tian, H., Kolotkov, D., Ofman, L., Guo, M., Arregui, I., De Moortel, I., and Pascoe, D. (2020). Coronal Heating by MHD Waves. *Space Science Reviews*, 216(8):140. 88, 103

Vasil, G. M., Lecoanet, D., Augustson, K., Burns, K. J., Oishi, J. S., Brown, B. P., Brummell, N., and Julien, K. (2024). The solar dynamo begins near the surface. *Nature*, 629(8013):769–772. Publisher: Nature Publishing Group. 1

Vasquez, B. J. and Hollweg, J. V. (1996). Formation of arc-shaped Alfvén waves and rotational discontinuities from oblique linearly polarized wave trains. *Journal of Geophysical Research: Space Physics*, 101(A6):13527–13540. _eprint: https://onlinelibrary.wiley.com/doi/pdf/10.1029/96JA00612. 117

Velli, M. (1993). On the propagation of ideal, linear Alfven waves in radially stratified stellar atmospheres and winds. *Astronomy and Astrophysics*, 270:304–314. ADS Bibcode: 1993A&A...270..304V. 18, 19, 25, 32, 101, 128, 132

Velli, M. (1994). From supersonic winds to accretion: comments on the stability of stellar winds and related flows. *The Astrophysical Journal*, 432:L55–L58. ISBN: 0004-637X. 31

Velli, M., Grappin, R., and Mangeney, A. (1989). Turbulent cascade of incompressible unidirectional Alfvén waves in the interplanetary medium. *Physical Review Letters*, 63(17):1807–1810. 22, 26, 52, 53, 67, 104

Velli, M., Grappin, R., and Mangeney, A. (1991). Waves from the sun? *Geophysical & Astrophysical Fluid Dynamics*, 62(1-4):101–121. 32, 54, 85, 101, 131

Velli, M., Grappin, R., and Mangeney, A. (1992). MHD turbulence in an expanding atmosphere. *AIP Conference Proceedings*, 267(1):154–159. Publisher: American Institute of Physics. 39, 50

Velli, M., Pucci, F., Rappazzo, F., and Tenerani, A. (2015). Models of coronal heating, turbulence and fast reconnection. *Philosophical Transactions of the Royal Society A: Mathematical, Physical and Engineering Sciences*, 373(2042):20140262. Publisher: Royal Society. 103

Verdini, A., Grappin, R., Pinto, R., and Velli, M. (2012). ON THE ORIGIN OF THE $1/f$ SPECTRUM IN THE SOLAR WIND MAGNETIC FIELD. *The Astrophysical Journal*, 750(2):L33. 52, 67, 98, 104

Verdini, A. and Velli, M. (2007). Alfvén Waves and Turbulence in the Solar Atmosphere and Solar Wind. *The Astrophysical Journal*, 662(1):669. Publisher: IOP Publishing. 54

Vernazza, J. E., Avrett, E. H., and Loeser, R. (1981). Structure of the solar chromosphere. III. Models of the EUV brightness components of the quiet sun. *The Astrophysical Journal Supplement Series*, 45:635–725. Publisher: IOP ADS Bibcode: 1981ApJS...45..635V. 4

Vial, J.-C. and Engvold, O., editors (2015). *Solar Prominences*, volume 415 of *Astrophysics and Space Science Library*. Springer International Publishing, Cham. 3

Virtanen, P., Gommers, R., Oliphant, T. E., Haberland, M., Reddy, T., Cournapeau, D., Burovski, E., Peterson, P., Weckesser, W., Bright, J., van der Walt, S. J., Brett, M., Wilson, J., Millman, K. J., Mayorov, N., Nelson, A. R. J., Jones, E., Kern, R., Larson, E., Carey, C. J., Polat, İ., Feng, Y., Moore, E. W., VanderPlas, J., Laxalde, D., Perktold, J., Cimrman, R., Henriksen, I., Quintero, E. A., Harris, C. R., Archibald, A. M., Ribeiro, A. H., Pedregosa, F., and van Mulbregt, P. (2020). SciPy 1.0: fundamental algorithms for scientific computing in Python. *Nature Methods*, 17(3):261–272. Number: 3 Publisher: Nature Publishing Group. 121

Völk, H. J. and Aplers, W. (1973). The propagation of Alfvén waves and their directional anisotropy in the solar wind. *Astrophysics and Space Science*, 20(2):267–285. 40

Vourlidas, A., Howard, R. A., Plunkett, S. P., Korendyke, C. M., Thernisien, A. F. R., Wang, D., Rich, N., Carter, M. T., Chua, D. H., Socker, D. G., Linton, M. G., Morrill, J. S., Lynch, S., Thurn, A., Van Duyne, P., Hagood, R., Clifford, G., Grey, P. J., Velli, M., Liewer, P. C., Hall, J. R., DeJong, E. M., Mikic, Z., Rochus, P., Mazy, E., Bothmer, V., and Rodmann, J. (2016). The Wide-Field Imager for Solar Probe Plus (WISPR). *Space Science Reviews*, 204(1):83–130. 27

Wang, X., He, J., Tu, C., Marsch, E., Zhang, L., and Chao, J.-K. (2012). LARGE-AMPLITUDE ALFVÉN WAVE IN INTERPLANETARY SPACE: THE WIND SPACECRAFT OBSERVATIONS. *The Astrophysical Journal*, 746(2):147. Publisher: The American Astronomical Society. 117

Wedemeyer, S., Bastian, T., Brajša, R., Hudson, H., Fleishman, G., Loukitcheva, M., Fleck, B., Kontar, E. P., De Pontieu, B., Yagoubov, P., Tiwari, S. K., Soler, R., Black, J. H., Antolin, P., Scullion, E., Gunár, S., Labrosse, N., Ludwig, H.-G., Benz, A. O., White, S. M., Hauschildt, P., Doyle, J. G., Nakariakov, V. M., Ayres, T., Heinzel, P., Karlicky, M., Van Doorsselaere, T., Gary, D., Alissandrakis, C. E., Nindos, A., Solanki, S. K., Rouppe van der Voort, L., Shimojo, M., Kato, Y., Zaqarashvili, T.,

Perez, E., Selhorst, C. L., and Barta, M. (2016). Solar Science with the Atacama Large Millimeter/Submillimeter Array—A New View of Our Sun. *Space Science Reviews*, 200(1):1–73. 8

Whang, Y. C. (1973). Alfvén waves in spiral interplanetary field. *Journal of Geophysical Research*, 78(31):7221–7228. 26, 32, 48, 54, 129

Whitham, G. B. (1965). A general approach to linear and non-linear dispersive waves using a Lagrangian. *Journal of Fluid Mechanics*, 22(2):273–283. Edition: 2006/03/28 Publisher: Cambridge University Press. 32, 33, 36, 48

Woolley, T., Matteini, L., Horbury, T. S., Bale, S. D., Woodham, L. D., Laker, R., Alterman, B. L., Bonnell, J. W., Case, A. W., Kasper, J. C., Klein, K. G., Martinović, M. M., and Stevens, M. (2020). Proton core behaviour inside magnetic field switchbacks. *Monthly Notices of the Royal Astronomical Society*, 498(4):5524–5531. 57

Wu, H., Tu, C., Wang, X., He, J., and Yang, L. (2020). Energy Supply for Heating the Slow Solar Wind Observed by Parker Solar Probe between 0.17 and 0.7 au. *The Astrophysical Journal Letters*, 904(1):L8. Publisher: American Astronomical Society. 102, 104

Wu, H., Tu, C., Wang, X., He, J., Yang, L., and Yao, S. (2021a). Energy Supply by Low-frequency Break Sweeping for Heating the Fast Solar Wind from 0.3 to 4.8 au. *The Astrophysical Journal*, 912(2):84. Publisher: American Astronomical Society. 102, 104

Wu, H., Tu, C., Wang, X., and Yang, L. (2021b). Magnetic and Velocity Fluctuations in the Near-Sun Region from 0.1-0.3 au Observed by Parker Solar Probe. *The Astrophysical Journal*, 922(2):92. Publisher: The American Astronomical Society. 102

Yang, L., Zhang, L., He, J., Peter, H., Tu, C., Wang, L., Zhang, S., and Feng, X. (2015). NUMERICAL SIMULATION OF FAST-MODE MAGNETOSONIC WAVES EXCITED BY PLASMOID EJECTIONS IN THE SOLAR CORONA. *The Astrophysical Journal*, 800(2):111. Publisher: American Astronomical Society. 31

Yu, L., Huang, S. Y., Yuan, Z. G., Jiang, K., Wei, Y. Y., Zhang, J., Xu, S. B., Xiong, Q. Y., Wang, Z., Lin, R. T., Li, Y. J., Wang, C. M., and Song, G. J. (2022). Small-Scale Magnetic Holes in the Solar Wind Observed by Parker Solar Probe. *Journal of Geophysical Research: Space Physics*, 127(8):e2022JA030505. _eprint: https://onlinelibrary.wiley.com/doi/pdf/10.1029/2022JA030505. 74

Yu, L., Huang, S. Y., Yuan, Z. G., Jiang, K., Xiong, Q. Y., Xu, S. B., Wei, Y. Y., Zhang, J., and Zhang, Z. H. (2021). Characteristics of Magnetic Holes in the Solar Wind Revealed by Parker Solar Probe. *The Astrophysical Journal*, 908(1):56. Publisher: The American Astronomical Society. 74

Zank, G. P., Zhao, L.-L., Adhikari, L., Telloni, D., Kasper, J. C., and Bale, S. D. (2021). Turbulence transport in the solar corona: Theory, modeling, and Parker Solar Probe. *Physics of Plasmas*, 28(8):080501. 22

Zank, G. P., Zhao, L.-L., Adhikari, L., Telloni, D., Kasper, J. C., Stevens, M., Rahmati, A., and Bale, S. D. (2022). Turbulence in the Sub-Alfvénic Solar Wind. *The Astrophysical Journal Letters*, 926(2):L16. Publisher: American Astronomical Society. 60, 89

Zanna, L. D., Matteini, L., Landi, S., Verdini, A., and Velli, M. (2015). Parametric decay of parallel and oblique Alfvén waves in the expanding solar wind. *Journal of Plasma Physics*, 81(1):325810102. Publisher: Cambridge University Press. 67

Zhang, J., Huang, S. Y., Yuan, Z. G., Jiang, K., Xu, S. B., Bandyopadhyay, R., Wei, Y. Y., Xiong, Q. Y., Wang, Z., Yu, L., and Lin, R. T. (2022). Higher-order Turbulence Statistics in the Sub-Alfvénic Solar Wind Observed by Parker Solar Probe. *The Astrophysical Journal*, 937(2):70. 89

Zhong, S., Nakariakov, V. M., Kolotkov, D. Y., Chitta, L. P., Antolin, P., Verbeeck, C., and Berghmans, D. (2023). Polarisation of decayless kink oscillations of solar coronal loops. *Nature Communications*, 14(1):5298. Number: 1 Publisher: Nature Publishing Group. 10, 88

Zhu, X., He, J., Verscharen, D., Duan, D., and Bale, S. D. (2020). Wave Composition, Propagation, and Polarization of Magnetohydrodynamic Turbulence within 0.3 au as Observed by Parker Solar Probe. *The Astrophysical Journal*, 901(1):L3. 32

Zhugzhda, I. D. and Dzhalilov, N. S. (1982a). Transformation of magnetogravitational waves in the solar atmosphere. *Astronomy and Astrophysics*, 112:16–23. ISBN: 0004-6361. 32, 46, 51

Zhugzhda, Y. D. (1979). Magnetogravity waves in an isothermal conductive atmosphere. *Soviet Astronomy*, 23:42. ISBN: 0038-5301. 32, 46, 51

Zhugzhda, Y. D. and Dzhalilov, N. S. (1981). Conversion of magnetogravitational waves in the solar atmosphere. *Soviet Astronomy*, 25:477. ISBN: 0038-5301. 32, 46, 51

Zhugzhda, Y. D. and Dzhalilov, N. S. (1982b). Linear conversion of magnetogravity waves in an exponential atmosphere. *Sov. J. Plasma Phys.(Engl. Transl.);(United States)*, 8(5). 32, 46, 51